Non-Linear Spectroscopic Studies at Interfaces: Experiment and Theory

A thesis submitted to the University of Southampton
for the degree of
Doctor of Philosophy

Lefteris Danos

School of Chemistry
University of Southampton

· September 2003 ·

To Sensei

UNIVERSITY OF SOUTHAMPTON

ABSTRACT

FACULTY OF SCIENCE
SCHOOL OF CHEMISTRY

Doctor of Philosophy

NON-LINEAR SPECTROSCOPIC STUDIES AT INTERFACES: EXPERIMENT AND THEORY

by Lefteris Danos

The work presented in this thesis is concerned with the study of the air/liquid interface using the non-linear spectroscopic technique of surface second harmonic generation (SHG). The structure of the neat air/toluene interface was studied and the interfacial properties of phenylalanine and rhodamine 6G (R6G) molecules present at the air/water interface were investigated respectively. Computational studies were carried out to evaluate the non-linear optical properties, such as hyperpolarisabilities, of the molecules studied in the SHG experiments and the calculation results were compared to the experimental values.

The structure and properties of the neat air/toluene interface were studied with SHG using a fundamental wavelength of 532 nm. The second harmonic wavelength (266 nm) was resonantly enhanced with the first electronic transition and a polarisation dependence study showed the toluene molecule to be oriented by 36° to the surface normal. Extensive theoretical calculations were carried out using Hartree-Fock (HF), Møller-Plesset (MP2) and Density Functional Theory (DFT) methods on the geometries, harmonic frequencies, excitation energies and frequency dependent (hyper)polarisabilities on the toluene molecule.

The non-linear optical properties of the aromatic amino acid L-phenylalanine (Phe) were investigated at the air/water interface. Polarisation and concentration dependence studies were performed on the air/phenylalanine$_{(aq)}$ interface for concentrations up to 0.08 M. The phenylalanine molecules were found to complete a monolayer for concentrations above 0.02 M and the adsorption could be described by a Langmuir isotherm. The orientation of the molecule at the interface didn't change significantly with increasing bulk concentration and the molecule could be approximated to being weakly aligned at the interface. The surfactant C_{20}-Phe was studied as a Langmuir-Blodgett (LB) film at the air/water interface. The orientation of the Phe chromophore was studied by SHG from the gas phase of the film monolayer and it was found to be shifted 6° away from the surface normal with respect to the orientation of the free Phe molecule at the air/water interface. A frequency dependent calculation on the hyperpolarisability of the Phe molecule with different Phe conformations revealed the sensitivity of the hyperpolarisability values on the conformation of the molecule.

An investigation of the polarisation dependence of the SHG signal at different bulk R6G concentrations at the air/water interface revealed a change in the surface non-linear susceptibility and the possible formation of dimers at the surface. The concentration dependence of the SHG signal showed the formation of a monolayer at bulk dye concentrations of ~ 75 μM and the possibility of further increase in the SHG signal intensity upon the formation of dimers at the surface.

Memorandum

This thesis is an account of original research performed by the author in the Department of Chemistry of the University of Southampton, between October 1999 and October 2002. Where findings of other work have been used, due reference has been given.

Contents

List of Figures

List of Tables

Acknowledgments

I would like to thank my supervisor Jeremy Frey for his trust and patience he showed towards me, without his support this work won't have been possible. I am grateful to the EPSRC for the studentship. I thank John Dyke, and Ed Lee for valuable help with the calculations, and Bob Greef and Bill Brocklesby for useful guidance.

The Hayden Group (Tim, Mike, Scott, Sam, Oli, Claire, Ben, Chris, Jon, Karen, Rafael) and the Frey Group (Naruo, Sam, Hong Chen, Esther, Howard, Fabrice, Alison) over the years have been instrumental in my education into British and international culture, I thank them. Thanks to the Russell group for their water supply.

Many thanks to the Mechanical Workshop, Glassblowers, Physical Teaching Laboratory and the ISVR electronics workshop for all the support and professional work. I am grateful to Colin and Sam for their help in reading parts of the manuscript and their help in financial matters.

My most heartfelt thanks goes to Naruo and all SGI-UK members for their support and encouragement.

Finally my family's support over the years has been greatly appreciated and I will always owe them a debt of gratitude.

Chapter 1

Introduction

1.1 Interfaces

Interfaces occur everywhere and define the boundaries between two bulk materials. The bulk materials can be two liquids or a liquid and its vapour, and are separated by a surface plane with unique chemical and physical properties, which differ from either bulk medium [1,2]. Any chemical species that transfers between the bulk regions must cross the interface. Molecules at the interface experience different forces than the molecules in the bulk phases resulting in different physical properties than the two bulk media. The air/liquid interface is very important and in particular aqueous solution interfaces play an important role in environmental processes, biology and in surfactant science. Each interface possess a free energy change associated with its formation which represents the excess free energy the surface molecules acquire by being at the interface. The adsorption of molecules at the interface creates multilayers but in some cases a layer dimension can be one molecule thick making a monolayer.

Over the past decades, many powerful techniques have been invented for surface characterization [3,4]. Among the existing surface probes the optical techniques are particularly advantageous. They can be applied to all interfaces accessible by light and therefore they are not restricted to surfaces studied in vacuum. Within the interfacial region the molecules are in constant motion. The highly directional probe of an optical technique can study an interface *in situ* without destroying the surface and can reveal information about the structure, dynamics and specific interactions of the molecules present at the surface. A host of different optical spectroscopic techniques are currently used to probe liquid surfaces giving information about their structural properties and stability, and specific techniques will be briefly discussed here.

1.2 Bulk Spectroscopic techniques

1.2.1 Absorption Spectroscopy

UV-visible absorption spectroscopy [5, 6] is concerned with electronic transitions and it can be used to characterize and identify molecules present in a solution, in gas phase or in a solid in a reflection geometry. The electronic transitions depend on the environment and the nature of the absorbing chromophore. The aromatic absorption bands of the three natural occurring amino acids, namely, phenylalanine, tyrosine and tryptophan can be used as a probe in biomolecules using absorption spectroscopy. These molecules can act as probes being sensitive to various environmental factors such as pH change, solvent polarity and orientational effects. Reflection absorption spectroscopy can be used to study the properties of monolayers at the water/air interface and the effect of the molecular orientation on the absorption bands. Absorption of a photon raises the energy of individual molecules within a gas or liquid sample. Collisions within the sample cause the energy to be transferred from the excited species to the bulk resulting in a local increase in temperature and hence pressure. This photoacoustic signal originates solely from heat deposition and can be detected and this is the basis in photoacoustic spectroscopy [7] where the amplitude of the acoustic wave is proportional to the sample absorbance.

1.2.2 Fluorescence Spectroscopy

Fluorescence is one of the possible fates that an electronically excited state can have after absorbing a UV-visible photon. The role of the environment in fluorescence emission is more important than in UV-visible absorption. Fluorescence emission occurs at lower energy (higher wavelength) than absorption because some of the vibrational energy has been lost to the surroundings. Fluorescence spectroscopy has been used extensively for the study of biological systems and recently fluorescence has been employed for single molecule detection [8].

Multiphoton excitation resulting from the simultaneous absorption of two or more photons has been used to study fluorescence of various aromatic compounds, and the tyrosine and tryptophan residues of proteins [9]. In general multiphoton excitation obeys different selection rules from single photon excitation and can therefore be applied to study forbidden transitions which cannot be studied with single photon excitation.

1.3 Surface Probing Techniques

1.3.1 Surface Tension

The inherent asymmetry of forces at an interface results in the generation of a surface tension. Molecules at the surface will make bonds to half as many molecules as their counterparts in the bulk and this will raise the energy of the surface molecules. A liquid surface will try to minimize the surface to volume ratio in order to maximize the number of molecules present at the bulk.

The surface tension γ of a liquid can be defined as the work needed to change the surface area σ of a sample by a small amount $d\sigma$. Thus can be written as: $d\omega=\gamma\ d\sigma$. The surface tensions of liquids are well defined and any deviation from their values can act as an indication of the presence of organic or inorganic impurities. Surface tension measurements though can offer no distinction between the nature of the adsorbed species as it is a macroscopic measurement technique [10].

1.3.2 Ellipsometry

Ellipsometry [11] uses optical frequencies of polarised light incident at an oblique angle to probe surfaces. It can yield information about the thickness of layers, the optical constants of materials, and morphology of surface layers. It is widely used to monitor growth and deposition of films. When a probing laser beam impinges on a surface layer, it undergoes multiple reflections between the phase boundaries of the substrate and the overlayed film (or films). The change in the phase and amplitude of the polarisation of the input beam upon reflection will contain information about the layer on the surface.

1.3.3 Total Internal Reflection Spectroscopy

Total internal reflection fluorescence (TIRF) is a sensitive method for the detection of interfacial species containing appropriate fluorophores and for the measurement of their dynamics [12]. It has been widely used in biological systems to monitor protein adsorption at surfaces by detecting chromophores like tryptophan or using fluorescent labels. The depth of the penetration of the incident electromagnetic wave depends on the angle of incidence, wavelength and the ratio of the refractive indices and typically lies in the range of 200-400 nm. TIRF can measure real time kinetics and allows conformational changes of biomolecules at the interface to be monitored.

1.3.4 Non-Linear Spectroscopy

Most of the techniques discussed so far suffer from insufficient surface sensitivity, especially when submonolayer sensitivity is required, or have difficulty discriminating against the bulk contribution. These drawbacks arise because they are intrinsically not surface specific. Non-linear optical techniques are inherently surface specific because of symmetry requirements forbidding non linear signals occurring in centrosymmetric media. The most important non-linear optical techniques are Second Harmonic Generation (SHG) [13–17] and Sum Frequency Generation SFG [18]. In SHG two photons of frequency ω are converted to a single photon of frequency 2ω which, in the electric dipole approximation occurs in media where the inversion symmetry is broken. In SFG, two photons with frequencies ω_1 and ω_2 are converted to a single photon of frequency (ω=ω_1 + ω_2). The fact that SHG occurs in non-centrosymmetric media makes it an excellent tool for investigating interfaces, as long as they are accessible by light. Interfaces have distinct chemical and physical properties from that of the bulk medium. Using non-linear methods such as SHG it is possible to monitor the structure and properties of interfaces down to submonolayer coverages.

1.4 Computational Chemistry

Computational chemistry [19] has grown significantly in the past two decades with the availability of relative inexpensive and fast computers. It can be applied to single molecule calculations, assemblies of molecules or reactions of molecules. Also with the aid of computer graphics it is possible to simplify complex chemical structures. *Ab Initio* (from the beginning) and Semi-Empirical calculations make use of a quantum-mechanical description of a molecule. This approach is of vital importance for modelling chemical reactions and also is frequently used for the parameterisation of empirical force fields used in molecular mechanics calculations.

The calculation of non-linear properties of molecules using *ab initio* methods has been a rapidly growing field in the past two decades. Time dependent approximating methods have been developed for the calculation of response properties such as (hyper)polarisabilities. Comparison between computed and experimental hyperpolarisabilities has been problematic because of the gas phase environment of the theoretical values versus the solvent environment of the experimental values. Despite these difficulties there is on-going research into efficient theoretical methods for the accurate calculation of the non-linear properties of molecules. In many cases theoretical calculations can aid in the interpretation of experimental results and useful trends and systematic analysis of the properties of molecules can be established.

1.5 Aims and Structure of Thesis

The aim of this work is to use the technique of surface second harmonic generation (SHG) to study the interfacial properties of the air/liquid interface. The understanding of the experimental results is augmented by theoretical calculations on the non-linear properties of molecules present at the interface.

Chapter 1 introduces the importance of the interface environment and of non-linear spectroscopic methods for the study of surfaces and their advantage over linear spectroscopies. The significance of computational methods in conjunction with experiment is highlighted. In Chapter 2 the basic theory of the SHG technique is explained. The experimental details and description of the equipment used is presented in Chapter 3. A description of the theoretical methods and computing packages used in this work is presented in Chapter 4.

Chapters 5, 6, and 7 contain the experimental and theoretical results obtained in this work. Chapter 5 contains SHG studies on the air/toluene interface and results of extensive calculations on geometries, frequencies, excitation energies and hyperpolarisabilities on the free gas phase molecule. Chapter 6 studies the phenylalanine molecule adsorbed at the air/water interface and investigates the conformational dependence of the molecular hyperpolarisability with each theoretical method used. Chapter 7 focuses on the monomer-dimer structure occurring at the air/water interface in the presence of the R6G molecule.

Chapter 8 contains concluding remarks and suggestions to further the experimental work. Finally Chapter 9 contains an Appendix with equations and predicted polarisation curves for different assumptions about the dominant hyperpolarisability tensors based on values produced in this work.

Chapter 2

Theory

2.1 Introduction

2.1.1 The Nature of Light

Light can be thought as a transverse electromagnetic wave consisting of an electric and magnetic field, with their vectors perpendicular to each other and to the propagation vector of the wave. Electromagnetic radiation can be represented by a harmonic wave which vary sinusoidal in space and time and the wave is characterised fully when the frequency, phase and propagation direction and the direction of the electric and magnetic field is known. The relative orientation of these vectors with the propagation vector defines the polarisation of light. Consider the electric field vector for simplicity. In ordinary light sources the orientation and magnitude of the electric field vector will rotate and vary arbitrarily with respect to the propagation vector. This kind of light is referred as unpolarised light. When the orientation of the electric field is constant, but its magnitude varies in time, the light is referred to as linearly or plane polarised light, Figure 2.1.

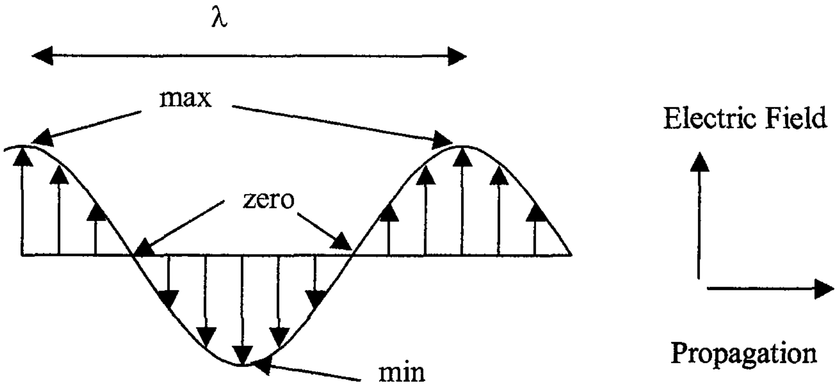

Figure 2.1: The E-field vector linearly polarised at a fixed time.

The polarisation of any light may be treated as the superposition of two harmonic, co-linear, linearly polarised lightwaves of the same frequency. Plane waves polarised in the plane of incidence are called P waves and plane waves polarised perpendicular to the plane of incidence are called S waves. Plane polarised light can be thought as the superposition of these two collinear waves when they are in phase. When their phase difference is 90° and they have equal amplitudes, the light is circularly polarised, and at any other phase difference the light is elliptically polarised.

2.1.2 Laser Radiation

With the discovery of the first laser (Light Amplification by Stimulated Emission of Radiation) by Theodore Maiman [20] in 1960, the scientific community was armed with a powerful investigating tool. In the early years it was said that lasers were a solution looking for a problem. Nowadays lasers are used for many purposes in many fields such as medicine, electronics, and research. Laser radiation has the following characteristics [21–23], which make it very distinct and useful from ordinary light sources.

- Monochromaticity: Each type of laser emits a characteristic wavelength or range of wavelengths. This stems from the fact that only a particular frequency is emitted and amplified.

- Coherence: When light waves are in phase with each other they are said to be coherent. Coherence takes the form of spatial and temporal coherence in terms of the variation of two points in a wave with time and the variation of the electric field at a given point with time.

- Directionality: Electromagnetic waves are directional because they are placed inside a cavity (two parallel mirrors) to oscillate. Nevertheless, the laser beam will always have a finite divergence angle.

- Brightness: A laser beam has a brightness several orders of magnitudes higher than that of conventional sources even at moderate powers. This is mainly due to the high directionality of the lasers.

- Short pulse duration: Pulses come in various durations and with repetition rates. The duration of a pulse can range from milliseconds to femtoseconds. With the technique called mode locking, it is possible to produce pulses whose duration is roughly equal to the inverse of the linewidth of the laser transition frequency.

2.1.3 Refractive Index

When a light beam reaches a surface, some of the light is reflected and some moves into the material, Figure 2.2. According to the law of reflection the angle of incidence is equal to the angle of reflection, i.e,

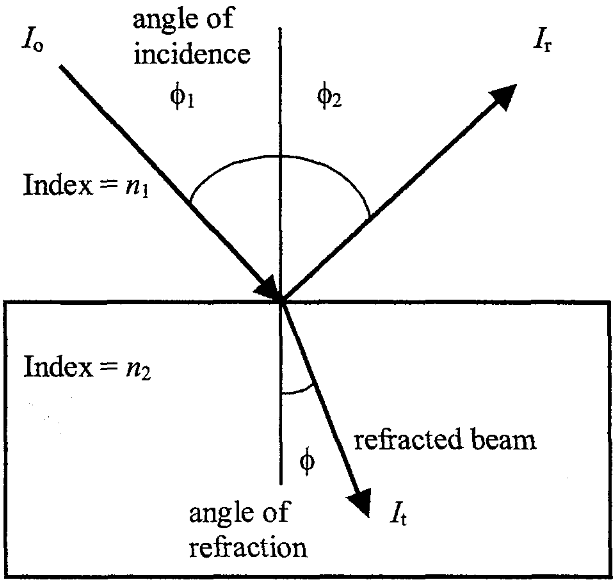

Figure 2.2: Schematic of light reflecting from and passing an interface between air and a material with index of refraction n_2. The incident light with intensity I_o is directed at the interface at an incidence angle ϕ_1 and partially reflected to an angle ϕ_2 with intensity I_r. The rest of the light is refracted with intensity I_t through the interface with an angle of refraction ϕ.

$$\phi_1 = \phi_2 \tag{2.1}$$

The interaction of light with a material is best described with the complex index of refraction n, which is a combination of a real part and a complex part and is given as

$$n = n_o - \imath k \tag{2.2}$$

where n_o is the real component index of refraction and k is called the extinction coefficient and exists when the material absorbs the incident light. For a dielectric material such as glass, visible light is not absorbed and so $k = 0$, so glass is characterised only by n_o (real index of refraction). For light absorbing materials, the refractive index, n, is wavelength dependent and a typical example of how n_o and k are varied with wavelength is shown in Figure 2.3.

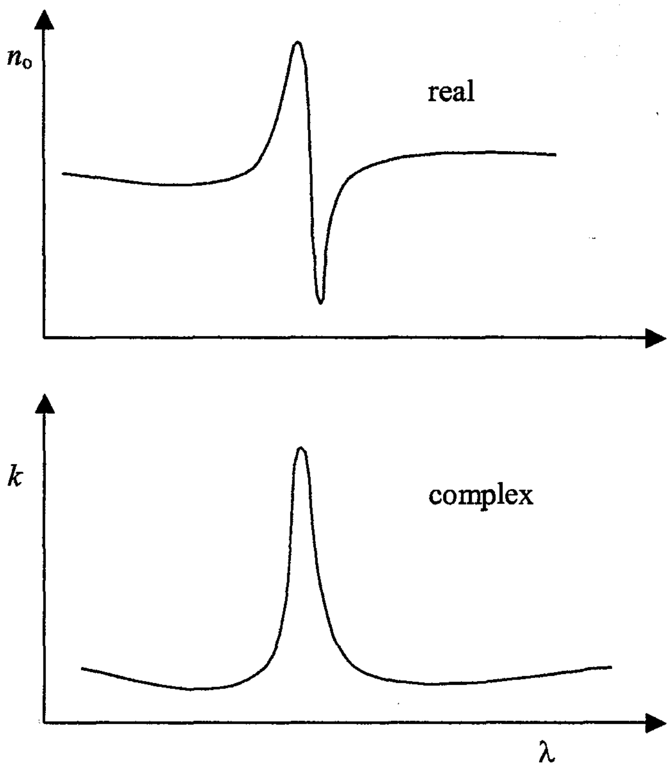

Figure 2.3: The wavelength dependence for n_o and k for light absorbing materials.

2.1.4 Reflected and Transmitted Light

When a light beam is reflected at an interface between medium 1 and medium 2 as shown in Figure 2.2, some of the light is reflected and some is transmitted. The amount of light reflected and transmitted can be estimated by using the Fresnel's equations of reflection. The amplitudes of the reflected and refracted light beams are related to the incident light beam via the Fresnel reflection, r, and refraction, t, coefficients. The Fresnel equations give the relationship between these coefficients, the refractive indices (n_1, n_2), and the angles of incidence and refraction (ϕ, θ). For a non-magnetic material the amplitude coefficients are:

$$r_p = \frac{n_2 \cos\phi - n_1 \cos\theta}{n_2 \cos\phi + n_1 \cos\theta}, r_s = \frac{n_1 \cos\phi - n_2 \cos\theta}{n_1 \cos\phi + n_2 \cos\theta} \tag{2.3}$$

$$t_p = \frac{2n_2 \cos\phi}{n_1 \cos\theta + n_2 \cos\phi}, t_s = \frac{2n_1 \cos\phi}{n_1 \cos\phi + n_2 \cos\theta} \tag{2.4}$$

2.2 Non-Linearity

Non-linear optical phenomena were discovered only after the invention of the laser. The optical properties of materials are independent of the intensity of light at low intensities. However, at high laser power intensities the optical properties begin to depend on intensity and other characteristics of light. The light waves begin to interact with each other and the medium. The intensities necessary to observe optical non-linearity are in the range produced by a laser. The behaviour of light in the non-linear regime can provide valuable information about the properties and structure of matter.

2.2.1 Second Harmonic Generation (SHG)

The essence of second harmonic generation is the conversion of two photons of frequency ω to a single photon with frequency 2ω. In the electric dipole approximation [15], this non-linear optical conversion takes place in media which are non-centrosymmetric and vanishes in centrosymmetric media. The occurrence of SHG in non-centrosymmetric crystals have made them useful as frequency doublers in lasers. At interfaces where the symmetry is broken SHG can be generated and it has been proved capable of being able to probe a few monolayers of atoms.

2.2.2 Basic Theory of SHG

When a dielectric material is subjected to light the electric field causes a distortion to the internal charge distribution. This has the effect of the generation of electric dipole moments, which re-radiate at the same frequency. The total dipole moment per unit volume is called electric polarisation **P** and is proportional to the incident electric field **E**

$$\mathbf{P} = \varepsilon_o \chi^{(1)} \mathbf{E} \tag{2.5}$$

where ε_o, is the permittivity of free space and $\chi^{(1)}$, the electric susceptibility of the medium. At higher electric fields, non-linear effects start to take place and the induced electric polarisation is best described as a power series expansion:

$$\mathbf{P} = \varepsilon_o(\chi^{(1)}\mathbf{E} + \chi^{(2)}\mathbf{E}^2 + \chi^{(3)}\mathbf{E}^3 + ...) \tag{2.6}$$

where $\chi^{(2)}$, $\chi^{(3)}$, are the second and third order susceptibilities and contribute noticeably only at high light powers (i.e. laser powers) giving rise to doubled and tripled frequency radiation generated. Suppose an electromagnetic light, which can be described by:

$$\mathbf{E} = E_o cos(\omega t) \tag{2.7}$$

is incident in a dielectric medium, the resulting polarisation would be:

$$\mathbf{P} = \varepsilon_o(\chi^{(1)} E_o \cos(\omega t) + \chi^{(2)} E_o^2 \cos^2(\omega t) + \chi^{(3)} {E_o}^3 \cos^2(\omega t) + ...) \tag{2.8}$$

In an isotropic medium a change in the direction of the E-field will induce by symmetry a change in the direction of the polarisation P vector, *i.e.* **P**(t)→-**P**(t). Although the sign of the E-field is changed the polarisation sign doesn't change, *i.e.* $(-E^2) = E^2$ and remains positive. In that case the even powers of Equation 2.8 must vanish because although the polarisation changes direction, its magnitude remains unchanged. This is possible only if the even power of χ are zero. Materials therefore with an inversion of symmetry cannot produce SHG or higher even powers of radiation. On the other hand at the interfacial region the symmetry is broken and SHG is possible which makes this technique surface specific. SHG can be described in terms of the second order induced polarisation in the interface by the incoming light.

$$\mathbf{P}^{(2)} = \varepsilon_o \chi^{(2)} E_o^2 \cos^2(\omega t) \tag{2.9}$$

After using the trigonometric relationship between $\cos^n$(x) and cos(nx) Equation 2.9 becomes:

$$\mathbf{P}^{(2)} = \frac{1}{2} \varepsilon_o \chi^{(2)} E_o^2 [\cos(2\omega t) + 1] \tag{2.10}$$

It is apparent that there is a component of the induced second order polarisation that will oscillate at twice the incident frequency, leading to the emission of radiation at this frequency. The second order susceptibility contains all the information on the chemical species which comprise the interface and is a measurable quantity. The second harmonic radiation can be analysed in various ways and provide valuable information about interfacial species [13–16, 24–28]. The strength of the second harmonic signal gives information about the interface population [29, 30], whereas the frequency dependence yields information about the electronic and vibrational energy levels of the molecules at the interface [31]. Also the polarisation and the phase of the generated second harmonic light gives information on absolute interfacial molecular orientation [32]. Finally the change of the above quantities with time gives information about dynamic processes that occur at the interfaces [33–36].

2.2.3 Geometric Description of the Interface

The geometry described below can be applied to any system containing a source of non-linear polarisation with a thickness much smaller than the harmonic wavelength. It can apply to monolayers of molecules adsorbed onto solid or liquid substrates. The three layer geometry shown in Figure 2.4 consists of media 1 and 2 with refractive indices $n_1(\omega)$, $n_1(2\omega)$ and $n_2(\omega)$, $n_2(2\omega)$ at the fundamental ω and harmonic 2ω frequencies, respectively. In the interfacial region lies medium s with thickness d very small compared to the wavelength of the light, $d \leq \lambda$. This non-linear slab, has it's own characteristic refractive indices $n_s(\omega)$, $n_s(2\omega)$ at the fundamental and the harmonic frequencies, respectively. The laboratory frame is defined with the surface normal along the Z-axis pointing upwards and the X-axis along the interface. The Y-axis then defines a X, Y, Z laboratory frame. The polarisation of the incident light makes an angle γ, with the XZ plane. For a P-polarised wave the angle γ is 0° whereas for an S-polarised wave the angle γ is 90°. By varying the angle γ with a half-wave plate the incident polarisation is carefully controlled.

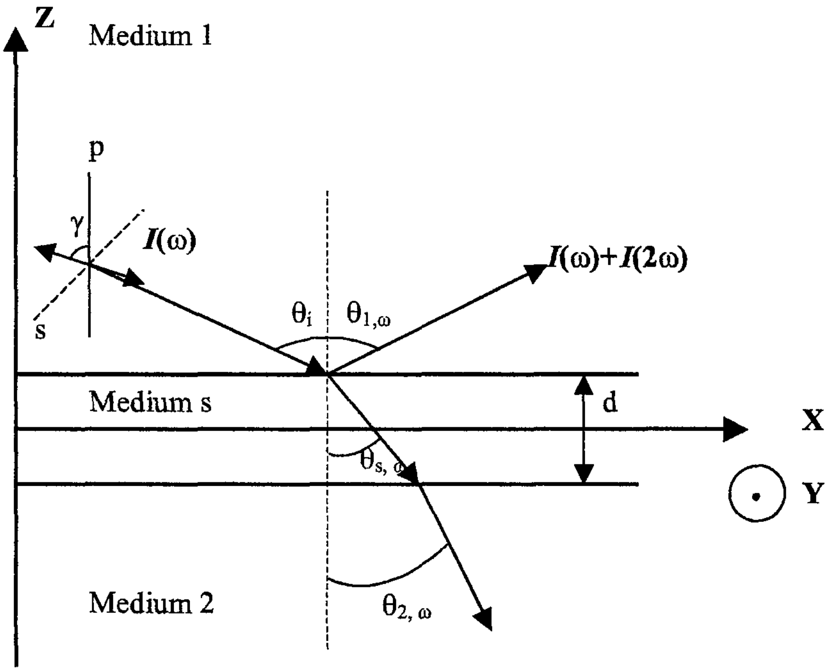

Figure 2.4: Geometry of SHG from an interface in the reflected direction [17].

2.2.4 Signal Intensity

The second harmonic intensity generated at an interface, $I_{SHG}(2\omega)$, is given by the following relation: [15]

$$I_{SHG}(2\omega) = \frac{32\pi^3\omega^2 \sec^2 \theta^{2\omega}}{c^3}|\mathbf{e}^{2\omega} \cdot \chi^{(2)} : \mathbf{e}^{\omega}\mathbf{e}^{\omega}|^2 (I(\omega))^2 \qquad (2.11)$$

where the subscripts ω and 2ω depict parameters calculated at the fundamental or the second harmonic respectively, $\theta^{2\omega}$ is the angle of the incident light beam and the surface normal, c is the speed of light, $\mathbf{e}$ is the product of the incident polarisation vectors and their corresponding Fresnel coefficients at frequencies ω and 2ω, and $\chi^{(2)}$ is the second-order non-linear polarisability tensor. For SHG experiments conducted at a liquid non-chiral surface with azimuthal symmetry, there are only three non-zero independent tensor elements: $\chi^{(2)}_{ZZZ}$, $\chi^{(2)}_{ZXX}$ and $\chi^{(2)}_{XZX}$ [17].

2.2.5 Non-Linear Polarisation

In the one-dimensional case, P, E, and χ, are scalars. In three dimensions, P and E have a direction associated with them and become vectors. Consequently χ is linking one vector to the product of two others and becomes a third rank tensor. So Equation 2.9 can be rewritten:

$$P_i^{(2)}(2\omega) = \frac{1}{2}\varepsilon_o \sum_{jk} \chi^{(2)}_{ijk}(2\omega; \omega, \omega) E_j(\omega) E_k(\omega) \qquad (2.12)$$

where i, j and k take the values X, Y, and Z (Z is the normal, ZX is the plane of incidence). For SHG signals we have index symmetry $\chi^{(2)}_{ijk}=\chi^{(2)}_{ikj}$, furthermore at a air/liquid interface the nonlinear elements $\chi^{(2)}_{ijk}$ reduces to four for a liquid surface with rotational isotropy about the surface normal [22]. Therefore the polarisations P_i are given by:

$$\begin{bmatrix} P_X \\ P_Y \\ P_Z \end{bmatrix} = \begin{bmatrix} 0 & 0 & 0 & \chi^{(2)}_{XYZ} & \chi^{(2)}_{XZX} & 0 \\ 0 & 0 & 0 & \chi^{(2)}_{XZX} & -\chi^{(2)}_{XYZ} & 0 \\ \chi^{(2)}_{ZXX} & \chi^{(2)}_{ZXX} & \chi^{(2)}_{ZZZ} & 0 & 0 & 0 \end{bmatrix} \begin{bmatrix} E_X^2(\omega) \\ E_Y^2(\omega) \\ E_Z^2(\omega) \\ 2E_Z(\omega)E_Y(\omega) \\ 2E_Z(\omega)E_X(\omega) \\ 2E_X(\omega)E_Y(\omega) \end{bmatrix} \qquad (2.13)$$

In the absence of chirality (presence of a mirror plane) the component $\chi^{(2)}_{XYZ}$ becomes zero. From Equation 2.13 the following predictions can be made (see Figure 2.4): For an S-polarised (along the Y-axis) fundamental beam ($\gamma = 90^o$, $P_X = P_Y = 0$ and $P_Z = \chi^{(2)}_{ZXX}\ E_Y^2$) the $I_{SHG}(2\omega)$ is P-polarised and depends on a single tensor component. Also a P-polarised ($\gamma = 0^o$) incident fundamental beam leads to a purely P-polarised $I_{SHG}(2\omega)$ and only a mixed input polarisation can result in a S-polarised $I_{SHG}(2\omega)$ signal. The fields E_i in Equation 2.13 are the fields in the interfacial layer s of Figure 2.4. They are calculated as a function of the input polarisation angle γ:

$$\begin{bmatrix} E_X \\ E_Y \\ E_Z \end{bmatrix} = \begin{bmatrix} e_X \cos\gamma \\ -e_Y \sin\gamma \\ e_Z \cos\gamma \end{bmatrix} E_o \tag{2.14}$$

where γ is the angle between the electric field vector and the ZX-plane and e_i are the Fresnel coefficients for transmission of the fundamental beam from medium 1 to medium s. E_o is the incident radiation field. Combining Equations 2.12, 2.13 and 2.14 results in the following expressions for P out and S out polarisation $I_{SHG}(2\omega)$:

$$I_P^{(2\omega)} \propto |(A\cos^2\gamma + B\sin^2\gamma|^2 I^2(\omega) \tag{2.15}$$

$$I_S^{(2\omega)} \propto |C\sin 2\gamma|^2 I^2(\omega) \tag{2.16}$$

$$A = a_2\chi^{(2)}_{XZX} + a_3\chi^{(2)}_{ZXX} + a_4\chi^{(2)}_{ZZZ} \tag{2.17}$$

$$B = a_5\chi^{(2)}_{ZXX} \tag{2.18}$$

$$C = a_1\chi^{(2)}_{XZX} \tag{2.19}$$

The coefficients a_1-a_5 are functions of the refractive indices and angles of the media in Figure 2.4 and represent the electric field components at the surface

$$a_1 = e_Y(\omega)e_Z(\omega)e_Y(2\omega) \tag{2.20}$$

$$a_2 = 2e_X(\omega)e_Z(\omega)e_X(2\omega) \tag{2.21}$$

$$a_3 = |e_X(\omega)|^2 e_Z(2\omega) \tag{2.22}$$

$$a_4 = |e_Z(\omega)|^2 e_Z(2\omega) \tag{2.23}$$

$$a_5 = |e_Y(\omega)|^2 e_Z(2\omega) \tag{2.24}$$

where for the three layer model of the surface,

$$e_X(\omega) = \cos(\theta_{in})\{1 - \frac{n_2(\omega)\cos(\theta_{in} - n_1(\omega)\cos(\theta_{ref})}{n_1(\omega)\cos(\theta_{ref} + n_2(\omega)\cos(\theta_{in})}\} \tag{2.25}$$

$$e_X(2\omega) = -\frac{2n_1(2\omega)\cos(\theta_{in})\cos(\theta_{ref})}{n_1(2\omega)\cos(\theta_{ref} + n_2(2\omega)\cos(\theta_{in})} \tag{2.26}$$

$$e_Y(\omega) = 1 + \frac{n_1(\omega)\cos(\theta_{in} - n_2(\omega)\cos(\theta_{ref})}{n_1(\omega)\cos(\theta_{in} + n_2(\omega)\cos(\theta_{ref})} \tag{2.27}$$

$$e_Y(2\omega) = \frac{2n_1(2\omega)\cos(\theta_{in})}{n_1(2\omega)\cos(\theta_{in} + n_2(2\omega)\cos(\theta_{ref})} \tag{2.28}$$

$$e_Z(\omega) = \frac{n_1(\omega)^2\sin(\theta_{in})}{n_3(\omega)^2}\{1 + \frac{n_2(\omega)\cos(\theta_{in} - n_1(\omega)\cos(\theta_{ref})}{n_1(\omega)\cos(\theta_{ref} + n_2(\omega)\cos(\theta_{in})}\} \tag{2.29}$$

$$e_Z(2\omega) = \frac{1}{n_3(\omega)^2} - \{\frac{2n_1(2\omega)\cos(\theta_{in})\cos(\theta_{out})}{n_1(2\omega)\cos(\theta_{ref}) + n_2(2\omega)\cos(\theta_{in})}\} \tag{2.30}$$

where, θ_{in} is the angle of incidence, θ_{out} is the angle of reflection, θ_{ref} is the angle of refraction and where, $n_i(\omega)$, $n_i(2\omega)$ are the refractive indices of the interfacial system as shown in Figure 2.4. The calculation of the Fresnel coefficients has the extra difficulty of assuming the value of the interfacial refractive index, which in the case of resonant enhancement SHG can be complex. The experimentally determined non-linear susceptibility $\chi^{(2)}$ may contain other terms due to non-local contributions of the bulk, field gradient effects and quadrupole terms [17].

2.2.6 Theoretical SHG Intensities

The theoretical SHG intensities generated for the four output polarisation arrangements typically used are shown below.

$$I_{\mathrm{P}}^{(2\omega)} \propto |A\cos^2\gamma + B\sin^2\gamma|^2 I^2(\omega) \tag{2.31}$$

$$I_{\mathrm{S}}^{(2\omega)} \propto |C\sin 2\gamma|^2 I^2(\omega) \tag{2.32}$$

$$I_{+45}^{(2\omega)} \propto |\frac{1}{\sqrt{2}}(A\cos^2\gamma + B\sin^2\gamma + C\sin 2\gamma)|^2 I^2(\omega) \tag{2.33}$$

$$I_{-45}^{(2\omega)} \propto |\frac{1}{\sqrt{2}}(A\cos^2\gamma + B\sin^2\gamma - C\sin 2\gamma)|^2 I^2(\omega) \tag{2.34}$$

where γ is the input polarisation angle and the A, B and C coefficients can be complex in the case when the interfacial refractive index is complex. The experimentally determined second harmonic intensities are fitted to Equations 2.31-2.34 and the constants A, B and C are determined along with their phase difference. From them we can determine the second non-linear susceptibility $\chi^{(2)}$, which is a macroscopic quantity.

Once the A, B and C coefficients have been determined from the experimental measured intensities the three $\chi^{(2)}$'s of interest can be obtained. Using Equations 2.17-2.19 we get:

$$\chi_{XZX}^{(2)} \propto \frac{C}{a_1} \tag{2.35}$$

$$\chi_{ZXX}^{(2)} \propto \frac{B}{a_5} \tag{2.36}$$

$$\chi_{ZZZ}^{(2)} \propto \frac{A - (\frac{a_2C}{a_1}) - (\frac{a_3B}{a_5})}{a_4} \tag{2.37}$$

The $\chi^{(2)}$ ratios can now be calculated and are important in the estimation of the molecular orientation parameter and the hyperpolarisability ratios (see appendix A1):

$$\frac{\chi_{ZXX}^{(2)}}{\chi_{ZZZ}^{(2)}} = \frac{Ba_4}{a_5(A - \frac{a_2C}{a_1} - \frac{a_3B}{a_5})} \tag{2.38}$$

$$\frac{\chi_{XZX}^{(2)}}{\chi_{ZZZ}^{(2)}} = \frac{Ca_4}{a_1(A - \frac{a_2C}{a_1} - \frac{a_3B}{a_5})} \tag{2.39}$$

$$\frac{\chi^{(2)}_{ZXX}}{\chi^{(2)}_{XZX}} = \frac{Ba_1}{Ca_5} \tag{2.40}$$

The non-linear susceptibility tensors $\chi^{(2)}_{ZZZ}$, $\chi^{(2)}_{ZXX}$ and $\chi^{(2)}_{XZX}$ can then be related to the molecules that make up the interface, hence obtaining molecular information on orientation.

2.2.7 Resonant Enhancement and the Interfacial Layer

When the adsorbed molecules at an interface are in resonance with an electronic transition with the fundamental or harmonic frequency, the non-linear susceptibility $\overline{\chi}^{(2)}$ increases considerably. As a result of this absorption the interfacial refractive index becomes complex. For dilute aqueous solutions the bulk refractive index remains very similar to that of water. The determination of the refractive index of the interfacial area poses a difficulty in the calculation of the Fresnel coefficients and the evaluation of $\overline{\chi}^{(2)}$ [37]. For adsorbed monolayers the interfacial refractive index can be measured via a Kramers-Kronig analysis of the absorption spectrum [38] or ellipsometric studies. The effective surface region probed with these linear optical techniques can be different from the one actually probed by SHG, limiting the certainty of the interfacial refractive index measured. Using SHG studies it is possible to measure the interfacial refractive index under certain conditions [39].

2.2.8 Molecular Orientation Measurements

Using SHG measurements it is possible to obtain the average orientation of the molecules at the interface. The average molecular orientation of an adsorbed monolayer can be determined from a polarisation dependence of the surface SHG signal intensity. Once the macroscopic non-linear susceptibility $\vec{\chi}^{(2)}$ is determined it is related to the hyperpolarisability β_{ijk},

$$\chi_{IJK} = N_s \sum_{ijk} < \mathbf{T}_{IJK}^{ijk}(\varphi, \theta, \psi) > \beta_{ijk} \tag{2.41}$$

where N_s is the surface number density of molecules, **T** is the transformation matrix which relates the hyperpolarisability in the laboratory coordinate system (*I*,*J*,*K*) and surface molecular coordinate system (*i*,*j*,*k*), as shown in Figure 2.5, and the brackets indicate an average over all molecules. The transformation is achieved by consecutive rotations with angles ϕ, θ, and ψ around the laboratory fixed axis X,Y,Z. The angle θ is the angle between the molecular z-axis and the surface normal(Z-axis), ψ is the rotation about the z-axis and ϕ is the azimuthal angle which for liquid surfaces can be assumed to be an isotropic, random distribution. The following factors affect the derived microscopic parameters:

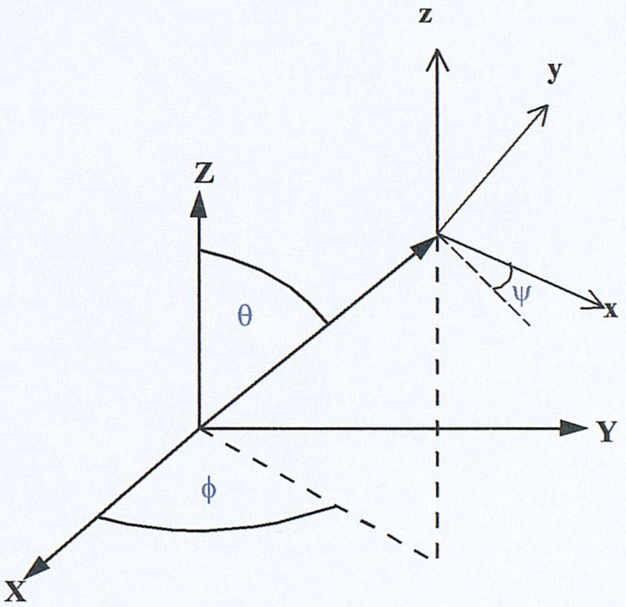

Figure 2.5: Schematic of the relationship between the laboratory frame axis system (X, Y, Z), the molecular axis system (x, y, z) and the Euler angles (ϕ, θ, ψ).

- Assumptions about the value of the interfacial refractive index
- How many and which hyperpolarisability components β_{ijk} are significant

- What is the form of the orientational distribution function

In principle the significant non-zero hyperpolarisability for an approximated C_{2v} symmetry components are three, β_{zzz}, β_{zxx} and β_{xzx} [17,22] but the analysis can be further simplified if the number is reduced to one or two. Different cases are discussed and shown in Appendix A1.

2.3 Adsorption of Molecules at the Air/Liquid Interface

The energetics of adsorption of small molecules at the water interface can be studied with SHG. The SH field amplitude of the observed S-polarised SHG signal is proportional to the number of adsorbed molecules. Using the Langmuir model, a liquid surface can be treated as a lattice of noninteracting sites. The adsorption process can be described as the exchange between bulk molecules (M) and empty surface sites (ES) to give filled sites (FS): M+ES→ FS. At equilibrium we get:

$$\Theta = \frac{kC}{(1+kC)} \tag{2.42}$$

$$I_{SHG}(2\omega) = S\Theta^2 \tag{2.43}$$

where $\Theta = \frac{N}{N_{\mathrm{max}}}$ is the surface coverage with N being the number of molecules present at the interface and N_{max} its maximum number, S is a scaling factor, C is the bulk concentration, and k is the surface adsorption equilibrium constant. The adsorption free energy $\Delta G^{\ominus}{}_{ads}$=-$RTlnK$ where K=55.5k with 55.5 being the molarity of water [32,40].

The above analysis assumes that the molecular orientation distribution remains unchanged with increasing surface coverage. In general the SHG intensity measured for a given polarisation is dependent on the surface number density of molecules and the molecular orientation. In many cases a constant orientation with coverage is observed [32] but apparent orientation angle changes have been observed and an orientation-insensitive methodology has been suggested [29,30].

Chapter 3

Experimental

3.1 Introduction

This chapter contains details about the equipment and methods used during this work. The nanosecond optical system used in Southampton is described followed by the different methods employed for the study of the air/liquid interface by SHG. The study of the bare air/water interface has been used as an example to demonstrate the different experimental methods employed.

3.2 The Nanosecond System in Southampton

3.2.1 Optical Arrangement

The laser source was a Q switched Nd:YAG laser (Continuum NY61 or NY661 or Miniite) with an output wavelength at 1064 nm. The output frequency was doubled (532 nm) using a KD*P doubling crystal. The laser light used for all experiments was at a wavelength of 532 nm with a pulse width of 5 ns and a repetition rate of 10 or 20 Hz.

For some experiments the output beam was split (8%) by a plate glass beamsplitter oriented at 45° to the input beam and focused to a quartz crystal. The second harmonic signal generated from the quartz crystal was detected with a photomultiplier (RCA IP28) after blocking the fundamental frequency with 4 UG5 filters. The second harmonic signals (266 nm) were averaged using a boxcar integrator (SRS 250) and used as a reference signal for the normalisation of the detected signals at different laser powers. Alternatively a photodiode was used to monitor the laser power fluctuations during the SHG experiment.

The remainder of the beam is guided through mirrors to an angle of incidence of 60° with the surface normal. It is passed through a half-wave plate and a beam splitting polariser, which serves as a fine power modulator, shown in Figure 3.1. The beam splitting polariser transmits only S-plane polarised light, so when the angle of the half-wave plate (Ealing Optics) is varied the polarisation presented to the polariser its controlled and hence the power of the S-polarised laser beam leaving the beam splitting polariser.

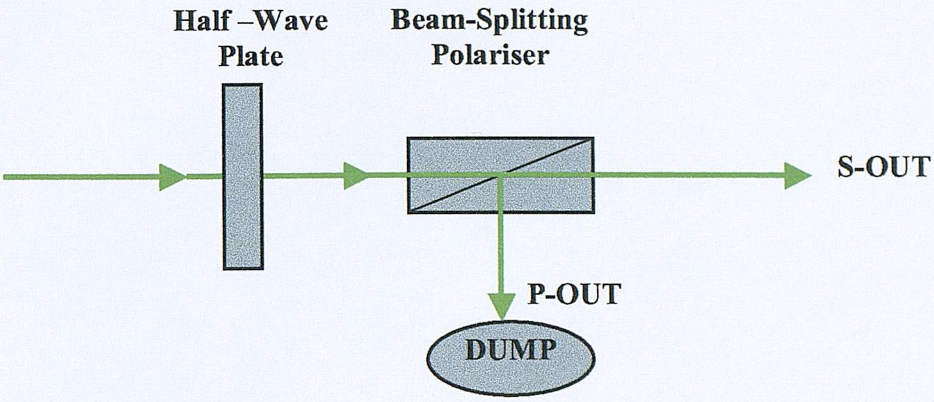

Figure 3.1: Optical arrangement of the power modulator.

The basic experimental arrangement is shown in Figure 3.2. The laser beam exiting the beam splitter is S-polarised and is passed through a second half-wave plate (Ealing Optics). Since the polarisation of the light is known before entering the half-wave plate (S), by varying the angle of the half-wave plate the incidence polarisation angle γ can be carefully controlled. For $\gamma = 0^o$ the input light is P-polarised, whereas for $\gamma = 90^o$ the input light is S-polarised. The beam is passed through a plano convex lens (Comar) and focused (f = 160mm) at the interface. A linear stage (Spindler Hoya TS 10M) was introduced to control the distance of the focusing lens on the sample surface. A yellow glass Schott UV filter was used after the lens to block any unwanted SHG generated from the optics.

The reflected beam is collected with a quartz plano-convex lens (Comar, f = 150mm) and passed through a Rochon (Karl Lambrecht, divergence angle = 3^o) or a Glan Taylor (Halbo Optics) polariser. A focusing lens (Comar fused silica 100 PS 25 f = 100mm) was added to the exit arm in order to recollimate and focus the SHG signal at the entrance slit of the monochromator. The presence of UG5 filters blocks the fundamental frequency. The light then passes through a monochromator (PTI International, grating blazed at 300 nm with 1200 lines/mm) set at 266 nm and to a PMT (Hamamatsu R166). The transmitted and reference signals are averaged using a boxcar integrator. An A/D card linked to a PC (NI PC lab+) digitises the outputs and a Lab view program or Visual Basic program is used for the acquisition of the signals.

A Perspex box encloses the sample area where the sample container usually a petri dish is positioned on a z-axis moveable mount. The petri dish is usually covered with a glass cover fitted with apertures. A steady flow of nitrogen is usually maintained above the sample area to avoid oxidation of the sample by oxygen in the air.

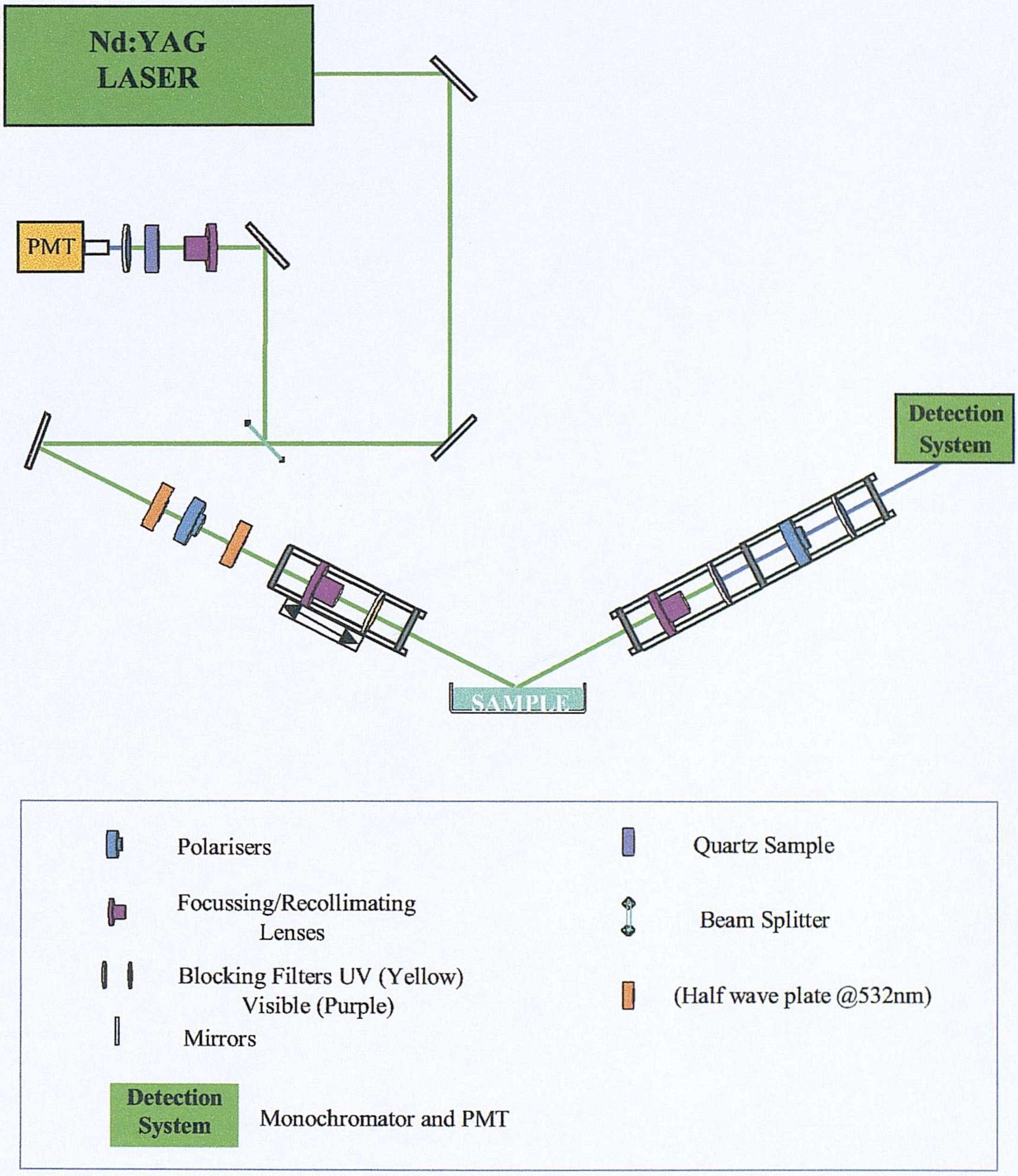

Figure 3.2: Schematic of the optical arrangement used in the SHG experiments.

3.2.2 Development of the Optical Arrangement

The original optical arrangement was altered gradually after initial experiments in order to optimise the experimental performance. A photomultiplier tube sensitive only in the UV range was incorporated. The background signals were lowered because visible light entering the monochromator could not be detected by the PMT. Also in this way the experiment could be operated in the presence of overhead lights making the whole experimental procedure easier and safer.

The introduction of a focusing lens in the output arm acted as a collecting lens increasing the SHG signal detected. The laser beam was focused in the entrance slit of the monochromator. The output Glan Taylor polariser was replaced by a Rochon polariser increasing the sensitivity of the whole experiment appreciably. Glan Taylor polarisers are made from calcite, which have overall transmittance less than 50% in the harmonic wavelength (266 nm). Rochon is made from quartz and the transmittance increases up to 90%.

The half-wave plate rotation angle was controlled via a stepper motor (RS) increasing the accuracy and reproducibility of the input polarisation angle. The time required for the acquisition of SHG signals was shortened significantly.

3.3 Experimental Methods

3.3.1 Sample Handling

The sample was placed in a petri-dish and the surface was cleaned up from any contaminants by applying suction from a vaccum pump or using a micropipette. A glass cover was fitted on top of the petri-dish with windows allowing the incoming beam to enter and leave the sample area, see Figure 3.3. A steady slow flow of nitrogen was applied during the experimental runs. The laser beam was focused slightly above the surface (1 cm) in order to avoid breakdown of the interface induced by the laser beam. Experiments were performed at room temperature (20 °C) or the temperature was controlled via circulating water around the cell with a water bath.

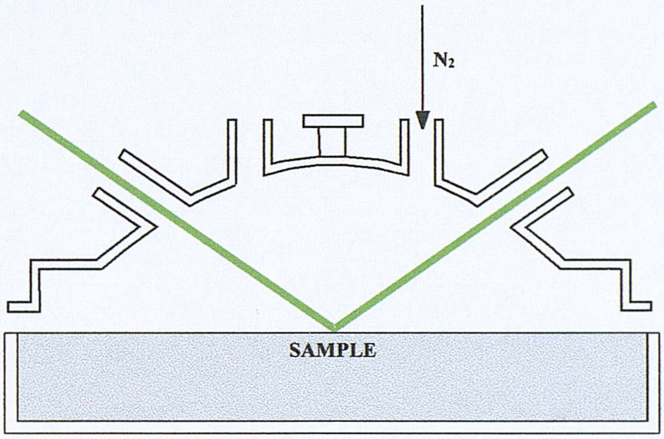

Figure 3.3: Schematic of the sample area

3.3.2 Polarisation Dependence

The polarisation of the incident light beam was controlled with a wavelength (532 nm) specific half-wave plate. The polarisation angle was varied between 0^o and 90^o degrees in increments of 7^o degrees and the harmonic signal was detected for different output polarisations (S, P, 45^o, -45^o) over 1000-2000 laser shots depending on signal intensity. The half-wave plate was controlled via a stepper motor allowing faster acquisition times and higher accuracy. An example of a polarisation dependence plot of the SHG signal for the air/water interface is shown in Figure 3.4. For samples which exhibit resonance enhancement in their SHG response, 1000 laser pulses were sufficient to adequately obtain signal averages. The polarisation dependence acquisition had a duration of about 35 minutes. Background signals were acquired at the beginning and the end of every harmonic output polarisation.

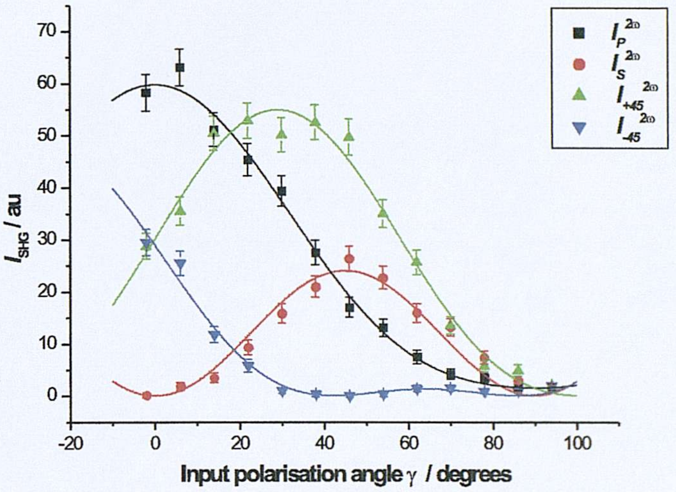

Figure 3.4: Polarisation dependence of SHG signal from the air/water interface for S, P, -45 and +45 , output polarisation planes as a function of the input polarisation angle γ. The solid lines are theoretical fits to equations 2.32-2.34. Error bars are the standard deviation of the mean.

3.3.3 Monochromator Scan

An experimental difficulty when studying organic molecules that absorb strongly at the harmonic wavelength is the presence of an appreciable two photon fluorescence (TPF) signal. In the case of the air/water interface, fluorescence problems do not arise because water does not absorb at either the fundamental or harmonic wavelength. The presence of filters is sufficient to block the fundamental and no special care has to be taken for the width of the monochromator slits. The case is different when studying molecules showing strong fluorescence signals near the harmonic wavelength (266 nm). The widths of the monochromator slits play an important role in separating the overwhelming fluorescence signal from the desired SHG signal. An example of the behaviour of the SHG signal intensity with increasing the entrance slit width of the monochromator is shown in Figure 3.5.

A monochromator scan is shown in Figure 3.6 for the the air/water interface. A gaussian line has been fitted. The half height width is 1.8 nm and by reducing the monochromator slits can be further reduced down to 1 nm.

The bandpass of the monochromator is defined as the range of wavelengths that the monochromator emits about a central wavelength setting. The bandpass depends on the grating (lines/mm) and the slit widths (mm), ignoring the variation of the wavelength. Hence the bandpass (in nm) is the product of the slit width (*W*) (in mm) and the reciprocal linear dispersion (*Rld*) (nm/mm); other values comprised within the (*Rld*) are the Order Integer n (1,2,3,...;use n=1 for highest throughput), grating L (lines/mm), and focal length of Monochromator

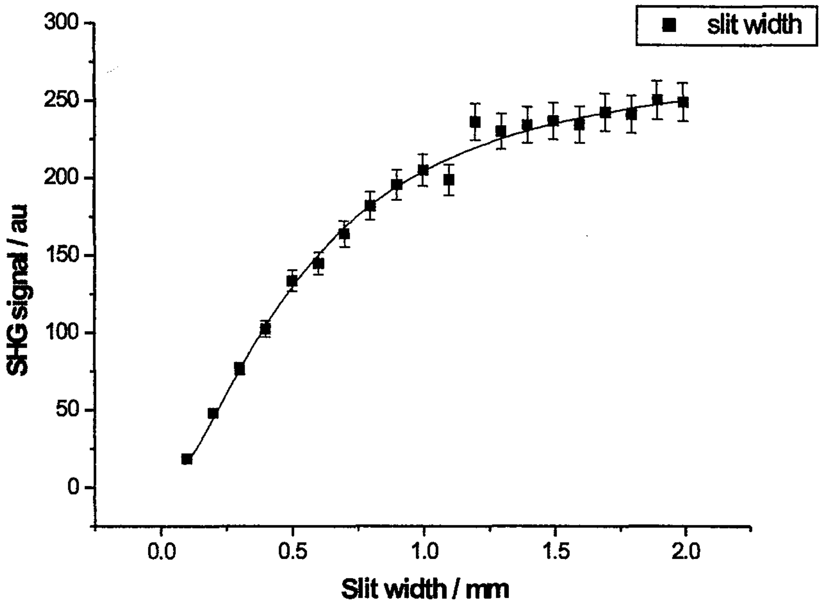

Figure 3.5: Dependence of the SHG signal generated from the air/water interface with variation of the entrance slit width (mm) of the monochromator. A logistic line has been fitted. Error bars are ± 5%.

F(200 mm):

$$Rld = \frac{10^6}{n \times L \times F} \tag{3.1}$$

$$BP = Rld \times W \tag{3.2}$$

Therefore the calculated bandpass for L=1200 lines/mm and W=0.5 mm is 2.1 nm.

3.3.4 Concentration Dependence

One of the sources of errors during experimental runs is the gradual evaporation of the solution under investigation, resulting in a surface drift. Since the region of probing is of a few nm, this reduction in sample height can result in intensity gradients of the light incident to the surface. A high concentration solution was prepared, and diluted with the base solvent (water) during experimental runs using a micropipette (Eppendorf reference 200-1000 mL). A known volume of the solution was extracted and the same volume of solvent was added ensuring constant volume and the vertical position of the interface all the time. Also measurements were taken starting with the base solvent (water) and adding a known concentration solution using the micropipette. In this way both high and low concentration ranges could be probed. The concentration C_{final} was

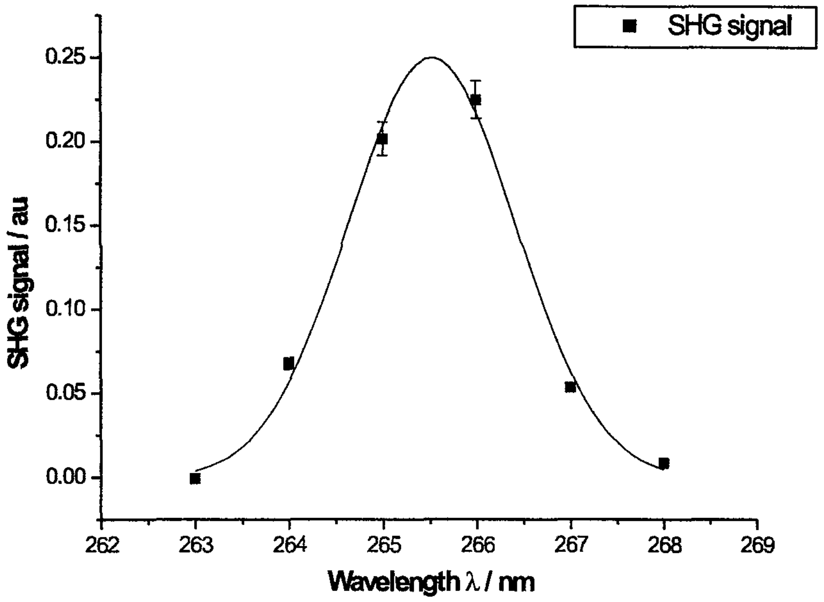

Figure 3.6: Dependence of the SHG signal generated from the air/water interface with variation of the monochromator wavelength. A gaussian line has been fitted. Error bars are ± 5%.

calculated after each dilution or dissolution according to the following equations respectively:

$$C_{final} = \frac{C(V_o - V_{out})}{V_o} \tag{3.3}$$

$$C_{final} = \frac{C_o V_{in} + (C V_o)}{V_o} \tag{3.4}$$

where V_o is the initial volume, V_{out} is the volume taken out and C is the current concentration of the solution. Also for dissolution C_o is the stock solution, C is the concentration after each addition, V_{in} is the added volume.

3.3.5 Laser Stability

The power stability of the laser beam during the SHG experiment is very important in order that accurate and reproducible signal intensities can be acquired. Any power fluctuations during the SHG acquisition time are usually compensated by normalising the measured SHG signal to the SHG signal from a reference quartz sample or a photodiode response. Warm up times for the laser to reach a stable output power where necessary and a typical laser output energy plot versus time is shown in Figure 3.7. Once the desired laser stability is reached the SHG experiment could be carried out with the pulse energy of the laser beam remaining effectively constant throughout, Figure 3.8.

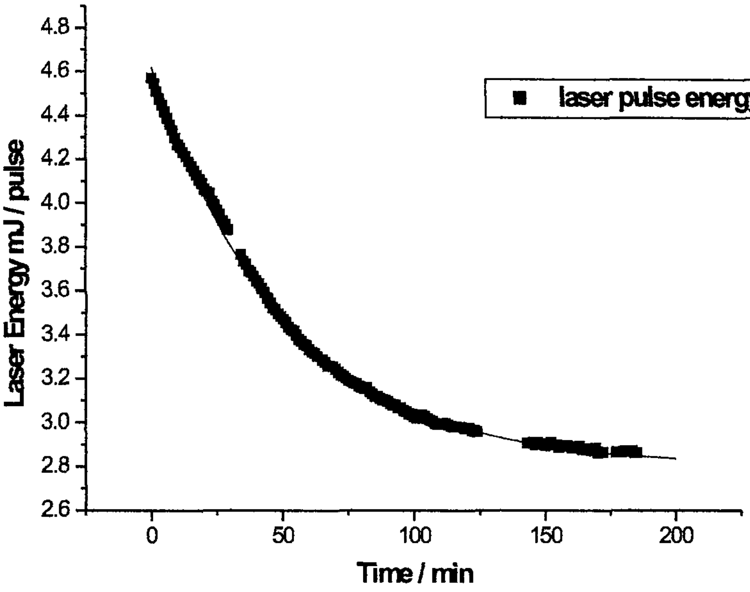

Figure 3.7: Plot of the output laser pulse energy with time from switching on the laser power supply. The long (2-3 hours) warm up time was necessary in order to achieve stability in the output laser energy.

3.3.6 Power Dependence

The SHG signal $I_{SHG}(2\omega)$ intensity is proportional to the quadratic input fundamental intensity $I(\omega)$. A plot of $\mathrm{Ln}I_{SHG}(2\omega)$ vs $\mathrm{Ln}I(\omega)$ should give a straight line with slope 2. A plot of the SHG signal intensity versus the incoming laser intensity is shown in Figure 3.9. The slope of the fitted straight line is 2.06 indicative of the non-linear second harmonic generation process.

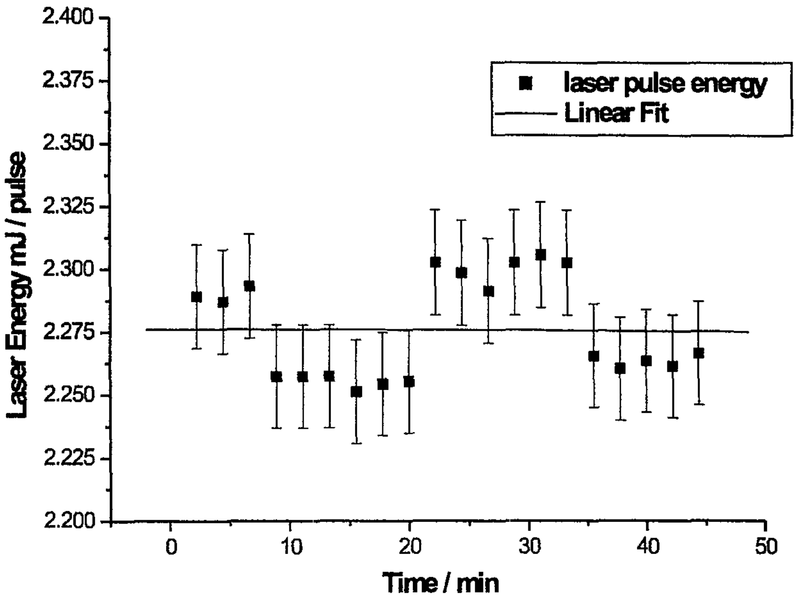

Figure 3.8: Plot of the laser pulse energy with usual SHG acquisition times.

3.4 Sample Preparation

All glassware (class A) was cleaned with a soapy solution rinsed with an excess of water followed by dilute nitric acid and water. Samples were made up in de-ionised water and degassed with nitrogen. All weight measurements were made using a Mettler AE 160 microbalance.

3.4.1 Water Purification

De-ionised water was obtained using a Purite Analyst HP water purification system. Also for the purposes of comparing purity de-ionised water was purchased from Aldrich (ACS reagent) and two different systems were used from the Physical Chemistry Teaching Laboratory (USF Elga, Medica 15) and a Fistreem Cyclon Calypso doubly distilled water system coupled to a Barnstead filter system.

3.4.2 Langmuir-Blodgett Films

Langmuir Blodgett (LB) films [41] are formed at the surface of a liquid when amphiphilic molecules orient themselves with the hydrophobic part of the molecule pointing away from the surface and the hydrophilic part dissolved in the liquid, usually water. A Langmuir Blodgett trough can be used with a moveable barrier and changes in the surface tension of the monolayer at the water

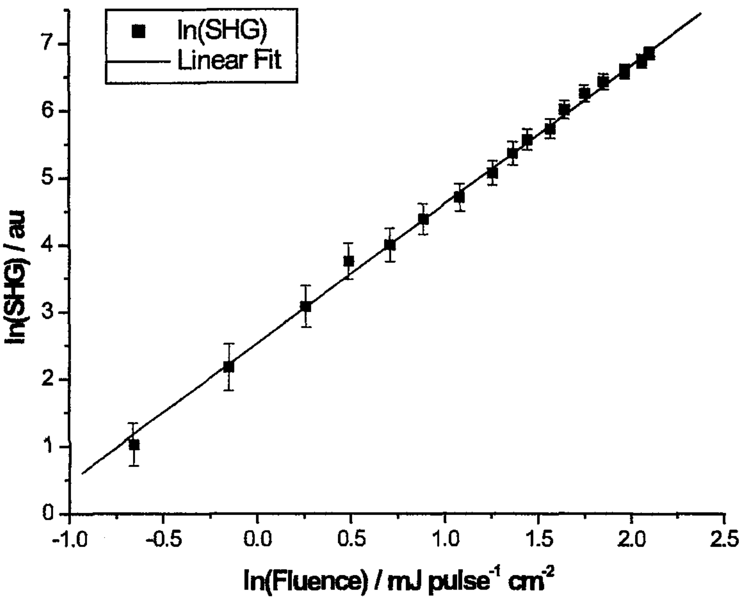

Figure 3.9: ln-ln plot of the SHG signal versus incoming laser intensity obtained for the air/water interface. The slope of the line is 2.06 (regression coefficient r^2=0.9968).

surface can be measured upon compressing the film. The surface tension reduction is monitored as a surface pressure and films are monitored using a Wilhelmy plate. A plot of the surface pressure versus the area occupied by a molecule is recorded as a pressure-area isotherm. The isotherm recorded is a characteristic of the molecule studied and displays well defined regions which correspond to phase changes in the monolayer. At low surface pressure areas the molecules are randomly oriented at the surface. The phase is termed gas phase because the molecules on the surface behave as a two dimensional gas. On further compression the molecules begin to orient themselves with respect to each other and the film behaves as a two-dimensional liquid. Continuing closing the barrier, the pressure causes all the molecules to order and the monolayer film behaves as a quasi solid. This change is accompanied by a steep change in the surface pressure. Eventually if the film is compressed more the collapse pressure is reached where the monolayer film properties are lost and the molecules are ejected out of the monolayer phase.

A NIMA (type 601) LB trough was used for all pressure-area isotherms at room temperature. The amphiphilic molecule studied was C_{20}-Phenylalanine and it was used as a solution in chloroform to assist the spreading of the monolayer.

3.5 Data Acquisition and Processing

3.5.1 Data Sampling

The data were collected over 1000 or 2000 laser shots depending on signal intensities. An acquisition A/D card (National Instruments) was used and the raw data were treated in a software program written in Visual Basic. The averaged signals together with standard deviations of the mean were produced in the form of an output file for the sample signal, the reference signal, and the normalised signal (reference/sample). Background signals were obtained, averaged and subtracted from the sample and reference signals. Averaging was over 1000 or 2000 laser shots using a data acquisition card.

3.5.2 The Fresnel Coefficients

The calculation of the a_1-a_5 fresnel coefficients was done with a software written in Fortran. A knowledge of the three refractive indices was required (n_1, n_3 and n_2) at the fundamental ω and harmonic 2ω frequencies. If an adsorbate was present and absorb at either the fundamental or the harmonic the extinction coefficient, the concentration and the surface coverage were needed. The overlying bulk layer was always air (N_2) and the value of n_1 was set to unity for both the fundamental ω and the harmonic 2ω frequencies. The refractive index n_2 of the underlying bulk liquid was taken from the literature.

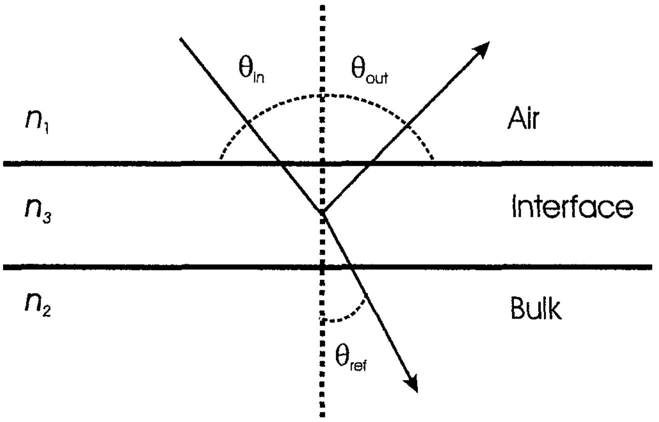

Figure 3.10: Labelling of the refractive indices used in the analysis.

The assignment of the value for the interfacial refractive n_3 is a subject of much controversy in this field [37,39,42]. In this work the value of the interfacial refractive index is assumed to lie between the values of n_1 and n_2, and three cases are discussed where it takes the average of these two indices or the value of either of them. When the system is on resonance then the refractive indices (n_2 and n_3) become complex and they have a non-zero imaginary component values. Their imaginary components are extracted from their absorption spectra [43].

3.5.3 Data Analysis and Optimisation

The observed intensities were fitted to the theoretical equations 2.31-2.34 in order to determine the A, B and C coefficients. In the case of resonance enhancement the parameters of the model (A, B and C) become complex. The parameters can be treated in the Euler representation in which the complex parameters are expressed in terms of their magnitudes and phase angles as $A = r_a \exp(i\phi_a)$, $B = r_b \exp(i\phi_b)$ and $C = r_c \exp(i\phi_c)$. The set of real coefficients to be determined are $(r_a, r_b, r_c, \phi_a, \phi_b, \phi_c)$ which overparametrises the model because absolute phases cannot be determined in the experiment. One of the real coefficients is set to zero, in this case ϕ_a so making A real. Only the relative phases can be estimated and the absolute value of the magnitudes. The parameters are estimated simultaneously by weighted least square minimisation [44] with software written in an R statistical package [45].

Statistical diagnostic methods such as residual plots and normal probability plots can be used to investigate the quality of the fitted data [46]. Examples of diagnostics plots are shown in Figures 3.11 and 3.12 and illustrate the difference between a good quality fit and a bad one. The residual and normal probability plots for the toluene data set, Figure 3.11 show a significant curvature in the plotted values. This is illustrated in the SHG plot where there is scatter in the SHG intensities and a deviation from the theoretical fitting curves. The situation is different for the phenylalanine data set shown in Figure 3.12. The residual plots show the desired even scatter of the plotted values and the SHG signal intensities are fitted well within the theoretical model.

The ratios of the coefficients A, B and C are important when comparing several experiments and also for the estimation of the orientational parameter D and the hyperpolarisability ratios. Consider the ratio between A and B, since the treatment of the other ratios is similar, then in the Euler parameterisation we get:

$$R_{AB} = \frac{r_a \exp(i\phi_a)}{r_b \exp(i\phi_b)} = \frac{r_a}{r_b} \exp(i(\phi_a - \phi_b)) = r_R \exp(i\phi_R) \tag{3.5}$$

from which the variance of the magnitude and phase angle for the ratio can be estimated together with the covariance of the estimated magnitude and phase angle, where the quantities $\hat{r}_R$ and $\hat{\phi}_R$ are the estimated magnitude and phase of the ratio respectively.

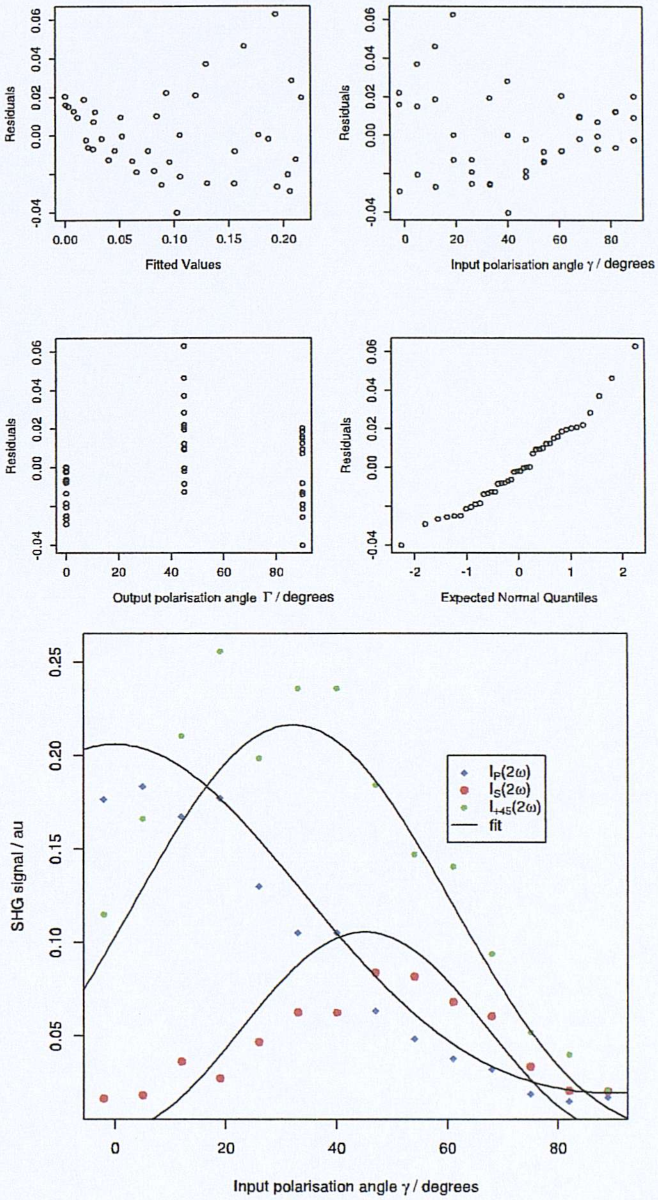

Figure 3.11: Residual and normal probability plots for the simultaneously fitting of the Euler parametrisation to a toluene data set. The residual values (calculated subtracted from fitted) are plotted against the fitted values, the input polarisation angle γ, the output polarisation angle, and the expected normal quantiles. The lower plot shows the polarisation dependence of the SHG signal generated in the S, P and $+45^o$ linear polarisation planes as a function of the input polarisation angle (γ), for the air/toluene interface. The solid lines have been estimated by the simultaneous fitting of the Euler parametrization of A, B, and C parameters in the S, P, and $+45^o$ SHG data assuming A to be real and B and C to be complex. λ=532/266

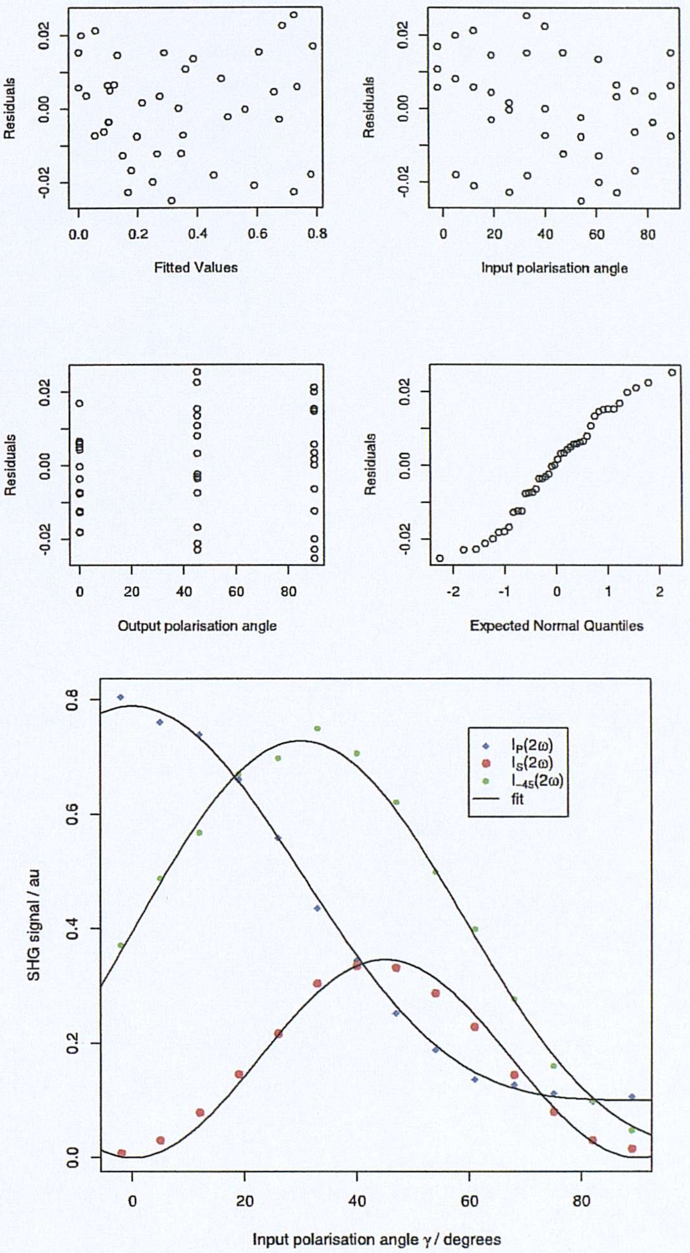

Figure 3.12: Residual and normal probability plots for the simultaneously fitting of the Euler parametrisation to a toluene data set. The residual values (calculated subtracted from fitted) are plotted against the fitted values, the input polarisation angle γ, the output polarisation angle, and the expected normal quantiles. The lower plot shows the polarisation dependence of the SHG signal generated in the S, P and $+45^o$ linear polarisation planes as a function of the input polarisation angle (γ), for 5mM phenylalanine solution. The solid lines have been estimated by the simultaneous fitting of the Euler parametrization of A, B, and C parameters in the S, P, and $+45^o$ SHG data assuming A to be real and B and C to be complex. λ=532/266

Chapter 4

Computational

4.1 Introduction

This chapter aims at giving a description of the theoretical approximation methods used in the thesis for the calculation of molecular structure and properties of molecules studied by experiment. *Ab initio* (from the beginning) molecular orbital calculations can aid in the prediction and better understanding of molecular properties, such as hyperpolarisabilities. In recent years computer programs have evolved and are becoming easier to use by non-experts. With the advent of even faster computers with bigger memory and hard disk space many theoretical calculations have been performed by chemists even without knowing the exact theory. However these black box procedures can often produce results which are not meaningful. In order for the results to aid the understanding of the calculated molecular property, the theoretical method and basis set influence need to be taken into account. In the area of hyperpolarisability calculation, the situation is not clear as to which method is more appropriate for calculation. Theoretical methods can provide an extra help in the interpretation of the experimental results and also predict the direction of appropriate experiments.

4.2 Basis Sets

The description of molecular orbitals is needed for theoretical calculations. Expanding a molecular orbital into a set of known functions is an approximation inherent in all *ab initio* calculations. The size of the basis set determines the accuracy of the representation of the molecular orbital. For an infinite number of functions the basis set is complete but this is impossible in practice. The computational time for carrying out *ab initio* calculations scales as M^4 (or higher), with the number M of the basis functions. It is important therefore to make the basis set small, but without compromising the accuracy of the calculations.

The basis set type also influences the accuracy of the outcome of the calculations. The better the molecular orbital is represented by the single basis function, the fewer of them are needed to adequately describe it giving high accuracy results. Two types of basis functions are used in the construction of basis sets:

Slater Type Orbitals (STO) and *Gaussian Type Orbitals* (GTO). The choice of the atomic orbitals to be used to describe the molecular orbital are taken from solutions of the Schrödinger equation for hydrogen like systems and have the form:

$$\chi_{nlm_l}(r, 0, \phi) = R_{nl}(r)Y_{lm_l}(0, \phi) \tag{4.1}$$

where n, m and m_l are quantum numbers and the R_{nl} and $Y_{lm_l}(\theta, \phi)$ are the radial and angular part of the wavefunction respectively [47, 48].

4.2.1 Slater Type Orbitals

Slater Type Orbitals (STO) are used to approximate the atomic orbitals used to describe the molecular orbital and have the form:

$$\chi^{STO}_{nlm_l}(r, \theta, \phi) = Nr^{n-1}e^{-\zeta r}Y_{lm_l}(\theta, \phi) \tag{4.2}$$

where N is a normalisation constant and ζ is the orbital exponent.

The exponent can be chosen carefully to express each atomic orbital as one STO making the STO orbitals physically reasonable and able to reproduce the exact electron distribution. The evaluation of molecular integrals containing STO functions is not possible with analytical techniques and time consuming numerical methods are needed for their evaluation.

4.2.2 Gaussian Type Orbitals

Gaussian Type Orbitals (GTO) have the general form

$$\chi^{GTO}_{nlm_l}(r, \theta, \phi) = N'p(\alpha)e^{-\alpha r^2}Y_{lm_l}(\theta, \phi) \tag{4.3}$$

with N' being a normalisation constant, $p(\alpha)$ a polynomial in α and α the gaussian orbital exponent. The GTO type functions give rise to molecular integrals which are easy and less time consuming to calculate using analytical methods. Nevertheless they give a less reasonable physical description of the atomic orbitals when compared to the STO functions. Therefore a larger number of GTO is needed to adequately represent each atomic orbital.

4.2.3 Split Valence Basis Sets

These basis sets were introduced in order to achieve a good balance between economy and flexibility in molecular orbital calculations. Different basis sets have been defined based on K-LMG design where K, L, and M are integers and G stands for Gaussian. The symbolism of the letters can be applied to first row element for example with K-s-type inner shell functions and an inner shell of valence s and p type functions (L Gaussians for each) and an outer valence sp set (M Gaussians for each). An example of a split valence basis set is the 6-31G basis set consisting of combining 6 primitive Gaussians for the inner shells and 3 primitive Gaussians for the inner set of valence shells and one primitive

Gaussian for the outer shell. The construction of the full set of basis functions (primitive GTO) into a smaller set of functions employing linear combinations forms a contracted basis set and the resulting basis functions are called contracted GTOs.

4.2.4 Classification of Basis Sets

Once the type of basis set function has be chosen (STO/GTO) the number of functions to be used needs to be determined. A minimal basis set is when each atomic orbital is represented by one basis set function. In the case of STO basis type functions, one STO (one exponent ζ) is used and the basis set is called Single Zeta (SZ). If two, three and four different STO functions are used to describe the occupied atomic orbitals the basis sets are designated as Double Zeta (DZ), Triple Zeta (TZ) and Quadruple Zeta (QZ) respectively.

4.2.5 Polarisation and Diffuse Functions

For most theoretical calculations higher angular momentum functions are important. These are called polarisation functions and are added to the chosen basis set. For example adding a single set of polarisation functions (p-functions on hydrogens and d-functions on the first row elements) to the DZ-basis set used to describe first row elements, produces a Double Zeta plus Polarisation (DZP) basis set. The addition of polarisation functions for a GTO type basis set is denoted by a star (*) sign.

Diffuse functions are functions with low angular momentum quantum number but they have exponents such that they can describe the outer part of the wavefunction (small exponents). Diffuse functions are needed when the calculation of interest depends on the wave function tail (for example hyperpolarisability).

A description and some examples of the basis sets used in this work are shown in Tables 4.1 and 4.2 for STO functions and GTO functions respectively.

Basis set	Description
SZ	A single zeta basis set
DZ	A double zeta basis set
DZP	A double zeta polarised basis set
TZP	A triple zeta polarised basis set
TZ2P	Same as TZP with additional polarisation function added
DZPpolar	An even tempered double zeta basis set with added diffuse functions. The representation for C/H is (7s3p3d/3s3p)
DZPhypol	An even tempered double zeta basis set with added diffuse functions. The representation for C/H is (7s4p3d1f/3s3p1d)
Vdiff	A frozen core (heavy atoms 1s) basis set with added diffuse s-, p- and d-functions. The representation for C/H is (5s4p2d1f/3s2p1d)
ET1	An even tempered quadruple zeta polarised basis set (QZ3P) with added diffuse functions. The representation for C/H is (7s5p3d2f/5s3p2d)

Table 4.1: Basis sets used in this thesis consisting of STO basis functions and contained in the ADF [49] basis set library.

Basis set	Description
6-31G	A split valence basis with 6 contracted PGTOs describing the core orbitals and 3 contracted PGTOs describing the inner valence and 1 PGTO describing the outer valence orbitals.
6-311G	A triple split valence basis with 6 contracted PGTOs describing the core orbitals and three, one and one PGTOs describing the three valence functions respectively
6-31G**	Same as 6-31G with added d-type and p-type polarisation functions on the heavy and hydrogen atoms respectively
6-311G**	Same as 6-311G with added d- and p-polarisation functions on the heavy and hydrogen atoms respectively
6-31++G**	Same as 6-31G** with added diffuse s- and p-functions on heavy atoms and diffuse s-functions added to hydrogens
6-311++G**	Same as 6-311G** with added diffuse s- and p-functions on heavy atoms and diffuse s-functions added to hydrogens
6-31++G(2df,2pd)	A split valence basis 6-31++G with additional diffuse sp functions and two d- and one f-functions on heavy atoms and diffuse s- and two p- and one d-functions on hydrogens
6-311++G(2df,2pd)	A triple split valence basis 6-311++G with additional diffuse sp functions and two d- and one f-functions on heavy atoms and diffuse s- and two p- and one d-functions on hydrogens
Sadlej	This is a triple zeta basis set with added diffuse functions designed for the calculation of molecular electric properties
aug-cc-pVDZ	A correlation consistent polarised valence double zeta with additional diffuse 1s-, 1p- and 1d-functions
6-31GE	This basis set is denoted as 6-31G extended and is available in the Cadpac basis set library. This basis set is obtained from the 6-31G basis by adding diffuse s and p functions and using two sets of polarisation functions

Table 4.2: Basis sets used in this thesis consisting of GTO basis functions and are contained in the Gaussian 94 & 98 [50, 51], Cadpac [52] and Gamess-US [53] basis set libraries.

4.3 The Hartree-Fock (HF) SCF Method

Computational chemistry [19] has grown significantly in the past two decades with the availability of inexpensive and fast computers. It can be applied to single molecule calculations, assemblies of molecules or reactions of molecules. Also with the aid of computer graphics it is possible to simplify complex chemical structures. *Ab Initio* calculations make use of a quantum-mechanical description of the molecule. This approach is of vital importance for modelling chemical reactions and also is frequently used for the parameterisation of empirical force fields used in molecular mechanics calculations. The starting point of *ab initio* calculations is the Schrödinger equation [54]. The time-independent formulation can be given as [47]

$$\mathbf{H}\Psi = E\Psi \tag{4.4}$$

where $\mathbf{H}$ is the Hamiltonian operator, Ψ is the wavefunction describing the state of the system having energy E. A number of approximations are made such as:

- The Born-Oppenheimer approximation: The electronic and nuclear motion are treated as being separate - calculate electronic energy with fixed internuclear distances.

- The Molecular Orbital approximation: The total wavefunction is treated as a product of a series of one electron wavefunctions enforcing Fermion antisymmetry:

$$\Psi = \phi_1\phi_2\phi_3...\phi_N \tag{4.5}$$

- The Linear Combination of Atomic Orbitals approximation (LCAO): Every one electron molecular orbital is treated as a linear combination of known atomic orbitals:

$$\phi_i = \sum_k c_{ik}\chi_k \tag{4.6}$$

The χ_k are the traditional atomic orbitals: s, p, d etc. The choice of the appropriate functional form of the χ_k, together with the parameters used is referred to as the basis set. It's necessary to calculate the c_{ik} values. The Self Consistent Field approach [55] is adopted for complicated systems which makes use of the variation principle. In the HF method, each electron moves in an average field due to all the other electrons. As a result the electron correlations are averaged out, a result which arises from the neglect of the instantaneous interactions (correlations) between electrons [56]. Although the implicit antisymmetry in the wave function allows electron of the same spin partially correlated, the motion of electrons with opposite spin is neglected. The quality of the calculations depend on the size of the basis set. The bigger the LCAO expansion the bigger the basis set would be. For an infinite expansion the Hartree-Fock limit is reached where the calculated energy is the minimum, *i.e.* the most negative. The difference between the HF energy and the exact energy is called the electron correlation energy.

4.4 Density Functional Theory (DFT)

Density functional theory [57] aims at the determination of the exact ground state energy and electron density. In traditional wave function methods the n-electron wave function depends on 3n variables whereas the electron density is a function of 3 variables. The fundamental DFT theorems were developed by Hohenberg and Kohn (HK) [58] 40 years ago. The HK theory states that the electron density of a molecular system of given nuclear coordinates determines the energy and all associated molecular properties of that system. However the functional form of the energy on the electron density function is not known. The theory also states that the exact electron density function is the one that minimises the energy and can be used as a variational method to determine the electron density.

The Kohn-Sham (KS) reformulation of DFT [59] enable the redefinition of the exchange correlation (XC) functional and a KS-DFT calculation leads to a HF calculation. The KS-DFT calculations are different from the HF calculations by the form of the exchange and correlation treatment. The HF method contains exact non-local exchange terms and no correlation and the DFT contains an exchange-correlation functional of the density which includes the electron-electron interaction (non-classical analogue), a correction for the self interaction and a kinetic energy component.

The functional form of the exchange-correlation energy can be approximated using the local density approximation (LDA), gradient corrected approximating (GGA) and hybrid methods and a plethora of exchange-correlation functionals have been developed in the past 20 years [60]. In recent years time dependent density functional theory (TDDFT) has been developed for the calculation of response molecular properties such as frequency dependent (hyper)polarisabilities and excitation energies [61–64]

4.5 MØller-Plesset (MP2) Perturbation Method

MØller-Plesset (MP) Perturbation theory [65] applies perturbation theory for the calculation of the electron correlation energy. The perturbation is carried out on a Hamilton H_0 operator of a model system, which is usually the sum of the one-electron operators. The Hamiltonian expressed as a perturbation of the model system is:

$$H = H_o + \lambda V \tag{4.7}$$

where V is the fluctuation potential corresponding to the difference between the real and model systems and λ is a perturbation parameter. The order of perturbation depends on the powers of λ and the wave function and energy are expanded as power series of the perturbation. MP0 gives the energy of the model system, MP1 gives the HF energy and MP2 gives the electron correlation which typically accounts for 80-90% of the correlation energy [66,67].

4.6 Computing Methods

4.6.1 Calculation of Minimum Energy Geometries and Vibrational Frequencies

An important aspect of *ab inito* calculations is to obtain accurate molecular structures. In order for the calculation of molecular properties to be meaningful optimised geometries are needed for the molecule under study. In conjunction with the calculation of vibrational frequencies global minima and saddle points can be determined and compared to experimental data available (*e.g.* gas phases electron diffraction, spectroscopy). Analytic energy gradients are employed in computing programs to achieve this efficiently but the choice of the theoretical method greatly influences the accuracy and reliability of the geometry minimisation. The convergence rate of the optimisation depends largely on the initial estimation of the molecular geometry.

Harmonic vibrational frequencies can be calculated from the minima geometries from force constant calculations. They can be used as a check for finding out if the calculated optimised geometry corresponds to a global or local minima. The calculation of harmonic frequencies is carried out by evaluating analytic second order derivatives of the total energy with respect to the nuclear coordinates.

4.6.2 Calculation of Excitation Energies

The calculation of excitation electronic energies can be very useful in predicting the resonant enhancement observed in SHG experiments. Theoretical methods have been developed for the calculation of vertical excitation energies with relative success for low lying excited states. TDDFT methods especially are able to reproduce reasonable accuracy with experiment. The situation is not that clear for excitation to Rydberg states but the development of new DFT functionals with correct asymptotic behaviour has greatly improved the predictability of the calculations.

4.6.3 Calculation of Frequency Dependent Hyperpolarisabilities

The calculation of (hyper)polarisabilities and molecular electric properties in general are concerned with the response of the charge distribution in a molecule to an applied external field. The properties are calculated as derivatives of the energy with respect to the applied field. For example the first derivative of energy with respect to a fixed applied electric field defines the dipole moment (μ) of the molecule, the second derivative defines the polarisability tensor (α) and the third derivative defines the hyperpolarisability tensor (β). The calculations usually refer to the electronic hyperpolarisability and the vibrational and rotational contributions need to be considered [68].

There are two different ways in which the derivatives of energy can be calculated. These are the finite difference technique and the analytic method. In the finite field method the energy of the molecular system is calculated for different values of the applied external electric field and the derivative of the energy is calculated from a finite differentiation. This method is easily implemented with any computational program and with careful choice of the external field strengths it can give static (hyper)polarisabilities. It is not possible to calculate frequency dependent properties using the finite field method. In the analytic method the desired molecular property is calculated by evaluating the energy derivatives analytically. This requires considerable computational effort to implement which increases for higher energy derivatives, but once in place it can give faster and more accurate results than the finite field method and can lead to calculation of frequency dependent properties as well. Electronic structure codes such as Cadpac, ADF and Gaussian 98 have implemented finite field and analytic methods for DFT and HF and frequency dependent hyperpolarisabilities of medium sized molecules can now be routinely evaluated.

The presence of a field will influence the molecular system which leads to an induced dipole, quadrupole,... etc moments. The energy E of the molecule in the presence of the electric field can be written in terms of a Taylor expansion with respect to the applied electric field F:

$$E = E(0) + \frac{dE}{dF}F + \frac{1}{2}\frac{d^2E}{dF^2}F^2 + \frac{1}{3!}\frac{d^3E}{dF^3}F^3 + ... \qquad (4.8)$$

where $E(0)$ is the energy of the molecule in the absence of the external electric field. The induced dipole moment can then be calculated as the derivative of energy with respect to the applied electric field.

There have been different conventions adopted for reporting experimental hyperpolarisabilities and making comparison with theoretical values [69]. In this study the Taylor series definition has been adopted and the theoretical results can be compared directly with the experimental determined hyperpolarisability ratios. In a time-dependent field $F = F_o + F_\omega \cos\omega t$ [or equivalently $F = F_o + F_\omega\ e^{i\omega t}$], the induced dipole moment is

$$\begin{aligned} \mu_{ind} = {} & \mu_0 + \alpha_0(-\omega;\omega)F_\omega \cos\omega t + \frac{1}{2}\beta_0 F_0^2 + \beta(-\omega;\omega,0)F_0F_\omega \cos\omega t + \\ & + \frac{1}{4}\beta(0;\omega,-\omega)F_\omega^2 + \frac{1}{4}\beta(-2\omega;\omega,\omega)F_\omega^2 \cos 2\omega t + \frac{1}{6}\gamma_0 F_0^3 + \frac{1}{2}\gamma(-\omega;\omega,0,0)\cdot \\ & \cdot F_0^2 F_\omega \cos\omega t + \frac{1}{4}\gamma(0;\omega,-\omega,0)F_0F_\omega^2 + \frac{1}{4}\gamma(-2\omega;\omega,\omega,0)F_0F_\omega^2 \cos 2\omega t + \\ & + \frac{1}{24}\gamma(-3\omega;\omega,\omega,\omega)F_\omega^3 \cos 3\omega t + \frac{1}{8}\gamma(-\omega;\omega,\omega,-\omega)F_0^3 \cos\omega t + ..., \end{aligned} \qquad (4.9)$$

where μ_0 is the permanent dipole moment, α is the linear polarisability, β is the first hyperpolarisability, and γ is the second hyperpolarisability;$\alpha_0, \beta_0, \gamma_0$ are the static values (at $\omega = 0$) of the linear polarisability, and first and second hyperpolarisability respectively. The advantage of using the Taylor series convention is that as the frequency approaches zero($\lambda = \infty$) the dependent hyperpolarisability tensor tends towards its static value.

The static electronic hyperpolarisability is calculated by finite field calculations, which are based on the Taylor series expansion for the energy given by [68]:

$$E = E_o - \mu F_o - \frac{1}{2!}\alpha_o F_o^2 - \frac{1}{3!}\beta_o F_o^3 - \frac{1}{4!}\gamma_o F_o^4 - ... \tag{4.10}$$

The finite field energies can be calculated at a given level of theory for an appropriate choice of the electric field strengths and, with enough terms included in Equation 4.10, allows an accurate determination of β.

Frequency dependent hyperpolarisabilities are calculated using analytic derivative methods [70,71]. Time dependent Hartree Fock (TDHF) [70,72–74] and time dependent density functional theory (TDDFT) [61,62,64] methods have been developed over the past years and give access to the calculation of excitation energies and frequency dependent molecular properties such as polarisabilities and hyperpolarisabilities. The energies are calculated in terms of the hamiltonian and the wavefunction of the molecule and different implementations have been developed for the HF and DFT theories.

In DFT methods, all calculations are implemented by numerical integration procedures because the integrals involving the exchange correlation functional have to be evaluated numerically. The numerical integration procedure separates the molecular region into a grid with different points taken at different regions of the molecule. The accuracy is determined by the number of points making up the grid which makes it user friendly. For hyperpolarisability calculations, a high grid accuracy is required as important regions outside the molecule need accurate treatment.

There are different conventions employed by theoreticians and experimentalists in reporting hyperpolarisability values. In order to compare between experiment and theory, the convention adopted must be clearly stated. In the case of dc-electric field second harmonic generation experiments the relation between the hyperpolarisabilities expressed in various conventions is [69]:

$$\frac{1}{2}\beta^T = \beta^B = 3\beta^{B^*} = 2\beta^X \tag{4.11}$$

where β^T is the Taylor series convention, β^B is the perturbation series convention [75], β^{B^*} is the EFISH convention [76] used by experimentalists and β^X is the phenomological convention [69]. The atomic units and their SI equivalents are shown in Table 4.3.

	au	SI
E	1 $E_h e^{-1}\alpha_o^{-1}$	5.142×10^{11}V m^{-1}
μ	1 $e\alpha_o$	8.478×10^{-30}C m
α	1 $e^2\alpha_o^2 E_h{}^{-1}$	1.648×10^{-41}C^{2}m^{2}J^{-1}
β	1 $e^3\alpha_o^3 E_h{}^{-2}$	3.206×10^{-53}C^{3}m^{3}J^{-2}

Table 4.3: Atomic units equivalents in the SI system from reference [68].

Chapter 5

Toluene

5.1 Introduction

5.1.1 Preface

This chapter contains experimental and computational work performed on toluene. Interfacial Second Harmonic Generation (SHG) studies have been used to study the neat air/toluene interface at room temperature. The SHG technique [13–16] is a powerful tool to study the air/liquid interface. The interfacial region is probed using a pulsed laser wavelength of 532 nm and information is gained about the structure of the interface and the orientation of the toluene molecules at the interface. Toluene absorbs at the second harmonic laser wavelength at 266 nm, and the SHG signal is expected to be resonance enhanced.

The polarisation dependence of the SHG signal allows some of the tensor components of the non-linear susceptibility, $\bar{\chi}^{(2)}$, to be extracted. Once the non-linear susceptibility tensors are obtained, the significant molecular first hyperpolarisability tensors, β_{ijk}, that get enhanced, can then be determined. The symmetry of the resonance transition that might occur, when the molecules absorb at the fundamental and/or the harmonic, determines the dominant hyperpolarisability tensors. The ratio of the dominant hyperpolarisability tensor elements are determined experimentally and compared to gas phase time dependent *ab initio* calculations. Different computational approximation methods are employed to study the eclipsed and staggered configurations of toluene. The methods used were Hartree Fock (HF), Moller Plesset (MP2), and Density Functional Theory (DFT) approximations with emphasis on the DFT methods. The computational study evaluates the performance of currently available approximation methods in predicting optimization geometries, vibrational frequencies, excitation energies and frequency dependent first molecular hyperpolarisabilities.

It is intended that this computational study will serve as a benchmark in order to evaluate currently available computational methods for the determination of frequency dependent molecular hyperpolarisabilities. Time dependent density functional theory (TDDFT) [60] calculations have recently been applied in the evaluation of response molecular properties such as excitation energies and frequency dependent hyperpolarisabilities. The first applications of TDDFT methods for the calculation of non-linear properties in relatively small molecules (i.e. HF, NH_3, H_2O, CO) were encouraging in comparison to experiment [61,62,64,77]. However in the case of large conjugated organic molecules, TDDFT methods have failed [78, 79] in predicting the correct size of the hyperpolarisabilities. The crucial factor in all DFT methods is the choice of the exchange correlation energy functional. Currently there is much research occurring in the development of successful exchange correlation functionals for the calculation of field dependent properties [80–86]. The results from this study would test the predictability and efficiency of current computational methods to calculate molecular properties, such as first molecular hyperpolarisabilities, β_{ijk}, and compare them to SHG experimentally determined values. The conclusions will be very useful in deciding the appropriate approximation method to be used for more complex molecules, like amino acids and crown ethers.

The SHG studies at the air/toluene interface will provide information about the non-linear response of the benzene chromophore responsible for the resonance enhancement observed in the SHG signal. When a molecule is in near resonance with either the fundamental or the harmonic frequency of the SHG experiment the magnitude of the signal is large and all secondary contributions arising from non-local electric quadrupole terms can be ignored [26]. The SHG signal arising from the interface can solely be attributed to the presence of the molecules in the interfacial region, within the electric dipole approximation. In the case of the air/solvent interface however, previous studies on alcohol solvents [87] have shown that the harmonic response from the air/alcohol interface had major contributions from non-local electric quadrupole terms as well. The SHG signal though was not in resonance enhancement with an electronic transition as is the case for the toluene $\pi \rightarrow \pi^*$ transition.

The comparison between experiment and theory is not intended to be rigorous. Although the respective environments are different, one is in the air/liquid interface and the other in the gas phase, conclusions and trends will be drawn as to whether it is possible to predict the hyperpolarisability size of simple organic molecules like toluene. The theoretical results are an aid to interpret the SHG experiments in order to gain an understanding of molecular behaviour and environment at the air/toluene interface.

5.1.2 Previous Studies

Toluene is an important solvent and synthetic substrate. The conformation of the methyl group is important in order to understand the structure and dynamics of ground and excited state conformations. Also the fluorescence and phosphorescence spectra involve electronic $\pi \rightarrow \pi^*$ transitions.

The methyl group rotation generates two minima symmetric conformers:

1. The staggered conformation, see Figure 5.1, has the methyl C-H bond lying perpendicular to the benzene ring, and the molecule has C_s symmetry.
2. The eclipsed configuration, see Figure 5.1, has one of the methyl C-H bonds

lying in the benzene ring plane and the molecule has C_s symmetry.

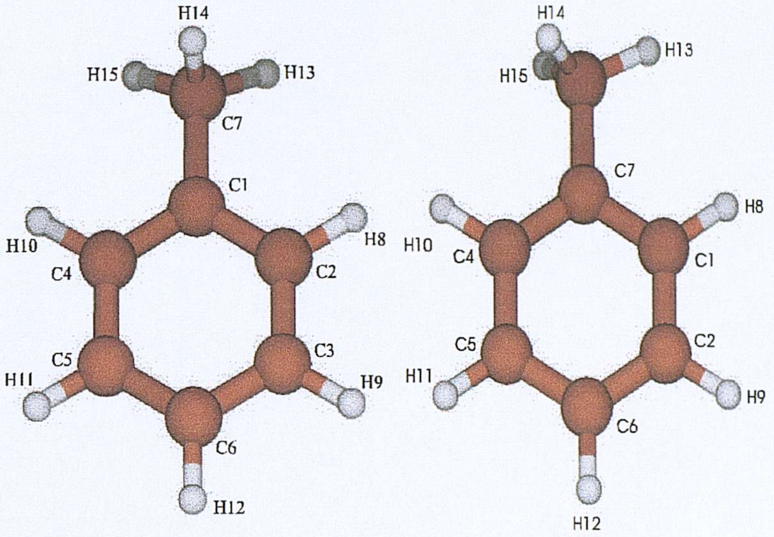

Staggered

Eclipsed

Figure 5.1: Staggered and eclipsed conformation of toluene with the numbering scheme.

The energy difference of these two stable conformers has been studied by microwave spectroscopy [88] and laser supersonic molecular jet spectroscopy [89]; and it was shown that the staggered conformer is lower in energy than the eclipsed conformer by 4.9 cm^{-1} [90]. This small energy difference makes toluene essentially a free rotor with the barrier increasing only slightly in the excited state. Recent computational studies on toluene [91–93] have produced energies, geometries, and vibrational frequencies on ground and excited states for the staggered conformation using HF and MP2 methods. Both conformations were studied and the results are in good agreement with experiments within the reported experimental error [94, 95]. There has been a previous SHG study on the air/toluene interface [96], but the analysis was incomplete. The authors found the toluene molecular plane to be inclined by 42^o, but their study was focusing more on the added solute than the toluene solvent. There have been no previous calculations on the first molecular hyperpolarisability, β, of toluene reported in the literature.

5.1.3 The Absorption Spectrum of Toluene

The absorption spectrum of toluene involves three electronic transitions. The third electronic transition which occurs at longer wavelengths is known as the B-band and shows vibrational fine structure. The maximum wavelength of absorption for toluene dissolved in cyclohexane occurs at 261.75 nm with a molar extinction coefficient of 2864 $M^{-1}cm^{-1}$ [97, 98]. The absorption spectrum of toluene in cyclohexane is shown in Figure 5.2.

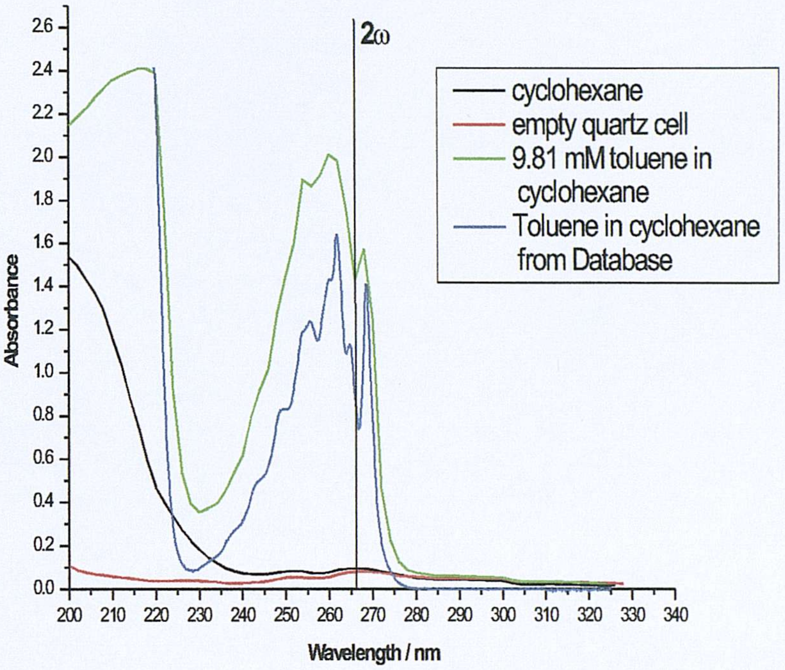

Figure 5.2: The UV spectrum of toluene in cyclohexane. The absorption of cyclohexane and the quartz cell used are shown for reference. Also the UV spectrum obtained from the PhotochemCad Database [97] is shown for comparison.

The absorption maximum for toluene is very close to the second harmonic generated from the toluene-air interface of 266 nm with a molar extinction coefficient of 1527 $M^{-1}cm^{-1}$. We therefore expect the SHG signal to be resonance enhanced. Because of the possibility of two photon fluorescence emission from the toluene molecule, the experimental conditions need to be optimised in order to avoid interference of fluorescence with the SHG signal. The linear fluorescence emission spectrum exhibits a maximum at a wavelength of 292 nm [98] which is very close to the SHG wavelength of 266 nm.

Figure 5.2 shows the absorption trace from the quartz cell used to acquire the absorption spectrum for comparison. Because toluene is a very strong absorber, it needs to be dissolved in cyclohexane. A solution of 9.81 mM was prepared and the absorption spectrum measured. The cyclohexane absorption is shown to start from 240 nm onwards, indicating the possible presence of impurities. For reference, a spectrum obtained from the PhotochemCad package [97] of toluene dissolved in cyclohexane is also shown.

5.2 Experimental

5.2.1 Optical Arrangement

The basic optical arrangement used has been described in chapter 3. Briefly, the SHG experiments were performed with the second harmonic output of a Nd: YAG laser delivering pulses of 5 mJ and 5 ns duration at a wavelength of 532 nm and a repetition rate of 20 Hz. The incident beam was directed at the air/liquid interface at an angle of 60^o (angle between the incident beam and the surface normal). The reflected SH signal at 266 nm was collected with a lens and passed through 3 Schott UG5 UV filters to reject residual light at 532 nm and focused onto the entrance slit of a monochromator. The signal was detected with a fast response photomultiplier tube and sent to a gated boxcar averager. Data was recorded onto a computer using Visual Basic software for further processing. The fundamental input and harmonic output polarisations were controlled by a half-wave plate and quartz Rochon polarizer, respectively.

5.2.2 Data Acquisition and Analysis

Using an in-house software, (Visual Basic, ver. 5.0), data was collected over 1000 shots depending on signal intensities. Background signals and laser power measurements were obtained and averaged over 1000 laser shots and subtracted from the sample signal. The collected data were fitted to the equations described in chapter 2 using R [45] and built-in minimisation functions [44]. In-house software was used for the calculation of the Fresnel coefficients described in chapter 3.

5.2.3 Preparation of Solutions and Sample Handling

Toluene, (Fluka, $\geq$ 99.5% for UV spectroscopy, ACS), was placed in a petri-dish and any contaminants present were cleaned up by applying suction with a vacuum pump or using a micropipette. A glass cover was fitted on top of the petri-dish with windows allowing the incoming beam to enter and leave the sample area. The laser beam was focused slightly above the surface (1 cm) forming a spot size of 0.25 μm in order to avoid breakdown of the interface induced by the laser beam. All experiments were performed at room temperature (19 ^{o}C). Cyclohexane, (Fluka $\geq$ 99.5% for UV spectroscopy free from benzene), was used for the UV spectra.

5.3 Computational Details

The following packages were used for the calculations performed on toluene. Gaussian 94/98 [50, 51], Cadpac [52], Gamess-US [53] and ADF [49]. The Gaussian package was used for the calculation of optimised geometries, frequencies in MP2/6-311G** and HF/6-311G** level. The excitation energies and static hyperpolarisabilities for toluene were computed employing the Sadlej basis set

Functional	Type	Ref
	CADPAC	
LDA	Local Density approximation	[99]
LDAX	A hybrid analogue of LDA	[100]
BLYP	General Gradient Approximation (GGA)	[101,102]
PBE	A non-empirical GGA	[103]
BP86	General Gradient approximation	[101,104]
BP91	General Gradient approximation	[101,105]
HCTH	A 15 parameter GGA fitted to 93 atoms and molecules	[83]
HCTH147	A 15 parameter GGA fitted to 147 atoms and molecules	[106]
HCTH407	A 15 parameter GGA fitted to 407 atoms and molecules	[107]
B3LYP	A three parameter hybrid functional	[108,109]
B97	Hybrid Functional	[84]
B97-1	A 10 parameter hybrid functional	[83]
PBE0	The hybrid analogue of PBE	[110,111]
B3P86	Hybrid Functional	[104,108]
B3P91	Hybrid Functional	[105,108]
	ADF	
LB94	Asymptotic corrected GGA	[86]
GRACLB	Gradient Regulated Asymptotic Correction	[112]
SAOP	Statistical Averaging of Orbital Potentials	[113]

Table 5.1: Summary of the DFT exchange correlation functionals used in this work and are available in Cadpac, ADF and Gaussian computational computing packages.

which corresponds to a 10s6p4d for C and 6s4p for H. Cadpac was used for all DFT methods. For optimizations and frequency calculations the 631GE basis set was employed which corresponds to a 6s5p2d for C and 5s2p for H. The Sadlej basis set was used for the calculation of excitation energies and frequency dependent (hyper)polarisabilities. Gamess-US was used for time dependent HF hyperpolarisability calculations with the Sadlej basis set. ADF was used for the calculation of excitation energies and hyperpolarisabilities employing a variety of Slater type orbital basis sets. Table 5.1 summarizes the exchange correlation functionals used within the different computational packages. Initially the staggered and eclipsed configuration of toluene was optimised using all the available DFT exchange functionals in the Cadpac computational package. The optimised geometries were compared with the HF and MP2 optimised ones. For all the DFT calculations a high computational grid was employed. In addition the staggered geometry of toluene was optimised at the MP2 level employing a variety of Gaussian basis sets in order to investigate the effect of the basis set on the final optimised geometry using the Gaussian package. The above procedure was repeated for the calculation of the harmonic frequencies of the staggered and eclipsed configuration of toluene. The low lying excited states, $\pi \rightarrow \pi^*$ were mainly calculated using the MP2/6-311G** optimised staggered configuration of toluene. The Sadlej basis set was employed and the calculations were performed using the above mentioned computing packages. In the case of ADF a different basis set was employed because ADF uses Slater type orbitals. The results were also compared between packages for the same method to check for any inconsistencies. The static (hyper)polarisability of the staggered conformation of toluene was calculated and compared with different theoretical methods. The effect of the basis set was also investigated. The frequency dependent hyperpolarisability was calculated at various frequencies and a spectrum was obtained indicating a resonance enhancement of the hyperpolarisability tensor.

5.4 Results and Discussion

5.4.1 Calculations

5.4.1.1 Geometry Optimisation and Frequencies

The energies at the optimised geometries for the staggered and the eclipsed conformation of toluene were calculated using HF, MP2 and DFT computational methods available in the CADPAC computational package. A variety of recently developed exchange-correlational functionals were employed in the DFT calculations, see Table 5.1. The basis set used was 631GE corresponding to a 6s5p2d for C and 5s2p for H. For comparison both configurations were optimised at the MP2 level employing different Gaussian basis sets with the Gaussian 98 computing package. No symmetry restrictions were imposed on any of the two conformers and full optimization of all bond lengths, bond angles, and torsional angles was allowed. The calculated values were then cross-checked with the results obtained by fixing the symmetry in both cases. In the staggered configuration there exists plane of symmetry perpendicular to the benzene ring containing the methyl carbon. In the eclipsed configuration the benzene ring was required to constitute a plane of symmetry. No significant changes in the computed results were discovered with or without the imposed symmetry. The energy of the staggered conformation was always lower than the energy of the eclipsed one. It was found that the benzene ring was not planar with the benzene carbons and hydrogen atoms slightly out of plane.

The optimised geometry bond lengths and bond angles of the staggered and eclipsed conformations show good agreement with those obtained in previous studies computational [91–93] on the toluene molecule. The computed bond lengths and angles are in good agreement with the experimental data [94, 95]. On comparison, the computed C-H bond distances are consistently smaller than the experimental ones for all the applied computational methods. The functionals BLYP, LDA, PBE, BP86 and BP91 compute C-H values closer to the experimental values than the rest of the functionals. The computed bond angles do not diverge significantly from the experimentally obtained angles. The performance of all the DFT methods in the computation of bond angles is somewhat better than that of the HF method. The MP2 method predicts the experimental bond angles more reliably.

The harmonic frequencies of the staggered conformation of toluene were computed analytically using HF, MP2, and DFT methods employing the 631GE basis set. The experimental frequencies [93] are compared with the computed values for different approximation methods. The sum of absolute errors has been calculated for each method and the results are shown in Table 5.2. Overall the DFT methods seem to perform better than HF and MP2. The HCTH class of functionals show the best predictive ability.

The sum of absolute errors of the experimental versus the calculated over all bond lengths, bond angles, and harmonic frequencies are shown in Table 5.2. The best performing functional for the determination of the bond lengths was PBE; A recent study [114] suggested that the PBE functional, a non-empirical GGA functional, is very good at bond length prediction. For bond angle determination, the MP2 level of theory provided the best values. The energies of optimised geometries for the staggered and eclipsed conformations of toluene are essentially the same. The difference between the two conformations corresponds to the methyl rotation barrier which has been determined experimentally to be 4.9 cm^{-1} [89]. The small barrier of rotation of the methyl group approaches the accuracy of the *ab initio* calculations, making impractical the energy difference calculation.

Calculation Method	Sum of errors in bond lengths/Å	Sum of errors in bond angles/^{o}	Sum of errors in frequencies/cm^{-1}
		CADPAC/631GE	
HF	0.250	3.46	4636
BLYP	0.125	3.52	846
LDA	0.109	3.37	1003
B3LYP	0.129	3.49	1442
PBE	0.084	3.53	994
PBE0	0.153	3.46	1771
B3P91	0.141	3.46	1597
B3P86	0.133	3.35	1600
BP86	0.091	3.52	-
BP91	0.097	3.62	960
B97	0.122	3.34	1389
BP97-1	0.116	3.31	1362
HCTH	0.112	3.52	1084
HCTH147	0.113	3.77	1072
HCTH407	0.132	3.98	1209
		GAUSSIAN98/6-311G**	
HF	0.268	3.75	4683
MP2	0.131	2.96	2255

Table 5.2: Sum of absolute bond length and bond angle errors for the staggered conformation of toluene between the theoretical and the experimental value: Error=$\sum |experimental - theoretical|$. The vibrational frequency error was calculated according to: Error=$\sum |experimental - theoretical|$ where the experimental and theoretical frequencies were used for each method. The evaluation of the harmonic frequencies with the BP86 method did not converge.

In conclusion the Generalised Gradient Approximation (GGA) functionals PBE, BP86, and BP91 and Local Density Approximation (LDA) functionals perform slightly better at the prediction of the molecular geometry and frequencies of toluene than other GGA functionals. The PBE, BP86, BP91 functionals are non-empirical and are determined only from theoretical considerations. Their performance surpasses the other empirical and heavily parametrised GGA functionals. In addition, the hybrid functionals do not perform as well as the above mentioned functionals contrary to expectation. In any case the DFT methods are performing better than HF methods and some of the DFT functionals perform better than the MP2 approach. It appears that the GGA and LDA approximation methods produce bond lengths of very similar quantitative accuracy with mean errors of 0.01 to 0.02 Å. Bond angles are usually underestimated but generally accurate to within 1^o on average.

5.4.1.2 Excitation Energies

DFT methods are effective at the calculation of energies, geometries and vibrational frequencies. Their performance is comparable to those of demanding wavefunction-based methods. The use of time dependent DFT methods for the computation of excitation energies involving low energy transitions in valence states provides accurate predictions [60] that compare favorably to more computationally demanding wavefunction methods. The TDDFT results cease to be reliable for the modelling of higher lying excited states up to the molecular ionization energy [115]. This arises because the correlation-exchange functionals used, do not to describe adequately energetically important regions far away from the molecule [80, 116]. Over the last ten years asymptotically correct exchange-correlation functionals have been developed in order to accurately predict molecular response properties [83, 86, 112, 113].

In the case of toluene however the low lying $\pi \rightarrow \pi^*$ transitions are of interest because of the possibility of resonance enhancement in the (hyper)polarisability. The calculated energy of the excited states are compared with experimental results in the gas phase and in solution. A selection of functionals was used (PBE, B97-1, B3LYP, HCTH, LB94) in order to calculate the low lying excitation energies of toluene. The orbitals involved in the transitions are shown in Figure 5.3. The π orbitals are no. 24-27. The excited state calculation of toluene will prove useful in determining the possible observed resonance enhancement in the time dependent hyperpolarisability calculations.

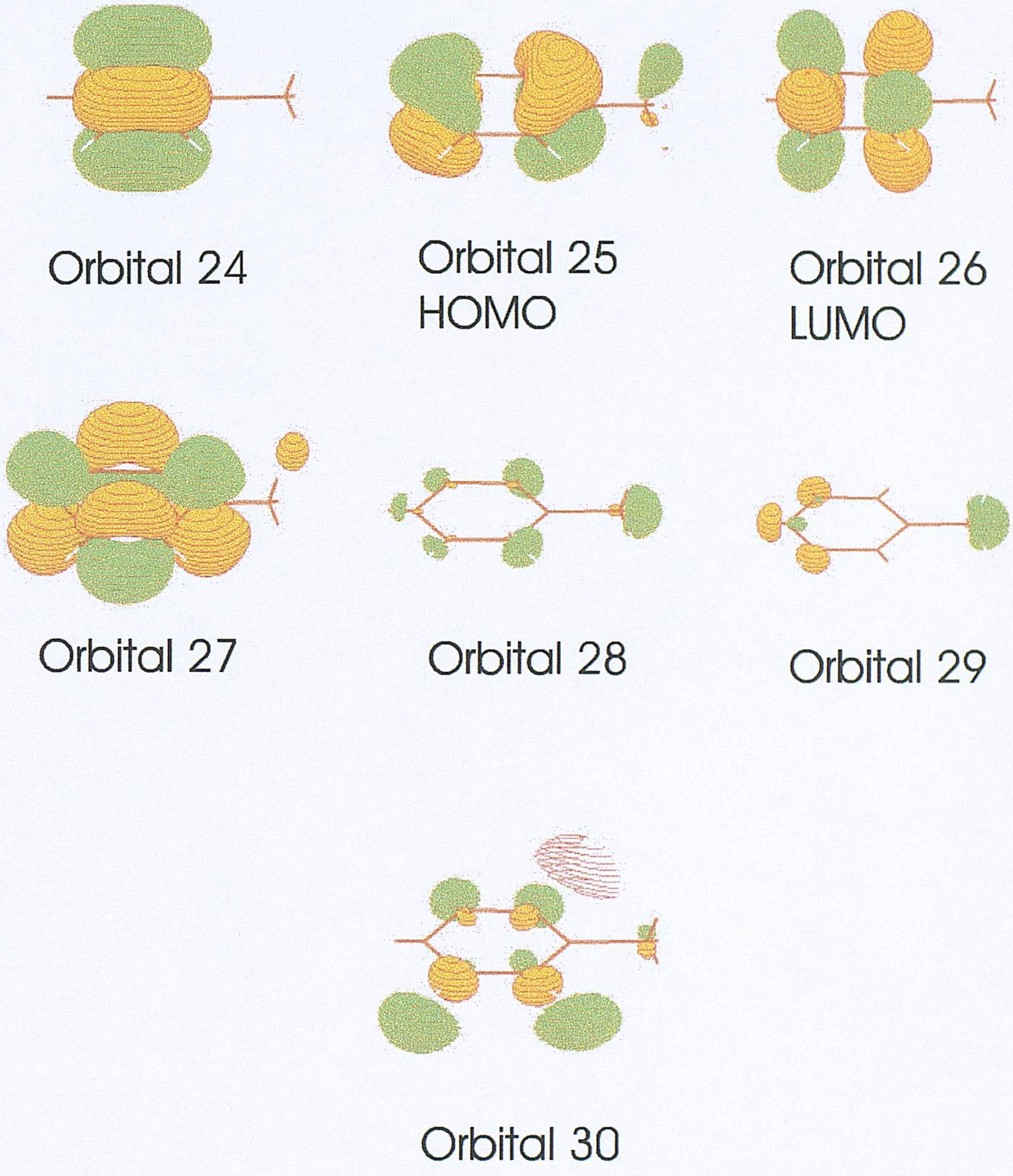

Orbital 24

Orbital 25
HOMO

Orbital 26
LUMO

Orbital 27

Orbital 28

Orbital 29

Orbital 30

Figure 5.3: Molecular orbitals for toluene involved in the transitions.

State, transition	Phase	λ_{max}/nm	Oscillator strength/au
A$''$, a$'(\pi) \rightarrow$ a$''$ (π^*)	Gas	261	0.03
A$'$, a$'(\pi) \rightarrow$ a$'$ (π^*)	Gas	204	0.13
A$'$, a$'(\pi) \rightarrow$ a$'$ (π^*)	Gas	185	0.80
A$''$, a$'(\pi) \rightarrow$ a$''$ (π^*)	Cyclohexane	261.8	0.03

Table 5.3: Experimental wavelength and oscillator strength values [97,117] of the electronic transitions of toluene in the gas phase and in cyclohexane.

Oscillator strength/au		0.0017	0.0157
Symmetry		Singlet, A$''$	Singlet, A$'$
Main Orbitals		25→26	25→27
		a$'(\pi) \rightarrow$ a$''$ (π^*)	a$'(\pi) \rightarrow$ a$'$ (π^*)
Involved		24→27	24→26
		a$''(\pi) \rightarrow$ a$'$ (π^*)	a$''(\pi) \rightarrow$ a$''(\pi^*)$
Method, Package	Basis set	λ_{max}/nm	λ_{max}/nm
B3LYP (Cadpac)	Sadlej	238.5	213.3
PBE (Cadpac)	Sadlej	246.3	217.2
B97-1 (Cadpac)	Sadlej	236.5	210.3
HCTH (Cadpac)	Sadlej	245.3	217.3
B3LYP (Gaussian 98)	Sadlej	238.4	213.1
BPW91 (Gaussian 98)	Sadlej	245.6	216.4

Table 5.4: Calculated excitation energy for the homo-lumo transition in toluene. The DFT functional B3LYP was used both in Gaussian 98 and Cadpac computing packages for comparative purposes. The Oscillator strengths shown (in atomic units) are computed from the B3LYP/Sadlej method in Gaussian 98 package.

In Tables 5.4 and 5.5, the low lying singlet calculated vertical energies using B3LYP, PBE, B97-1, HCTH, and LB94 in Gaussian, CADPAC, and ADF computing packages are tabulated. The main orbitals involved in the transitions and the oscillator strengths for one method are also shown. The basis set used for Gaussian and CADPAC was the Sadlej, whereas for ADF a choice of different STO basis sets was employed. There is good agreement between Gaussian and CADPAC within the same level of theory, B3LYP/Sadlej. The lowest $\pi \rightarrow \pi^*$ transition which corresponds to a$'(\pi) \rightarrow$ a$''$ (π^*) transition is singlet, A$''$ involving the degenerate homo π and lumo π^* valence orbitals. The experimental values for that transition in the gas phase and in solution are shown in Table 5.3. The functionals PBE, HCTH, for CADPAC and BPW91 for Gaussian calculate this excitation energy with the least error.

The LB94 functional computes the A$''$ $(\pi) \rightarrow (\pi^*)$ transition closer to the measured value of 261.8 nm. The second transition corresponds to the 204 nm experimental electronic excitation and the last two correspond to 185 nm experimental electronic transition. The oscillator strength for the first transition A$''$ $(\pi) \rightarrow (\pi^*)$ has a value of 0.0017 au for the B3LYP case and 0.0013 au for the LB94/TZ2P case. The TZ2P basis set is sufficient for the accurate prediction

Oscillator strength		0.0013	0.0270	0.6135	0.3033
Symmetry		Singlet-A$''$	Singlet-A$'$	Singlet-A$'$	Singlet-A$''$
Main Orbitals Involved		25→26 $a'(\pi) \rightarrow a''\ (\pi^*)$ 24→27 $a''(\pi) \rightarrow a'\ (\pi^*)$	25→27 $a'(\pi) \rightarrow a'\ (\pi^*)$ 24→26 $a''(\pi) \rightarrow a''(\pi^*)$	25→27 $a'(\pi) \rightarrow a'\ (\pi^*)$ 24→26 $a''(\pi) \rightarrow a''(\pi^*)$	25→26 $a'(\pi) \rightarrow a''\ (\pi^*)$ 24→27 $a''(\pi) \rightarrow a'\ (\pi^*)$
Method	Basis set				
LB94	TZ2P	252	216	188	190
LB94	Vdiff	252	217	190	192
LB94	ET-QZ3P	252	217	189	191
PBE	ET-QZ3P	243	213	193	190

Table 5.5: Computed low lying excitation energies for toluene using the asymptotically corrected functional LB94 in the ADF computing package. The computed results with DFT functional PBE is also shown for comparison. The oscillator strengths shown (in atomic units) are computed for the LB94/TZ2P method.

of the excited energies and no improvement is achieved with the bigger basis set ET-QZ3P.

5.4.1.3 (Hyper)polarisability

All (hyper)polarisability calculations were carried on the MP2/6-311G** optimised geometry of the staggered conformation of toluene. No significant difference in the calculated first molecular hyperpolarisability tensor values was observed between the two conformations. The Taylor expansion convention was used for the calculation of the hyperpolarisabilities [69]. Much of the current research into nonlinear materials has concentrated on molecular systems in the form of push-pull molecules [118]. These molecules possess a group of delocalized electrons, usually several aromatic rings, that bridge an electron donor and an electron acceptor group. Example of such molecules are p-Nitrophenol, and p-Nitroaniline. The symmetry of these systems can be approximated to a C_{2v} point group, which reduces the number of the non-zero first hyperpolarisability tensors. Molecules with C_{2v} point group symmetry have no delocalization of electrons in the direction perpendicular to the molecular plane. Charge transfer occurs only on the plane of symmetry. This makes any hyperpolarisability tensor with one of the indices equal to the perpendicular axis equal to zero. In the case of toluene however, there is hyper conjugation occurring between the aromatic carbon and the presence of the methyl group. This will generate a small electron density above and below the aromatic resulting in some delocalization in the direction perpendicular to the molecular axis. Toluene has C_s point group symmetry and the number of the nonzero hyperpolarisability tensors reduce to 10 tensor elements: β_{zzz}, β_{zxx}, β_{zzx}, β_{xxx}, β_{xzx}, β_{xxy}, β_{yxx}, β_{yyx}, β_{yzx}, and β_{yyy}. The second harmonic generation case has been considered $\beta(-2\omega;\omega,\omega)$, we have $\beta_{ijk}=\beta_{ikj}$. The molecular frame used for toluene is shown in Figure 5.4.

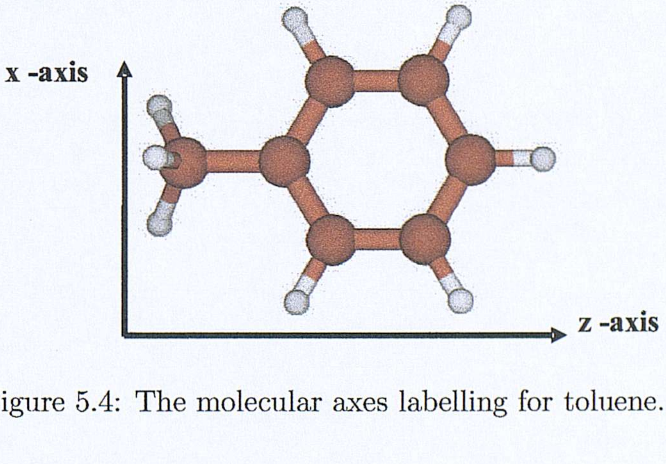

Figure 5.4: The molecular axes labelling for toluene.

Initially the static first electronic (hyper)polarisability was calculated numerically at the MP2 level in Gaussian 98 using different Pople basis sets. For comparison the PBE functional was used in CADPAC and the LB94 functional in ADF for the calculation of the static (hyper)polarisabilities. (Hyper)polarisability calculations are very sensitive towards basis sets and electron correlation. Therefore large basis sets including polarisation and diffuse functions are needed for reasonable calculations. In the case of diffuse basis functions the basis set risks being linear dependent leading to numerical problems. Linear dependence means that one or more of the basis functions can be written as a linear combination of the other making the basis set used essentially overcomplete.

The average molecular polarisability of toluene was calculated at the MP2, HF, LB94, and PBE levels of theory and employing different basis sets. The results are shown in Table 5.6 and are compared across different computing packages. The experimental value of the average static polarisability is 12.31 $\AA^3$ [119] and the calculated value (MP2/Sadlej, 12.31 $\AA^3$) has been obtained using the diagonal polarisability tensors α_{zz}, α_{zz}, α_{zz} according to the formula α=1/3(α_{zz}+ α_{yy}+ α_{xx}). The importance of the addition of diffusion functions can been seen in both the MP2 and LB94 calculations, with more profound effects at the MP2 case. At the MP2 level of theory the use of Pople type basis functions with a lot of polarisation functions does not significantly improve the calculated value a lot. On the other hand the Sadlej basis set which has been constructed for calculating response molecular properties, calculates the molecular polarisability with excellent agreement with experiment. As a comparison the correlation consistent valence double zeta Dunning basis set with additional diffuse functions is shown. The LB94 calculations use Slater type orbitals with the DZP basis set with added diffuse functions being sufficient to calculate the polarisability within accuracy. The Vdiff basis set has the 1s electrons for carbon frozen and because it is a large basis set the calculations have been repeated whilst rejecting any basis sets functions where the overlap eigenvector value is smaller than 10^{-4} avoiding to cause linear dependence of the basis functions. The default used by the program is 10^{-5}. The polarisability values for both calculations (LB94/Vdfiff) are the same indicating that the rejected basis functions have not altered the computed value.

The gradient regulated asymptotic correction, (GRACLB) method [112] is also used which in the outer region resembles the LB94 functional. It requires the ionization potential of the molecules and is more computationally expensive. The statistical averaging of (model) orbital potentials (SAOP) [113] method is also shown for comparison. The PBE functional is used in Cadpac as part of two different program routines. The first calculates the dipole polarisability using the Sadlej basis set as part of an analytical calculation of the hyperpolarisability while the second algorithm using the 631GE basis set calculates directly and analytically the polarisability. Both routines can calculate frequency dependent polarisabilities. It is interesting that the first routine miscalculates the polarisability and this discrepancy cannot be attributed to the difference in the basis sets because both basis sets are similar in their performance and have added diffuse functions.

The static hyperpolarisability was calculated at the MP2 and PBE levels of theory according to the above procedure and the results are shown in Table 5.7. The tensor elements β_{xxx}, β_{yyx}, β_{yzx}, and β_{zzx} are negligible and are not shown in this case. It can be seen that the β_{zzz} tensor is the largest one. The β_{yyz}

Method, Basis Set	α /$\AA^3$ (Exp. 12.31)
Gaussian98/MP2	
6-31G	9.43
6-311G	10.14
6-31G**	9.74
6-311G**	10.50
6-31++G**	11.58
6-311++G**	11.65
6-31++G(2df,2pd)	11.87
6-311++G(2df,2pd)	11.99
Sadlej	12.31
aug-cc-pVDZ	12.27
ADF	
LB94/SZ	6.07
LB94/DZ	10.45
LB94/DZP	11.58
LB94/TZP	11.99
LB94/TZ2P	12.00
LB94/(DZPpolar)DZP-Diffuse(3s1p2d)	12.39
LB94/(DZPhypol)DZP-Diffuse(3s2p2d1f)	12.43
LB94/Vdiff	12.42
LB94Vdiff(10^{-4})	12.42
LB94/(ET1)QZ3P-Diffuse(1s1p1d1f)	12.44
LB94/(ET1)QZ3P-diffuse(10^{-4})	12.45
GRACLB/Vdiff(10^{-4})	12.63
SAOP/DZPpolar(10^{-4})	12.58
Cadpac	
HF/Sadlej	11.98
PBE/Sadlej	8.05
PBE/631GE(anal.)	12.52

Table 5.6: The average static polarisability, α of toluene calculated at the MP2 level of theory in Gaussian 98, and with the LB94 functional in ADF using different basis sets. The GRACLB and SAOP methods are also shown. The HF/Sadlej and the PBE/Sadlej values are also shown calculated in Cadpac. See text for details. The experimental value is 12.31 $\AA^3$. The MP2/6-311G** geometry is used in all cases.

Basis set	β_{yyy}	β_{yyz}	β_{yzz}	β_{zzz}	β_{yxx}	β_{zxx}
			MP2-Gaussian			
6-31G	-21.73	25.65	3.66	-51.82	16.66	7.37
6-311G	-21.04	22.47	6.15	-39.15	16.90	13.57
6-31G(d,p)	-19.61	23.52	3.45	-47.04	15.19	5.59
6-311G(d,p)	-19.61	23.14	4.99	-33.50	15.27	12.42
6-31++G(d,p)	-2.68	-45.99	-7.53	-53.04	10.71	18.10
6-311++G(d,p)	-4.26	-32.54	-8.07	-38.06	11.21	17.85
6-311++G(2df,2pd)	-4.69	-30.16	-6.69	-36.18	9.38	13.22
6-31++G(2df,2pd)	-3.58	-40.91	-7.62	-48.48	9.94	14.87
Sadlej	-4.23	-33.39	-1.21	-48.54	4.28	-2.76
cc-pVDZ	-3.31	-31.17	-2.29	-39.61	4.99	4.26
			PBE-CADPAC			
6-31G	236.70	-114.08	210.50	888.50	188.18	342.65
6-31G**	7.50	-8.51	-0.75	16.76	-5.86	-6.31
6-311G	6.22	-4.54	-0.63	21.87	-4.91	-7.52
6-311G**	4.69	-3.61	-0.43	14.27	-3.79	-5.31
631G(2d,2p)	4.84	-1.02	0.01	16.74	-4.25	-4.21
631GE	2.98	-0.40	-0.02	12.92	-2.64	-3.22
Sadlej	-3.03	-0.90	0.18	15.24	2.69	-2.54

Table 5.7: Static first hyperpolarisability tensors calculated at the MP2 level of theory in Gaussian 98 and with the PBE functional in CADPAC using different basis sets. All values shown are in atomic units with 1.0 au of first hyperpolarisability = 3.2063 × 10^{-53} C^3 m^3 J^{-2}= 8.641 × 10^{-33} esu. The MP2/6-311G** geometry is used in all cases.

tensor appears to be significant as well although the output frequency occurs along the y axis which is vertical in the benzene ring. The Pople style basis sets with added diffuse (++) and polarisation (d,p) functions are affecting the outcome of the hyperpolarisability calculations. In the MP2 level of theory, the β_{yyy} tensor decreases significantly on the inclusion of diffuse functions. Similarly the tensors β_{yyz}, β_{yzz}, β_{yzz} and β_{zzz} values change as well. The inclusion of higher polarisation functions on heavy atoms and hydrogens doesn't significantly affect the calculated tensor. The hyperpolarisability tensors calculated with the PBE functional used in Cadpac computational program are quite different from the results at the MP2 level of theory. The β_{zzz} tensor value is much smaller and of opposite sign than the MP2 calculated one. The size of the β_{yyz} tensor is not comparable to the MP2 computed value. The effect of increasing the basis set size is not as profound as in the MP2 case and the tensor values seem to converge to a limit.

The LB94 results employing different STO basis sets are shown in Table 5.8. The significance of the addition of diffuse basis sets functions is more profound than in the polarisability calculations. The basis sets SZ-TZ2P do not have added diffuse functions. The basis sets DZPpolar, DZPhypol, Vdiff, and ET1 include added diffuse functions. It can been seen that the addition of diffuse

Method/Basis set	β_{zxx}	β_{yxx}	β_{zzz}	β_{yzz}	β_{yyz}	β_{yyy}
	ADF					
LB94/SZ	-3.05	-1.94	82.10	-7.38	-2.45	3.28
LB94/DZ	-15.86	-18.19	73.75	-12.14	-24.79	24.53
LB94/DZP	-11.88	-13.46	56.42	-9.05	-19.39	19.55
LB94/TZP	-21.23	-13.50	39.92	-7.76	-9.35	11.43
LB94/TZ2P	-20.91	-13.19	39.52	-7.70	-8.92	11.00
LB94/DZPpolar	-5.49	-6.73	55.83	-2.18	0.44	7.52
LB94DZPhypol	-6.43	-7.12	54.80	-2.84	0.41	7.47
LB94/Vdiff	-5.03	-7.53	64.17	-3.11	-0.10	8.34
LB94/Vdiff(10^{-4})	-6.53	-7.08	53.56	-2.84	-1.75	8.27
LB94/ET1	-8.61	-6.18	48.98	-1.66	-0.84	8.33
LB94/ET1(10^{-4})	-6.76	-6.94	55.01	-2.31	0.19	7.42
GRACLB/Vdiff(10^{-4})	-7.12	-7.49	44.86	1.13	18.67	8.21
SAOP/DZPpolar(10^{-4})	-8.19	-7.11	56.18	1.12	18.78	6.88
	PBE and HF at CADPAC and MP2 at Gaussian 98					
PBE/Sadlej	-2.54	2.69	15.24	0.18	-0.90	-3.03
MP2/Sadlej	-2.76	4.28	-48.54	-1.21	-33.39	-4.23
HF/Sadlej	-1.96	4.64	59.28	-1.96	32.48	-4.88

Table 5.8: Dominant static first hyperpolarisability tensors of Toluene calculated at the LB94 level of theory in ADF using different STO basis sets. The GRACLB and SAOP level of theory results are also shown employing the Vdiff and DZPpolar basis sets respectively. Some calculations have been repeated with the value of the eigenvector overlap increased to avoid linear dependence problems, see text for details. The PBE/Sadlej and HF/Sadlej results in Cadpac and MP2/Sadlej in Gaussian 98 are also shown for comparison. All values shown are in atomic units with 1.0 au of first hyperpolarisability = 3.2063×10^{-53} C^3 m^3 J^{-2}= 8.641×10^{-33} esu. The MP2/6-311G** geometry is used in all cases.

functions corrects the hyperpolarisability tensor values significantly, indicating that the addition of diffuse functions for accurate hyperpolarisability calculations is significant. The increased size of the basis set ET1 does not improve the results that much so a DZP basis set with added diffuse functions is sufficient for the reliable prediction of the hyperpolarisability tensors. For large basis sets with added diffuse functions there is the danger of linear dependency of the basis sets. The results are shown with and without a restriction to the overlap eigenvector value indicating the significance of the linear dependency of the basis set. The LB94 functional does not predict similar size for the β_{yyz} when compared to the HF and MP2 results. The GRACB and SAOP approximation methods predict the significance of the β_{yyz} tensor.

The PBE results were very similar to all the other available functionals in Cadpac. The polarisability calculations employing the PBE functional, see Table 5.6, indicate the possibility of an error in the Cadpac routine. Also the difference in the prediction of the dominant tensor size β_{zzz} with the other approximation methods confirm this. In order to check the consistency of the results across packages within the same level of theory and investigate the possibility of an error in the analytical routine in the Cadpac package, the static polarisability and hyperpolarisability were calculated at the HF, MP2, BLYP level using the same basis set, 6-31G, in Gaussian 98 and Cadpac packages. The ADF computing package was used to calculate the polarisability and hyperpolarisability at the BLYP level of theory employing a double zeta slater basis set with added polarisation functions. The size of the basis set is very small and the calculations are performed only for comparative purpose among the different packages within the same level of theory which ought to be the same. For the calculation of polarisabilities Cadpac offers the possibility of two routines. The first one calculates analytically dynamic polarisabilities and the second one calculates them as part of the analytical calculation of the hyperpolarisabilities. The results are shown in Table 5.9.

It can be seen that although the polarisability tensor values are in good agreement across the different packages within the same level of theory, there is a disagreement in the calculated hyperpolarisability values at the BLYP/6-31G level between the Gaussian and Cadpac package. The ADF/DZ hyperpolarisability tensor values are closer in agreement with the Gaussian values than the Cadpac ones, although they have opposite sign and the basis set used is different. The sign indicates the alignment of the molecule's dipole moment with the applied electric field. The Cadpac routines for the calculation of the polarisability and hyperpolarisability are different as mentioned earlier, indicating that there might be an error in the analytical routine for the calculation of the hyperpolarisabilities within the Cadpac package.

The authors have not published any results with the analytical calculation of the hyperpolarisabilities. The results published calculate the polarisability analytically and the hyperpolarisability is calculated for the static case using the finite field method [64]. It is possible that the applied analytical routine for the frequency dependent calculation of the hyperpolarisabilities contains an error. Although the analytical routine for the calculation of the time dependent polarisabilities appears to be working fine.

A series of hyperpolarisability calculations at three different frequencies (static, 532 nm, and 1064 nm) with the Sadlej basis set in CADPAC and using all the available functionals revealed that the calculated values are very similar with each other across the different functionals employed. The results are shown in Table 5.10. Only the β_{zzz} tensor is found to be significant with all other terms negligible. The dominant tensor β_{zzz} is shown to increase in value with the applied frequency as expected as it becomes resonant enhanced. The calculated HF value is showing a larger increase than any of the DFT calculated ones which are all very similar in size. The values for the static and frequency dependent hyperpolarisabilities calculated using the TDDFT routine in the Cadpac program

	HF			BLYP			MP2		
Package/Basis	α_{zz}	α_{yy}	α_{xx}	α_{zz}	α_{yy}	α_{xx}	α_{zz}	α_{yy}	α_{xx}
Gaussian/6-31G	86.04	28.43	76.72	90.81	28.93	78.96	85.95	28.28	76.60
CADPAC/6-31G	86.04	28.43	76.72	90.82	28.94	78.98	85.95	28.27	76.60
ADF/STO-DZ				92.74	34.29	80.15			
	β_{zxx}	β_{yxx}	β_{zzz}	β_{yzz}	β_{yyz}	β_{yyy}			
Gaussian/6-31G	9.28	16.90	-70.89	5.35	28.32	-22.51			
CADPAC/6-31G	425.30	171.87	67.61	453.14	9.52	263.21			
ADF/DZ	-15.86	-18.19	73.75	-12.14	-24.79	24.53			

Table 5.9: Static polarisability and hyperpolarisability tensors calculated at the MP2, HF, and BLYP levels of theory in Gaussian 98, CADPAC, and ADF packages. The 6-31G basis set was used for Gaussian and CADPAC and the STO double zeta (DZ) basis set for the ADF program. All values shown are in atomic units. The MP2/6-311G** geometry is used in all cases.

	$\lambda=\infty$ nm		$\lambda=1064$ nm		$\lambda=532$ nm	
Method/Cadpac	β_{zzz}	β_{zxx}/β_{zzz}	β_{zzz}	β_{zxx}/β_{zzz}	β_{zzz}	β_{zxx}/β_{zzz}
MP2	-48.54	0.06	-	-	-	-
HF	59.282	-0.032	69.686	-0.014	127.725	0.049
LDA	16.812	-0.163	18.446	-0.168	26.618	-0.2
LDAX	18.142	-0.152	19.935	-0.155	28.882	-0.183
BLYP	15.226	-0.189	16.638	-0.194	23.549	-0.232
PBE	15.242	-0.166	16.646	-0.171	23.526	-0.204
BP86	14.341	-0.179	15.633	-0.184	21.936	-0.223
BP91	14.577	-0.174	15.879	-0.179	22.221	-0.216
HCTH	14.752	-0.17	16.046	-0.174	22.273	-0.209
B3LYP	18.556	-0.143	20.386	-0.145	29.363	-0.165
B97	17.838	-0.144	19.586	-0.145	28.137	-0.164
B97-1	17.633	-0.143	19.354	-0.144	27.778	-0.164
PBE0	19.307	-0.128	21.217	-0.128	30.571	-0.143
HCTH147	14.698	-0.18	16.01	-0.185	22.35	-0.22
HCTH407	15.145	-0.184	16.508	-0.188	23.108	-0.222
B3P86	17.65	-0.143	19.348	-0.145	27.651	-0.167
B3P91	17.825	-0.14	19.527	-0.142	27.827	-0.163

Table 5.10: Computed β_{zzz} tensor and β_{zxx}/β_{zzz} ratio of toluene with various DFT and ab initio methods at $\lambda=\infty$, 532, 1064 nm. All DFT methods used a high grid and the Sadlej basis set in CADPAC. The MP2/Sadlej values were calculated in Gaussian 98.

are too low in comparison to the HF values. There is a striking similarity of the hyperpolarisabilities values across all the DFT functionals employed in the program.

The LB94 functional was used in the ADF package and the frequency dependent hyperpolarisability tensors were calculated at 532 nm employing a variety of basis sets with added diffuse functions. The SAOP and GRACLB methods have also been used for comparison. The results are shown in Table 5.11 together with the TDHF obtained values and three DFT functionals used in the Cadpac package as well. Toluene has C_s symmetry and the non zero tensor elements are reduced to ten for the SHG case. The LB94 functional predicts the β_{zzz} tensor to be dominant with β_{xzx} the second most important tensor. The GRACLB and SAOP methods predicts the β_{zzz}, β_{yzz}, and β_{zyy} tensors to be dominant which agrees well with the HF prediction. The Cadpac functionals underproduce the value of the β_{zzz} tensor and no other tensor gets enhanced. The linear dependence in the large basis set Vdiff is evident although the tensor component values do not differ that much and their ratios remain constant.

	Hyperpolarisability of Toluene at 532 nm									
	ADF						CADPAC			
	LB94				SAOP	GRACLB	PBE	B97-1	HCTH	HF
	Basis set									
β tensor /au	DZPpolar	DZPhypol	Vdiff	Vdiff(10^{-4})	DZPpolar(10^{-4})	Vdiff(10^{-4})	Sadlej	Sadlej	Sadlej	Sadlej
β_{zxx}	-7.88	-8.94	-5.70	-9.10	-7.23	-1.79	-4.81	-5.13	-4.66	6.19
β_{yxx}	-11.34	-11.88	-12.50	-12.07	-14.73	-15.05	2.92	3.22	2.83	5.62
β_{xzx}	30.07	29.50	37.19	30.37	15.30	10.20	-2.33	-1.89	-2.41	8.78
β_{xyx}	-10.90	-11.32	-12.35	-11.50	-9.57	-8.63	2.79	3.05	2.70	2.27
β_{zzz}	167.48	167.29	186.60	166.37	152.63	110.53	23.53	27.78	22.27	127.73
β_{yzz}	-7.74	-8.89	-8.89	-8.88	3.35	6.15	0.33	0.36	0.27	-4.94
β_{zyz}	-2.16	-3.35	-3.23	-3.44	11.15	14.81	0.16	0.12	0.10	-6.65
β_{yyz}	7.02	7.14	7.47	3.67	73.98	73.20	-0.62	1.18	-0.54	85.79
β_{zyy}	12.46	13.20	14.23	10.04	79.62	72.92	-0.01	2.28	0.05	89.79
β_{yyy}	10.74	10.53	11.80	11.71	11.83	13.85	-3.34	-3.51	-3.29	-6.08

Table 5.11: Computed β tensors at 532 nm for toluene with various basis set and employing the LB94, functional and SAOP, GRACLB methods in the ADF package. The HF/Sadlej values are shown together with PBE/Sadlej, HCTH/Sadlej, and B97-1/Sadlej calculations in CADPAC. All values are shown in atomic units

The PBE functional in the Cadpac program was used to calculate the frequency dependent hyperpolarisability for toluene. There is a resonance enhancement of the hyperpolarisability tensors observed at λ=425 nm which corresponds to the singlet (A$'$, $\pi \longrightarrow \pi^*$) transition. The values are plotted for the 1064-400 nm range and are shown in Figure 5.5. The singlet (A$''$, $\pi \longrightarrow \pi^*$) transition responsible for the resonant enhancement in the SHG experiment is not affecting the hyperpolarisability values a lot because of the small oscillator strength as already seen, although there is a small noticeable increase in the hyperpolarisability tensor due to this transition.

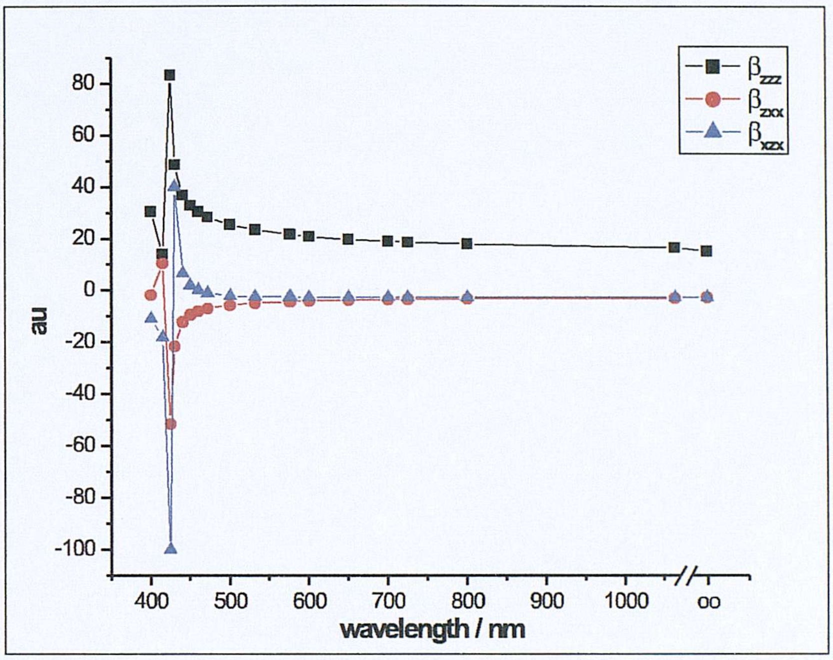

Figure 5.5: β_{zzz}, β_{zxx}, β_{xzx} values in atomic units, 1.0 au of first hyperpolarisability = 3.2063×10^{-53} C^3 m^3 J^{-2}= 8.641×10^{-33} esu for different wavelengths using the PBE functional.

The LB94 functional was used in ADF with the Vdiff basis set to calculate the hyperpolarisability tensors of toluene in the 1064-400 nm frequency range. The results are shown in Table 5.12. The dominant tensors that get enhanced on increasing frequency are the β_{zzz} and β_{xzx} hyperpolarisability components. The β_{xzx} tensor gets bigger in size than β_{zzz} when the frequency is 500 nm which is almost equal to the first excitation energy as calculated with the LB94 functional (252 nm). The other tensors do not change significantly with increasing frequency. Also the sign of the β_{xzx} tensor changes near the resonance with the first excitation energy.

The GRACLB and SAOP methods were used with the Vdiff and DZPpolar basis set respectively in order to compute the hyperpolarisability tensors of toluene at various applied field frequencies. The results are shown in Table 5.13. The β_{zzz} and β_{xzx} tensors are predicted to be dominant near resonance but unlike the LB94 functional these two methods predict the significance of the β_{zyy} and β_{yyz} tensors as well.

The time dependent Hartree Fock (TDHF) method was used with the Sadlej basis set for the calculation of the dominant hyperpolarisability tensor components of toluene at various field frequencies. The results are shown in Table 5.14. The dominant tensors that are resonance enhanced are the β_{zzz}, β_{zyy} and β_{yyz}.

	LB94/Vdiff												
Wavelength/nm	∞	1064	800	700	650	600	575	550	532	515	500	472	400
β tensor/au													
β_{zxx}	-6.53	-7.15	-7.67	-8.05	-8.31	-8.63	-8.81	-8.99	-9.10	-9.15	-9.10	-8.18	-25.50
β_{yxx}	-7.08	-7.92	-8.68	-9.32	-9.80	-10.49	-10.96	-11.55	-12.07	-12.68	-13.34	-15.07	-31.48
β_{xzx}	-6.53	-5.88	-4.61	-2.90	-1.02	2.98	7.10	15.52	30.37	87.67	-240.62	-27.97	173.28
β_{xyx}	-7.08	-7.65	-8.13	-8.52	-8.82	-9.29	-9.68	-10.37	-11.50	-15.76	8.78	-6.72	-8.96
β_{xxz}	-6.53	-5.88	-4.61	-2.90	-1.02	2.98	7.10	15.52	30.37	87.67	-240.62	-27.97	173.28
β_{zzz}	53.56	66.49	80.20	92.85	103.48	120.13	132.47	149.50	166.37	188.11	214.96	309.09	494.70
β_{yzz}	-2.84	-3.55	-4.28	-4.95	-5.51	-6.39	-7.04	-7.96	-8.88	-10.08	-11.59	-17.15	-17.91
β_{zyz}	-2.84	-3.08	-3.26	-3.37	-3.44	-3.49	-3.50	-3.49	-3.44	-3.34	-3.17	-2.35	12.99
β_{yyz}	-1.75	-1.08	-0.36	0.30	0.85	1.66	2.23	2.98	3.67	4.49	5.39	7.77	32.56
β_{xxy}	-7.08	-7.65	-8.13	-8.52	-8.82	-9.29	-9.68	-10.37	-11.50	-15.76	8.78	-6.72	-8.96
β_{zzy}	-2.84	-3.08	-3.26	-3.37	-3.44	-3.49	-3.50	-3.49	-3.44	-3.34	-3.17	-2.35	12.99
β_{yzy}	-1.75	-1.08	-0.36	0.30	0.85	1.66	2.23	2.98	3.67	4.49	5.39	7.77	32.56
β_{zyy}	-1.75	-0.52	0.87	2.20	3.32	5.10	6.42	8.24	10.04	12.34	15.15	24.80	50.99
β_{yyy}	8.27	8.96	9.56	10.03	10.36	10.81	11.10	11.43	11.71	12.01	12.29	12.82	22.10

Table 5.12: Frequency dependent hyperpolarisability tensor values for toluene using the LB94/Vdiff method in ADF. All values shown are in atomic units

	GRACLB/Vdiff										SAOP/DZPpolar		
Wavelength β tensor/au	∞	1064	800	700	600	532	504	472	425	400	∞	532	500
β_{zxx}	-12.05	-13.37	-14.43	-15.16	-16.05	-15.84	-14.29	-6.55	-246.39	-76.87	-8.19	-7.23	-2.82
β_{yxx}	-7.11	-7.99	-8.84	-9.56	-11.02	-13.29	-15.14	-19.50	143.04	31.78	-7.11	-14.73	-18.25
β_{xzx}	-12.05	-12.62	-12.69	-12.28	-9.52	5.92	71.49	-91.90	-65.13	-112.36	-8.19	15.30	146.20
β_{xyx}	-7.11	-7.51	-7.79	-7.96	-8.17	-8.89	-13.46	1.51	12.20	44.39	-7.11	-9.57	-18.63
β_{xxz}	-12.05	-12.62	-12.69	-12.28	-9.52	5.92	71.49	-91.90	-65.13	-112.36	-8.19	15.30	146.20
β_{zzz}	55.44	67.72	80.46	91.98	116.09	154.91	186.96	261.42	-395.38	277.72	56.18	152.63	188.22
β_{yzz}	-1.47	-1.62	-1.74	-1.83	-2.01	-2.43	-2.99	-5.32	118.71	-8.14	1.12	3.35	3.65
β_{zyz}	-1.47	-1.20	-0.81	-0.37	0.77	3.19	5.68	12.92	-21.08	324.55	1.12	11.15	17.09
β_{yyz}	13.21	17.49	22.00	26.10	34.74	48.61	59.85	84.31	-253.90	1075.50	18.78	73.98	99.17
β_{xxy}	-7.11	-7.51	-7.79	-7.96	-8.17	-8.89	-13.46	1.51	12.20	44.39	-7.11	-9.57	-18.63
β_{zzy}	-1.47	-1.20	-0.81	-0.37	0.77	3.19	5.68	12.92	-21.08	324.55	1.12	11.15	17.09
β_{yzy}	13.21	17.49	22.00	26.10	34.74	48.61	59.85	84.31	-253.90	1075.50	18.78	73.98	99.17
β_{zyy}	13.21	18.36	23.79	28.73	39.03	55.29	68.28	96.84	-44.77	151.77	18.78	79.62	104.30
β_{yyy}	7.01	7.55	8.04	8.43	9.15	10.18	11.01	13.11	-197.62	-109.69	6.88	11.83	14.41

Table 5.13: Frequency dependent hyperpolarisability tensor values for toluene using the GRACLB and SAOP methods with the Vdiff and DZPpolar basis sets respectively in ADF. All values shown are in atomic units

HF/Sadlej Wavelength/nm β tensor/au	∞	1064	800	700	600	532	500	472	425	400
β_{zxx}	-1.93	-1.03	-0.02	0.92	2.93	6.11	9.06	13.79	2.33	37.36
β_{yxx}	-4.53	-4.75	-4.93	-5.06	-5.27	-5.51	-5.71	-6.04	-5.52	-21.96
β_{xzx}	-1.93	-0.91	0.25	1.38	3.95	8.77	14.54	28.14	-91.17	-38.65
β_{xyx}	-4.53	-4.41	-4.19	-3.93	-3.29	-2.15	-1.11	0.16	21.33	44.41
β_{xxz}	-1.93	-0.91	0.25	1.38	3.95	8.77	14.54	28.14	-91.17	-38.65
β_{zzz}	59.42	69.85	79.96	88.55	105.04	128.05	147.29	175.25	124.57	271.60
β_{yzz}	1.99	2.44	2.90	3.30	4.08	5.17	6.03	6.99	23.43	35.20
β_{zyz}	1.99	2.66	3.35	3.96	5.19	7.01	8.59	10.90	6.76	-4.67
β_{yyz}	32.52	39.96	47.40	53.90	66.83	85.79	102.23	125.91	232.74	565.95
β_{xxy}	-4.53	-4.41	-4.19	-3.93	-3.29	-2.15	-1.11	0.16	21.33	44.41
β_{zzy}	1.99	2.66	3.35	3.96	5.19	7.01	8.59	10.90	6.76	-4.67
β_{yzy}	32.52	39.96	47.40	53.90	66.83	85.79	102.23	125.91	232.74	565.95
β_{zyy}	32.52	40.76	48.96	56.06	69.97	89.80	106.60	130.99	108.10	235.46
β_{yyy}	4.08	4.10	4.09	4.06	3.96	3.79	3.62	3.32	13.40	38.29

Table 5.14: Frequency dependent hyperpolarisability tensor values for toluene using the HF method with the Sadlej basis set in Cadpac. All values shown are in atomic units

In conclusion, the response properties of the toluene molecule were studied at various different levels of theory and the effect of the basis set size was investigated on the calculated property. Different computational packages were used and the results obtained were compared to establish the reproducibility of the results and the efficiency of the applied calculation routines. The static polarisability calculations in Table 5.6 show that the MP2/Sadlej level of theory reproduces the experimental value exactly. The DFT methods predict the static value with high accuracy. The PBE/631GE value is within the accuracy of the experimental result. The basis set size investigation has revealed that in order to adequately reproduce the polarisability of the molecule diffuse basis set functions are paramount. The inclusion of higher order polarisation functions is not that important. As in the case of the LB94 functional shown in Table 5.6 a DZP basis set functional augmented with diffuse functions predicts the polarisability value better than the QZP + diffuse calculated value. The Cadpac program employs two different algorithms for the calculation of the polarisability. The first computes the dipole polarisability as part of an analytical calculation of the hyperpolarisability of the molecule and has been shown to be inaccurate. The second calculates the polarisabilities of the molecule analytically and is shown to be accurate within experimental error.

The hyperpolarisability calculations are proven to be even more sensitive towards the choice of the basis set. In the absence of experimental results the calculations can only be compared among the different levels of theory. The MP2/Sadlej calculations can be taken as reliable and the other calculations compared with them. In the static case shown in Table 5.7, the MP2/Sadlej results indicate that the dominant tensors are the β_{zzz} and β_{yyz}. The HF/Sadlej values shown in Table 5.8 are similar in size but opposite in sign. The HF/Sadlej results were calculated in Cadpac and the MP2/Saldej results in Gaussian 98 so there might be a difference in the orientations of the applied fields. The DFT calculations using the Cadpac program shown in Table 5.7 underpredict the size of the β_{zzz} and β_{yyz} tensors. All DFT functionals available in Cadpac gave similar results. The LB94 functional using the ADF program predicts the correct size for the β_{zzz} tensor but not for β_{yyz} shown in table 5.8. The SAOP and GRACLB methods in ADF predict the significance of the β_{yyz} tensor component and compare favorably with the MP2 and HF results. The β_{zzz} and β_{xzx} tensors describe changes in the polarisability parallel to the aromatic ring. The β_{yyz} tensor describes changes in the polarisation perpendicular to the aromatic ring due to a field in the z direction. The significance of the β_{yyz} tensor cannot be explained using this simple model. There might be contribution from more than one excitation in the molecule so contributing to the significance of charge transfer along the y axis which is perpendicular to the aromatic ring. If the molecule is polarised perpendicular to the aromatic ring then charge flows above and below the ring. Recent studies on p-Nitrophenol have revealed that charge transfer can occur perpendicular to the aromatic ring [62].

The time dependent hyperpolarisability calculations reveal the expected resonance enhancement according to the oscillator strengths predicted in the excitation energies calculations. The LB94/Vdiff method predicts the resonance enhancement of the β_{zzz} and β_{xzx} tensor at 500 nm as expected according to the calculated excitation energy of 252 nm, see Table 5.12. There is a change in sign for the β_{xzx} tensor near the electronic transition. The GRACLB/Vdiff method shown in Table 5.13 predicts the β_{zzz}, β_{xzx}, β_{yyz} and β_{zyy} tensors enhancement near the first electronic transition with the β_{xzx} tensor changing sign near the transition. The three tensors β_{xzx}, β_{yyz}, and β_{zyy} are similar in size at 504 nm. There is a further increase of these tensors near the second transition at 217 nm as shown in the results for the 425 nm calculation, see Table 5.13. The HF/Sadlej results shown in Table 5.14 are similar to the GRACLB results with the β_{zzz}, β_{yyz}, and β_{zyy} tensors getting enhanced near the first electronic transition. The significant tensors to be considered for the SHG analysis experiments will be the β_{zzz}, β_{xzx}, β_{yyz}, and β_{zyy} components.

5.4.2 SHG Results

5.4.2.1 Monochromator Scan

The SHG experiment is conducted using an input fundamental wavelength of 532 nm; toluene exhibits an absorption in the region of the second harmonic wavelength (266 nm) with a molar extinction coefficient of 1527 $M^{-1}cm^{-1}$, therefore the SHG signal will be resonant enhanced. The linear emission fluorescence spectrum of toluene exhibits a maximum wavelength at 292 nm [98] which is close to the second harmonic wavelength and might interfere with the SHG intensity. The fluorescence observed in the SHG experiment is a resonant process which involves a two-photon absorption followed by excited fluorescence emission and differs from the linear fluorescence emission. The angular distribution emission is determined by the symmetry of molecular configuration and the orientation of the molecule. The two photon fluorescence (TPF) differs from SHG, in that unlike SHG it is not a coherent process.

The presence of fluorescence can interfere with the SHG signal leading to distortion of the SHG results. The experimental conditions need to be carefully optimised in order to eliminate any unwanted fluorescence interference with the SHG signal. This is achieved by optimization of the monochromator settings. Because the observed two photon fluorescence occurs at longer wavelengths than the SHG signal, it is possible by adjusting the monochromator slits, to separate the two signals and avoid overlap. A monochromator scan was carried out in order to determine the position of toluene's two-photon fluorescence (TPF). The wavelength setting of the monochromator was scanned across the 250-300 nm region and the signal intensities were recorded. The widths of the entrance and exit slits of the monochromator were adjusted to achieve separation of the TPF and SHG signals.

The monochromator scan, for the air/toluene interface, is shown in Figure 5.6 where the signal intensity is plotted against the wavelength setting of the monochromator. Three plots are shown on the same graph. The first shows the intensity dependence in the S-polarised harmonic wavelength for an input polarisation angle, $\gamma=0^o$. The SHG signal at 266 nm is essentially zero as expected, confirming the absence of unwanted contributions from the TPF signal. The other two plots show the intensity dependence for output harmonic polarisations S and P. The input polarisation angle γ, is 45^o and 0^o respectively corresponding to maximum SHG intensities. It can be seen that the TPF signal is much larger than the SHG signal, but they are well resolved. The maximum for the SHG signal occurs at 266 nm and the maximum for the TPF signal at 287 nm. The ratio of I_{TPF}/I_{SHG} is 10 and 17 for P output polarisation and S output polarisation respectively. The SHG signal can be separated and resolved even when the TPF signal is 17 times higher. The entrance and exit width of the slits were set to 0.5 mm, corresponding to a 2.1 nm bandpass centered about the wavelength setting.

Figure 5.7 shows the TPF signal polarisation dependence with input polarisation angle γ for the P and S harmonic polarisations. The monochromator wavelength was set at the maximum of the TPF signal which occurred at 287 nm. It can be seen that there is a slight polarisation dependence of the TPF sig-

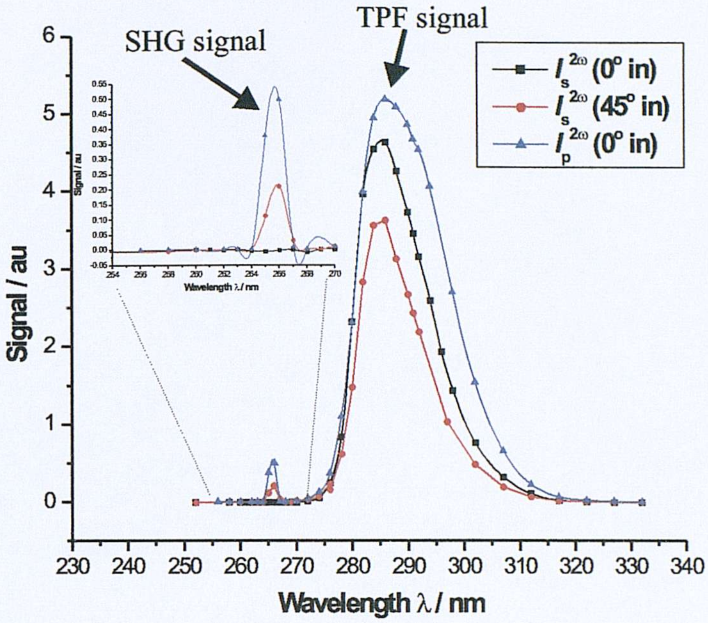

Figure 5.6: Monochromator scan for the air/toluene interface. The signal intensity is monitored versus the monochromator wavelength setting. The output polarisation angles are set to P and S and the input polarisation angles are set to 0^o and 45^o degrees respectively. The input and output monochromator slits are set to 0.5 mm giving an estimated bandpass of 2.1 nm. Spline curves are fitted to the signal intensities

nal with the incoming polarisation angle γ. In order to check for any correlation between the two output harmonic polarisations, the ratio $I_{\mathrm{P}}^{(2\omega)}/I_{\mathrm{S}}^{(2\omega)}$ of the TPF signals is plotted versus the input polarisation angle γ, as shown in Figure 5.8. It can be seen that the ratio $I_{\mathrm{P}}^{(2\omega)}/I_{\mathrm{S}}^{(2\omega)}$ exhibits a slight polarisation dependence on the input angle γ.

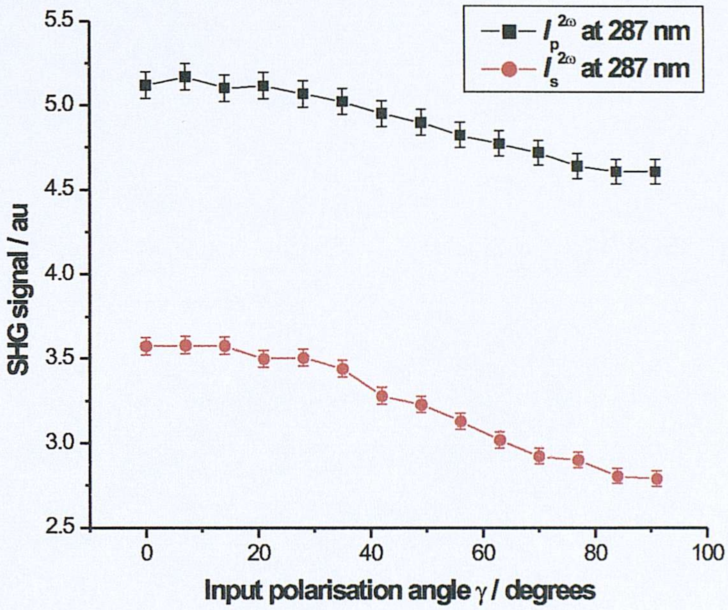

Figure 5.7: Polarisation dependence of the TPF signal at the air/toluene interface for $I_{\mathrm{P}}^{(2\omega)}$ and $I_{\mathrm{S}}^{(2\omega)}$ output polarisations. The monochromator wavelength setting was set to 287 nm. Error bars are shown to indicate standard errors.

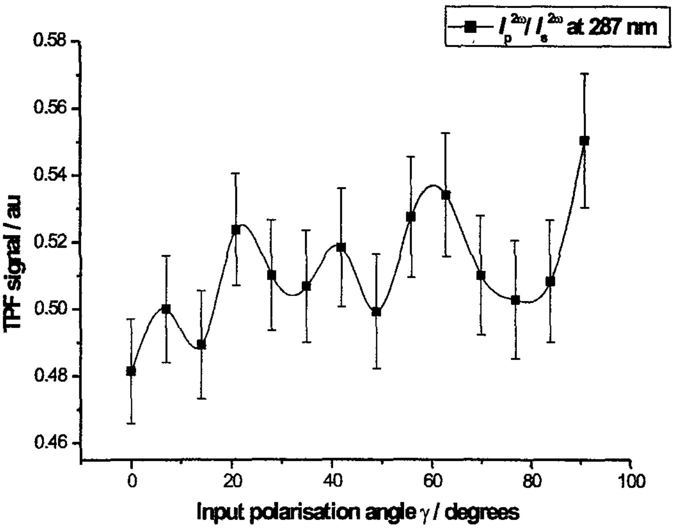

Figure 5.8: Polarisation dependence of the TPF signal at the air/toluene interface for the ratio $I_{\mathrm{P}}^{(2\omega)}/I_{\mathrm{S}}^{(2\omega)}$ output polarisations. The monochromator wavelength was set to 287 nm.

5.4.2.2 Polarisation Dependence

The polarisation dependence of the SHG signal from the air/toluene interface was monitored for the linear output polarisations $I_{\mathrm{P}}^{(2\omega)}$, $I_{\mathrm{S}}^{(2\omega)}$, $I_{+45}^{(2\omega)}$ and $I_{-45}^{(2\omega)}$, where P, S, +45, -45 correspond to the output harmonic polarisation angle Γ. Several repetitions of the experiment were performed, and a representation of the fit obtained is shown in Figures 5.9-5.14. The plots indicate the reproducibility of the results obtained and also the quality of the fit. Because of the inherent difficulty of the SHG experiment at the air/toluene interface due to possible fluorescence interference and the good solvent property of toluene, some of the experimental results obtained had to be abandoned and not taken into account in further analysis. The SHG technique is very sensitive towards organic impurities present at the air/liquid interface and the experimental results can be altered significantly if impurities are present. The decision on the quality of the fits was based on statistical diagnostics plots and the actual fittings to the non-linear model. An example of the polarisation dependence of the SHG signal for the S, P, +45 harmonic polarisations together with their diagnostic plots is shown. The diagnostics plots shown in Figures 5.9-5.14 show plots of the residual (observed-fitted) values versus fitted values, the input polarisation angle γ, and the output polarisation angle Γ respectively. The even scattering observed of the points above and below the zero value is an indication of the validity of the fitted model and the assumption that the experimental errors have normal distributions [44]. The analysis of the SHG intensities used the Euler representation of the A, B, and C parameters fitted simultaneously to the nonlinear model [44].

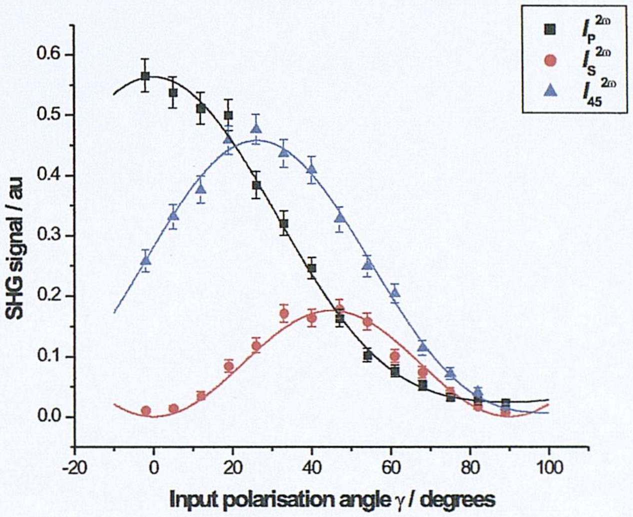

Figure 5.9: The polarisation dependence of the SHG signal generated in the S, P and $+45^o$ linear polarisation planes as a function of the input polarisation angle (γ), at the air/toluene interface. The solid lines have been estimated by the simultaneous fitting of the Euler parametrization of A, B and C parameters in the S, P and $+45^o$ SHG data. λ=532/266 nm. The error bars added are 2σ.

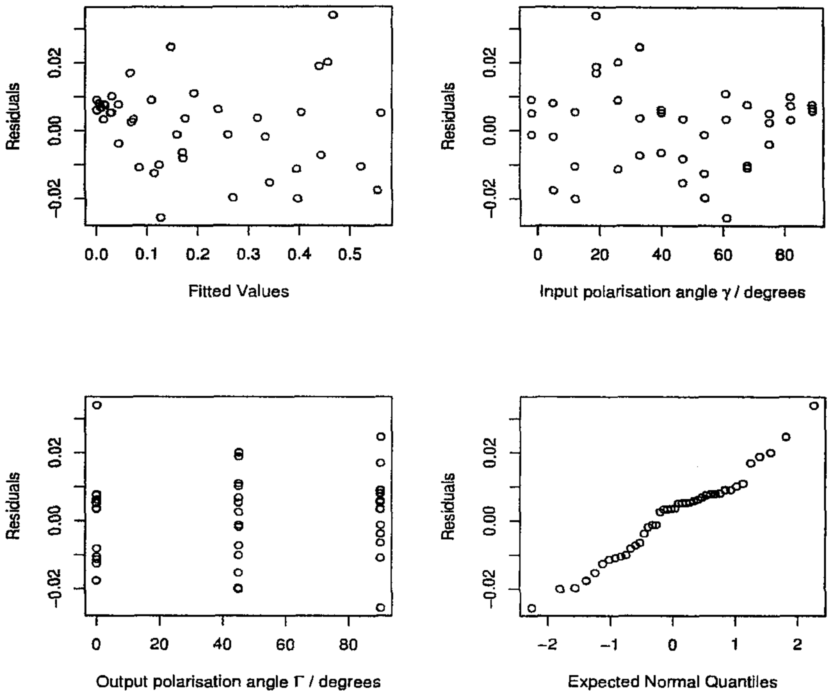

Figure 5.10: Residual and normal probability plots for the model fitted to the SHG data from Figure 5.9. The residual values (calculated subtracted from fitted) are plotted against the fitted values, the input polarisation angle γ, the output polarisation angle Γ, and the expected normal quantiles.

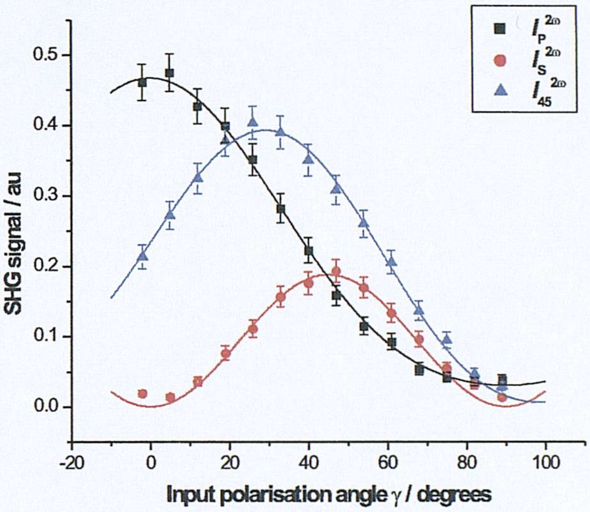

Figure 5.11: The polarisation dependence of the SHG signal generated in the S, P and +45 linear polarisation planes as a function of the input polarisation angle (γ), at the air/toluene interface. The fitted solid lines have been estimated by the simultaneous fitting of the Euler parametrization of A, B and C parameters in the S, P and +45 SHG data. λ=532/266 nm. The error bars added are 2σ.

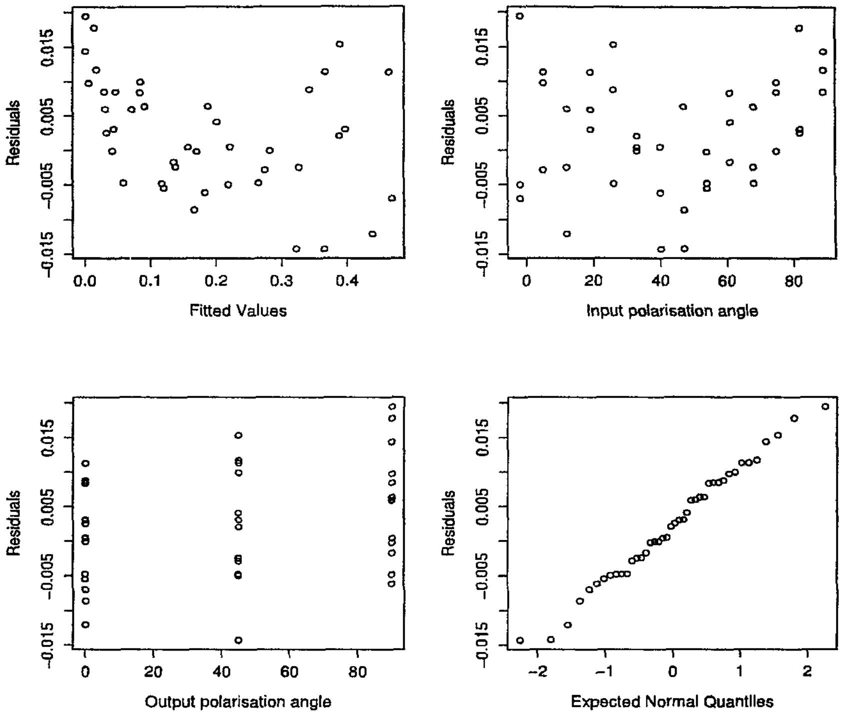

Figure 5.12: Residual and normal probability plots for the model fitted to the SHG data from Figure 5.11.

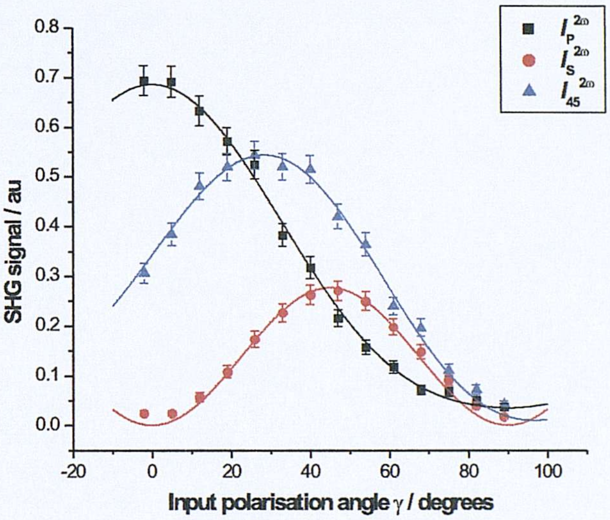

Figure 5.13: The polarisation dependence of the SHG signal generated in the S, P and +45 linear polarisation planes as a function of the input polarisation angle (γ), at the air/toluene interface. The fitted solid lines have been estimated by the simultaneous fitting of the Euler parametrization of A, B and C parameters in the S, P and +45 SHG data. λ=532/266 nm. The error bars added are 2σ.

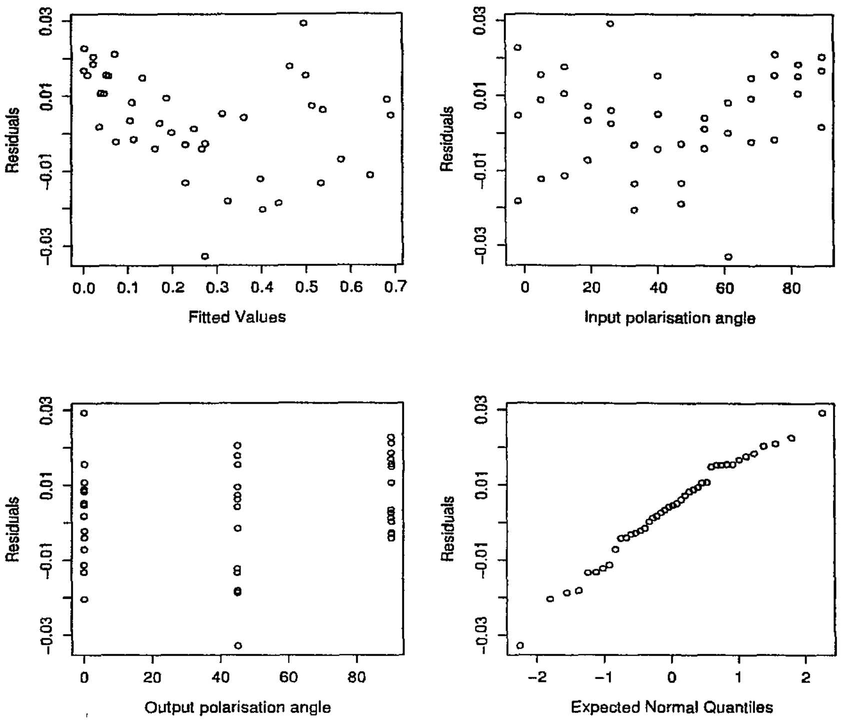

Figure 5.14: Residual and normal probability plots for the model fitted to the SHG data from Figure 5.13

It can be seen from the polarisation dependence plots that there is a strong dependence of the SHG signal on the input polarisation. The S output polarisation curve indicates a much weaker signal than the P output polarisation curve, with a maximum at γ=45^o. The P output polarisation curve has a maximum at γ=0^o and decreases monotonically with the input polarisation angle. The +45 output polarisation curve is slightly weaker than the P output polarisation curve with a maximum at 25^o. The statistical diagnostic plots shown above indicate an acceptable amount of spread in the plotted points and no significant curvature is observed in the residuals.

At the harmonic wavelength there is resonance enhancement so we expect the fitting parameters to be complex. The Euler parametrization of A, B, and C fitted simultaneously indicates a good quality fit. The estimated components (magnitude i.e r_a, and phase i.e ϕ_b, see chapter 3 for definitions) of the fitted parameters and their standard errors for ten data sets are shown in Table 5.15.

Data set	r_a s.e.(r_a)	t-value	r_b s.e.(r_b)	t-value	r_c s.e.(r_c)	t-value	ϕ_b s.e.(ϕ_b)	t-value	ϕ_c s.e.(ϕ_c)	t-value
1	0.727	225.53	0.171	11.65	0.497	11.65	1.141	10.04	0.000	
	(0.003)		(0.015)		(0.004)		(0.114)		0.000	
2	0.732	165.51	0.163	8.34	0.496	95.01	0.738	2.87	0.000	
	(0.004)		(0.019)		(0.005)		(0.257)		0.000	
3	0.683	229.08	0.173	26.11	0.436	88.87	0.000		0.652	13.95
	(0.003)		(0.007)		(0.005)		0.000		(0.047)	
4	0.491	85.89	0.112	7.91	0.332	43.49	0.000		0.000	
	(0.006)		(0.014)		(0.008)		0.000		0.000	
5	0.537	99.59	0.115	8.34	0.323	39.94	0.000		0.000	
	(0.005)		(0.014)		(0.008)		0.000		0.000	
6	0.828	207.90	0.187	19.99	0.525	83.91	0.000		0.780	18.06
	(0.004)		(0.009)		(0.006)		0.000		(0.043)	
7	0.808	117.33	0.225	8.55	0.498	53.53	1.077	5.72	0.000	
	(0.007)		(0.026)		(0.009)		(0.188)		0.000	
8	0.609	103.04	0.157	11.21	0.420	53.89	0.000		0.000	
	(0.006)		(0.014)		(0.008)		0.000		0.000	
9	0.738	125.05	0.196	8.62	0.477	60.93	0.965	4.51	0.479	3.99
	(0.006)		(0.023)		(0.008)		(0.214)		(0.120)	
10	0.712	128.60	0.173	13.38	0.458	53.44	1.014	19.06	0.000	
	(0.006)		(0.013)		(0.009)		(0.053)		0.000	

Table 5.15: Parameter estimates and approximate standard errors, s.e. (in parentheses), for the model fitted to the toluene experimental data sets. The t-value for each parameter is shown indicating the significance of that parameter. Some phase angles have been set to zero because they turned out to be nonsignificant during the non-linear fitting process (t-value<2).

Because the estimates of the parameters are at different scales and since absolute intensities are not measured, we are interested in comparing ratios of the parameters A, B and C from these different experimental runs. Although absolute phase information is lost, we retain phase information between the parameters. The absolute phase for these parameters can be obtained only with phase experiments with a quartz plate [120].

The above data were collected on different days but the same conditions were maintained for all the experiments. The non-linear models were fitted to these data sets and where possible the model was simplified by excluding any non significant parameters. The final model for each experiment is reported in Table 5.15. The parameter with the largest magnitude is A. The magnitude of the B parameter is small and less significant in the non-linear model. The magnitude of C is bigger than B and with stronger dependency in the non-linear model. Our model assumes the parameter A to be real and B and C to be complex. The same results were obtained if any of the other parameters were assumed to be real. The estimated phase angle for B is not well determined, because the estimated magnitude of B is small, indicating there is a weak dependency in the fitted model. The estimated phase angle for C is not significant with a t-value smaller than 2 and has been reduced to zero except in three cases. The fitting parameters A, B, and C depend on the assumption of surface SHG within the electric dipole approximation and the isotropic symmetry of the interface, $C_{\infty v}$, in the absence of chiral molecules present.

	B/A		C/A	
Data Set	$\hat{r}_R$	$\hat{\phi}_R$	$\hat{r}_R$	$\hat{\phi}_R$
	$2\sigma(\hat{r}_R)$	$2\sigma(\hat{\phi}_R)$	$2\sigma(\hat{r}_R)$	$2\sigma(\hat{\phi}_R)$
1	0.23	1.14	0.68	
	(0.02)	(0.11)	(0.01)	
2	0.22	0.74	0.68	
	(0.03)	(0.26)	(0.01)	
3	0.25		0.64	0.65
	(0.01)		(0.01)	(0.05)
4	0.23		0.68	
	(0.03)		(0.02)	
5	0.21		0.60	
	(0.03)		(0.02)	
6	0.22	0.45	0.63	
	(0.01)	(0.24)	(0.01)	
7	0.28	1.08	0.62	
	(0.03)	(0.19)	(0.01)	
8	0.26		0.69	
	(0.02)		(0.01)	
9	0.27	0.97	0.65	0.48
	(0.03)	(0.21)	(0.01)	(0.12)
10	0.24		0.64	1.01
	(0.02)		(0.01)	(0.05)
Mean	0.24	0.87	0.65	0.71
St.Dev.	(0.02)	(0.28)	(0.03)	(0.27)

Table 5.16: Estimates of the ratios of parameters A, B, and C and their errors(2σ), (in parentheses), for the model fitted to the toluene experimental data sets. Some of the phase angles are zero because the fitted models were simplified when the phase angles were considered negligible. The average of the parameter estimates is shown together with the estimated standard deviation of the mean.

When considering the Euler parametrization, the magnitude and phase angle component of the ratio can be estimated separately. The estimates $\hat{r}_R$ and $\hat{\phi}_R$ of the ratios and their errors(2σ) are given in Table 5.16. The coefficient with the largest magnitude is A, so the other two coefficients are compared to A in the ratios. The components of ratios B/A and C/A are shown with estimates of the magnitude and phase angle. The average value of the components of the parameters has been calculated and is shown at the bottom of the table.

Our model assumes that the A, B and C parameters are complex quantities with one of them set to real, in this case A. It is possible that because of the weak dependency of the phase angles within the model, the parameter determination to be sufficient, assuming A, B and C are real. This hypothesis was tested and the data sets were refitted to the non-linear model assuming they were real. The averaged values for B/A and C/A determined were compared with the averaged

Parameter	Value
Wavelength, $\lambda(\omega, 2\omega)$	532/266 nm
Angle of incidence, θ	60^o
Extinction coefficient (in cyclohexane), ϵ	1527 M^{-1} cm^{-1}
Concentration, C	9.442 M
Coverage, Θ	1
$n_1(\omega/2\omega)$	1/1
$n_2(\omega/2\omega)$	1.4983/1.5257
$n_3(\omega/2\omega)$	1.2491/1.2628

Table 5.17: The parameters used for the calculations of the a_i coefficients. The real part of the refractive indices for both wavelengths has been calculated from a fitting to the Cauchy's equation ($n_\lambda = M + N/\lambda^2$, n_λ is the value of the refractive index at wavelength λ, M and N are constants specific to the sample under study.). The estimated constants M and N are taken from a recent interferometric study of toluene [123].

values from Table 5.16. The averaged estimate for C/A was similar for both approaches but the B/A averaged estimate was different. The resulting fits when considering A, B and C to be real were not of the same quality as before. Therefore the complex parametrization has to be adopted for the analysis, assuming A to be real and B and C to be complex.

5.4.2.3 $\vec{\chi}^{(2)}$ Calculation

The significant $\vec{\chi}^{(2)}$components at the air/toluene interface are three, $\chi^{(2)}_{ZZZ}$, $\chi^{(2)}_{ZXX}$, and $\chi^{(2)}_{XZX}$. They can be calculated from the A, B and C parameters using equations (see theory chapter). The calculation of the a_i coefficients is needed and the parameters used for the calculation are shown in Table 5.17. The a_i Fresnel coefficients depend on the experimental geometry, the model used and the refractive indices of the bulk phases and the interfacial region. The interfacial layer refractive index is difficult to measure directly [121,122] so certain assumptions have to be made. The a_i terms calculated and the determined effective $\vec{\chi}^{(2)}$ tensor components will therefore depend on the value of the interfacial layer refractive index [37]. The effective tensors derived would still contain non-local contributions arising from the bulk and higher order terms [17].

The n_1 refractive index, corresponds to the overlying layer which is always air, so it is assumed to be real and independent of wavelength and its value is set to one. The n_2 refractive index, corresponds to the bulk phase of toluene. Because toluene absorbs at the harmonic wavelength (266 nm), its refractive index will be complex at that wavelength. The imaginary component of the refractive index at the harmonic wavelength is calculated from the absorption spectrum and for the fundamental is set to zero assuming no absorbance. The real component has been taken from literature [123] for the fundamental and the harmonic wavelengths.

The interfacial refractive index, n_3, will be complex. Its real component value

	$n_3=(n_1+n_2)/2$		$n_3=n_1$		$n_3=n_2$	
a_i	Re	Im	Re	Im	Re	Im
a_1	0.156	-0.053	0.240	-0.080	0.107	-0.036
a_2	-0.165	0.036	-0.255	0.055	-0.114	0.025
a_3	0.087	-0.030	0.132	-0.050	0.058	-0.019
a_4	0.090	-0.032	0.334	-0.127	0.029	-0.009
a_5	0.108	-0.038	0.164	-0.062	0.072	-0.023
a_6	0.281	-0.095	0.431	-0.143	0.192	-0.064
a_7	-0.092	0.020	-0.142	0.031	-0.063	0.014

Table 5.18: The a_i coefficients for the toluene-air interface calculated for different assumptions about the interfacial refractive index n_3.

could be expected to be between the two refractive indices n_1 and n_2 [42]. Its imaginary component can be calculated assuming a complete surface coverage and a very small layer thickness assuming a single molecule layer at the interface. Then the imaginary component of the refractive index can be determined from the absorption spectrum assuming the surface coverage is known. Another approach will be to set the interfacial refractive index, n_3 equal to unity and scale [39]. The calculated Fresnel, a_i, coefficients are shown in Table 5.18 for different assumptions about the refractive index for the interface. It has been shown that the interfacial refractive index has an effect on the SHG molecular orientation measurements [37]. The value of the interfacial refractive index n_3 has been chosen for three cases, $n_3=n_1$, $n_3=n_2$, $n_3=(n_1+n_2)/2$. The calculated effective $\chi^{(2)}$ tensors for the case where the interfacial refractive index $n_3=n_1$, $n_3=(n_1+n_2)/2$ and $n_3=n_2$ are shown in Tables 5.19-5.21 respectively with the ratios of the effective $\chi^{(2)}$ tensors shown as well.

The $\chi^{(2)}$ tensor components shown in Tables 5.19, 5.20 and 5.21 are the effective ones. They contain contributions from the bulk phase and higher electric multipole terms such as quadruple moments, ignoring any magnetic moments. These terms can contribute significantly to the SHG signal in the case of a air/liquid interface [124]. In the case of the air/toluene interface where there is strong resonant enhancement of the SHG signal these terms can be ignored and the SHG signal can be attributed to the surface susceptibility tensor, $\chi^{(2)}$, within the electric dipole approximation. Tables 5.19, 5.20 and 5.21 show that the $\chi^{(2)}_{ZZZ}$ tensor is the dominant tensor with $\chi^{(2)}_{XZX}$ the second most dominant and $\chi^{(2)}_{ZXX}$ the least contributing term. The SHG experimental results are consistent and reproducible on the same day, but day-to-day reproducibility of the experiments is difficult to maintain. For example, in Table 5.20 the experimental runs 4 and 5 were acquired on the same day using the same toluene solution. As the results indicate there is a consistency of the $\chi^{(2)}$ tensors and ratios across these two experimental runs.

The choice of the interfacial refractive index value affects the outcome of the determined $\chi^{(2)}$ tensor values but it might be possible to exclude certain values of the refractive index based on intuition and on the fact that the results might

	Case: n_3=n_1									
	$\chi^{(2)}_{ZZZ}$		$\chi^{(2)}_{ZXX}$		$\chi^{(2)}_{XZX}$		$\chi^{(2)}_{ZXX}/\chi^{(2)}_{ZZZ}$		$\chi^{(2)}_{XZX}/\chi^{(2)}_{ZZZ}$	
Run	Re	Im	Re	Im	Re	Im	Re	Im	Re	Im
1	3.16	0.99	0.07	0.97	1.87	0.62	0.11	0.27	0.59	0.01
2	3.03	1.05	0.42	0.83	1.86	0.62	0.21	0.20	0.61	-0.01
2	1.97	1.67	0.92	0.35	0.97	1.43	0.36	-0.13	0.64	0.18
4	1.91	0.83	0.60	0.23	1.25	0.42	0.31	-0.02	0.63	-0.06
5	1.99	0.86	0.61	0.23	1.21	0.40	0.30	-0.01	0.59	-0.05
6	2.25	2.11	1.00	0.38	0.94	1.85	0.32	-0.13	0.63	0.23
7	3.33	0.95	0.17	1.27	1.87	0.62	0.15	0.34	0.57	0.03
8	2.34	1.03	0.84	0.32	1.58	0.53	0.35	-0.02	0.65	-0.06
9	2.63	1.42	0.27	1.09	1.32	1.36	0.25	0.28	0.60	0.19
10	2.97	0.92	0.19	0.97	1.72	0.57	0.15	0.28	0.58	0.01
						Mean	0.25	0.11	0.61	0.05
						StdDev	(0.09)	(0.18)	(0.03)	(0.11)

Table 5.19: The calculated $\vec{\chi}^{(2)}$ tensors and $\vec{\chi}^{(2)}$ ratios for the case of the interfacial refractive index being one.

	Case: n_3=$(n_1 + n_2)/2$									
	$\chi^{(2)}_{ZZZ}$		$\chi^{(2)}_{ZXX}$		$\chi^{(2)}_{XZX}$		$\chi^{(2)}_{ZXX}/\chi^{(2)}_{ZZZ}$		$\chi^{(2)}_{XZX}/\chi^{(2)}_{ZZZ}$	
Run	Re	Im	Re	Im	Re	Im	Re	Im	Re	Im
1	12.35	3.45	0.15	1.54	2.91	0.97	0.04	0.11	0.24	0.01
2	11.86	3.70	0.71	1.30	2.91	0.97	0.09	0.08	0.25	0.00
3	7.83	6.25	1.49	0.51	1.51	2.23	0.15	-0.05	0.26	0.08
4	7.48	3.00	0.97	0.33	1.95	0.65	0.13	-0.01	0.25	-0.02
5	7.83	3.10	0.99	0.34	1.89	0.63	0.12	-0.01	0.24	-0.01
6	8.97	7.92	1.60	0.55	1.47	2.89	0.13	-0.05	0.25	0.10
7	13.02	3.28	0.33	2.02	2.92	0.97	0.06	0.14	0.23	0.02
8	9.20	3.70	1.35	0.46	2.46	0.82	0.14	-0.01	0.26	-0.02
9	10.35	5.20	0.48	1.72	2.05	2.12	0.10	0.11	0.24	0.08
10	11.62	3.22	0.35	1.53	2.69	0.89	0.06	0.11	0.23	0.01
						Mean	0.10	0.06	0.24	0.02
						StdDev	(0.04)	(0.08)	(0.01)	(0.04)

Table 5.20: The calculated $\vec{\chi}^{(2)}$ tensors and $\vec{\chi}^{(2)}$ ratios for the case of the interfacial refractive index being half, n_3=$(n_1 + n_2)/2$.

	Case: n_3=n_2									
	$\chi^{(2)}_{ZZZ}$		$\chi^{(2)}_{ZXX}$		$\chi^{(2)}_{XZX}$		$\chi^{(2)}_{ZXX}/\chi^{(2)}_{ZZZ}$		$\chi^{(2)}_{XZX}/\chi^{(2)}_{ZZZ}$	
Run	Re	Im	Re	Im	Re	Im	Re	Im	Re	Im
1	37.46	9.64	0.27	2.24	4.19	1.40	0.02	0.05	0.11	0.01
2	36.00	10.44	1.07	1.87	4.18	1.39	0.04	0.04	0.12	0.00
3	24.00	18.38	2.18	0.70	2.18	3.20	0.07	-0.03	0.12	0.04
4	22.75	8.59	1.42	0.46	2.80	0.93	0.06	0.00	0.12	0.00
5	23.80	8.89	1.45	0.47	2.72	0.91	0.06	0.00	0.11	0.00
6	27.56	23.33	2.36	0.76	2.11	4.16	0.06	-0.03	0.12	0.05
7	39.49	9.10	0.54	2.93	4.20	1.40	0.03	0.07	0.11	0.01
8	28.00	10.61	1.98	0.64	3.54	1.18	0.07	0.00	0.12	-0.01
9	31.55	15.06	0.75	2.49	2.95	3.04	0.05	0.05	0.11	0.04
10	35.25	9.01	0.56	2.23	3.86	1.29	0.03	0.06	0.11	0.01
						Mean	0.05	0.02	0.12	0.01
						StdDev	(0.02)	(0.04)	(0.02)	(0.02)

Table 5.21: The calculated $\vec{\chi}^{(2)}$ tensors and $\vec{\chi}^{(2)}$ ratios for the case of the interfacial refractive index being equal to the bulk refractive index, n_3=n_2 at ω and 2ω.

not be physically reasonable. The interfacial refractive index of the air/toluene interface is expected to have a value between the refractive indices of the two bulk phases. It remains to be seen how air-like or toluene-like the behaviour of the toluene molecules sitting at the interface is. Under certain conditions it is possible to determine the interfacial refractive index. In the limit of a weak orientation [39] the refractive index can be determined from SHG measurements. Assuming the toluene molecule is aligned weakly at the interface then the following relationship among the effective $\vec{\chi}^{(2)}$ tensors holds [39], $n_3{}^4\chi^{(2)}_{ZZZ}=\chi^{(2)}_{ZXX}+2\chi^{(2)}_{XZX}$. Assuming no optical dispersion the interfacial refractive index, n_3, can then be determined if the molecules at the interface can be treated in the weak order limit. The value obtained for the refractive index is 1.07 for the above experimental runs. This value is determined from the $\vec{\chi}^{(2)}$ tensors obtained assuming the interfacial refractive index is one and real and it was then allowed to vary in order to satisfy the above relationship. Previous interfacial refractive index values obtained for molecules satisfying the weak order limit were close to the half value of the bulk phases enclosing the interface. The value determined in this case is essentially 1, indicating that (assuming that molecules are weakly aligned at the interface then) the interfacial region properties are air like. So on the grounds that it doesn't hold physically, we assume that the toluene molecule has a preferred orientation at the air/toluene interface and the weak field limit is not applicable in this case.

5.4.2.4 Molecular Orientation

Toluene has C_s symmetry, the hyperpolarisability tensor $\vec{\beta}$, has ten independent elements but only four tensors contribute significantly to $\vec{\beta}$. These four independent tensor elements are β_{zzz}, β_{xzx}, β_{yyz}, and β_{zyy} where the z coordinate is taken along the long molecular axis, the x coordinate along the short molecular axis, and the y coordinate perpendicular to the aromatic ring, see Figure 5.15. The previous theoretical calculations presented in this work, indicate that the significance of these tensors is found to be $\beta_{zzz}>\beta_{xzx}$ for the LB94/Vdiff calculations and $\beta_{zzz}>\beta_{yyz}\approx\beta_{zyy}$ for the GRACLB/Vdiff and HF/sadlej calculations at the fundamental wavelength (532 nm). Near resonances the symmetry of the transition will only enhance certain tensor elements with adequate symmetry as in the case of phenol [125].

Different cases where only one or two tensors dominate will be discussed and the average molecular orientation will be determined. The relationship between the $\vec{\chi}^{(2)}$ and $\vec{\beta}$ has been described in the section A1 in the appendix chapter. The ratio $R=\beta_{xzx}/\beta_{zzz}$ and the orientational parameter D can be obtained and the results for the three cases for the value of the interfacial refractive index will be presented. The choice of the interfacial refractive index can have a dramatic effect on the calculated molecular orientation angle. It has been found that the difference of the refractive index between the two bulk media surrounding the interface determines the uncertainty in the estimated molecular orientation of the molecule [37]. For the case of the air/toluene interface the difference between the value of the refractive index of toluene and that of air is 0.5. This difference between the values of the refractive indices can introduce uncertainties in the estimation of the molecular angle of the order of 20 °. Recently it has been found that there is a linear relationship between the difference in the refractive indices of the two bulk phases and the error introduced in the determined molecular orientation angle [37]. The trend suggests that as the refractive indices difference gets smaller, down to difference values of ~0.08, the error introduced in the determination of the molecular tilt angle is negligible.

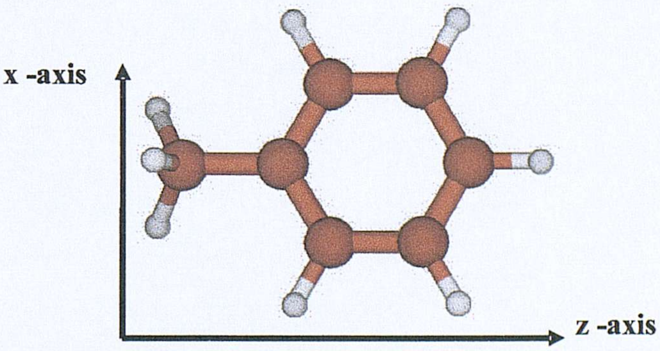

Figure 5.15: The molecular axes labelling for toluene.

The cases to be considered are β_{zzz} tensor dominant, β_{zzz} and β_{xzx} dominant,

β_{zzz} dominant, $D=\frac{<\cos^3\theta>}{<\cos\theta>}$

	$n_3=n_1$			$n_3=1/2(n_1+n_2)$			$n_3=n_2$		
Run	Re D	Im D	$\theta/^\circ$	Re D	Im D	$\theta/^\circ$	Re D	Im D	$\theta/^\circ$
1	0.68	-0.31	34.2	0.88	-0.18	20.1	0.95	-0.10	13.0
2	0.65	-0.19	36.1	0.84	-0.12	23.8	0.92	-0.07	16.6
3	0.57	0.08	41.1	0.77	0.06	28.9	0.87	0.04	20.9
4	0.62	0.01	38.2	0.80	0.01	26.7	0.89	0.00	19.3
5	0.62	0.01	37.8	0.80	0.01	26.5	0.89	0.00	19.1
6	0.59	0.10	39.5	0.79	0.07	27.5	0.89	0.04	19.8
7	0.60	-0.32	38.9	0.84	-0.21	23.6	0.93	-0.12	15.4
8	0.59	0.01	39.9	0.78	0.01	28.2	0.88	0.01	20.4
9	0.59	-0.22	40.1	0.80	-0.15	26.6	0.90	-0.09	18.4
10	0.65	-0.28	36.4	0.85	-0.17	22.5	0.93	-0.10	15.0
Average	0.62	-0.11	38.2	0.81	-0.07	25.4	0.91	-0.04	17.8
St.Dev	0.04	0.17	2.1	0.04	0.11	2.8	0.03	0.06	2.6

Table 5.22: Real and imaginary components of the orientational parameter D for the three different cases of the value for the interfacial refractive index. The determined angle θ, is the angle between the main molecular axis and the interface normal. The other two Euler angles , ϕ and ψ are not considered in this case. The angle ϕ, has a uniform distribution because the surface is isotropic and the angle ψ cannot be determined because only one hyperpolarisability tensor is considered to be significant. The average values and the standard deviation of the mean is shown.

and β_{zzz} and $\beta_{zyy}\approx\beta_{yyz}$ dominant.

- β_{zzz} dominant.

  In this case the molecule has only one dominant hyperpolarisability tensor, namely the β_{zzz} component. The charge transfer will occur exclusively along the main molecular axis. The orientational parameter D can be determined (see appendix chapter) and the molecular axis angle θ with respect to the laboratory z axis can be estimated, shown in Table 5.22. In this case the molecule must exhibit Kleinman symmetry $(\chi^{(2)}_{ZXX}=\chi^{(2)}_{XZX})$. The determined components of the $\vec{\chi}^{(2)}$ tensor for toluene do not suggest this to be the case. The theoretical calculations have shown that near resonance the β_{xzx}, β_{yyz}, and β_{zyy} tensor components become important. It can be seen from Table 5.22 that the choice of the refractive index for the interface region can have a drastic effect on the estimated molecular orientation angle. In this case the error introduced can be as big as 20° depending on the choice of the refractive index.

β_{zzz}, β_{xzx} dominant, ψ=90°, $D=\frac{<\cos^3\theta>}{<\cos\theta>}$

	$n_3=n_1$			$n_3=1/2(n_1+n_2)$			$n_3=n_2$		
Run	Re D	Im D	θ/°	Re D	Im D	θ/°	Re D	Im D	θ/°
1	0.77	0.24	28.8	0.66	-0.03	35.9	0.89	-0.11	19.60
2	0.74	0.38	30.9	0.67	-0.01	35.3	0.87	-0.07	20.73
3	0.68	-0.36	34.3	0.72	-0.08	32.0	0.85	0.00	23.00
4	-0.56	0.74		0.66	0.03	35.7	0.86	0.01	21.88
5	-0.19	0.37		0.69	0.02	33.8	0.87	0.01	21.28
6	0.77	-0.32	28.4	0.75	-0.09	30.0	0.86	0.00	22.06
7	0.69	0.21	33.7	0.66	-0.04	35.6	0.86	-0.12	21.63
8	-0.27	0.40		0.65	0.03	36.3	0.85	0.01	22.87
9	0.33	0.48	54.8	0.61	-0.14	38.5	0.86	-0.10	21.82
10	0.72	0.26	31.7	0.66	-0.03	35.4	0.88	-0.10	20.55
Average	0.37	0.24	34.7	0.67	-0.04	34.9	0.86	-0.05	21.5
St.Dev	0.51	0.34	9.2	0.04	0.06	2.4	0.01	0.06	1.0

Table 5.23: Real and imaginary components of the orientational parameter D for the three different cases for the value of the interfacial refractive index. The determined angle θ, is the angle between the main molecular axis and the interface normal. The Euler angle , ϕ is not considered in this case. The angle ϕ, has a uniform distribution because the surface is isotropic. The angle ψ has been considered as 90° degrees. The average and the standard deviation of the mean is shown.

- β_{zzz} and β_{xzx} dominant

  In this case the Kleinman symmetry is broken and a second tensor is significant. The hyperpolarisability component β_{xzx} is enhanced by the electronic transition. It is then possible to determine the ratio $\frac{\beta_{xzx}}{\beta_{zzz}}$ of the two components (see theory chapter). The theoretical calculations indicate the significance of the tensor component β_{xzx} at resonance. Previous theoretical studies on phenol [125], which, can be approximated to the toluene molecule, have revealed the significance of the β_{xzx} tensor near resonance. The case where ψ=90° is shown here and it is assumed that the results for ψ=random are similar. The determined orientational parameter D for three different values of the interfacial refractive index is shown in Table 5.23 together with the determined orientational molecular angle.

  The ratio $\frac{\beta_{xzx}}{\beta_{zzz}}$ is calculated and the results are shown in Table 5.24. The determined value of 0.21 ± 0.05 will be used for comparison with the theoretical calculations discussed in the next section.

  The case where the β_{zzz} and β_{zxx} tensors are dominant was rejected based on the grounds that the theoretical calculations showed that near resonance, which is where this experiment is conducted, the β_{zxx} tensor is smaller than the β_{xzx} one. The determined orientational angle shown for the case where

	$n_3=n_1$		$n_3=1/2(n_1+n_2)$		$n_3=n_2$	
	β_{zzz}, β_{xzx} dominant, $R=\frac{\beta_{xzx}}{\beta_{zzz}}$					
Run	Re R	Im R	Re R	Im R	Re R	Im R
1	0.50	-0.66	0.31	-0.25	0.17	-0.11
2	0.45	-0.42	0.25	-0.17	0.14	-0.08
3	0.27	0.40	0.15	0.22	0.08	0.12
4	0.40	-0.04	0.20	-0.01	0.11	0.00
5	0.35	-0.04	0.18	-0.01	0.09	0.00
6	0.30	0.49	0.17	0.26	0.09	0.14
7	0.31	-0.65	0.23	-0.28	0.13	-0.13
8	0.35	-0.04	0.18	-0.01	0.10	0.00
9	0.37	-0.25	0.21	-0.09	0.11	-0.03
10	0.41	-0.59	0.26	-0.24	0.14	-0.10
Average	0.37	-0.18	0.21	-0.06	0.12	-0.02
St.Dev	0.07	0.41	0.05	0.19	0.03	0.09

Table 5.24: The real and imaginary components of the ratio, $R=\frac{\beta_{xzx}}{\beta_{zzz}}$, for the three cases for the value of the interfacial refractive index. The average and standard deviation of the mean is shown.

the interfacial refractive index is taken as the average of the two phases is the same to the orientation angle obtained in the β_{zzz} and β_{xzx} dominant case shown in Table 5.23 within the estimated error. The ratio of the dominant hyperpolarisability tensors are similar in size but have opposite signs.

- β_{zzz} and $\beta_{yyz}\approx\beta_{zyy}$ dominant.

  This case is considered based on the theoretical calculations performed on the toluene molecule. The β_{yyz} and β_{yyz} tensor component values are approximated to be equal based on the results at 532 nm and 504 nm, see Tables 5.13 and 5.14. The β_{zyy} and β_{yyz} tensors are equivalent to the β_{zxx} and β_{xxz} tensors because of the azimuthal symmetry of the surface. Assuming $\beta_{yyz}\approx\beta_{zyy}$ then the molecule must exhibits Kleinman symmetry (see appendix) and $\chi^{(2)}_{ZXX}=\chi^{(2)}_{XXZ}$, but this is not observed experimentally.

It was shown earlier that the toluene molecule cannot be weakly aligned at the air/toluene interface because that would require the interfacial refractive index to be almost 1. This was considered to be unrealistic, and is supported from the results shown in Table 5.23 for the case where the interfacial refractive index is equal to the refractive index of air,($n_3=n_1$). The orientational parameter is a measurable macroscopic quantity, which in principle should have a very small imaginary part, and it can be approximated to $(\cos\theta)^2$, for an assumed narrow distribution of angles in the molecular orientation. The negative values obtained for the real part and the high imaginary values of the orientational parameter indicate that the preferred choice of the interfacial refractive index should be more than one. This agrees with physical intuition as the molecule is expected to retain some of the hydrocarbon character in the interface. Recent studies have shown that the value of the refractive index for the air/liquid interface could be chosen with respect to the value of the liquid phase refractive index, based on a simple local field correction in a modified Lorentzian model [42]. Assuming no optical dispersion and choosing a value of 1.5 for the refractive index of toluene, the interfacial refractive index value determined in the case of toluene is 1.21, which is very close to the averaged value of the refractive index results shown here. The orientational parameter D determined in this way has a small imaginary part and the orientational angle (averaged over all experiments) is found to be 35 $\pm 3°$ as shown in Table 5.23 assuming a narrow angle distribution about the mean. This determined angle suggests that the toluene molecules are not lying flat in the surface but that they are oriented away from the surface. Information about the angular distribution of the determined angle cannot be obtained from the experiment but it is possible to be determined experimentally with additional spectroscopic studies such as angle resolved absorption photoacoustic spectroscopy [126].

5.4.2.5 Experiment vs Theory

All theoretical calculations carried out in this work have been considering isolated molecules in the gas phase. Furthermore only the electronic (hyper)polarisability has been calculated and any vibrational or rotational effects have been ignored. Experimental determined hyperpolarisabilities will contain electronic, vibrational and rotational contributions and is not trivial to separate the electronic contribution from the rest.

The SHG experiments are conducted at the air/toluene interface and the dominant hyperpolarisability ratio of the molecule can be estimated from the polarisation dependence of the SHG signal. The influence of the solvent molecules (in this case toluene and air) and the presence of intermolecular forces can affect the non-linear polarisation behaviour of the medium. Since absolute hyperpolarisability values cannot be obtain from SHG experiments, ratios can be compared to the theoretical ones instead. Only one experimental frequency is available and the comparison can be made directly to the gas phase ratios.

From the computational study it was determined that the β_{zzz} and β_{xzx} are significant and their experimental measured ratio (Real part, β_{xzx}/β_{zzz}) can vary from 0.37 to 0.12 depending on the choice of the value for the interfacial refractive index. The calculated dynamic (532 nm) hyperpolarisability ratio (β_{xzx}/β_{zzz}) at the LB94/DZPpolar level of theory is 0.18, Table 5.25 which is close to the experimental value of 0.21 assuming the refractive index value to take the average of the two bulk phases. The GRACLB and SAOP methods predict similar values for the ratios β_{zyy}/β_{zzz} and β_{yzy}/β_{zzz} and are in good agreement with the HF computed values. The other methods (LB94, PBE, B97-1, HCTH) do not predict the significance of the β_{zyy} and β_{yzy} with respect to the β_{zzz} tensor. The PBE, B97-1 and HCTH calculated results are similar to each other and the value for the

Method	β_{xzx}/β_{zzz}	β_{zxx}/β_{zzz}	β_{yzy}/β_{zzz}	β_{zyy}/β_{zzz}
LB94/DZPpolar	0.18	-0.05	0.04	0.07
LB94/DZPhypol	0.18	-0.05	0.04	0.08
LB94/Vdiff	0.20	-0.03	0.04	0.08
LB94/Vdiff(10^{-}4)	0.18	-0.05	0.02	0.06
LB94/ET1	0.16	-0.08	0.03	0.06
LB94/ET1(10^{-}4)	0.17	-0.06	0.04	0.07
GRACLB(Vdiff(10^{-}4)	0.09	-0.02	0.66	0.66
SAOP/DZPpolar	0.10	-0.05	0.48	0.52
PBE/Sadlej	-0.10	-0.20	-0.03	0.00
B97-1/Sadlej	-0.12	-0.22	0.05	0.10
HCTH/Sadlej	-0.07	-0.16	-0.02	0.00
HF/Sadlej	0.07	0.05	0.67	0.70

Table 5.25: Calculated dynamic (532 nm) hyperpolarisability ratios at different levels of theory. The LB94, GRACLB and SAOP methods were used in ADF, the PBE, B97-1 and HCTH functionals were used in Cadpac. The experimental measured real values of the ratios β_{xzx}/β_{zzz} and β_{zxx}/β_{zzz} were 0.21 ± 0.05 and -0.19 ± 0.04 respectively.

β_{zxx}/β_{zzz} tensor is close to the experimental one. These methods fail to predict the correct phase for the β_{xzx}/β_{zzz} ratio with respect to experiment. The LB94 functional predicts the correct phase for the β_{zxx} and β_{xzx} tensors with respect to the β_{zzz} tensor and the ratio β_{xzx}/β_{zzz} agrees with the experimental value of 0.21 within the estimated experimental error.

5.5 Conclusions and Future Work

The toluene molecule has been studied theoretically using *ab initio* methods and experimentally at the air/toluene interface with the non-linear technique of surface second harmonic generation (SHG). The computationally study investigates the currently available computing packages for the calculation of optimised geometries, harmonic frequencies, excitation energies and dynamic (hyper)polarisabilities. The DFT methods proved to predict the geometries and frequencies closer to experiment than the HF and MP2 approximation methods. In particular the GGA exchange correlation functionals BLYP, PBE, BP86, BP91 and LDA methods performed better than their hybrid analogues. The PBE functional provided the best values for the optimised geometry. The HCTH class of functionals estimated the harmonic frequencies with the absolute error with respect to the experimental values. The MP2 method predicted more accurately the bond angles in the molecule than the rest of theoretical methods. The low lying $\pi \rightarrow \pi^*$ transitions were calculated closer to experiment using the LB94 functional in the ADF package. The accuracy of the excitation energies didn't improve with the further increase of the basis set size and the addition of diffuse functions, with TZ2P being sufficient when compared to experiment.

The calculation of the frequency dependent hyperpolarisabilities using different theoretical methods revealed the expected resonance enhancement in the UV region. The predicted significant hyperpolarisability tensors near resonance were the β_{zzz} and β_{xzx} with the LB94 functional and β_{zzz}, β_{zyy} and β_{yzy} with the GR-ACLB, SAOP and HF methods. The Cadpac routine for the calculation of the frequency dependent hyperpolarisabilities was found to contain a possible error. The new version of Gaussian 03 allows frequency dependence hyperpolarisabilities to be calculated and contains many functionals used in Cadpac such as the asymptotically corrected HCTH. Future work could repeat some of the calculation using these functionals and comparing with the Capdac results. Although the polarisability calculation of toluene was in good agreement with experiment the hyperpolarisability calculations are not conclusive. More experimental results are needed for the air/toluene interface at different frequencies in order to compare with the calculations. The addition of solvent molecules in any future calculations will be advantageous in order to mimic the air/toluene environment. The computational results showed the significance of the addition of diffuse functions to the basis set in order to predict reliable and meaningful hyperpolarisability values.

The second harmonic generation studies found the toluene molecules to have a preferred orientation with the molecular z-axis inclined to the surface normal by 35 ± 3^o, assuming a random distribution of the molecules in the surface plane. This implies that the toluene molecules are not lying flat at the surface but they have a definite orientation at the air/toluene interface which results from their intermolecular bonding and the minimisation of the surface energy. The toluene solution exhibits a strong two photon fluorescence emission near the harmonic signal that can be separated and resolved. The TPF maximum wavelength (287 nm) is blue shifted with regards to the linear emission fluorescence one (292 nm). Future studies might involve SHG studies of the adsorption of the toluene molecule at the air/cyclohexane interface.

Chapter 6

L-Phenylalanine

6.1 Introduction

6.1.1 Preface

Amino acids are important biological building blocks that can be linked together by forming peptide bonds. Any number of amino acids can be linked together to form proteins. Amino acids contain both acidic and basic groups in the same molecule. They can undergo tautomerism and exist in solution primarily in the form of a dipolar ion or zwitterion unlike the gas phase which the zwitterionic form does not exist [127]. The interaction of specific amino acids within a protein molecule affects the adsorption process to a membrane. Therefore the adsorption properties and surface activity of amino acids need to be understand.

This chapter contains experimental and theoretical investigations on the amino acid L-phenylalanine. Surface second harmonic generation [13–16] experiments were conducted at the air/water interface in the presence of the adsorbed phenylalanine molecule. The adsorption of phenylalanine at the air/water interface was investigated for concentrations up to 0.08 M. The polarisation dependence of the SHG signal revealed the preferred orientation of the molecule at the water surface. Calculations on the excitation energies ($\pi \rightarrow \pi^*$) and the frequency dependent hyperpolarisability on nine lowest energy conformations [128] of the molecule in the gas phase were undertaken. The results provide an insight into the dominant hyperpolarisability tensors that are responsible for the second harmonic signal. The effect of the conformation of the molecule on the hyperpolarisability tensor values was investigated for the nine most stable conformers.

6.1.2 Previous Studies

The SHG technique has been used over the years for providing information of the molecular interactions at liquid surfaces. The use of the natural occurring aromatic acids Tryptophan (Trp), Tyrosine (Tyr), and Phenylalanine (Phe) as SHG probes provides the potential for *in-situ* study of peptides at liquid interfaces. The accessible UV resonances of the aromatic residue can be used for resonance enhancement SHG experiments. The high specificity of the SHG technique can provide information of the orientation and local environment of the adsorbed amino acid, leading to a better understanding of the adsorption process. SHG-labels have been used for studying a variety of interfacial systems which are second harmonic-active moeities and can be attached to a molecule that is of particular interest and is not SHG active [129].

Phenylalanine have been previously studied at the air/water interface using the nulling technique [130, 131]. Butyloxycarbonyl (Boc) substituted phenylalanine was used to enhance surface adsorption, but no nulling angle could be obtained for Boc-Phe. At a monolayer surface coverage of the air/water interface the SHG signal was found to be 1.5 times that of the bare air/water interface signal and with a relative phase of 27 $\pm 10^{\circ}$ [130].

The electronic spectrum and the first excited states of phenylalanine have been previously studied [117, 132–134] and compared to computational calculations [135, 136]. A gas phase conformation spectroscopic investigation combined with ab initio calculations [128] has determined the nine lowest energy conformations with six of them been assigned experimentally. Monohydrated clusters of phenylalanine have been investigated by resonant two-photon ionization and the excitation spectra of the hydration complex were obtained and compared to gas phase calculations [137]. Cation-π interactions of the phenylalanine with sodium and potassium cations have been investigated to assess their importance [138,139].

6.1.3 The Absorption Spectrum of Phenylalanine

The two lowest electronic transitions of benzene involve the B_{1u} and B_{2u} excited states and they are symmetry forbidden. In substituted benzene residues the $\pi \rightarrow \pi^*$ transitions involve the excited states respectively. The oscillator strength of these transitions increases with decreasing symmetry of the aromatic ring. Toluene and phenylalanine exhibit very similar condensed phase absorption spectra. The L_a maximum absorption wavelength for aqueous phenylalanine occurs at 205 nm with molar absorption coefficient of 9600 M^{-1} cm^{-1}, and the L_b transition occurs at 258 nm with molar absorption coefficient of 190 M^{-1} cm^{-1} [132].

The absorption spectrum of an aqueous phenylalanine solution is shown in Figure 6.1. In the same Figure the linear emission fluorescence spectrum is also shown for an excitation wavelength of 266 nm. The molar absorption coefficient at the second harmonic wavelength (266 nm) is 88 M^{-1} cm^{-1}, indicating a possible resonance enhancement in the SHG signal. The emission fluorescence spectrum exhibits a maximum at 283 nm, indicating the likely interference of the two photon fluorescence (TPF) signal with the SHG one.

6.2 Computational Details

The nine most stable conformers were used from a previous study [128] to determine the static and dynamic hyperpolarisability, β, at the laser frequency of 532 nm. The first excitation energy of the lowest energy conformer was calculated

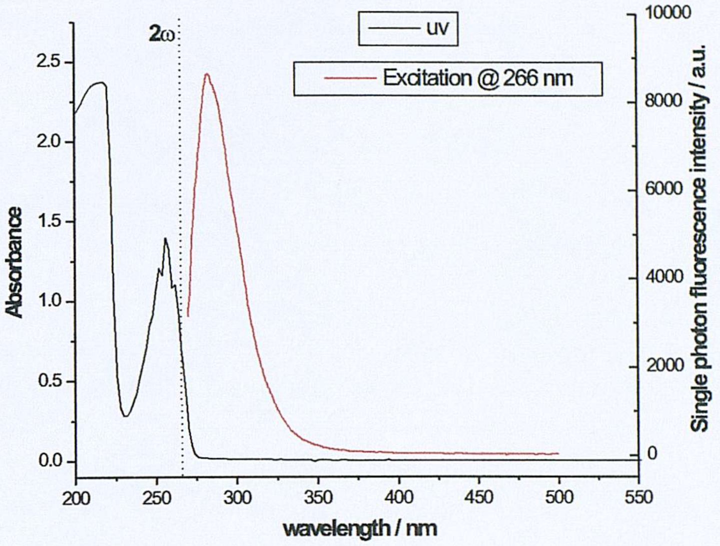

Figure 6.1: The absorption and emission fluorescence spectra of a 21 mM aqueous phenylalanine solution. The left axes indicates the UV absorption intensity. The right axes marks the fluorescence emission intensity, the excitation wavelength was 266 nm.

and compared with experiment. All calculations used the Gaussian 98, Gamess-US, Cadpac, and ADF packages. The static hyperpolarisability was calculated at the MP2/Sadlej and HF/Sadlej levels of theory using Gaussian 98. Gamess-US was used for the HF/Saldej calculations. Cadpac and ADF were used for all time dependent DFT methods. The basis sets employed were the Sadlej, for Gaussian 98, Cadpac, and Gamess-US packages and the Vdiff, and DZPpolar for the ADF package.

6.3 Experimental

6.3.1 Optical Arrangement

The basic optical arrangement used has been described in Chapter 3. Briefly, the SHG experiments were performed with the second harmonic output of a Nd:YAG laser delivering pulses of 5 mJ and 5 ns duration at a wavelength of 532 nm and a varied repetition rate from 10-20 Hz. The incident beam was directed at the air/liquid interface at an angle of 60° (angle between the incident beam and the surface normal) with an estimated laser energy of 2.5 mJ/pulse. The reflected SH signal at 266 nm was collected with a lens and passed through 3 filters to reject residual light at 532 nm and focused onto the entrance slit of a monochromator. The signal was detected with a fast response photomultiplier tube and sent to a gated boxcar averager. Data were recorded onto a computer using Visual Basic software for further processing. The fundamental input and harmonic output polarisations were controlled by a half-wave plate and quartz Rochon polarizer, respectively.

6.3.2 Data Acquisition and Analysis

Using a software acquisition program , written in Visual Basic, the data were collected with up to 2000 laser shots depending on signal intensities. Background signals and laser power measurements were obtained and averaged over 2000 laser shots and subtracted from the sample signal. The collected data were fitted to the equations described in Chapter 2 using R [45] and built-in minimisation functions [44]. The Fresnel coefficients were calculated as described in Chapter 3.

6.3.3 Preparation of Solutions and Sample Handling

Phenylalanine (Aldrich, $\geq$ 99%) solutions were prepared fresh on the day and deoxygenated with nitrogen. During the SHG experiments a steady flow of nitrogen was maintained above the cell to avoid sample photo-oxidation. The temperature of the sample holder was controlled with a water bath at 21 °C. The water used was ultrapure, 18.2 MΩ cm^{-1}.

6.4 Results and Discussion

6.4.1 SHG Results

6.4.1.1 Monochromator Scan

The linear photon fluorescence emission spectrum of phenylalanine shown in Figure 6.1 exhibits a maximum at 279 nm with an excitation wavelength of 266 nm. There is the possibility of signal interference between the two photon fluorescence (TPF) that occurs during the SHG experiment and the SHG signal. The single photon fluorescence lifetime of Phe in water is 7.4 ns [140]. In order to avoid this signal overlapping, the slits of the monochromator needed to be optimised. A monochromator scan was carried out where the signal intensity was monitored versus the monochromator wavelength (setting) and is shown in Figure 6.2.

The input and output slits of the monochromator were optimised to achieve the separation of the TPF and SHG signals. The P and S polarised harmonic SHG signals can be recovered and separated from the overwhelming bulk two photon fluorescence. It is interesting to note that the TPF emission fluorescence spectrum is blue shifted with respect to the linear emission fluorescence spectrum (283 nm) exhibiting a maximum wavelength at 275 nm. This might be because of different relaxation pathways available to the two photon absorption process leading to fluorescence emission at shorter wavelength. It can be seen that the TPF signal is predominantly P polarised and this is a characteristic feature of the two photon

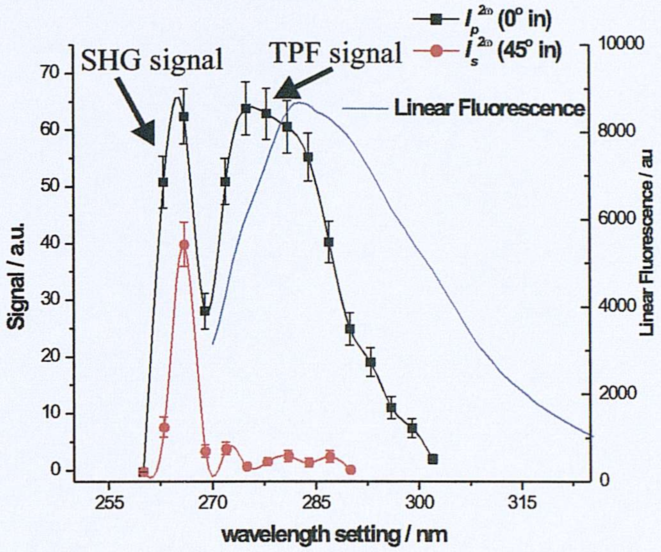

Figure 6.2: Monochromator scan for the air/water interface for phenylalanine. The signal intensity is monitored versus the monochromator wavelength setting. The output polarisation angles are set to P and S and the input polarisation angles are set to 0° and 45° degrees respectively. Spline curves are fitted to the signal intensities. Error bars are 1 σ. The linear fluorescence emission spectrum is also shown for comparison at an excitation wavelength of 266 nm.

absorption process with signal intensities depending on the polarisation of light [141]. On increasing the bulk concentration of the solution the slit widths need to be reduced further in order for the overlap of the signals to be achieved. Although this might results in a loss of the SHG signal intensity, the separation achieved is sufficient for the SHG signal to be treated as purely originating from the interface. In cases where the fluorescence is still present, the fluorescence signal might be subtracted from the overall signal if the percentage contribution and the phase between the SHG signal and the TPF signal is known.

The dependence of the SHG and TPF signals with incident laser power are shown in Figure 6.3. The expected quadratic relationship of the SHG signal with incident laser power is shown; An ln-ln plot of the SHG versus the incoming laser fluence and a regression line is fitted with slope 1.99. The ln-ln plot of the TPF signal has a slope of 1.27 contrary to the expected quadratic relationship [142].

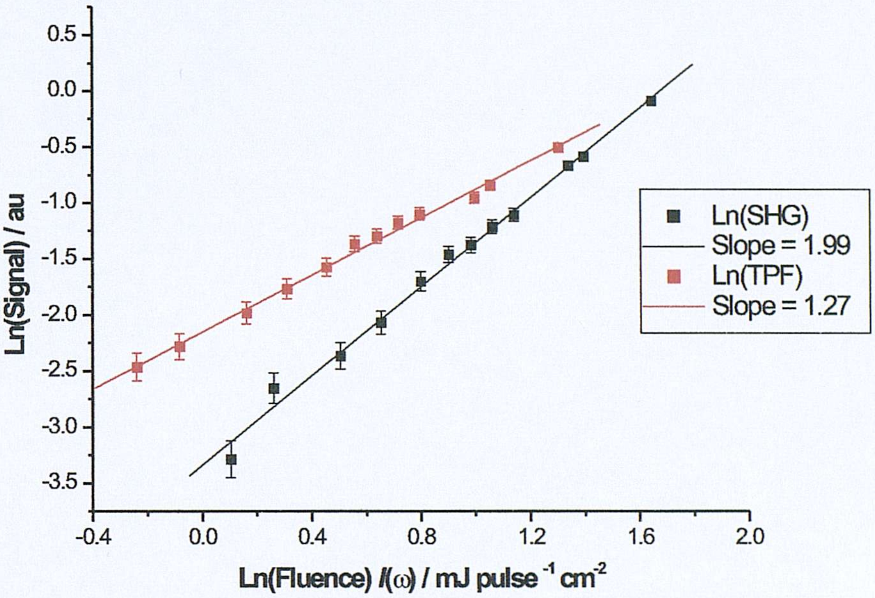

Figure 6.3: Linear regressions of the ln(SHG) signal and the ln(TPF) signal versus the ln of incoming laser fluence for a 21mM phenylalanine solution in water. The fluorescence signal was retrieved by setting the monochromator wavelength setting to 275 nm. The slope of the line for the SHG signal is 1.99 (regression coefficient r=0.9964) and the slope of the line for the TPF signal is 1.27 (regression coefficient r=0.9973). Error bars are ± 5%.

6.4.1.2 Polarisation Dependence

The polarisation dependence of the SHG signal was recorded for bulk phenylalanine concentrations from 0.005 M up to 0.8 M. This approach would reveal any change in the preferred orientation of the phenylalanine molecule at the air/water interface with increasing bulk concentration. The polarisation was monitored for the linear output polarisations $I_{\mathrm{P}}^{(2\omega)}$, $I_{\mathrm{S}}^{(2\omega)}$, and $I_{+45}^{(2\omega)}$, where P, S, and +45 correspond to the output harmonic polarisation angle Γ. The conditions were optimised to avoid the interference of the two photon fluorescence present with the SHG signal. A representative sample of six plots from all the acquired data at different concentrations are shown in Figures 6.4-6.7. Statistical diagnostics plots is shown to indicate the quality of the fit and the polarisation dependence behavior of the SHG signal.

The polarisation curves are similar to the air/toluene interface case although they are acquired from completely different environments. The polarisation curves remain the same in shape with increasing Phe concentration without any marked behavior change except the expected increase in signal [39]. This indicates no phase changes at the air/water interface even at high bulk concentrations and that the molecules are possibly weakly aligned at the air/water interface. The diagnostics plots shown next to the polarisation curves plots indicate the desired spread of the plotted points and no significant curvature in the plotted residuals is observed confirming the non-biased results and good quality fit.

The SHG data from twelve different bulk concentrations were fitted to the phenomological model with the A, B, and C coefficients, taking A to be real. Phenylalanine absorbs at the second harmonic wavelength (266 nm) so we expect the coefficients to be complex. The estimates of the coefficient ratios and their phases are shown in Table 6.1. Confidence intervals are shown for the estimates of the coefficient ratios and standard errors for the estimates of the phases. Some phases estimates are set to zero because they were insignificant during the fitting process.

From the polarisation plots it can be seen that there is a strong dependence on the A coefficient so all ratios have the A coefficient as denominator. The B coefficient is weakly dependent and the C coefficient has a medium dependency, similar to the air/toluene interface.

		B/A		C/A	
Data Set	C/mM	$\hat{r}_R$	$\hat{\phi}_R$	$\hat{r}_R$	$\hat{\phi}_R$
		(Delta C.I.)	$\sigma(\hat{\phi}_R)$	(Delta C.I.)	$\sigma(\hat{\phi}_R)$
1	2.1	0.250		0.727	
		(0.229, 0.372)		(0.714, 0.741)	
2	4.1	0.257		0.812	
		(0.230, 0.284)		(0.796, 0.829)	
3	5.0	0.356	1.086	0.662	0.346
		(0.328, 0.383)	(0.070)	(0.650, 0.674)	(0.086)
4	8.57	0.301	1.025	0.791	
		(0.255, 0.347)	(0.149)	(0.768, 0.814)	
5	8.90	0.323		0.849	
		(0.293, 0.352)		(0.828, 0.870)	
6	10.65	0.422	0.935	0.738	0.404
		(0.372, 0.472)	(0.147)	(0.711, 0.764)	(0.153)
7	20.19	0.412		0.823	
		(0.369,0.455)		(0.787,0.858)	
8	30.0	0.382		0.852	
		(0.311, 0.454)		(0.797, 0.906)	
9	36.0	0.393	0.712	0.713	0.308
		(0.364, 0.422)	(0.114)	(0.699, 0.727)	(0.110)
10	44.7	0.370		0.748	0.466
		(0.353, 0.387)		(0.734, 0.763)	(0.055)
11	55.9	0.356		0.829	0.976
		(0.327, 0.385)		(0.807, 0.851)	(0.039)
12	76.5	0.375		0.727	0.525
		(0.357, 0.394)		(0.711, 0.743)	(0.056)

Table 6.1: Ratios of parameters for the phenylalanine model. Confidence intervals (C.I.) are given for the ratios of the magnitude using the delta method. Standard errors are given for the phase angles $\hat{\phi}_R$ (in parentheses). Some of the phase angles are set to zero because the fitted models were simplified when the phase angles were considered negligible.

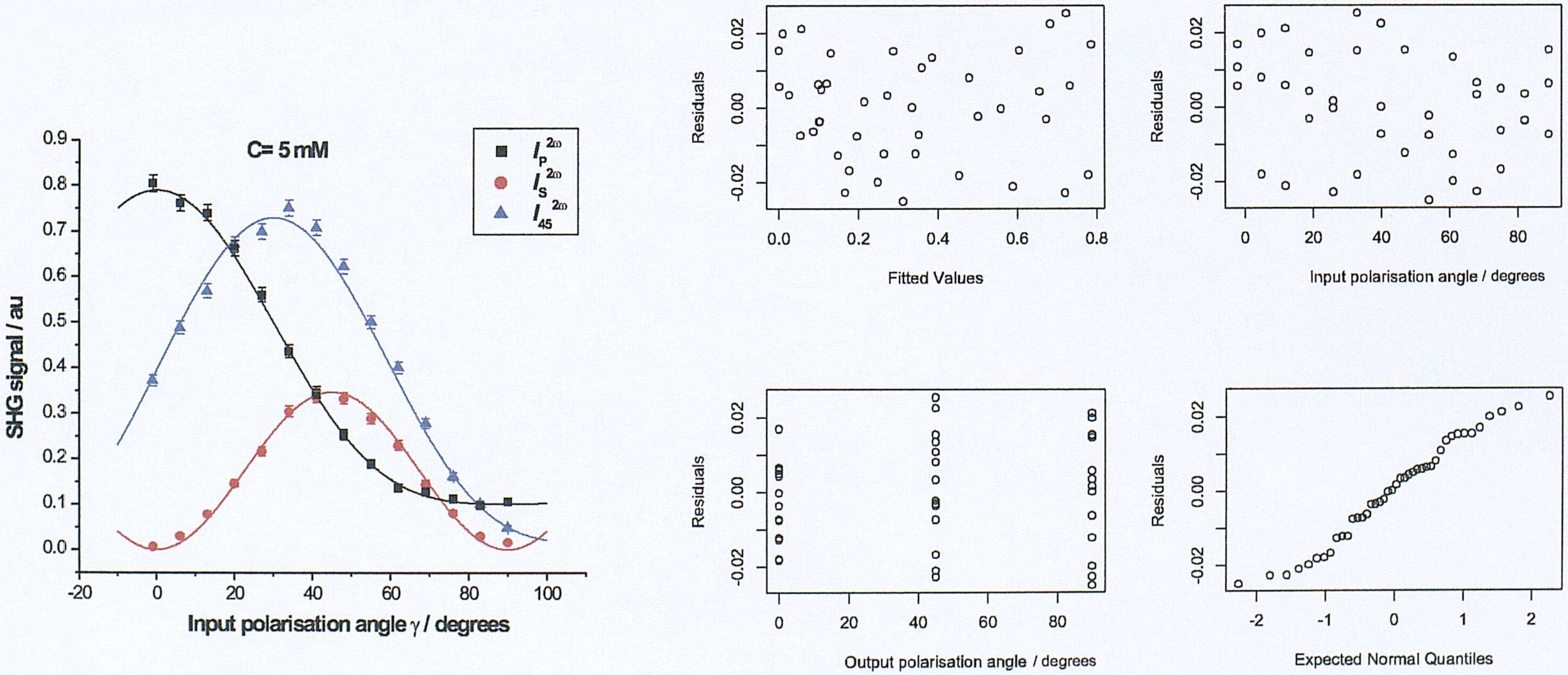

Figure 6.4: The polarisation dependence of the SHG signal generated in the S, P and +45° linear polarisation planes as a function of the input polarisation angle (γ), for a 5 mM phenylalanine solution. The solid lines have been estimated by the simultaneous fitting of the Euler parametrization of A, B, and C parameters in the S, P, and +45° SHG data assuming A to be real and B and C to be complex. λ=532/266 nm. The error bars added are σ. Residual and normal probability plots for the model fitted to the SHG data are shown. The residual values (calculated subtracted from fitted) are plotted against the fitted values, the input polarisation angle γ, the output polarisation angle, and the expected normal quantiles.

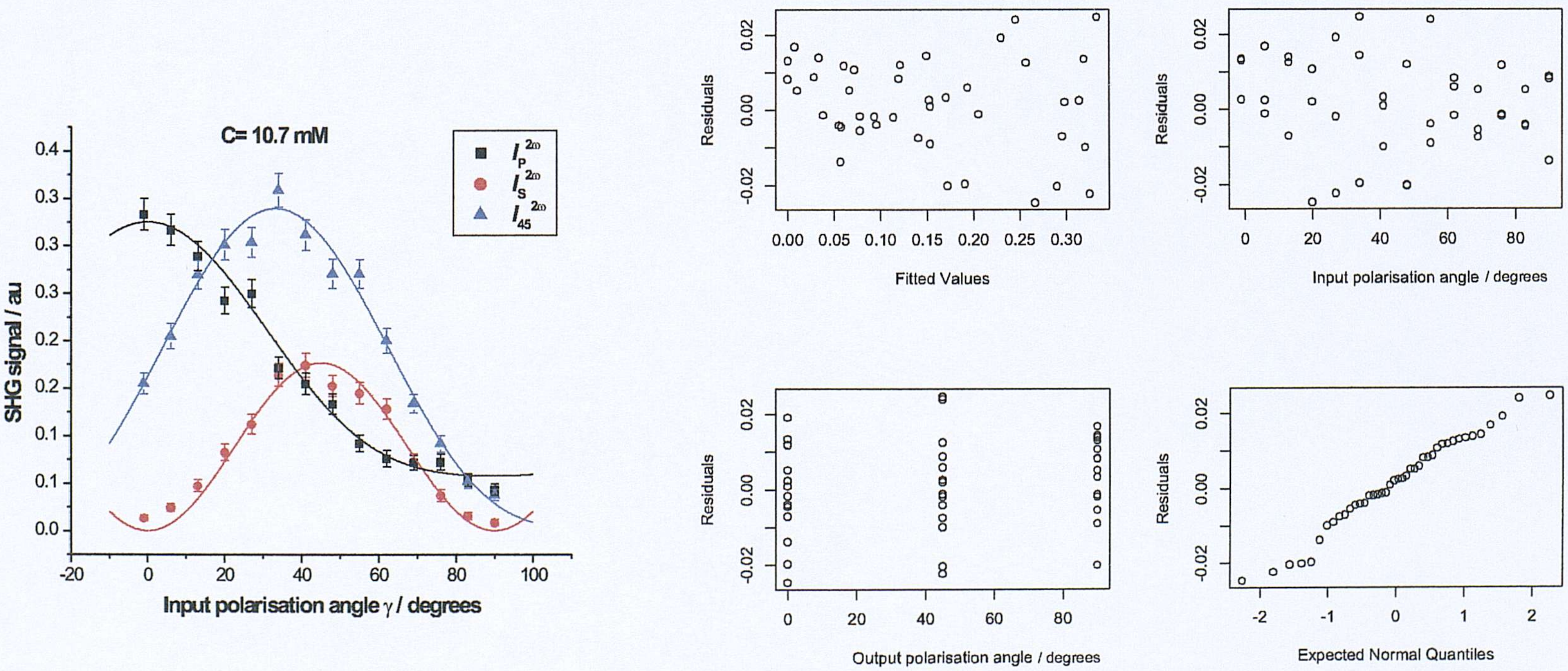

Figure 6.5: The polarisation dependence of the SHG signal generated in the S, P and +45° linear polarisation planes as a function of the input polarisation angle (γ), for a 10.7 mM phenylalanine solution. The solid lines have been estimated by the simultaneous fitting of the Euler parametrization of A, B, and C parameters in the S, P, and +45° SHG data assuming A to be real and B and C to be complex. λ=532/266 nm. The error bars added are σ. Residual and normal probability plots for the model fitted to the SHG data are shown. The residual values (calculated subtracted from fitted) are plotted against the fitted values, the input polarisation angle γ, the output polarisation angle, and the expected normal quantiles.

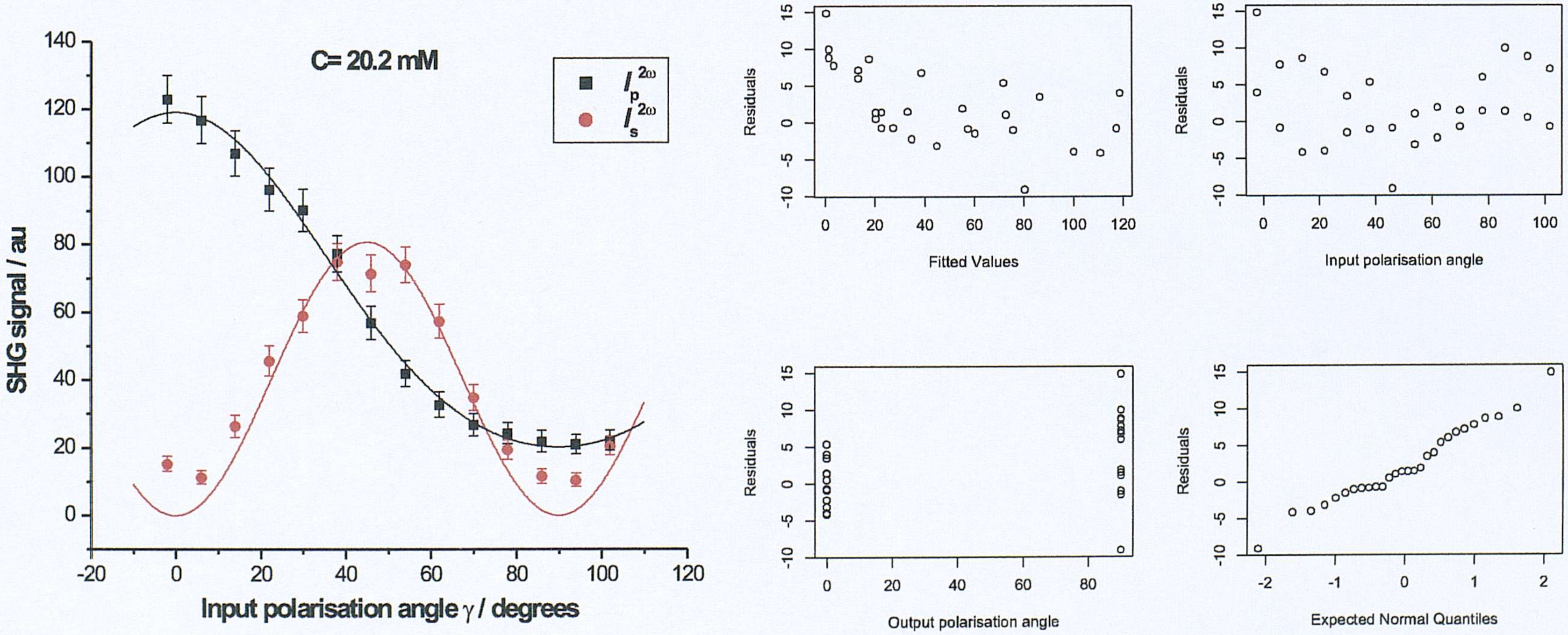

Figure 6.6: The polarisation dependence of the SHG signal generated in the S, P and +45° linear polarisation planes as a function of the input polarisation angle (γ), for a 20.2 mM phenylalanine solution. The solid lines have been estimated by the simultaneous fitting of the Euler parametrization of A, B, and C parameters in the S, P, and +45° SHG data assuming A to be real and B and C to be complex. λ=532/266 nm. The error bars added are σ. Residual and normal probability plots for the model fitted to the SHG data are shown. The residual values (calculated subtracted from fitted) are plotted against the fitted values, the input polarisation angle γ, the output polarisation angle, and the expected normal quantiles.

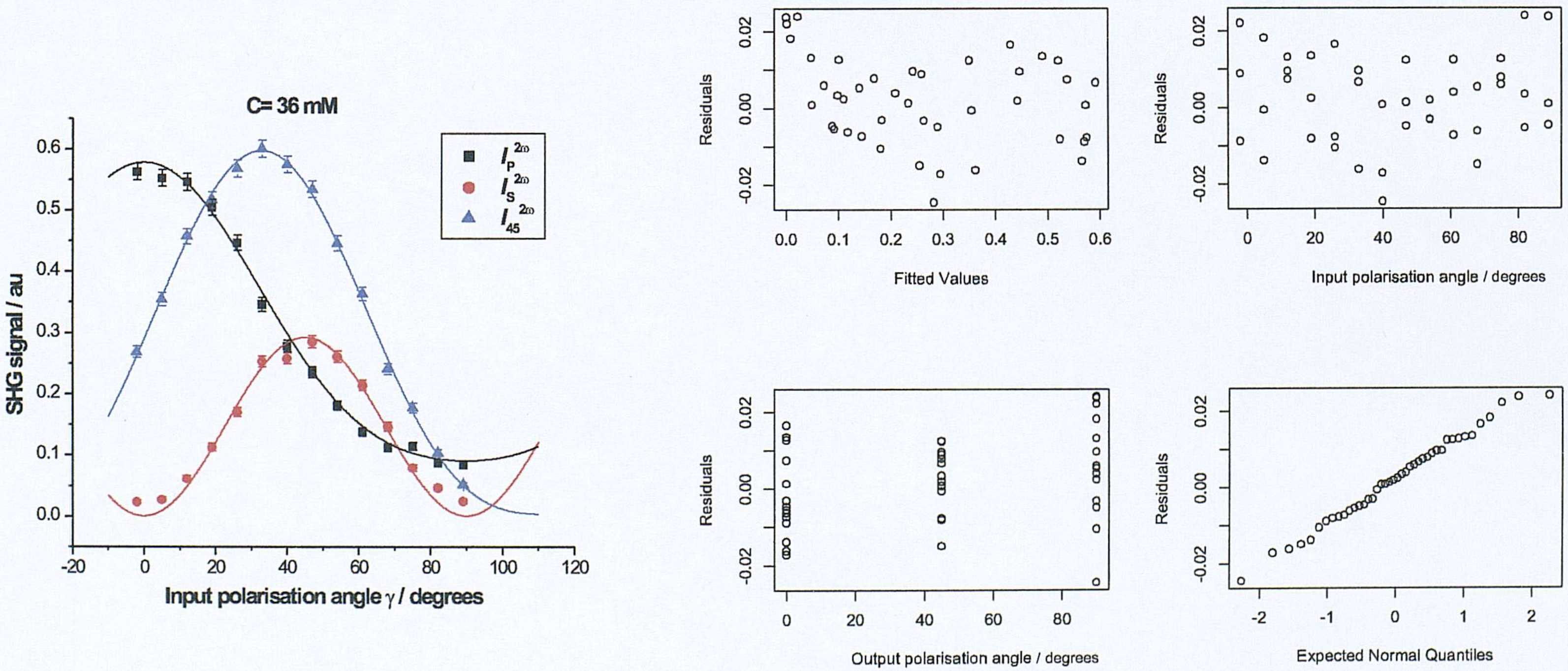

Figure 6.7: The polarisation dependence of the SHG signal generated in the S, P and +45° linear polarisation planes as a function of the input polarisation angle (γ), for a 36 mM phenylalanine solution. The solid lines have been estimated by the simultaneous fitting of the Euler parametrization of A, B, and C parameters in the S, P, and +45° SHG data assuming A to be real and B and C to be complex. λ=532/266 nm. The error bars added are σ. Residual and normal probability plots for the model fitted to the SHG data are shown. The residual values (calculated subtracted from fitted) are plotted against the fitted values, the input polarisation angle γ, the output polarisation angle, and the expected normal quantiles.

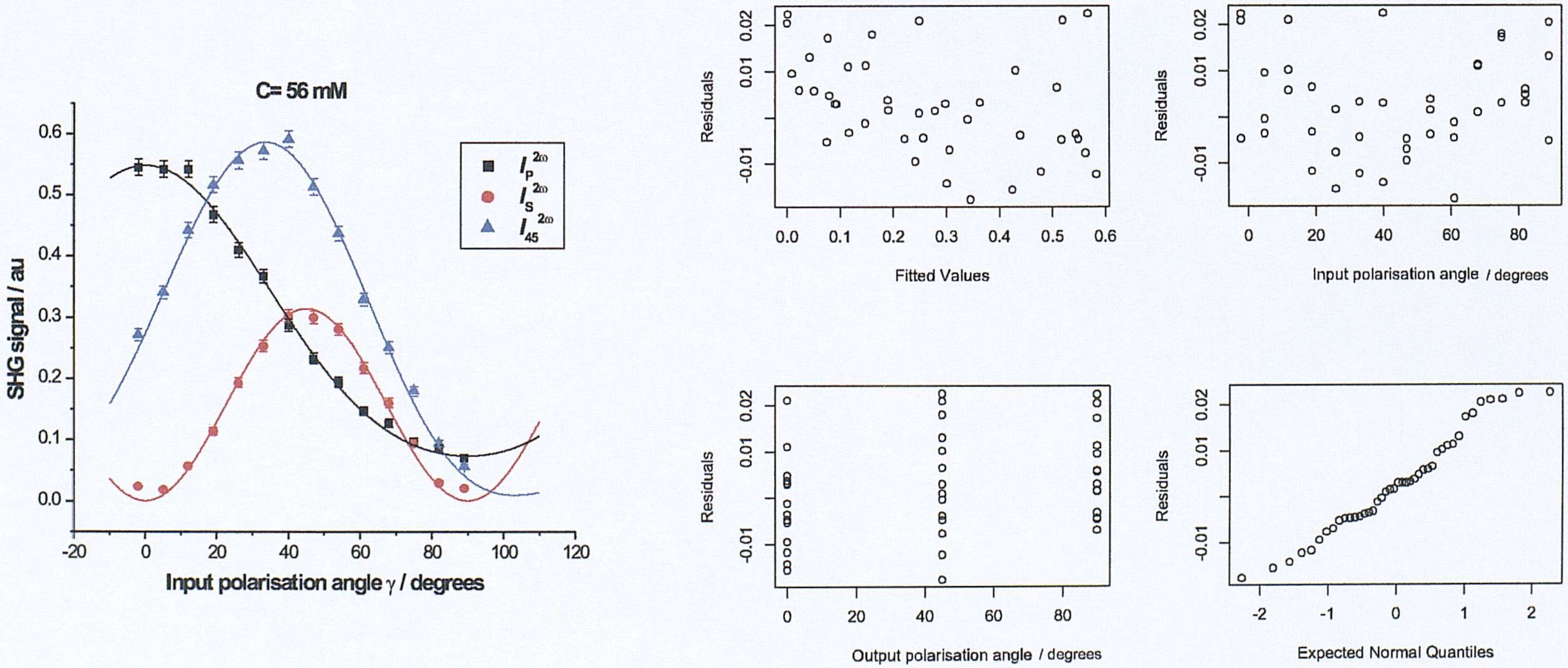

Figure 6.8: The polarisation dependence of the SHG signal generated in the S, P and +45° linear polarisation planes as a function of the input polarisation angle (γ), for a 56 mM phenylalanine solution. The solid lines have been estimated by the simultaneous fitting of the Euler parametrization of A, B, and C parameters in the S, P, and +45° SHG data assuming A to be real and B and C to be complex. λ=532/266 nm. The error bars added are σ. Residual and normal probability plots for the model fitted to the SHG data are shown. The residual values (calculated subtracted from fitted) are plotted against the fitted values, the input polarisation angle γ, the output polarisation angle, and the expected normal quantiles.

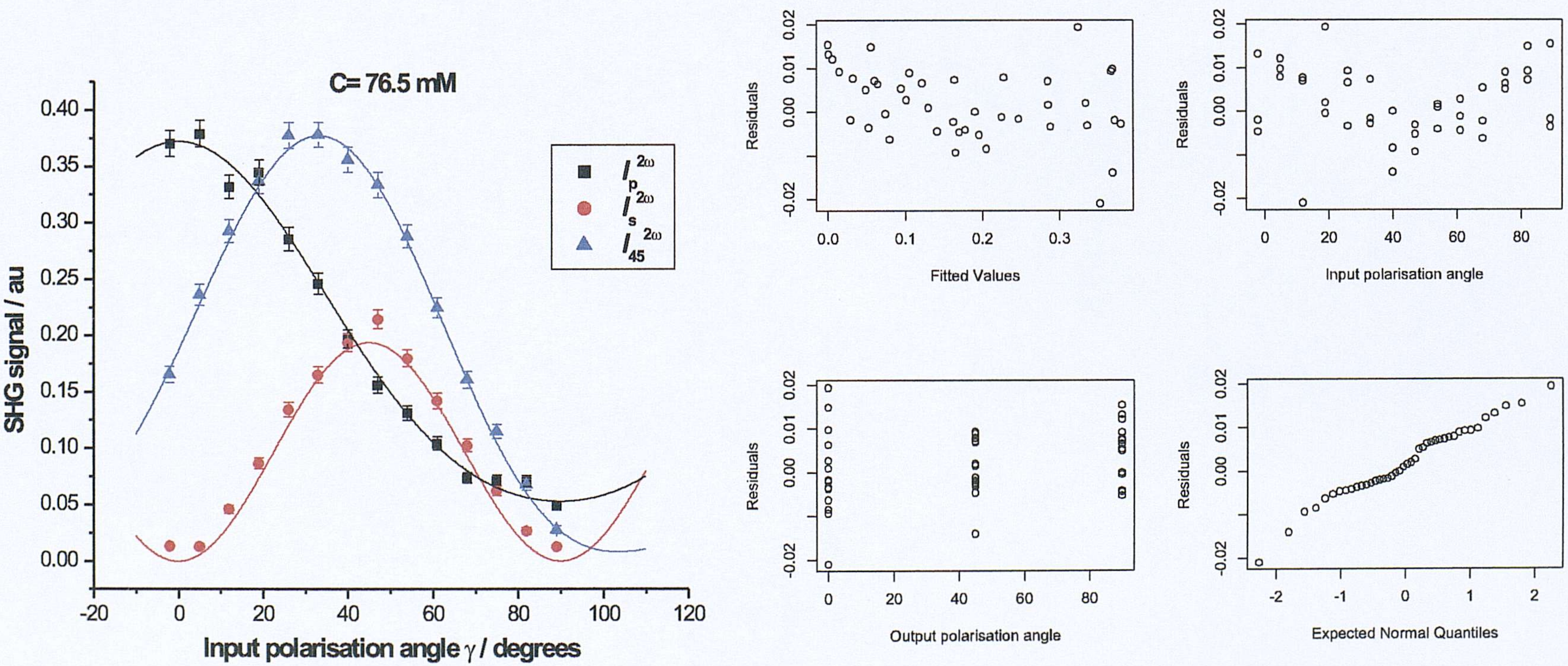

Figure 6.9: The polarisation dependence of the SHG signal generated in the S, P and +45° linear polarisation planes as a function of the input polarisation angle (γ), for a 76.5 mM phenylalanine solution. The solid lines have been estimated by the simultaneous fitting of the Euler parametrization of A, B, and C parameters in the S, P, and +45° SHG data assuming A to be real and B and C to be complex. λ=532/266 nm. The error bars added are σ. Residual and normal probability plots for the model fitted to the SHG data are shown. The residual values (calculated subtracted from fitted) are plotted against the fitted values, the input polarisation angle γ, the output polarisation angle, and the expected normal quantiles.

Parameter	Value
Wavelength, $\lambda(\omega, 2\omega)$	532/266 nm
Angle of incidence, θ	60°
Extinction coefficient (in water), ϵ	88.2 M^{-1} cm^{-1}
Coverage, Θ	1
$n_1(\omega/2\omega)$	1/1
$n_2(\omega/2\omega)$	1.334/1.334
$n_3(\omega/2\omega)$	see text

Table 6.2: The parameters used for the calculations of the a_i coefficients.

6.4.1.3 $\vec{\chi}^{(2)}$ Calculation

The air/water interface possess azimuthal symmetry and the $\vec{\chi}^{(2)}$ components of the phenylalanine can be reduced to three, $\chi^{(2)}_{ZZZ}$, $\chi^{(2)}_{ZXX}$, and $\chi^{(2)}_{XZX}$. In the presence of chiral molecules the addition of an extra component is possibly needed ($\chi^{(2)}_{XYZ}$), but this is not the case for phenylalanine since the polarisation combination (P in - S out) responsible for $\chi^{(2)}_{XYZ}$ is negligible. Both enantiomeric forms of phenylalanine produce similar polarisation curves.

The experimental parameters used for the calculation of the Fresnel coefficients are shown in Table 6.2. The refractive index of the phenylalanine bulk solution, n_2, has been taken as the refractive index of water and any dispersion has been ignored. In fact the refractive index of water changes very little in the region of 250-400 nm. The refractive index of the interfacial layer, n_3 was set to the refractive index of air or to water or to the average of the two. These different cases will be discussed. The refractive index of air, n_1 is set to one and assumed independent of wavelength.

The Fresnel coefficients, a_i, calculated for different values of the interfacial refractive index are shown in Table 6.3. Because of the weak absorbance of the phenylalanine molecules at the second harmonic wavelength (266 nm, ϵ=88.2 M^{-1} cm^{-1}), the imaginary part of the refractive index of the interfacial layer has been assumed zero to facilitate the use of one set of coefficients for all the different bulk concentrations used. The results remain essentially the same using the calculated fresnel coefficients at individual concentrations and coverages.

The determined $\vec{\chi}^{(2)}$ ratios ($\chi^{(2)}_{ZXX}/\chi^{(2)}_{ZZZ}$, $\chi^{(2)}_{XZX}/\chi^{(2)}_{ZZZ}$, and $\chi^{(2)}_{ZXX}/\chi^{(2)}_{XZX}$) for the adsorbed phenylalanine at different bulk concentrations are shown in Tables 6.4-6.6 for different assumptions about the value of the interfacial refractive index. For the case where n_3=n_1 shown in Table 6.4, the $\chi^{(2)}_{ZXX}/\chi^{(2)}_{ZZZ}$ ratio increases slightly up to 10 mM and then its value remains effectively constant. The other two ratios, $\chi^{(2)}_{XZX}/\chi^{(2)}_{ZZZ}$, and $\chi^{(2)}_{ZXX}/\chi^{(2)}_{XZX}$, remain effectively constant with increasing concentration within the 10 percent error from the determined confidence intervals for the ratios of the A, B and C coefficients shown in Table 6.1. It is also the case that the $\chi^{(2)}_{XZX}/\chi^{(2)}_{ZZZ}$, and $\chi^{(2)}_{ZXX}/\chi^{(2)}_{XZX}$ ratios can be approximated to be equal. The case where n_3=$(n_1 + n_2)/2$, shown in Table 6.5, shows similar behavior for the $\chi^{(2)}_{ZXX}/\chi^{(2)}_{ZZZ}$ tensor ratio as in the previous case, but with decreased ratio

	$n_3=(n_1+n_2)/2$		$n_3=n_1$		$n_3=n_2$	
a_i	Re	Im	Re	Im	Re	Im
a_1	0.353	0.000	0.259	0.000	0.198	0.000
a_2	-0.302	0.000	-0.222	0.000	-0.170	0.000
a_3	0.172	-0.001	0.126	-0.001	0.097	-0.001
a_4	0.397	-0.003	0.157	-0.001	0.070	0.000
a_5	0.264	-0.002	0.194	-0.001	0.149	-0.001
a_6	0.569	0.000	0.418	0.000	0.320	0.000
a_7	-0.187	0.000	-0.137	0.000	-0.105	0.000

Table 6.3: The a_i coefficients for Phe at the air/water interface calculated for different assumptions about the interfacial refractive index n_3.

values. The other two ratios, $\chi^{(2)}_{XZX}/\chi^{(2)}_{ZZZ}$, and $\chi^{(2)}_{ZXX}/\chi^{(2)}_{XZX}$, remain largely unaffected with increasing concentration but they are not equal in this case. At higher concentration and full monolayer coverage it is $\chi^{(2)}_{ZXX}/\chi^{(2)}_{XZX}$=2 $\chi^{(2)}_{XZX}/\chi^{(2)}_{ZZZ}$. Table 6.6 shows the case where n_3=n_2 for the interfacial refractive index and the trend about the $\chi^{(2)}_{ZXX}/\chi^{(2)}_{ZZZ}$ is similar to the other two cases with increasing concentration. The other two ratios, $\chi^{(2)}_{XZX}/\chi^{(2)}_{ZZZ}$, and $\chi^{(2)}_{ZXX}/\chi^{(2)}_{XZX}$, remain largely the same and at higher concentrations it is $\chi^{(2)}_{ZXX}/\chi^{(2)}_{XZX}$=3 $\chi^{(2)}_{XZX}/\chi^{(2)}_{ZZZ}$. For the above three cases the $\chi^{(2)}_{ZXX}/\chi^{(2)}_{XZX}$ ratio has remained the same and independent of the value of the interfacial refractive index. The measured non-linear susceptibilities $\chi^{(2)}_{XZX}$ and $\chi^{(2)}_{ZXX}$ are effective quantities which both depend inversely on the $n_3(\omega)^2$ and $n_3(2\omega)^2$ respectively [39]. The ratios remain the same because the refractive index of the interfacial layer has been assumed to be the same (no optical dispersion).

The polarisation dependence of the SHG signal with bulk concentration from phenylalanine adsorbed at the air/water interface remains essentially unaltered which might indicate that the molecule is weakly aligned at the interface. The observed increase in the nonlinear susceptibility ratios for concentrations up to 20 mM might reveal the formation of the monolayer occurring in the region 10-20 mM. Above 20 mM the monolayer has been completed and the polarisation dependence of the SHG signal remains largely unaffected. It can be seen that the choice of the value for the refractive index assigned to the interfacial region affects the determined $\chi^{(2)}$ ratios values. Phenylalanine is expected to be adsorbed with the carboxylic and amino group pointing towards the water and the benzene ring pointing towards the air. The strength of the SHG signal arising from the presence of a monolayer of phenylalanine molecules at the interface is approximately 1.5 times higher than that of the bare air/water interface. This low SHG signal intensity could be attributed to lack of alignment of the phenylalanine molecules at the interface. Although the molecules absorb at the harmonic wavelength and resonance enhancement of the SHG signal is expected, their orientation distribution angles could be large hence giving a relatively low SHG signal response. It is possible that the molecules follow the weak order limit, in which case the

		Case: $n_3=n_1$					
		$\chi^{(2)}_{ZXX}/\chi^{(2)}_{ZZZ}$		$\chi^{(2)}_{XZX}/\chi^{(2)}_{ZZZ}$		$\chi^{(2)}_{ZXX}/\chi^{(2)}_{XZX}$	
Run	C/mM	Re	Im	Re	Im	Re	Im
1	2.1	0.26	0.00	0.56	0.00	0.46	0.00
2	4.1	0.25	0.00	0.60	-0.01	0.42	0.00
3	5.0	0.17	0.33	0.49	0.18	0.52	0.49
4	8.6	0.12	0.26	0.56	0.05	0.26	0.44
5	8.9	0.32	0.00	0.63	-0.01	0.51	0.00
6	10.7	0.27	0.35	0.54	0.22	0.66	0.39
7	20.2	0.43	0.00	0.64	-0.01	0.67	0.01
8	30.0	0.39	0.00	0.65	-0.01	0.60	0.01
9	36.0	0.33	0.27	0.56	0.16	0.67	0.30
10	44.7	0.40	-0.12	0.60	0.21	0.53	-0.38
11	55.9	0.40	-0.09	0.60	0.15	0.59	-0.29
12	76.5	0.41	-0.10	0.59	0.17	0.60	-0.34

Table 6.4: The calculated $\tilde{\chi}^{(2)}$ ratios dependence with Phe bulk concentration C for the case of the interfacial refractive index being one. Errors were ± 10%.

		Case: $n_3=(n_1+n_2)/2$					
		$\chi^{(2)}_{ZXX}/\chi^{(2)}_{ZZZ}$		$\chi^{(2)}_{XZX}/\chi^{(2)}_{ZZZ}$		$\chi^{(2)}_{ZXX}/\chi^{(2)}_{XZX}$	
Run	C/mM	Re	Im	Re	Im	Re	Im
1	2.1	0.14	0.00	0.30	0.00	0.46	0.00
2	4.1	0.14	0.00	0.32	0.00	0.42	0.00
3	5.0	0.09	0.18	0.27	0.10	0.53	0.49
4	8.6	0.07	0.14	0.30	0.03	0.26	0.44
5	8.9	0.17	0.00	0.34	0.00	0.51	0.00
6	10.7	0.15	0.19	0.29	0.12	0.66	0.39
7	20.2	0.23	0.00	0.35	0.00	0.67	0.00
8	30.0	0.21	0.00	0.35	0.00	0.60	0.00
9	36.0	0.18	0.15	0.30	0.09	0.67	0.29
10	44.7	0.21	-0.06	0.32	0.11	0.53	-0.38
11	55.9	0.21	-0.05	0.32	0.08	0.59	-0.29
12	76.5	0.22	-0.05	0.32	0.09	0.60	-0.34

Table 6.5: The calculated $\tilde{\chi}^{(2)}$ ratios dependence with Phe bulk concentration C for the case of the interfacial refractive index being half, $n_3=(n_1+n_2)/2$. Errors were ± 10%.

		Case: n_3=n_2					
		$\chi^{(2)}_{ZXX}/\chi^{(2)}_{ZZZ}$		$\chi^{(2)}_{XZX}/\chi^{(2)}_{ZZZ}$		$\chi^{(2)}_{ZXX}/\chi^{(2)}_{XZX}$	
Run	C/mM	Re	Im	Re	Im	Re	Im
1	2.1	0.08	0.00	0.18	0.00	0.46	0.00
2	4.1	0.08	0.00	0.19	0.00	0.42	0.00
3	5.0	0.05	0.11	0.16	0.06	0.53	0.49
4	8.6	0.04	0.08	0.18	0.02	0.26	0.44
5	8.9	0.10	0.00	0.20	0.00	0.51	0.00
6	10.7	0.09	0.11	0.17	0.07	0.66	0.39
7	20.2	0.14	0.00	0.20	0.00	0.67	0.00
8	30.0	0.12	0.00	0.20	0.00	0.60	0.00
9	36.0	0.10	0.09	0.18	0.05	0.67	0.29
10	44.7	0.12	-0.04	0.19	0.07	0.53	-0.38
11	55.9	0.13	-0.03	0.19	0.05	0.59	-0.29
12	76.5	0.13	-0.03	0.19	0.05	0.60	-0.34

Table 6.6: The calculated $\chi^{(2)}$ ratios dependence with Phe bulk concentration C for the case of the interfacial refractive index being 1.334, n_3=n_2. Errors were ± 10%.

refractive index of the interfacial layer can be determined [39]. Assuming no optical dispersion for the interfacial refractive index, $n_3(\omega)$=$n_3(2\omega)$=n, then the measured effective susceptibility tensors are related so that

$$n^4\chi^{(2)}_{ZZZ} = \chi^{(2)}_{ZXX} + 2\chi^{(2)}_{XZX} \tag{6.1}$$

Assuming that the phenylalanine molecule can be treated within the weak order limit, then for the above concentrations the determined interfacial refractive indices values, optimised for the above equation to hold, are shown in Table 6.7. The determined mean value of 1.10 is not close to the average value of the refractive indices of the two bulk phases surrounding the interfacial layer, (1.16) as might have been expected [39]. The determined refractive index ascribed to the benzene chromophore responsible for the SHG signal is closer to the value of air. This is to be expected based on the hydrophobicity of the phenylalanine molecule.

In the above analysis the susceptibility tensor $\chi^{(2)}$ has been assumed to originate from the phenylalanine molecule and the contribution from the substrate, in this case water, has not been considered. Because the two SHG signals are comparable in strength, the contribution from the bare air/water interface needs to be included and this will be addressed in the concentration dependence studies on the next section. An extra susceptibility term that sometimes is important, namely the interaction term, has been ignored for the case of the phenylalanine molecule.

Run	C/mM	n
1	2.1	1.08
2	4.1	1.10
3	5.0	1.04
4	8.6	1.06
5	8.9	1.12
6	10.7	1.08
7	20.2	1.15
8	30.0	1.14
9	36.0	1.09
10	44.7	1.11
11	55.9	1.12
12	76.5	1.11
	Mean	1.10
	StdDev	0.03

Table 6.7: The determined interfacial refractive index for phenylalanine assuming the molecule can be treated in the weak order limit. The mean and the standard deviation of the mean are shown.

6.4.1.4 Molecular Orientation

Phenylalanine has C_i symmetry, and the hyperpolarisability tensor β_{ijk} can have 27 independent elements. If the molecule is approximated to have C_s symmetry like toluene, the non zero tensor elements are reduced to ten. The symmetry of the transition in the second harmonic generation wavelength will only enhance those tensor elements with adequate symmetry. Phenylalanine and toluene have very similar absorption spectra. Their spectral differences arise from the decrease in effective symmetry. In the following discussion the tensor elements β_{zzz}, β_{xzx}, and β_{zxx} are considered to be the dominant tensor components. The molecular axes for phenylalanine is shown in Figure 6.10 with the z axis to be the molecular axis going across the ring and the axis perpendicular to z to be the x axis.

The structure shown in Figure 6.10 is the lowest energy conformation of Phe as calculated by Simons and co-workers [128]. The neutral form of phenylalanine will be discussed here as this is believed to be the one mostly present at the air/water interface. The chromophore responsible for the SHG resonance enhancement in Phenylalanine is the benzene ring with the harmonic wavelength (266 nm) being close to the $\pi \longrightarrow \pi^*$ electronic transitions. The Phe absorption spectrum is similar to the toluene one and the molecule can be approximated to have a C_s symmetry if the amino acid chain is treated as a symmetric moiety. This allows only three hyperpolarisability tensor elements to be considered for the analysis of the molecular non-linear polarisation response, β_{zzz}, β_{zxx} and β_{xzx} and these cases will be discussed here. The computational study on the calculation of the frequency dependent hyperpolarisability tensor elements to follow will support this assumption.

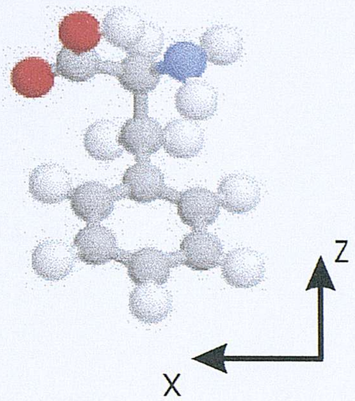

Figure 6.10: Molecular frame axes for Phenylalanine with the following color-atom coding: grey-Carbon, white-Hydrogen, red-Oxygen and blue-Nitrogen.

- β_{zzz} dominant.

  In this case the nonlinear response of Phe is assumed to originate from one dominant hyperpolarisability tensor, β_{zzz}. The molecular orientation parameter D is determined together with the molecular tilt angle between the molecular axis and the laboratory z axis, the results are shown in Table 6.8 for the three different assumptions about the value of the refractive interfacial index. There is a difference of 20° degrees on the tilt angle θ according to which value for the interfacial refractive index is chosen. The case with the β_{zzz} tensor to be the dominant tensor implies the molecule must obey Kleinman symmetry with $\chi^{(2)}_{ZXX}=\chi^{(2)}_{XZX}$. The nonlinear susceptibility tensor results do not suggest this since $\chi^{(2)}_{XZX}>\chi^{(2)}_{ZXX}$ similar to the case of toluene.

- β_{zzz} and β_{zxx} dominant.

  In this case the Kleinman symmetry is broken and a second tensor component must be included to adequately descibe the nonlinear polarisation of the molecule. It is possible that the nonlinear response cannot be approximated originating from the lowest electronic resonance transition in the molecule. In the case of phenylalanine this means that both L_a and L_b electronic transitions need to be invoked to describe the nonlinear polarisation of the molecule at the harmonic frequency. The ratio R of the two tensor components can be calculated and the results are shown in Table 6.9.

  The estimated orientational parameter D and the tilt molecular angle θ are shown in Table 6.10. The estimated tilt angle varies from 30° to 44°

	$n_3=n_1$			$n_3=1/2(n_1+n_2)$			$n_3=n_2$		
C/mM	Re D	Im D	$\theta/^\circ$	Re D	Im D	$\theta/^\circ$	Re D	Im D	$\theta/^\circ$
2.1	0.66	0.00	35.67	0.78	0.00	27.79	0.86	0.00	21.96
4.1	0.66	0.00	35.43	0.79	0.00	27.58	0.86	0.00	21.79
5.0	0.60	-0.30	39.39	0.77	-0.23	28.47	0.87	-0.17	21.07
8.6	0.69	-0.29	34.08	0.83	-0.21	24.07	0.91	-0.14	17.67
8.9	0.61	0.00	38.64	0.74	0.00	30.42	0.83	0.00	24.19
10.7	0.53	-0.25	43.03	0.71	-0.21	32.54	0.82	-0.16	24.88
20.2	0.54	0.00	42.86	0.68	0.00	34.27	0.79	0.00	27.54
30.0	0.56	0.00	41.38	0.71	0.00	32.90	0.80	0.00	26.34
36.0	0.55	-0.18	42.39	0.71	-0.15	32.82	0.81	-0.12	25.65
44.7	0.55	0.07	42.19	0.70	0.06	33.49	0.80	0.05	26.76
55.9	0.55	0.05	42.05	0.70	0.05	33.43	0.80	0.03	26.75
76.5	0.54	0.06	42.60	0.69	0.05	33.92	0.79	0.04	27.16
Mean	0.59	-0.07	39.97	0.73	-0.05	30.97	0.83	-0.04	24.31
StdDev	0.06	0.14	3.27	0.05	0.11	3.27	0.04	0.08	3.06

Table 6.8: Real and imaginary components of the orientational parameter D assuming the β_{zzz} tensor dominant for different phenylalanine concentrations. The orientational parameter $D=\frac{<\cos^3\theta>}{<\cos\theta>}$, for the three different cases of the value for the interfacial refractive index is shown. The determined angle θ, is the angle between the main molecular axis and the interface normal. The other two Euler angles , ϕ and ψ are not considered in this case. The angle ϕ, has a uniform distribution because the surface is isotropic and the angle ψ cannot be determined because only one hyperpolarisability tensor is considered to be significant. The average values and the standard deviation of the mean is shown.

		$n_3=n_1$		$n_3=1/2(n_1+n_2)$		$n_3=n_2$	
		β_{zzz}, β_{zxx} dominant, $R=\frac{\beta_{zxx}}{\beta_{zzz}}$					
Run	C/mM	Re R	Im R	Re R	Im R	Re R	Im R
1	2.1	-0.29	0.00	-0.20	0.00	-0.14	0.00
2	4.1	-0.31	0.00	-0.23	0.00	-0.16	0.00
3	5.0	-0.29	0.21	-0.21	0.14	-0.15	0.09
4	8.6	-0.40	0.21	-0.29	0.15	-0.20	0.10
5	8.9	-0.27	0.00	-0.20	0.00	-0.14	0.00
6	10.7	-0.22	0.18	-0.17	0.12	-0.12	0.08
7	20.2	-0.19	0.00	-0.14	0.00	-0.10	0.00
8	30.0	-0.23	0.00	-0.17	0.00	-0.12	0.00
9	36.0	-0.20	0.14	-0.14	0.09	-0.10	0.06
10	44.7	-0.23	-0.25	-0.16	-0.19	-0.11	-0.14
11	55.9	-0.21	-0.19	-0.15	-0.14	-0.10	-0.10
12	76.5	-0.20	-0.22	-0.14	-0.16	-0.09	-0.12
	Mean	-0.25	0.01	-0.18	0.00	-0.13	0.00
	StdDev	0.06	0.16	0.05	0.11	0.03	0.08

Table 6.9: The real and imaginary components of the ratio, $R=\frac{\beta_{zxx}}{\beta_{zzz}}$ for phenylalanine, for different values of the interfacial refractive index. The average and standard deviation of the mean is shown.

depending on the choice of the interfacial refractive index value. Assuming the molecule is weakly aligned at the interface then the determined magic angle is 39.2° [143], which indicates a very broad distribution in molecular distribution angles. The SHG magic angle is obtained experimentally when the adsorbate molecule has a broad distribution of angles about the mean tilt angle. In that case the determination of the orientation parameter $D = \frac{<\cos^3\theta>}{<\cos\theta>} \approx \cos^2 < \theta >$ is not valid any more. The above relationship holds for a narrow distribution of angles about the mean orientation angle. If the orientational angle θ is expressed as a Gaussian distribution with a width of distribution $\Delta\theta$ then the molecule is random oriented at the interface when $\Delta\theta \rightarrow \propto$ and the orientation parameter D=2/3. The SHG magic angle can be explained in terms of the Legendre polynomials P_1 and P_3 in order to relate the distribution width of the tilt angle and the orientational parameter D. When the width of the distribution is broadened the P_3 becomes small and the orientational parameter D equals 3/5. This will be equal to the magic angle, 39.2°.

The estimated angle for Phe, assuming the refractive index is in between the value of air (1.0) and the average of the two phases (1.16), is very close to the SHG magic angle. The apparent orientation angle of 39° for phenylalanine indicates either a narrow distribution centered around 39° or a broad distribution centered around a mean angle. The results suggest

	$n_3=n_1$			$n_3=1/2(n_1+n_2)$			$n_3=n_2$		
C/mM	Re D	Im D	$\theta/^\circ$	Re D	Im D	$\theta/^\circ$	Re D	Im D	$\theta/^\circ$
2.1	0.54	0.00	42.9	0.66	0.00	35.8	0.76	0.00	29.6
4.1	0.53	0.00	43.3	0.65	0.00	36.4	0.75	0.00	30.3
5.0	0.56	-0.12	41.4	0.68	-0.09	34.3	0.78	-0.07	28.2
8.6	0.56	-0.06	41.3	0.67	-0.04	34.9	0.76	-0.03	29.1
8.9	0.51	0.00	44.4	0.63	0.00	37.3	0.73	0.00	31.1
10.7	0.52	-0.12	43.7	0.65	-0.10	36.2	0.75	-0.08	29.7
20.2	0.48	0.00	45.9	0.62	0.00	38.3	0.72	0.00	31.7
30.0	0.49	0.00	45.4	0.62	0.00	38.1	0.73	0.00	31.6
36.0	0.52	-0.10	44.0	0.65	-0.08	36.4	0.75	-0.06	29.9
44.7	0.50	-0.02	45.2	0.62	-0.04	37.9	0.73	-0.05	31.3
55.9	0.50	-0.01	45.1	0.63	-0.03	37.7	0.73	-0.03	31.1
76.5	0.50	-0.01	45.2	0.63	-0.04	37.7	0.73	-0.04	31.1
Mean	0.52	-0.04	44.0	0.64	-0.03	36.7	0.74	-0.03	30.4
StdDev	0.03	0.05	1.5	0.02	0.04	1.3	0.02	0.03	1.1

Table 6.10: Real and imaginary components of the orientational parameter D assuming the β_{zzz} and β_{zxx} tensors are dominant for different phenylalanine concentrations. The orientational parameter $D=\frac{<\cos^3\theta>}{<\cos\theta>}$, for the three different cases of the value for the interfacial refractive index is shown. The determined angle θ, is the angle between the main molecular axis and the interface normal. The angle ϕ, has a uniform distribution because the surface is isotropic and the angle ψ is considered to be random. The average values and the standard deviation of the mean is shown.

that the latter holds. Similar results were obtained assuming the ψ angle to be 90°.

- β_{zzz} and β_{xzx} dominant.

  In this case the values for the real and imaginary components of the ratio β_{xzx}/β_{zzz} is shown in Table 6.11 for the different cases about the value of the refractive index assigned to the interface. The phase is the same for both tensor components but opposite from the β_{zxx}/β_{zzz} shown earlier.

  The results for the orientational parameter D and the tilt molecular angle is shown in Table 6.12.

The above cases demonstrate the sensitivity of the determined orientational molecular angle on the choice of the value for the interfacial refractive index. An appropriate value for the phenylalanine molecule adsorbed at the air/water interface will be in the range of 1.1-1.16. The hydrophobic nature of the benzene chromophore responsible for the SHG signal will force the molecule to adopt an orientation where the benzene ring will point away from the water surface. In order to adequately describe the nonlinear polarisation of the phenylalanine molecule two dominant molecular hyperpolarisability tensors need to be assumed.

		$n_3=n_1$		$n_3=1/2(n_1+n_2)$		$n_3=n_2$	
		β_{zzz}, β_{xzx} dominant, $R=\frac{\beta_{xzx}}{\beta_{zzz}}$					
Run	C/mM	Re R	Im R	Re R	Im R	Re R	Im R
1	2.1	0.40	-0.01	0.26	0.00	0.16	0.00
2	4.1	0.46	-0.01	0.29	0.00	0.19	0.00
3	5.0	0.29	-0.38	0.23	-0.21	0.16	-0.12
4	8.6	0.48	-0.53	0.35	-0.28	0.23	-0.15
5	8.9	0.38	-0.01	0.25	0.00	0.16	0.00
6	10.7	0.22	-0.28	0.18	-0.17	0.13	-0.10
7	20.2	0.23	-0.01	0.16	0.00	0.11	0.00
8	30.0	0.29	-0.01	0.20	0.00	0.13	0.00
9	36.0	0.21	-0.20	0.16	-0.12	0.11	-0.07
10	44.7	0.18	0.38	0.13	0.26	0.09	0.17
11	55.9	0.20	0.28	0.14	0.19	0.10	0.12
12	76.5	0.16	0.31	0.12	0.21	0.08	0.14
	mean	0.29	-0.04	0.20	-0.01	0.14	0.00
	StdDev	0.11	0.28	0.07	0.17	0.05	0.10

Table 6.11: The real and imaginary components of the ratio, $R=\frac{\beta_{xzx}}{\beta_{zzz}}$ for phenylalanine, for different values of the interfacial refractive index. The average and standard deviation of the mean is shown.

The electronic transitions that occur at 205 and 258 need to be both taken into account in order to describe the second harmonic response at 266 nm.

Assuming the value of the refractive index to be the average of that of water and air, the orientational parameter D for both cases (β_{zzz} and β_{zxx} assumed dominant) and (β_{zzz} and β_{xzx} assumed dominant) has a similar value corresponding to an orientational angle θ of 36 $\pm 2^{\circ}$ at a full monolayer coverage. The respective hyperpolarisability ratios values are β_{zxx}/β_{zzz}=-0.18 ± 0.05 and β_{zxx}/β_{zzz}=0.20 ± 0.07 which indicate that β_{zxx} and β_{xzx} have similar real estimates but with opposite phases.

	$n_3=n_1$			$n_3=1/2(n_1+n_2)$			$n_3=n_2$		
C/mM	Re D	Im D	$\theta/^\circ$	Re D	Im D	$\theta/^\circ$	Re D	Im D	$\theta/^\circ$
2.1	0.43	0.01	48.9	0.71	0.00	32.7	0.83	0.00	24.2
4.1	0.38	0.01	52.0	0.70	0.00	33.4	0.83	0.00	24.3
5.0	0.38	-0.09	51.7	0.65	-0.21	36.3	0.82	-0.17	25.0
8.6	0.43	0.04	49.2	0.67	-0.17	35.1	0.85	-0.15	22.8
8.9	0.37	0.01	52.4	0.66	0.00	35.8	0.80	0.00	26.6
10.7	0.37	-0.09	52.6	0.61	-0.18	38.5	0.78	-0.16	28.0
20.2	0.40	0.00	50.8	0.62	0.00	37.8	0.76	0.00	29.3
30.0	0.38	0.01	51.8	0.63	0.00	37.3	0.77	0.00	28.4
36.0	0.41	-0.08	50.5	0.63	-0.13	37.3	0.78	-0.11	27.9
44.7	0.52	-0.14	44.1	0.66	-0.03	35.8	0.77	0.01	28.3
55.9	0.48	-0.12	46.1	0.65	-0.02	36.1	0.77	0.01	28.3
76.5	0.50	-0.12	45.2	0.65	-0.02	36.1	0.77	0.01	28.6
Mean	0.42	-0.05	49.6	0.65	-0.06	36.0	0.80	-0.05	26.8
StdDev	0.05	0.06	3.0	0.03	0.08	1.7	0.03	0.08	2.2

Table 6.12: Real and imaginary components of the orientational parameter D assuming the β_{zzz} and β_{xzx} tensors are dominant for different phenylalanine concentrations. The orientational parameter $D=\frac{<\cos^3\theta>}{<\cos\theta>}$, for the three different cases of the value for the interfacial refractive index is shown. The determined angle θ, is the angle between the main molecular axis and the interface normal. The angle ϕ, has a uniform distribution because the surface is isotropic and the angle ψ is considered to be random. The average values and the standard deviation of the mean is shown.

6.4.1.5 Concentration Dependence

The dependence of the second harmonic signal with the concentration of phenylalanine was investigated for concentration up to 0.8 M. A plot of $\chi_{\text{phe}}/\chi_{\text{w}}$ versus the bulk concentration C of phenylalanine is shown in Figure 6.12, where χ_{phe} and χ_{w} are the nonlinear susceptibilities of phenylalanine and water respectively. Signals were obtained from a series of experiments and the SHG signal was normalised to that of water.

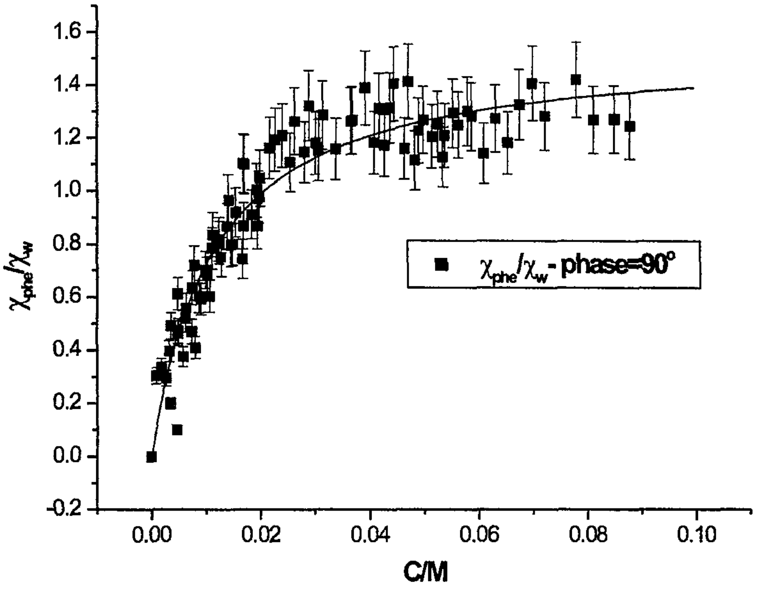

Figure 6.11: Langmuir isotherm measured for Phe is shown. The non-linear susceptibility ratio $\chi_{\text{phe}}/\chi_{\text{w}}$ has been obtained from SHG intensities and is plotted as a function of the bulk concentration C of Phe. The input polarisation angle γ was 45° and the output harmonic was S. Error bars are ± 10%.

The second harmonic signal will have contributions from both the surface water molecules and the adsorbed phenylalanine molecules. The SHG signal, $I_{SHG}(2\omega)$, can be written in terms of the surface second order susceptibilities of water,χ_{w}, and phenylalanine, χ_{phe}, as

$$I_{SHG}(2\omega) \propto (\mid \chi_{\text{w}} \mid^2 + \mid \chi_{\text{phe}} \mid^2 + 2 \mid \chi_{\text{w}} \mid\mid \chi_{\text{phe}} \mid cos\phi) I(\omega)^2 \qquad (6.2)$$

where $\mid \chi_{\text{w}} \mid^2 = I_{\text{w}}$ is the SHG signal intensity of the neat air/water interface, $\mid \chi_{\text{phe}} \mid^2 = I_{\text{phe}}$ is the SHG signal intensity of the phenylalanine molecules, and ϕ is the phase difference between the two SHG signals. For comparison between different experiments performed in different days equation 6.2 can be written as

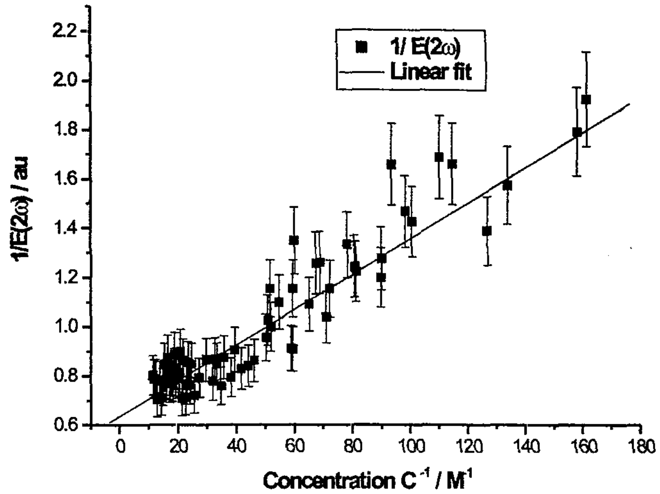

Figure 6.12: Reciprocal fit to the Langmuir equation is shown for Phe. The inverse of the harmonic field $E(2\omega)$ is plotted against the reciprocal of the bulk concentration. The equation used is obtained from Equation 6.4 and is given by the expression: $\frac{1}{N} = \frac{1}{kN_{max}}\frac{1}{C} + \frac{1}{N_{max}}$ where N is the number of adsorbed molecules per area and N_{max} is the maximum number. The harmonic field, $E(2\omega$, is proportional to the number of molecules present at the surface and $1/N$ is inversely proportional to the bulk concentration. The input polarisation angle γ was 45° and the output harmonic was S. Error bars are ± 10%.

$$\frac{I_{SHG}(2\omega)}{|\chi_{\rm w}|^2} \propto 1 + \frac{|\chi_{\rm phe}|^2}{|\chi_{\rm w}|^2} + 2\frac{|\chi_{\rm phe}|}{|\chi_{\rm w}|} cos\phi I(\omega)^2 \tag{6.3}$$

Equation 6.3 can be solved assuming different phase difference values for ϕ. The quadratic solution has two roots one of which is negative and not taken into account. So a plot of the experimental $\chi_{\rm phe}/\chi_{\rm w}$ versus the bulk concentration C could be used to fit an adsorption isotherm. Figure 6.12 shows a Langmuir adsorption isotherm fit to concentrations up to 0.8 M. The SHG intensity was fit to a Langmuir isotherm similar to the methods employed by Steinhurst et al [144] and Haslam et al [32]. The form of the isotherm is given by

$$\Theta = \frac{kC}{(1 + kC)} \tag{6.4}$$

$$I_{SHG}(2\omega) = S\Theta^2 \tag{6.5}$$

where Θ is the surface coverage of the molecules present at the interface, S is a scaling factor, C is the bulk concentration of Phe, and k is the surface adsorption equilibrium constant. The adsorption free energy $\Delta G^{\ominus}_{ads}$=-$RTlnK$ where K=55.5k [32,40]. The phase difference assumed between the two sources of SHG signals was

$\phi/^{\circ}$	$\Delta G^{\ominus}_{ads}$/kJ $\cdot$mol^{-1}	k /mol^{-1}dm^{-3}	error	S	error
0	-18.89	39.92	5.11	0.91	0.05
27	-18.97	41.20	5.18	0.96	0.05
45	-19.14	44.07	5.32	1.07	0.05
90	-20.83	88.05	7.39	1.55	0.04

Table 6.13: Parameters obtained to the optimised Langmuir fit of concentration dependence of the SHG signal of phenylalanine. The phase difference ϕ between the SHG signal from the phenylalanine molecules and the SHG signal from the bare air/water interface has been assumed to take different values. S is a scale factor.

90°. The SHG signal increases almost linearly for concentration up to 20 mmol dm^{-3}. The plateau region is assumed to be reached at a monolayer coverage. A non-least squares fit to Equation 6.4 describing the Langmuir isotherm produced the data shown in Table 6.13 for different assumptions about the phase difference between the SHG signal from Phe and water.

For comparison the dependence of the TPF signal with increasing bulk concentration of Phe is shown in Figure 6.13. The TPF signal was normalised to the SHG signal of water and recorded at the maximum emission wavelength at 275 nm. A linear regression is fitted to indicate the distinctive behaviour of the bulk two photon fluorescence from the SHG generated signal at the interface.

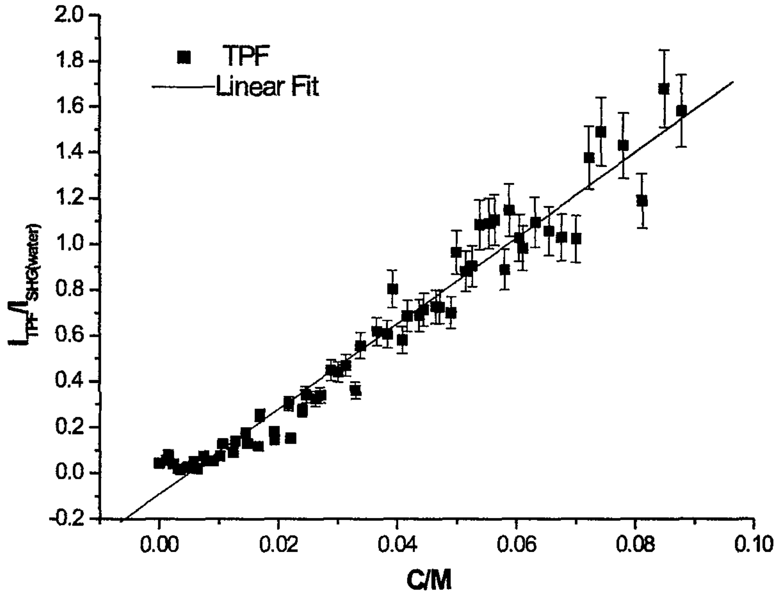

Figure 6.13: The Concentration dependence of the TPF signal normalised to the SHG signal of water. A linear fit is shown. Error bars are ± 10%.

6.4.1.6 Water contribution to the SHG signal

Because the SHG signal generated from the surface water molecules is comparable in strength with the SHG signal generated from the Phe molecules at the air/water interface, it will be advantageous to separate these two signals. The previous concentration studies were performed with an input polarisation angle γ=45^0 and a S-output harmonic polarisation. This polarisation combination measures the $\chi^{(2)}_{XZX}$ susceptibility term (see Equation 2.32, and the ratio shown in Figure 6.12 is the $\chi^{(2)}_{XZX}(\text{Phe})/\chi^{(2)}_{XZX}(\text{w})$ where $\chi^{(2)}_{XZX}(\text{Phe})$ and $\chi^{(2)}_{XZX}(\text{w})$ are the non-linear susceptibility terms of phe and water respectively. The polarisation studies measure the effective $\vec{\chi}^{(2)}$ terms in which the following relationships apply:

$$\chi^{(2)}_{ZZZ}(\text{eff}) = \chi^{(2)}_{ZZZ}(\text{Phe}) + \chi^{(2)}_{ZZZ}(\text{w}) \tag{6.6}$$

$$\chi^{(2)}_{ZXX}(\text{eff}) = \chi^{(2)}_{ZXX}(\text{Phe}) + \chi^{(2)}_{ZXX}(\text{w}) \tag{6.7}$$

$$\chi^{(2)}_{XZX}(\text{eff}) = \chi^{(2)}_{XZX}(\text{Phe}) + \chi^{(2)}_{XZX}(\text{w}) \tag{6.8}$$

where $\chi^{(2)}(\text{eff})$ are the effective measured susceptibility tensor values. Based on the above relationships and the determined adsorption isotherm for the $\chi^{(2)}_{XZX}(\text{Phe})/\chi^{(2)}_{XZX}(\text{w})$ ratio it is possible to determine any other tensor ratio for the polarisation results. The $\chi^{(2)}_{ZZZ}(\text{Phe})/\chi^{(2)}_{ZZZ}(\text{w})$ is calculated and a plot versus the concentration for the polarisation data is shown in Figure 6.14. The polarisation dependence of the SHG signal at various Phe concentrations is used to estimate the $\chi^{(2)}_{ZZZ}(\text{Phe})/\chi^{(2)}_{ZZZ}(\text{w})$ using the results obtained from the concentration dependence of the SHG signal. Similarly the other susceptibilities ratios can be determined and used to determine the molecular tilt angle of the phenylalanine molecule at the air/water interface without the water molecule contribution. The orientational parameter D for the Phe molecule can be expressed in terms of the susceptibility ratios ($\chi^{(2)}_{ZZZ}(\text{Phe})/\chi^{(2)}_{ZZZ}(\text{w})$, $\chi^{(2)}_{ZXX}(\text{Phe})/\chi^{(2)}_{ZZZ}(\text{w})$ and $\chi^{(2)}_{XZX}(\text{Phe})/\chi^{(2)}_{ZZZ}(\text{w})$). Using Equations 7.1-7.3 and the determined $\chi^{(2)}_{ZZZ}(\text{Phe})/\chi^{(2)}_{ZZZ}(\text{w})$ ratio the orientational parameter D was determined for different assumptions about the phase difference between the Phe and water SHG signal. The results for phase=90^o are shown in Table 6.14 and compared to the previous determined molecular tilt angle θ with the water contribution included.

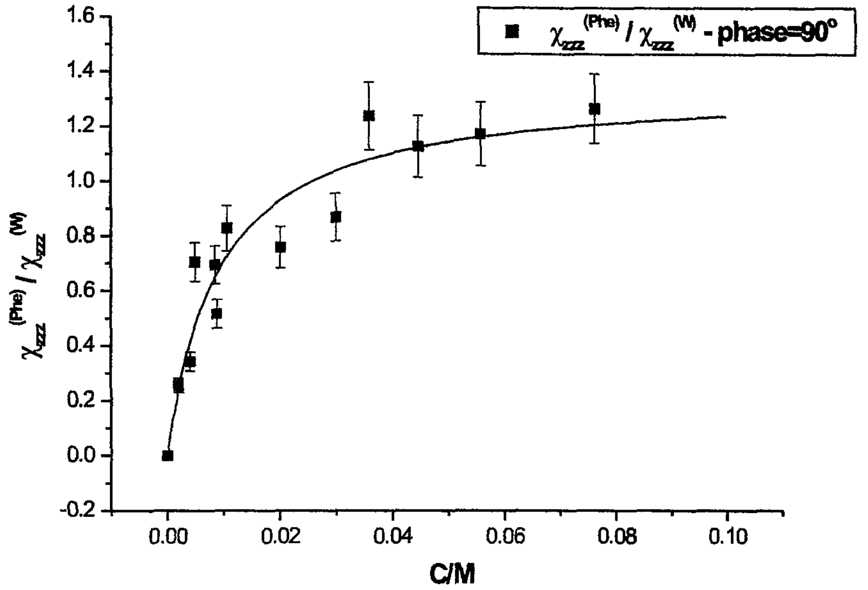

Figure 6.14: Langmuir fit for the determined $\chi^{(2)}_{ZZZ}$(Phe)/$\chi^{(2)}_{ZZZ}$(w) susceptibility ratio for the polarisation data. The ratio has been determined using the previous estimation of the $\chi^{(2)}_{XZX}$(Phe)/$\chi^{(2)}_{XZX}$(w) from the concentration studies and applied to the polarisation data. Error bars are ± 10%.

	Phe +water			
	β_{zzz}, β_{zxx} dominant		β_{zzz}, β_{xzx} dominant	
	$\theta/^o$, (ψ=random)	$\theta/^o$, (ψ=90^o)	$\theta/^o$, (ψ=random)	$\theta/^o$, (ψ=90^o)
Mean	36.7	35.0	36.0	41.4
Std.Dev	1.3	1.6	1.7	3.9
	Phe, phase=90^0			
	β_{zzz}, β_{zxx} dominant		β_{zzz}, β_{xzx} dominant	
	$\theta/^o$, (ψ=random)	$\theta/^o$, (ψ=90^o)	$\theta/^o$, (ψ=random)	$\theta/^o$, (ψ=90^o)
Mean	37.3	36.0	36.0	41.3
Std.Dev	3.1	3.5	6.4	7.7

Table 6.14: The estimated molecular tilt angle θ for Phe only assuming a phase difference of 90^o between the water and the Phe SHG signals. Two different cases for the dominant hyperpolarisabilities are shown (β_{zzz}, β_{zxx} and β_{zzz}, β_{xzx}) for ψ=random and 90^o. The results are compared to the previous determined angle θ with contribution from water.

6.4.1.7 SHG on Phe-C_{20}

The structure of C_{20}-Phe is shown in Figure 6.15. This compound has been studied by previous members in the group in attempt to understand marine films [145, 146]. Langmuir-Blodgett films have been studied and an extra phase, called raft phase, have been found to be formed at high pressures. C_{20}-Phe is an amphiphilic molecule that readily forms monolayers on water and LB films.

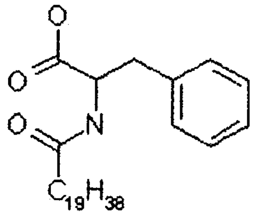

Figure 6.15: Structure of C_{20}-Phe, hydrogens have been omitted.

The monolayer properties of C_{20}-Phe can be followed by a plot of surface pressure as a function of the area of water surface available to each molecule. This is carried out at constant temperature using a Langmuir - Blodgett trough and is known as a surface pressure/area isotherm. An example of an isotherm for C_{20}-Phe is shown in Figure 6.16. C_{20}-Phe shows reproducible elastic behaviour below a critical value of $\Pi = 30$ mN/m as studied in our group [145]. Above this critical pressure the pressure reaches a plateau and the film shows inelastic recovery. Also a rigid film formation was observed at high surface pressures which was accompanied by deflections of the Wilhelmy plate from the vertical. For the solid phase the Langmuir trough gave ~ 45 A^2 as the average surface area occupied by a C_{20}-Phe molecule on a water substrate. The rigid film was comprised of stable holes of approximately 5 nm deep and 2 mm wide as studied by AFM [146]. The holes were scattered randomly and it was suggested that as the monolayer collapses from the solid phase to the rigid phase raft a bilayer was formed.

The polarisation dependence of the SHG signal of the gas phase of the C_{20}-Phe monolayer was recorded for the P and S output harmonic polarisations and is shown in Figure 6.17. The polarisation curves are different from the ones of the Phe molecule at the air/water interface. The P harmonic output polarisation is weakly dependent on the input polarisation angle and the S harmonic polarisation shows stronger dependence and higher signal values than the P analogue.

The determined tilt angle for the benzene chromophore (assuming the interfacial refractive index to take the average value between the refractive index of air and water) is shown in Table 6.15 for different assumptions about the dominant hyperpolarisability tensors and the value of the molecular ψ angle. The hyperpolarisability ratios (β_{zzz}/β_{zxx} and β_{zzz}/β_{xzx}) agree well with the values for the free Phe molecule at the air/water interface. The determine molecular tilt angle θ (assuming ψ=random) is different for the value estimated for the free Phe molecule. In the case where the β_{zzz} and β_{zxx} tensors are dominant the estimated

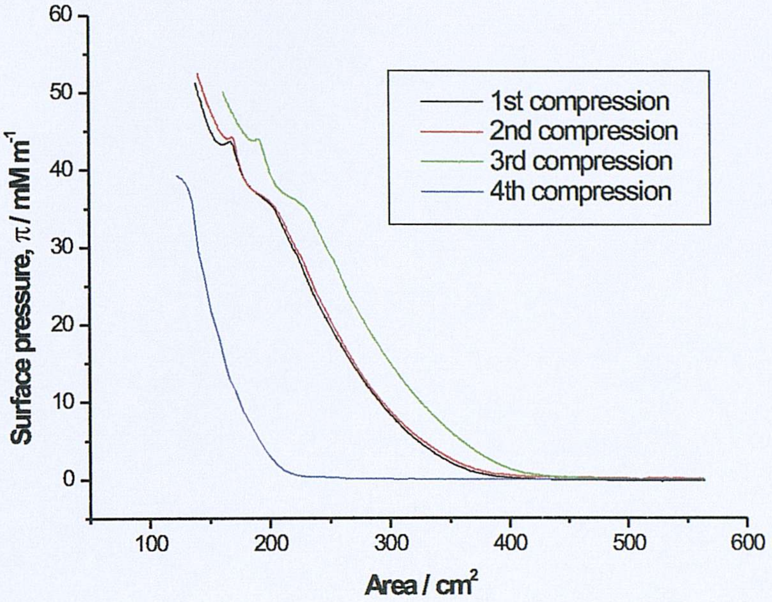

Figure 6.16: Surface pressure versus area isotherm for C_{20}-Phe. The liquid/solid transition occurs at a surface pressure of $\sim$ 35 mN/m and the solid/raft transition occurs at a surface pressure of $\sim$ 45 mN/m. Four consecutive compressions of the film are shown.

tilt angle is 5 degrees higher and in the case where β_{zzz} and β_{xzx} are dominant the tilt angle is 13 degrees higher. This shows that the observed different polarisation curves correspond to a change in the orientation of the phenylalanine molecule as induced by the bonding in the C_{20} fragment.

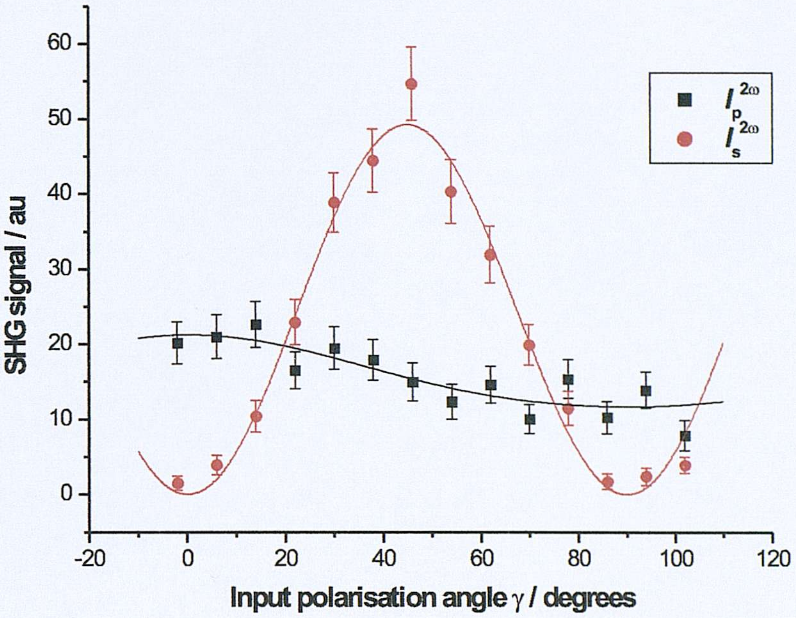

Figure 6.17: The polarisation dependence of the SHG signal generated in the S, and P linear polarisation planes as a function of the input polarisation angle (γ), at the air/water interface for the uncompressed C_{20}-Phe molecule oriented in the fully expanded region. The solid lines have been estimated by the simultaneous fitting of the Euler parametrization of A, B, and C parameters in the S, and P SHG data. λ=532/266 nm. The error bars added are 2σ.

β_{zzz}, β_{zxx} dominant	Re(β_{zzz}/β_{zxx})	-0.19
	Im(β_{zzz}/β_{zxx})	0.11
	Tilt angle θ/°(ψ=random)	41.5
	Tilt angle θ/° (ψ=90°)	39.2
β_{zzz}, β_{xzx} dominant	Re(β_{zzz}/β_{xzx})	0.22
	Im(β_{zzz}/β_{xzx})	-0.17
	Tilt angle θ/°(ψ=random)	49.5
	Tilt angle θ/° (ψ=90°)	44.4

Table 6.15: The determined molecular tilt angle θ for the benzene chromophore assuming the interfacial refractive index takes the average value of the two bulk indices. Two different cases are shown for the dominant hyperpolarisabilities as well as their ratios. The angle ψ is taken to be random or 90^o.

6.4.2 Computational Results

The most stable conformers of phenylalanine have been determined experimentally coupled with ab initio calculations [128]. Nine of the lowest energy neutral conformers are shown in Figure 6.18, optimised at the MP2/6-311G** level of theory. They are shown in increasing energy from conformer PheI to PheIX. Six of the nine structures were observed experimentally (PheI to PheVI). Structures PheI, pheIII, and PheIV exhibit an intramolecular hydrogen bond, connecting the carboxylic group to the amino group. A strong stabilizing factor is the interaction between the aromatic π electrons and the polar amino acid chain. In structures PheII, PheV, and PheVI the carboxyl hydrogen is pointing away from the amino group.

A recent study of the monohydrated complex of phenylalanine [137], obtained structures where the three lowest in energy structures contained a water-carboxyl hydrogen bond and the two other higher energy ones had a water-amino hydrogen bond. Those structures were derived from the PheII, PheV and PheVI phenylalanine structures where there is no intramolecular hydrogen bond present.

Recent calculations [128] predicted the strong dependence of the first electronic transition dipole moment with changes of the conformation in the amino acid chain. The transition dipole moment is shown for each conformer by the double headed arrow. Following that, the conformation of the amino acid chain should affect the values of the dominant hyperpolarisability tensor elements that get enhanced because hyperpolarisability is proportional to the transition dipole moment orientation. Furthermore the conformation changes of the different groups in the molecule will lead to a different distribution of partial charges around the molecule and affecting the electron density and the change in the permanent dipole moment between the ground and the first electronic excited state.

The hyperpolarisability of the nine most stable conformers of phenylalanine is calculated in the static case and at 532 nm. The lowest energy conformer (pheI) is used to calculate the low lying excitation energies corresponding to $\pi \rightarrow \pi^*$ electronic transitions. Because of the increased size of the molecule the calculations become increasing computationally expensive. The optimised structures of PheI-PheIX at the MP2/6-311G** level of theory have been used for all calculations from the work of Simons and co-workers [128]. The static hyperpolarisability of the lowest energy conformer PheI was calculated at the HF and MP2 level of theory employing the Sadlej basis set. The LB94 functional has been used to calculate the static and dynamic(532nm) hyperpolarisabilities for all nine conformers employing the Vdiff basis set in ADF. These calculations are not that computationally demanding.

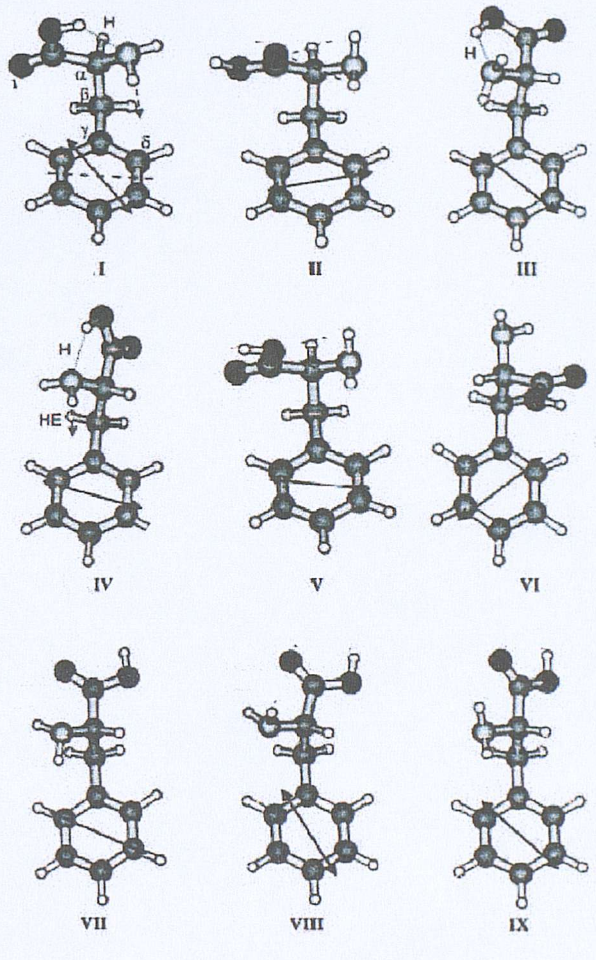

Figure 6.18: The nine lowest energy conformers of Phenylalanine adapted from reference [128]. They are shown in increasing energy. The transition moment of the first electronic transition is shown as a black arrow. For reference the transition moment of toluene is also shown, dotted line.

Transition	Energy eV	nm	Oscillator Strength/au	Exp
L_a $\pi \rightarrow \pi^*$	5.71	217	0.0387	205
L_b $\pi \rightarrow \pi^*$	4.83	257	0.0075	258

Table 6.16: The vertical excitation energies for the Phe molecule as calculated at the LB94/TZ2P level of theory. The two low lying transitions are shown and compared to the experimental values.

6.4.2.1 Excitation Energies

The low lying excitation energies were calculated for the lowest energy conformer of Phenylalanine(PheI). The results are shown in Table 6.16, and only the singlet transitions are shown. The experimental values (L_a and L_b) are also shown for comparison. The LB94 functional was used in ADF with the Vdiff basis set. It can be seen that there is good agrement between theory and experiment. Phenylalanine can be treated as a mono-substituted benzene analogue, similar to toluene.

6.4.2.2 Hyperpolarisability

The static hyperpolarisability of the lowest energy conformer (PheI) has been calculated using HF, MP2 and DFT methods. The size of the Phe molecule (23 atoms) makes the hyperpolarisability calculations with large basis sets such as Sadlej very time consuming and effectively impractical. The wave function methods have been restricted to only one conformer only (PheI) and the faster DFT methods have been employed for the rest of the conformers in conjunction with a frozen core (1s for C) basis set (Vdiff). The static hyperpolarisability results are shown in Table 6.17 for PheI and indicate the dominance of the β_{zzz} tensor over the other tensors. There is good agreement between the HF and MP2 calculated values for all the dominant tensors. The LB94 results predict the significance of the β_{zzz} but the tensors values have opposite sign than the MP2 and HF results. The β_{zxx} and β_{zyy} have significant contribution to the non-linear polarisation and are relevant to the SHG experiments. The basis set size and type influences the LB94 results. The ET1 basis set which is a QZ3P with added diffuse functions gives similar results to the smaller Vdiff basis set. All approximating methods predict the β_{xxx} and β_{yyy} tensors to be significant but are not considered in comparison to experiment because in SHG experiments only the tensors β_{zzz}, β_{zxx}, β_{xzx}, β_{zyy} and β_{yzy} are considered due to the azimuthal symmetry of the liquid surface and the symmetry of the molecule [17].

Table 6.18 shows the frequency dependent hyperpolarisability results at 532 nm with different theoretical methods. All methods predict the dominance of the β_{zzz} tensor as in the static case. Also the β_{zyy}, β_{yzy} tensor values are significant which are important in SHG experiments. The tensors β_{zxx} and β_{xzx} are predicted to be similar in value within the HF/Sadlej level of theory.

	Method /Basis set			
β_{ijk}/au	HF/Sadlej	MP2/Sadlej	LB94/Vdiff	LB94/ET1
β_{zzz}	-71.82	-59.03	57.45	42.34
β_{zzx}	14.02	25.71	-21.08	-19.43
β_{zxx}	-16.95	-13.81	5.54	2.86
β_{xxx}	43.20	47.78	-75.22	-66.20
β_{zzy}	1.15	-2.59	23.52	20.55
β_{zxy}	3.07	0.86	-3.04	-2.61
β_{xxy}	-5.76	-3.33	10.16	8.16
β_{zyy}	-28.98	-22.27	7.00	5.60
β_{xyy}	9.25	13.78	-20.27	-18.98
β_{yyy}	-16.30	-10.56	-15.18	-17.75

Table 6.17: The static hyperpolarisability tensors (in au) for the minimum energy phenylalanine conformer(PheI) calculated with HF/Sadlej, MP2/Sadlej, and LB94 methods.

	Method /Basis set		
β_{ijk}/au	HF/Sadlej	LB94/Vdiff	LB94/ET1
β_{yyy}	64.56	-8.58	-13.49
β_{xyy}	-12.91	-41.12	-39.28
β_{zyy}	59.84	57.84	46.75
β_{xxy}	-17.71	-33.71	-34.45
β_{xxy}	6.00	13.04	14.82
β_{zxy}	-3.84	-48.21	-41.64
β_{yzy}	57.49	12.37	10.26
β_{xzx}	-5.54	-55.66	-42.83
β_{zzy}	-18.62	-66.63	-55.06
β_{yxx}	-17.71	-33.71	-34.45
β_{yxx}	6.30	20.65	22.31
β_{xxx}	-65.00	-188.80	-170.95
β_{zxx}	30.30	32.62	23.06
β_{yzx}	-6.08	25.01	30.43
β_{xzx}	33.87	23.83	9.56
β_{zzx}	-27.29	245.91	196.43
β_{yzz}	-18.73	-56.13	-79.43
β_{xzz}	-23.80	204.81	117.54
β_{zzz}	139.40	839.14	261.33

Table 6.18: The frequency dependent(532 nm) hyperpolarisability tensors (in au) for the minimum energy phenylalanine conformer calculated with HF, MP2, and LB94 methods.

The frequency dependent hyperpolarisabilities at 532 nm were calculated for all nine Phe conformers using HF/6-31G and LB94/Vdiff level of theory. The conformational dependence of the β_{zzz} tensor for the static and dynamic case is shown in Figure 6.19 as calculated by the LB94/Vdiff method. It can be seen that the conformation of the Phe molecule affects the calculated hyperpolarisability value. In the static case, conformer PheVII exhibits the highest positive value for the β_{zzz} tensor and conformer PheVIII possess the highest negative value. Similarly in the dynamic case, conformer PheIII and conformer PheIV possess the highest positive and lowest tensor value respectively. The conformational change in the side chain of the Phe molecule greately influences the non-linear polarisability response of the molecule. Furthermore the relative orientation of the carboxyl and amine group in the molecule affects the π delocalisation in the aromatic ring. The donor and/or acceptor electron ability of these groups will change the appearance of the electron density of the molecule and thus the hyperpolarisabilty tensor value.

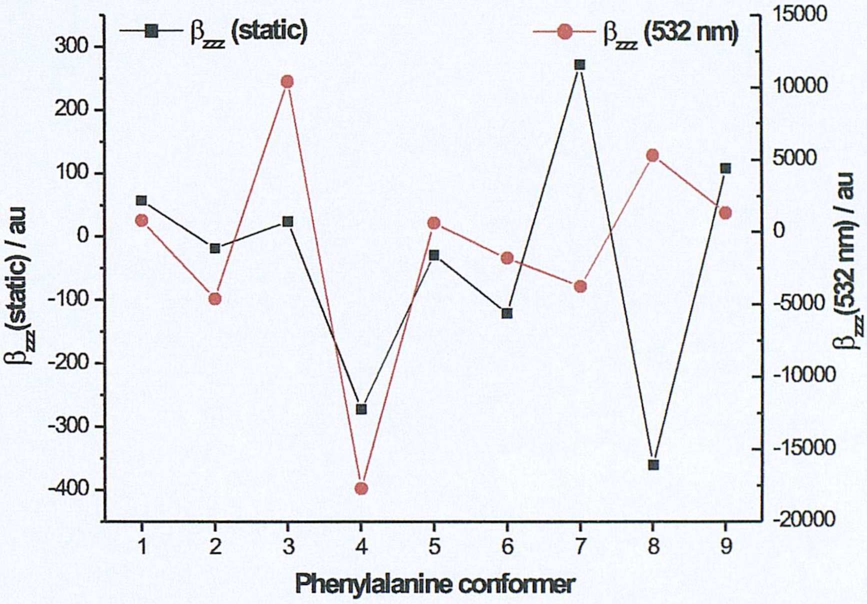

Figure 6.19: The variation of the β_{zzz} tensor component is shown for different phenylalanine conformers (1-9) as calculated at the LB94/Vdiff level of theory for the the static (left Y-axis) and frequency dependent (532 nm) (right Y-axis) cases respectively.

Figure 6.20 shows the conformational dependence of the frequency dependent hyperpolarisability ratios (β_{zxx}/β_{zzz} and β_{xzx}/β_{zzz}) as calculated by the HF/6-31G and LB94/Vdiff methods at 532 nm. The shape of the conformational dependence curve for the ratios is similar for both calculating methods except the for the values calculated for conformer PheIX. The tensor values for β_{zxx}/β_{zzz}

and β_{xzx}/β_{zzz} are very similar for all conformers indicating the equivalency of β_{zxx} with β_{xzx}.

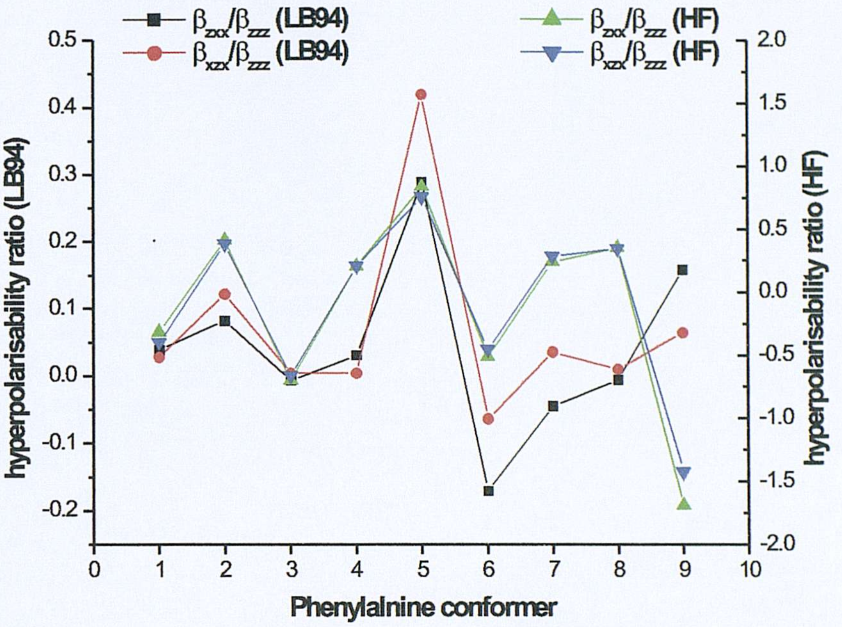

Figure 6.20: The variation of the frequency dependent (532 nm) hyperpolarisability ratios β_{zxx}/β_{zzz} and β_{xzx}/β_{zzz} for the different phenylalanine conformers (1-9). The LB94/Vdiff (left Y-axis) and HF/6-31G (right Y-axis) computed results are shown respectively.

6.4.2.3 Experiment vs Theory

In the absence of direct gas phase experimental hyperpolarisability measurements for phenylalanine it is difficult to compare to *ab initio* calculations and establish their quality quantitatively. SHG air/solution phase measurements can be compared to gas phase *ab initio* calculations. The SHG determined hyperpolarisability ratios could be compared directly with the gas phase calculations. Table 6.19 shows the experimental determined hyperpolarisability ratios (β_{zxx}/β_{zzz} and β_{xzx}/β_{zzz}) and the calculated ones for the different phenylalanine conformers in the static and dynamic (532 nm) case.

In Table 6.19 the calculated ratio value for β_{zxx}/β_{zzz} is equivalent to β_{xzx}/β_{zzz} in the static case. At the LB94/Vdiff level of theory the frequency dependent β_{zxx}/β_{zzz} value for conformers PheVI and PheIX compare with the experimental measured value of -0.18. In the HF/6-31G level of theory conformer PheIV has a comparable value to the experimental β_{zxx}/β_{zzz} ratio.

	LB94/Vdiff			HF/6-31G		
	β_{zxx}/β_{zzz}		β_{xzx}/β_{zzz}	β_{zxx}/β_{zzz}		β_{xzx}/β_{zzz}
	Exp=-0.18					Exp=0.20
Conformer	static	532 nm	532 nm	static	532 nm	532 nm
I	0.10	0.04	0.03	0.91	-0.32	-0.40
II	-1.32	0.08	0.12	0.48	0.41	0.38
III	-1.69	-0.01	0.00	-0.44	-0.70	-0.67
IV	0.12	0.03	0.00	0.24	0.20	0.20
V	0.18	0.29	0.42	0.97	0.83	0.75
VI	0.35	-0.17	-0.06	-0.55	-0.51	-0.46
VII	-0.11	-0.04	0.04	2.28	0.24	0.29
VIII	0.02	-0.01	0.01	0.77	0.36	0.35
IX	-0.19	0.16	0.06	-0.45	-1.69	-1.42

Table 6.19: Comparison of the calculated hyperpolarisability ratios (β_{zxx}/β_{zzz} and β_{xzx}/β_{zzz}) at LB94/Vdiff and HF/6-31G levels of theory with the SHG experimental measured values.

The calculated ratios (β_{zxx}/β_{zzz} and β_{xzx}/β_{zzz}) at the HF/Sadlej level of theory for PheI are 0.22 and 0.24 respectively and exhibit the equivalence that was found in the SHG results for the dominant hyperpolarisability ratios. The calculated ratio values are close with the experimental measured ones but the phase for the β_{zxx}/β_{zzz} ratio is opposite to the experimental measured one.

6.5 Conclusions and Future Work

The phenylalanine molecule has been studied by second harmonic generation studies at the air/water interface. The strong TPF signal was separated from the SHG signal and the maximum emission wavelength was found to be blue shifted (275 nm) with respect to the linear emission fluorescence maximum wavelength (283 nm). The SHG signal follows the expected quadratic relationship with incident laser power but the TPF signal was found to have a slope of 1.27 contrary to the expected slope of 2. The polarisation dependence of the SHG signal remain effectively unchanged for bulk phenylalanine concentrations up to $\sim$ 0.08 M. This suggests that the orientation of the molecule at the interface doesn't change significantly with increasing bulk concentration and the molecule may be approximated within the weak field limit [39]. The estimated tilt angle of 36 ± 2 is very close to the SHG magic angle of 39.2o [28]. This suggests that the molecules have a broad molecular tilt angle distribution at the interface or that the distribution is very narrow and centered around 36o. Because the molecule absorbs at the harmonic wavelength the SHG signal is expected to be resonant enhanced. The SHG signal intensity is only 1.5 times larger than the SHG signal from the air/water interface. This could indicate a weakly alignment of the Phe molecules at the interface with a wide distribution tilt molecular angles which results in an inefficient coherent addition of the SHG response from each molecule.

The concentration dependence of the SHG signal showed that the molecule adsorbs at the air/water interface and the adsorption can follow a Langmuir isotherm. The single molecule layer is formed at bulk concentrations above 0.02 M and the estimated adsorption energy is $\Delta G^{\ominus}_{ads} \sim$ -20 kJ/mol irrespective of the assumed phase between the SHG signal of Phe and water. The TPF signal was found to follow a linear relationship with respect to the Phe bulk concentration. The water signal contribution was separated from the Phe SHG signal and the polarisation data were used to fit a Langmuir adsorption isotherm. The determined molecular parameters did not change after the water contribution was taken away. The surfactant C_{20}-Phe was studied as an LB film and the polarisation dependence of the SHG signal was measured from the gas phase of the film. The polarisation curves were different from the free Phe molecule at the surface and the determined orientation angle was found to be higher from the free Phe molecule. The measured hyperpolarisability tensor ratios remain the same indicating that the SHG response originated from the benzene chromophore.

The above SHG study can be furthered by measuring the SHG signal as a function of the bulk pH in order to find out which form of Phe is present at the interface. Previous studies have revealed that the neutral form is likely to be present at the air/water interface [147–149]. The surfactant C_{20}-Phe can be studied as an LB film at the air/water interface and the polarisation dependence of the SHG signal at different phases would reveal the preferred molecular orientation of the molecule and information about the structure of the film.

The theoretical calculation on the hyperpolarisability of different Phe conformers have showed the sensitivity of the molecular hyperpolarisability response on the molecular conformation. The hyperpolarisability calculations have neglected the vibrational and solvent effects which might be important when comparing with experiment. Future calculations will involve the calculation of the vibrational contribution to the total hyperpolarisability and the inclusion of solvent molecules. The conformation dependence of the Phe molecule will be investigated at the air/water interface with force field methods.

Chapter 7

Rhodamine 6G

7.1 Introduction

7.1.1 Preface

Rhodamine dyes are a popular choice for usage as laser dyes due to their strong absorption near the harmonic wavelength of Nd:YAG lasers and their photostability. Rhodamine 6G (R6G) also known as rhodamine 590, shown in Figure 7.1 is one of the most efficient laser dyes. Aqueous solutions of R6G are known to aggregate and thus limiting their laser dye efficiency. The formation of dimers in solution does not contribute in the emission of the laser light. While the formation of dimers in solution is relatively understood the situation concerning the formation of dimers or trimers at the surface or interface is not clear. The formation of aggregates at the surface depends on the intermolecular distances and the geometric structure of the interface. The water surface is smooth and homogeneous thus allowing the molecules to orient themselves freely at the interface depending on their intermolecular forces.

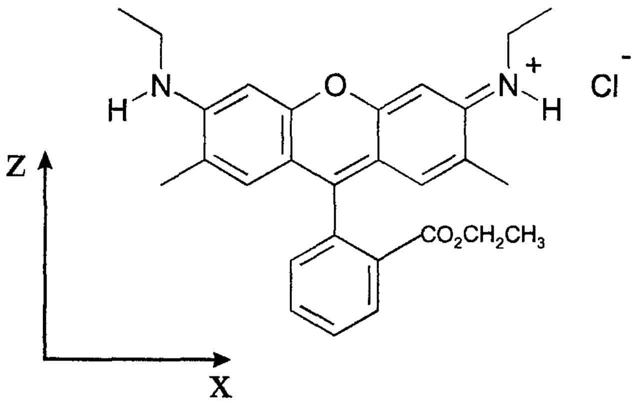

Figure 7.1: The structure of rhodamine 590 Chloride (6G) and the definition of the molecular xyz coordinate system.

SHG is a powerful analytical technique for investigating molecules with considerable solubility in the bulk. The surface specificity of the SHG technique provides a powerful optical spectroscopy method to study the structure and dynamics of the dyes present at the air/water interface. In this study aqueous solutions of the rhodamine 6G chloride salt were investigated for their adsorption properties and molecular orientation of the R6G molecule at the air/water interface. The presence of the dimer structures in the surface was observed at high bulk concentrations from a change in the polarisation dependence of the SHG signal.

7.1.2 Previous Studies

The aggregation of rhodamine molecules in aqueous solution has been studied extensively [150–155] and the results suggest the existence of both blue shifted (H-type) and red shifted (J-type) aggregate dimer formation. The interpretation of several three dimensional dimer structures existing in solution is based on the theory of exciton splitting [156–158]. The absorption spectra of different concentrations of aqueous solutions of R6G has revealed the presence of at least three species. In addition to dimers and monomers present in solution, data analysis have revealed the existence of trimers and tetramers. It was found that at concentrations of 4 μM the monomer exists in 98% of the dye. At concentrations up to 100 μM the presence of trimers and tetramers is negligible and can be neglected but at concentrations higher than 100 μM higher aggregates (trimer and tetramer) become significant. The dimer concentration reaches a maximum of 53 % of the dye and does not exceed this value.

The situation is different at the surface because only two dimensional structures can be formed due to the geometry of the interface. Recently the adsorption characteristics and polarisation dependence of R6G have been studied with SHG at the fused silica/air interface [159], at the air/water interface as an LB film [160] and at the methylene chloride/fused silica interface [30]. Second harmonic ellipsometric (SHE) studies [161] have estimated film thickness of 50 Å at the air/water interface. The SH wavelength dependence [31] and the dynamic process of rotational relaxation for dyes has been studied at the air/liquid interface [34,162] with implication on the adsorbate geometry and interfacial solvation. Aggregation of dyes has been studied on solid surfaces and recently the studies have been extended at the air/water interface for oxazine dyes [144]. Their results suggest the formation of H-type aggregate dimers at the interface and the SHG polarisation dependence results suggest the signal to originate from a single species (dimer) regardless of solution composition in agreement with previous results [163]. Their view of the preference of the dimer for the surface instead of the monomer is supported by previous SHG adsorption studies at the air/water interface indicating that is less polar than the bulk phase [147,164,165]. The dimer aggregates are considered to be less polar than the monomers and therefore have a high preference for the water surface. Previous studies on adsorbate properties such as adsorption free energies, δG_{ads} have shown that the air/water interface is less polar that the bulk aqueous phase [147–149]. In addition the determination of surface p*Ka* values suggests that their are higher for acids and lower for bases than their respective bulk values. This suggests that the neutral form is preferred at the interface.

7.1.3 The Absorption Spectrum of R6G

The R6G molecule belongs to the xanthene dye family and the optical properties are governed mainly by the π electrons in the xanthene chromophore. The chemical structure (Figure 7.1) can be approximated to have C_{2v} symmetry. The absorption spectrum shown in Figure 7.2 shows a peak at 529 nm which corresponds to a $S_0 \rightarrow S_1$ transition, and a peak at 347 nm which corresponds to a $S_o \rightarrow S_2$ transition. The absorption below 300 nm corresponds to the isolated aromatic ring. The transition dipole moments for the $S_o \rightarrow S_1$ and $S_o \rightarrow S_2$ transitions lie along the x and z-molecular axes respectively.

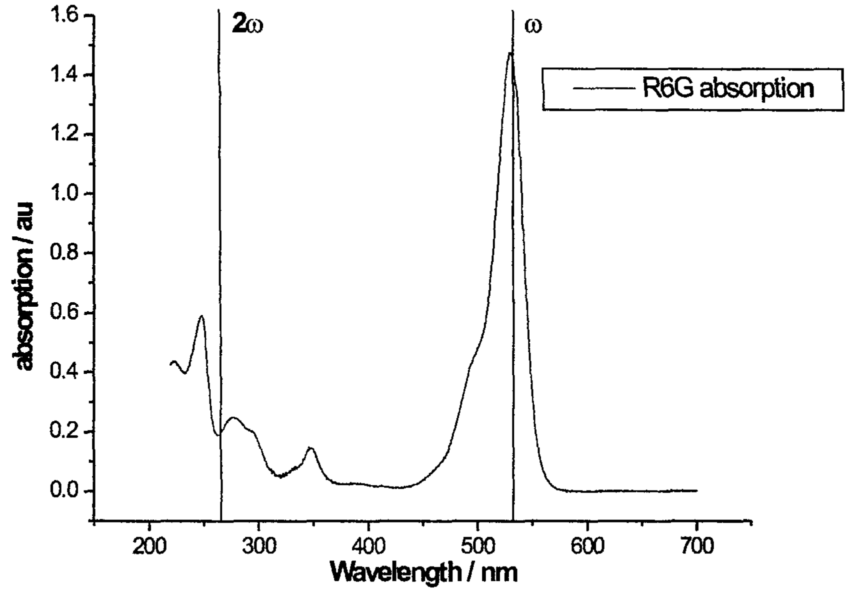

Figure 7.2: The UV-vis absorption spectrum of R6G in ethanol adapted from reference [97] with the fundamental (ω) and harmonic (2ω) wavelengths in the SHG experiment shown in the spectrum.

The absorption spectra of R6G in 10% methanol/90% water (v/v) for different concentrations is shown in Figure 7.3 where the formation of higher aggregates (dimer) of R6G can be seen. The peak at 526 nm decreases slowly in intensity with increasing concentration and a peak at 498 nm increases in intensity with increasing concentration. The spectra show an isosbestic point at $\sim$ 508 nm but not all curves cross clearly at that point indicating the possibility of higher aggregates (trimers, tetramers) [154]. The blue shifted peak observed at 498 nm originates from the presence of H-aggregate dimers. According to exciton splitting theory [156–158] the alignment of the dipole moments of the monomers comprising the dimer determines if the dimer band is blue or red shifted relative to the monomer band. The angle Ξ between the center of separation between the two monomers and the monomer transition moments determines the type of aggregate formed. H-type aggregates ($54.7^o \leq \Xi \leq 90^o$) are responsible for blue shifted transitions and J-type aggregates ($\Xi < 54.7^o$) have red shifted absorption bands.

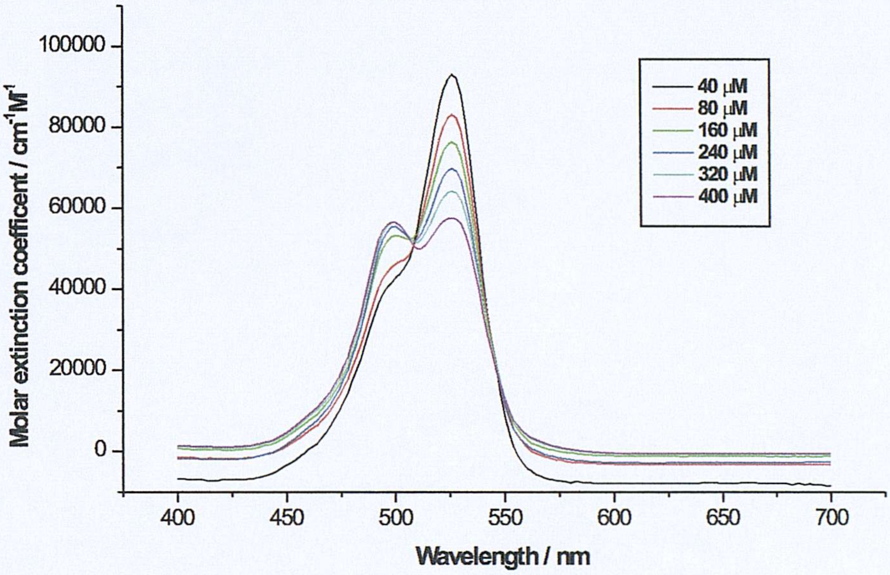

Figure 7.3: Normalised absorption spectra of R6G at different concentrations in 10% Methanol/90%Water (v/v) adapted from reference [155].

Fluorescence emission spectra of R6G in water have shown that the dimers are non-fluorescent whereas the monomers posses high quantum yields. Fluorescence emission of R6G after two photon absorption in ethanol solutions are very efficient and have shown a significant departure from the expected fluorescence square intensity law at high incident laser intensities [142].

7.2 Experimental

7.2.1 Optical Arrangement

The basic optical arrangement has been described in Chapter 3. The SH laser output of a Nd:YAG laser system (532 nm) was used as the fundamental laser intensity with pulse width of 5 ns at 20 Hz repetition rate. Because R6G absorbs at both the fundamental and the harmonic low laser intensities were used of the order 1-2 mJ/pulse. The monochromator input and output slits were optimised (0.1-0.5 mm) to separate the two photon fluorescence present.

7.2.2 Data Acquisition and Analysis

Data were collected over 1000 laser shots and background intensities and laser power measurements were obtained and subtracted from the signals. The average intensities were fitted to the non-linear equations described in Chapter 2 using R [45] and built-in minimisation functions [44]. In-house software was used for the calculation of the Fresnel coefficients described in chapter 3.

7.2.3 Preparation of Solutions and Sample Handling

Rhodamine 590 (6G) Chloride (Aldrich, $\geq$ 99.9%) was used as supplied. Solutions of R6G were prepared in water and the volumetric flasks were placed in a ultrasonic bath for 30 minutes to aid dissolution. A PTFE sample holder was used to hold the dye for the experiments at a temperature of 21 ^{o}C. The water used was ultrapure, 18.2 MΩ cm^{-1}.

7.3 Results and Discussion

7.3.1 Monochromator Scan

The linear emission fluorescence of the R6G molecule exhibits a maximum at 555 nm and could possibly interfere with the SHG signal. The presence of visible filters, the monochromator and a solar blind photomultiplier tube ensures that none of the strong fluorescence emission signal which results from absorption at the fundamental (532 nm) can interfere with the SHG signal. The R6G molecule exhibits a strong two photon fluorescence signal in the UV region. This signal can interfere with the SHG signal and in some cases overwhelm completely the second harmonic process as shown in Figure 7.4. The maximum of the observed TPF signal occurs at $\sim$ 278 nm and the emission peak extends in the SHG signal.

By reducing the entrance and exit monochromator slits to 0.15 mm it is possible to achieve the desired resolution of the TPF and SHG signals as shown in Figure 7.5.

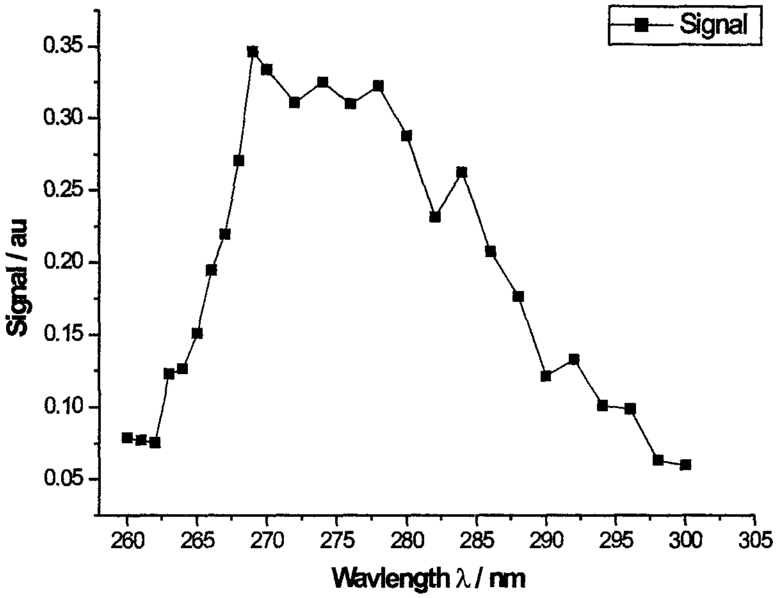

Figure 7.4: Monochromator scan of the detected signal at the air/water interface from a 1.6 μM R6G solution. The output polarisation angle is set to S and the input polarisation angle is set 45° degrees. The input and output monochromator slits are set to 0.5 mm giving an estimated bandpass of 2.1 nm.

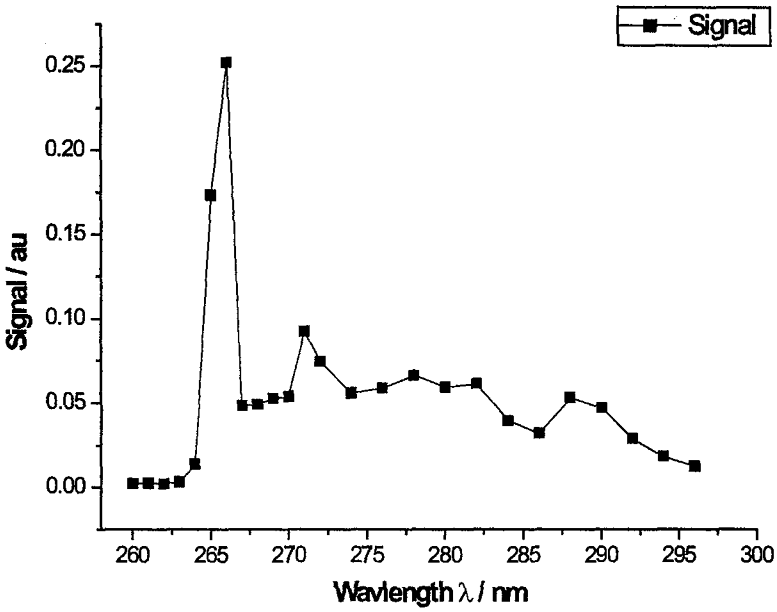

Figure 7.5: Monochromator scan of the detected signal at the air/water interface from a 1.6 μM R6G solution. The output polarisation angle is set to S and the input polarisation angle is set 45^o degrees. The input and output monochromator slits are set to 0.15 mm giving an estimated bandpass of 0.7 nm.

7.3.2 Power Dependence

The SH or TPF intensities should be quadratically proportional to the incident laser power. Figure 7.6 shows a ln-ln plot of the second harmonic S- and P-out intensities from the R6G molecule present at the air/water interface. The slope of the linear fit gave a value of 1.23 for S-out and 1.32 for P-out which are far off the expected value of 2. A possible reason for this dependency is that the surface susceptibility tensor has contributions from more than one species. In this case the concentration of the solution used was 300 μM indicating the presence of dimers in the solution and hence in the surface. The possibility of the interference of the TPF signal with the SHG should not be excluded as well since the slits were set to 0.5 mm allowing a substantial overlap of the two signals.

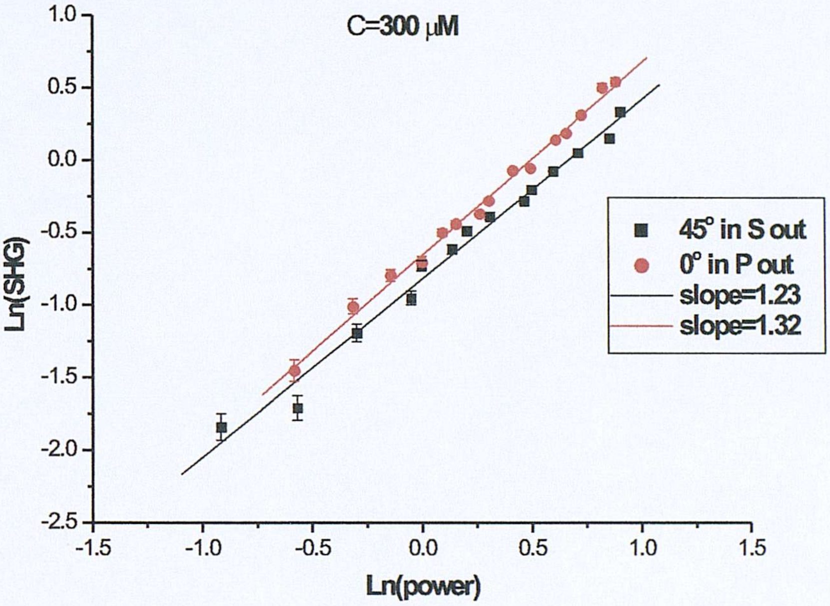

Figure 7.6: Linear regressions of the ln(SHG) signal versus the ln of incoming laser fluence for a 300 μM R6G solution in water. The slope of the line for the S-out SHG signal is 1.23 and the P-out SHG is 1.32. Error bars are within 5%.

A lower concentration R6G solution was investigated and the dependence of the P-out second harmonic signal is shown in Figure 7.7. The determined slope was 1.46. This is higher from 1.23 but still not close to the expected value of 2. It is likely that the TPF signal interferes with the SHG signal giving the distorted slope values and the experiment should be repeated with better monochromator resolution. It is possible that the excited state of the dye gets saturated at increasing incident laser powers since the fundamental wavelength used (532 nm) is on resonance with the first electronic transition (528 nm) of R6G.

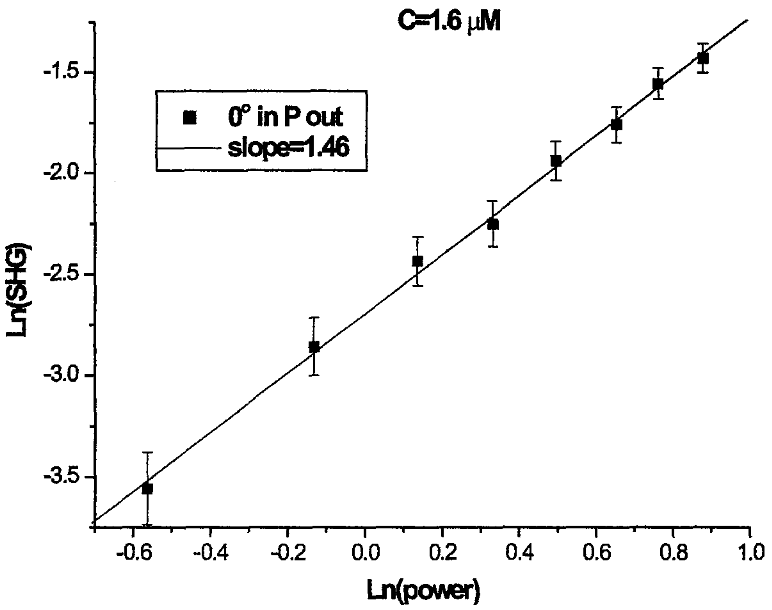

Figure 7.7: Linear regressions of the ln(SHG) signal versus the ln of incoming laser fluence for a 1.6 μM R6G solution in water. The slope of the line for the P-out SHG is 1.46. Error bars are within 5%.

7.3.3 Polarisation Dependence

SHG polarisation dependence studies can provide valuable information about the orientation of the adsorbed molecule at the surface. Furthermore they can give information about the ratio of molecular hyperpolarisabilities responsible for the non-linear polarisation of the molecule. The SHG signal intensity depends on both the number of molecules present at the surface and the molecular orientation. Any changes in the structure of the surface will be reflected as a change in the polarisation dependence of the SHG signal intensities.

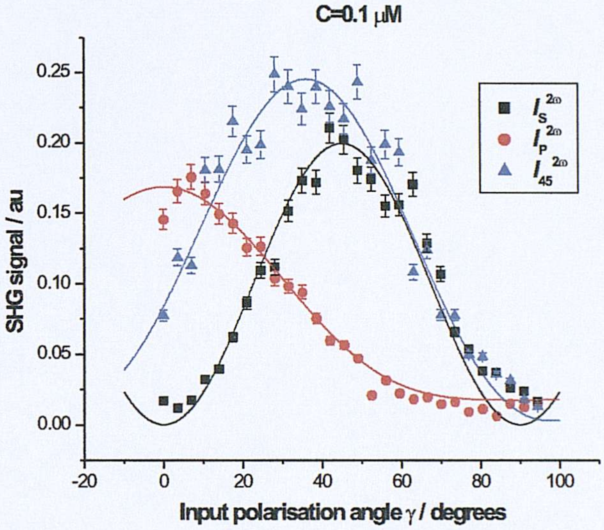
C=0.1 μM

Figure 7.8: The polarisation dependence of the SHG signal generated in the S, P and +45^o linear polarisation planes as a function of the input polarisation angle (γ), for a 0.1 μM R6G aqueous solution. The solid lines have been estimated by the simultaneous fitting of the Euler parametrization of A, B, and C parameters in the S, P, and +45^o SHG data assuming A to be real and B and C to be complex. λ=532/266 nm. Error bars are ± 5%.

The polarisation dependence of the SHG signal was recorded for S, P, +45 and -45 output harmonic polarisations as a function of the input polarisation angle γ. R6G solutions at three different concentrations (C=0.1, 1 and 167 μM) were used to obtain the polarisation dependence curves and the experiments were repeated twice at each concentration. The polarisation dependence of the SHG signal and the theoretical fitting to the phenomological model are shown in Figures 7.8-7.11.

The results presented demonstrate the change in the polarisation dependence of the SHG signal on increasing the bulk dye concentration. The S-output harmonic polarisation is indicative of an isotropic surface with azimuthal symmetry and no chirality present. The signals intensities for γ=0^o, 90^o are almost zero and symmetric as expected from theory. The small offset in their values is attributed to two photon fluorescence and can be subtracted. At low dye bulk concentrations

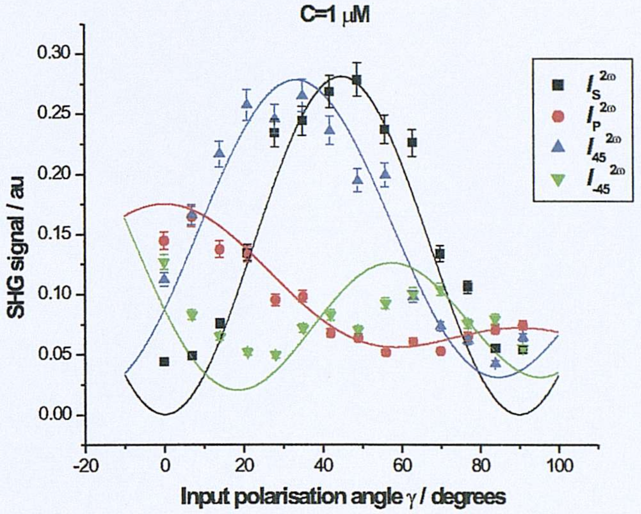

Figure 7.9: The polarisation dependence of the SHG signal generated in the S, P, -45^o and +45^o linear polarisation planes as a function of the input polarisation angle (γ), for a 1 μM R6G aqueous solution. The solid lines have been estimated by the simultaneous fitting of the Euler parametrization of A, B, and C parameters in the S, P, -45^o and +45^o SHG data assuming A to be real and B and C to be complex. λ=532/266 nm. Error bars are ± 5%.

(C=0.1 μM) the polarisation dependence of the SHG signal is similar in shape to the bare air/water interface. At higher bulk concentrations (C=1 μM) the shape of the P-output harmonic polarisation curves changes slightly. Increasing the bulk concentration further ((C=167 μM) there is a complete change in the shapes of the P, +45 and -45 output polarisation curves. At such concentration there is extensive dimer aggregation occurring in the bulk solution [154] and is expected that dimers will be present at the surface as well. The preference of the dimers for the water surface will depended on their adsorption free energy, equilibrium constant and their polarity.

This changes in the polarisation dependence behavior with increasing dye bulk concentration can be seen more clearly by fitting the data to the phenomological model with the A, B, and C coefficients, taking A to be real and obtaining the estimates of the coefficient ratios and standard errors for the estimates of the phases, shown in Table 7.1. The ratio estimates B/A and C/A and their phases $\hat{\phi}_R$ are quite different across the three concentrations.

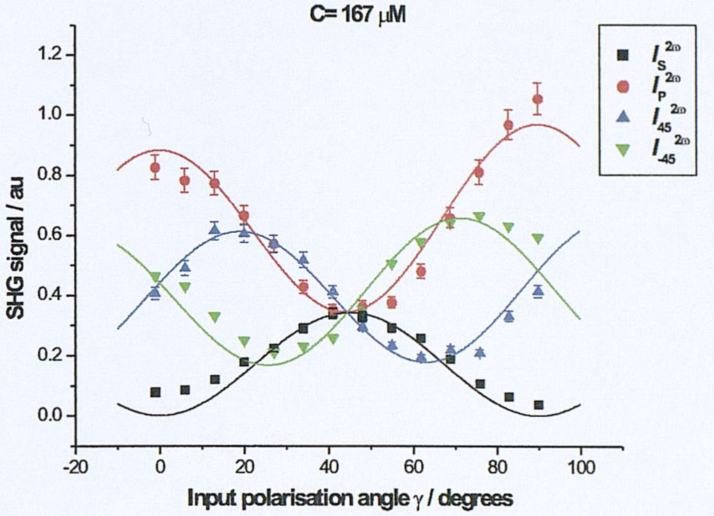

Figure 7.10: The polarisation dependence (data set 1) of the SHG signal generated in the S, P, -45^o and +45^o linear polarisation planes as a function of the input polarisation angle (γ), for a 167 μM R6G aqueous solution. The solid lines have been estimated by the simultaneous fitting of the Euler parametrization of A, B, and C parameters in the S, P, -45^o and +45^o SHG data assuming A to be real and B and C to be complex. λ=532/266 nm. Error bars are ± 5%.

		B/A		C/A	
Data Set	C/μM	$\hat{r}_R$ (Delta C.I.)	$\hat{\phi}_R$ $\sigma(\hat{\phi}_R)$	$\hat{r}_R$ (Delta C.I.)	$\hat{\phi}_R$ $\sigma(\hat{\phi}_R)$
1	0.1	0.322	1.189	1.087	0.542
		(0.231 , 0.413)	(0.235)	(1.046 , 1.129)	(0.125)
2	1	0.690	1.579	1.318	-0.476
		(0.580 , 0.799)	(0.182)	(1.222 , 1.413)	(0.175)
3	167	1.048	1.830	0.621	2.488
		(1.018, 1.079)	(0.042)	(0.589, 0.655)	(0.044)

Table 7.1: Ratios of parameters for the R6G molecule at the air/water interface at three different dye bulk concentrations. Confidence intervals are given for the ratios of the magnitude using the delta method. Standard errors are given for the phase angles $\hat{\phi}_R$ (in parentheses).

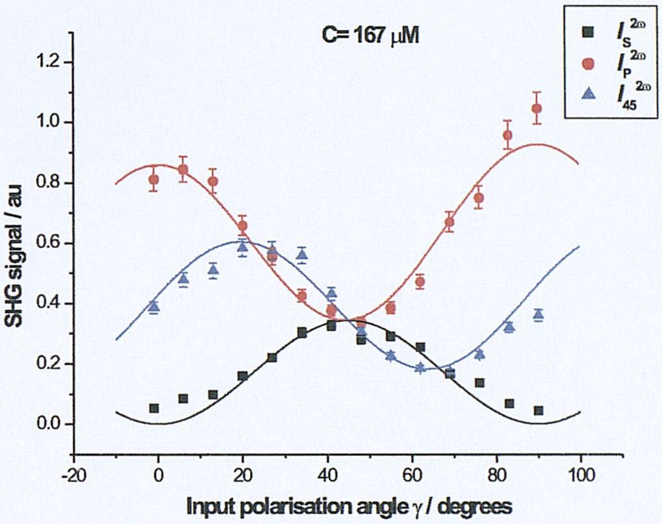

Figure 7.11: The polarisation dependence (data set 2) of the SHG signal generated in the S, P and +45^o linear polarisation planes as a function of the input polarisation angle (γ), for a 167 μM R6G aqueous solution. The solid lines have been estimated by the simultaneous fitting of the Euler parametrization of A, B, and C parameters in the S, P and +45^o SHG data assuming A to be real and B and C to be complex. λ=532/266 nm. Error bars are ± 5%.

C/μM	0.1	1	167
$\mid \chi^{(2)\prime}_{ZZZ} \mid$	1.8	2.3	1.95
$\mid \chi^{(2)\prime}_{ZXX} \mid$	0.5	1.07	3.72
$\mid \chi^{(2)\prime}_{XZX} \mid$	1.26	1.53	1.65
$\mid \chi^{(2)\prime}_{ZXX}/\chi^{(2)\prime}_{ZZZ} \mid$	0.28	0.47	1.91
$\mid \chi^{(2)\prime}_{XZX}/\chi^{(2)\prime}_{ZZZ} \mid$	0.7	0.67	0.85
$\mid \chi^{(2)\prime}_{ZXX}/\chi^{(2)\prime}_{XZX} \mid$	0.4	0.7	2.25

Table 7.2: The absolute effective χ tensors and their ratios. Errors for the χ ratios are ± 10 %.

7.3.4 $\vec{\chi}^{(2)}$ Calculation

From SHG measurements with azimuthal isotropy the three nonzero tensor elements ($\chi^{(2)}_{ZZZ}$, $\chi^{(2)}_{ZXX}$ and $\chi^{(2)}_{XZX}$) can be obtained subject to assumptions made about the value of the interfacial refractive index [37]. Because the values of the non-linear susceptibility elements depend on the value of the interfacial refractive index they can be calculated separately as a function of the refractive index of the interface [39]. These effective tensor elements are related to the interfacial refractive index via the equations:

$$\chi^{(2)\prime}_{ZZZ} = \frac{\chi^{(2)}_{ZZZ}}{n_3(\omega)^4 n_3(2\omega)^2} \tag{7.1}$$

$$\chi^{(2)\prime}_{ZXX} = \frac{\chi^{(2)}_{ZXX}}{n_3(2\omega)^2} \tag{7.2}$$

$$\chi^{(2)\prime}_{XZX} = \frac{\chi^{(2)}_{XZX}}{n_3(\omega)^2} \tag{7.3}$$

where $n_3(\omega)$ and $n_3(2\omega)$ are the refractive indices (complex) of the interfacial layer at the fundamental and harmonic wavelengths respectively.

The R6G molecule absorbs strongly at both the fundamental and the harmonic frequencies. The values of both the refractive indices $n_3(\omega)$ and $n_3(2\omega)$ will be complex and any orientational molecular information will depend on the choice of the values for the refractive indices. In this study only the effective tensor components are calculated and their ratios are compared with each other at different concentrations. The value of the refractive index for the interfacial R6G layer is unknown at the harmonic wavelength. The effective tensor components have been obtained by setting the interfacial refractive indices to one at both the fundamental and the harmonic wavelengths and assuming no absorption. The refractive index value of air and the liquid bulk phase was set to one and 1.334 (low concentrations) for both wavelengths assuming no dispersion. The results obtained for the effective $\chi^{(2)}$ tensors and their ratios are shown in Table 7.2.

The values of the $\chi^{(2)}$ ratios show distinct differences across the three concen-

Dye	C/μM	$\chi^{(2)}_{ZXX}/\chi^{(2)}_{ZZZ}$	$\chi^{(2)}_{ZXX}/\chi^{(2)}_{XZX}$
Nile Blue	50-200	7.14	5.00
oxazine 720	50-200	3.03	3.23
cresyl violet	50-200	2.33	3.33
R6G (this work)	167	1.91	2.25

Table 7.3: Comparison of χ ratios from reference [144] and from this work at high R6G dye bulk concentration.

trations and can be attributed to a definite change in the non-linear susceptibility of the surface. The errors in the estimated values are based on the confidence intervals of the B/A and C/A ratios shown in Table 7.1. The ratio increase of $\mid \chi^{(2)\prime}_{ZXX}/\chi^{(2)\prime}_{ZZZ} \mid$ across the concentrations reveal a definite increase of the value of $\chi^{(2)\prime}_{ZXX}$ with respect to the other tensor components. Previous SHG studies from Oxazine dyes at the air/water interface [144] did not detect the presence of monomers at the surface and their results originate solely from the aggregate dimers presence. Their determined χ ratios are indicative of the presence of dimer structure in the interface and compare favorable with the present R6G results at high concentration, Table 7.3

7.3.5 Molecular Orientation

The structure of the R6G molecule (Figure 7.1) can be approximated to C_{2v} symmetry. The χ ratio tensor results suggest that more than one β molecular tensors are significant because they depart significantly from Kleinman symmetry [166]. Earlier studies for similar planar aromatic dyes have assumed the β_{zxx} and β_{xzx} hyperpolarisability tensors to be significant [36,149,159,167]. This is to be expected since the two low lying electronic transition dipole moments ($S_0 \rightarrow S_1$ and $S_0 \rightarrow S_2$) lie in the plane (xz) of the molecule. Complementary *ab initio* calculations of the hyperpolarisabilities of the R6G molecule would be advantageous in predicting the significant contributing tensors [168].

A schematic representation of the R6G monomer orientation at the surface of water is shown in Figure 7.12 and in Figure 7.13 the potential orientation of two monomers at the surface upon the formation of the monolayer is depicted.

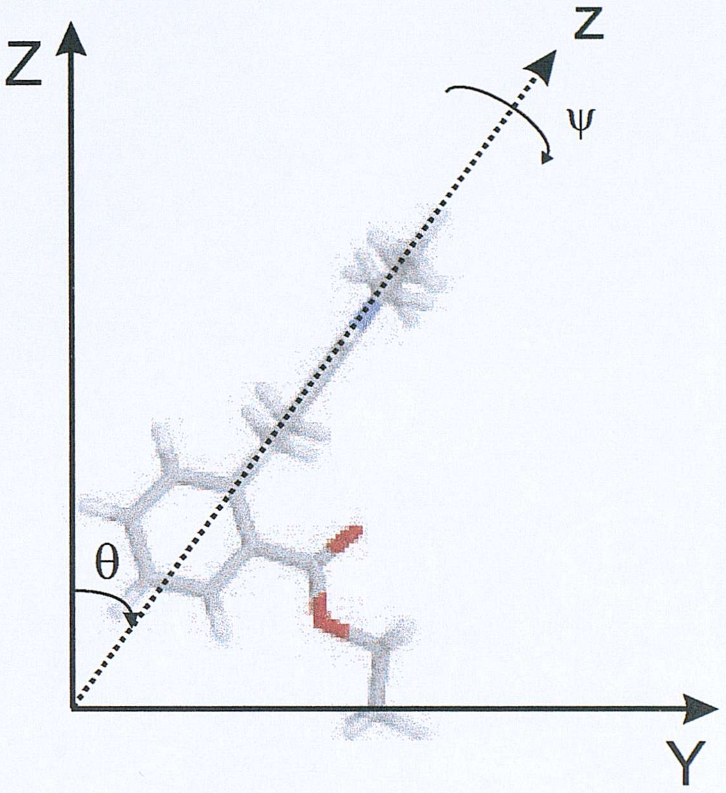

Figure 7.12: Schematic presentation of the R6G molecule orientation at the air/water interface with respect to the laboratory plane (YZ). The Euler angles (θ and ψ) are shown. The angle θ, is the angle between the main molecular axis z and the interface normal (laboratory axis Z). The angle ψ is defined as the angle of rotation around the molecular axis (z). The angle ϕ, has a uniform distribution because the surface is isotropic. The R6G structure has been optimised at the HF/6-31G level of theory.

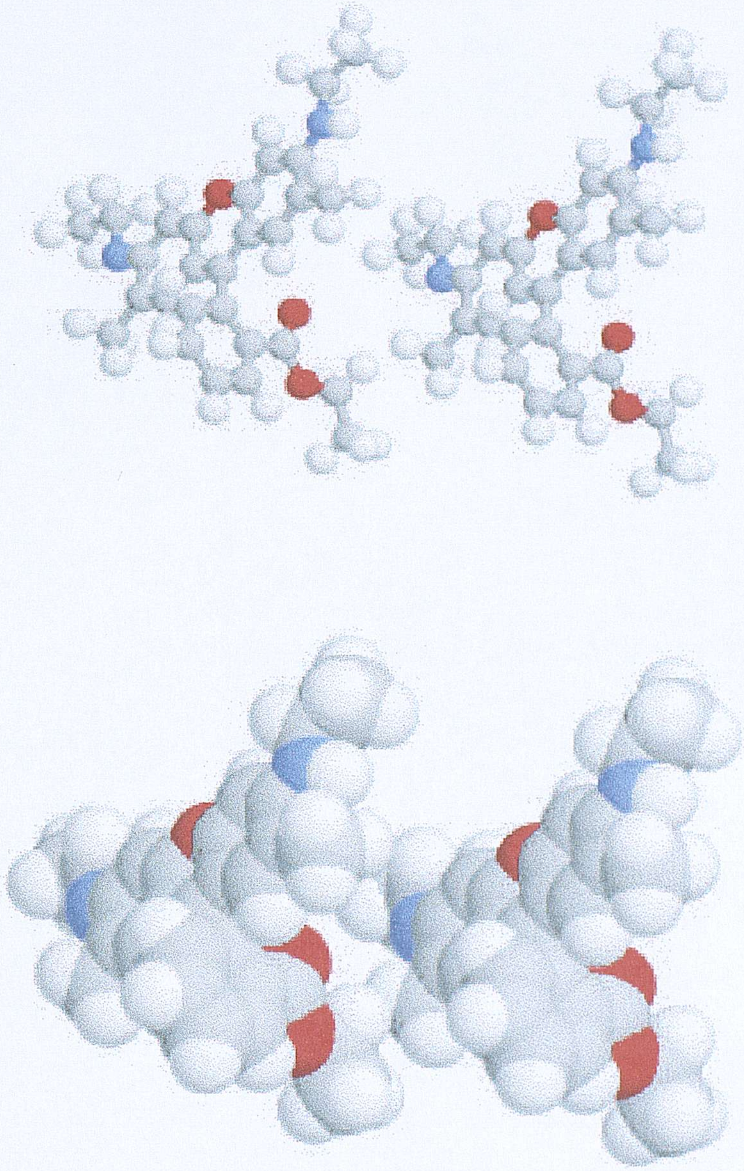

Figure 7.13: Schematic presentation of the potential arrangement of monomers at the air/water. Van der waals surfaces are shown.

7.3.6 Concentration Dependence

The dependence of the SHG signal intensity with the bulk R6G dye concentration was measured in two independent experiments and the results are shown in Figures 7.14 and 7.15. The dependence of the S-polarised harmonic signal with an input polarisation angle γ of 45^o was measured for bulk dye concentrations up to 200 μM. The SHG signal intensities were then fitted to a Langmuir isotherm assuming different phase difference between the SHG signal generated from the air/water interface and the R6G molecule adsorbed at the surface. The form of this is given by [32]:

$$\Theta = \frac{kC}{(1+kC)} \tag{7.4}$$

$$\chi^{(2)} = S\Theta \tag{7.5}$$

where Θ is R6G surface coverage, S is a scale factor, C is the R6G bulk dye

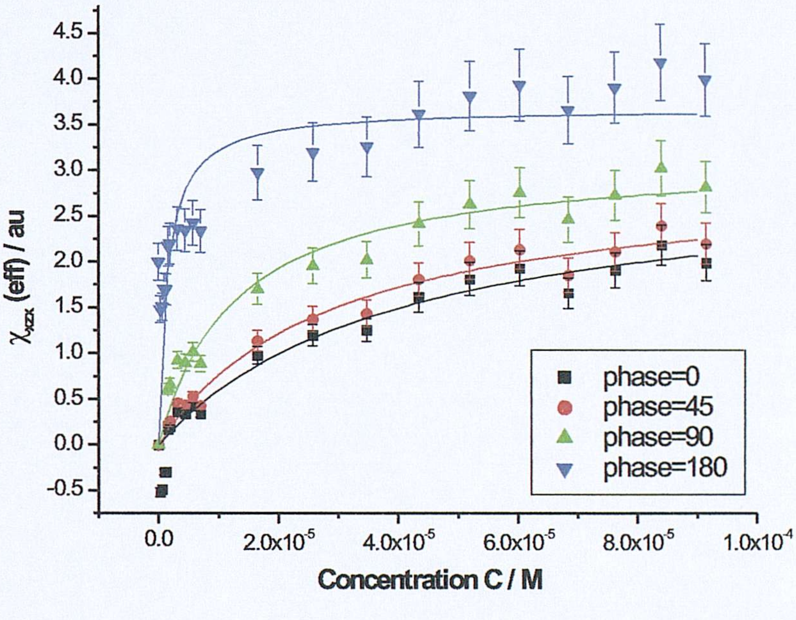

Figure 7.14: Langmuir isotherm measured for R6G (Exp1). The non-linear susceptibility χ_{eff} has been obtained from SHG intensities and is plotted as a function of the bulk concentration C of R6G for different assumptions about the phase difference between the R6G SHG signal and the water signal. The input polarisation angle γ was 45^o and the output harmonic was S. Error bars are ± 10%.

concentration and k is the surface adsorption equilibrium constant. Figures 7.14 and 7.15 show the dependence of the effective $\chi^{(2)}$ of the R6G molecule as determined according to equation 6.2. Because of the high SHG signals from the R6G molecule the SHG signal from the water interface can be ignored (phase=0^o) and

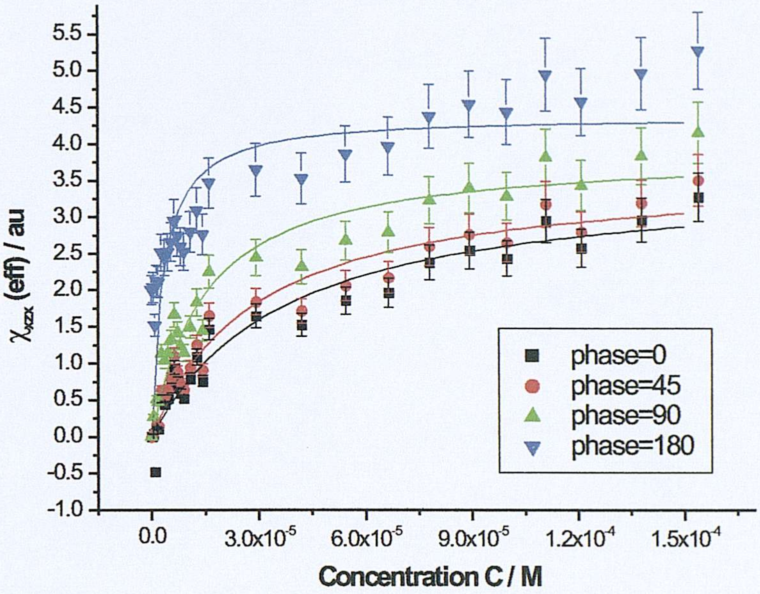

Figure 7.15: Langmuir isotherm measured for R6G (Exp2). The non-linear susceptibility χ_{eff} has been obtained from SHG intensities and is plotted as a function of the bulk concentration C of R6G for different assumptions about the phase difference between the R6G SHG signal and the water signal. The input polarisation angle γ was 45^o and the output harmonic was S. Error bars are ± 10%.

assumed insignificant. In that case a plot of the square root of the $I_{SHG}(2\omega)$ versus the bulk R6G concentration can be fitted to a Langmuir isotherm. Figure 7.16 shows a Langmuir fit to the combined SHG signal intensities from the two independent concentration dependence studies. The signal intensities have been normalised to the SHG signal of the bare air/water interface. The magnitude of the SHG signal depends on the number of molecules present on the surface, the molecular hyperpolarisability of the molecules and the averaged molecular orientation by which the molecules orient themselves at the surface. Changes in the SHG signal at high concentrations can reveal a change in the molecular orientation of the molecule. Figures 7.14-7.16 show a plateau at bulk concentrations of 75 μ M which can signify the formation of one monolayer of R6G molecules at the surface. The further increase of the SHG signal at higher bulk concentrations can be attributed to a change in the surface susceptibility $\chi^{(2)}$ of the surface and the onset of dimer aggregation.

The adsorption free energy can be determined from the Langmuir fitting and the values of the determined $\Delta G^{\ominus}_{\text{ads}}$ are shown in Table 7.4 for different assumptions about the phase between the SHG water signal and the R6G signal.

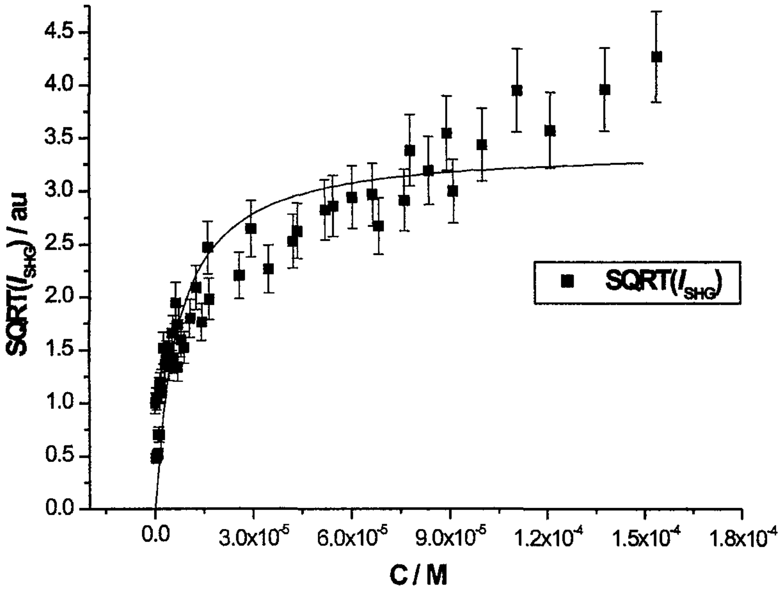

Figure 7.16: Langmuir isotherm measured for R6G (Expl+Exp2). The non-linear susceptibility ratio χ_{R6G}/χ_w has been obtained from SHG intensities and is plotted as a function of the bulk concentration C of R6G for different assumptions about the phase difference between the R6G SHG signal and the water signal. The input polarisation angle γ was 45^o and the output harmonic was S. Error bars are ± 10%.

	Expl		Exp2	
Phase, $\phi/^o$	$\Delta G^{\ominus}_{ads}$/kJ ·mol^{-1}	error	$\Delta G^{\ominus}_{ads}$/kJ ·mol^{-1}	error
0	-34.7	-13.3	-34.8	-6.5
45	-35.5	-5.8	-35.4	-5.7
90	-37.5	-6.2	-37.1	-5.5
180	-42.9	-13.1	-40.9	-10.9

Table 7.4: Adsorption free energy obtained to the optimised Langmuir fit of concentration dependence of the SHG signal of R6G for the two independent experiments. The phase difference ϕ between the SHG signal from the R6G molecules and the SHG signal from the bare air/water interface has been assumed to take different values.

7.4 Conclusions and Future Work

The adsorption characteristics and polarisation dependence of the SHG signal were carried out for the R6G molecule at the air/water interface. The polarisation dependence study showed that the surface non-linear susceptibility changed at high bulk concentrations with the possible formation of dimers at the surface. Because the refractive index of the monolayer and the bulk at the second harmonic was not known only the effective $\vec{\chi}^{(2)}$ quantities could be determined. The expected quadratic relationship for the SHG and TPF signals with incident laser power was not measured and this might be due to geometric factors on the beam shape due to loose focusing of the laser beam at the surface. Further work is needed to understand the power dependence of the SHG and TPF signals at low and high bulk concentrations. Also successive monochromator scans at different bulk concentrations could reveal the formation of the aggregate dimers in the bulk by monitoring the maximum of the TPF signal.

The concentration dependence studies showed that the R6G adsorption can be adequately described by a Langmuir isotherm for concentrations up to 75 μM where the monomer monolayer is believed to be formed. The adsorption free energy was estimated to be ~ -35 kJ/mol depending on the assumption about the phase difference between the water and R6G SHG signals. At higher concentrations the SHG signal was found to increase further indicating the possible formation of dimer structure. Further SHG studies at higher concentrations would reveal the dimer formation and determine the adsorption free energy.

Chapter 8

Conclusions

This second harmonic generation study at the air/toluene interface has shown that it is possible to probe the neat air/solvent interface even in the presence of strong two photon fluorescence. The non-linear fitting model developed has been used to allow the simultaneously determination of the parameters, A, B and C of the phenomological model with correct error estimation [44]. The polarisation dependence of the SHG signal revealed the preferred orientation of the toluene molecules at the interface. The molecules are not lying flat at the interface and the molecular plane is oriented at an angle of 35° to the surface normal. This orientational angle of the molecules at the interface signifies the balance between van der Waals bonding and the minimisation of the surface density. Previous SHG studies at the air/alcohol interface [87] revealed that harmonic signal generation could be explained if both the local electric dipole and the non local electric quadrupole contributions were taken into account and that the SHG signal amplitude was mostly due to non-local contributions. In the case of the air/toluene interface the SHG signal is resonance enhanced and the analysis of the results ignored any non local contributions and assumed that the electric dipole was the sole contribution to the harmonic response.

The toluene molecule was used as a benchmark in order to perform calculations and a broad range of currently available computational packages and approximate methods were employed. The calculation of geometries, harmonic frequencies and excitation energies was reliable and accurate when compared to experiment, with the DFT methods being more efficient. The static and frequency dependent hyperpolarisabilities were computed with current *ab initio* methods. The calculations proved that reliable estimation of the molecular hyperpolarisabilities required the use of extended basis sets with added diffuse functions and DFT exchange correlation functionals with the correct asymptotic behaviour (i.e. LB94). The experimental resonance enhancement of the SHG signal, because of the aromatic $\pi \longrightarrow \pi^*$ transition, was demonstrated in the frequency calculation of the hyperpolarisability tensor components and the significant molecular hyperpolarisability tensor components were estimated (β_{zzz}, β_{xzx} and β_{zxx}) and used for the analysis of the SHG results. The computed dominant hyperpolarisability tensor component ratios were used to compare with the corresponding experimentally determined values. The absence of solvent molecules in the model used in the calculations makes it difficult to make comparison with experimental values, but the correct phase was computed for the dominant hyperpolarisability tensor component ratios with respect to the experimental ones. Based on the toluene hyperpolarisability study, it is possible to select the correct approximate computational method for simple aromatic organic molecules and to obtain reliable static and dynamic hyperpolarisability tensor values.

The amino acid phenylalanine (Phe) was studied at the air/water interface using the SHG technique. Polarization dependence measurements of the harmonic signal revealed that the orientation of the molecule remains largely the same for bulk concentrations up to 0.08 M. The orientation of the molecule at the interface may be approximated within the weak field limit [39] and the estimated orientational angle is close to the SHG magic angle [29]. The SHG signal is resonanced enhanced because of the $\pi \rightarrow \pi^*$ transition but the intensity of the signal is only 1.5 times larger than the SHG signal from the bare air/water interface. This contribution to the SHG signal from the water molecules was taken into account and the two sources of harmonic contribution were separated. The newly determined orientational angle was similar to the previous value where the water contribution was not resolved. The adsorption of the Phe molecule at the air/water interface was studied and the free energy of adsorption was obtained using a Langmuir model.

The computational studies enabled the dominant hyperpolarisability tensor components to be determined at the static case and at 532 nm, and used in the SHG analysis of the results. The hyperpolarisability tensor components that get enhanced show possible contributions from higher transition dipole moments involving both the L_a and L_b transitions. The calculated static and frequency dependent hyperpolarisability at different levels of theory showed a significant dependence on the conformational change in the amino acid chain.

The calculation of frequency dependent hyperpolarisabilities is not that well established and further work is needed. Nevertheless, calculated values have been very helpful in the prediction of the significant hyperpolarisability tensors during resonant enhancement. The phenylalanine and toluene molecules both contain the benzene chromophore responsible for the resonant enhancement observed. The experimentally determined hyperpolarisability ratios for these molecules are similar in value although their orientation behaviour at the air/liquid interface is quite different. Future calculations on the hyperpolarisability of molecules could involve the effect of solvent by explicitly adding solvent molecules and the inclusion of vibrational and rotational contributions to the estimation of the hyperpolarisability.

Preliminary studies on the Rhodamine 6G (R6G) molecule at the air/water interface have shown that R6G forms aggregate dimers at the water surface at bulk concentrations ($> 10^{-4}$ M) and that it is possible to probe the monomer-dimer transition via a polarisation analysis of the SHG signal. The R6G molecule adsorbs at the air/water interface and the adsorption process can be described using a simple Langmuir model for bulk R6G concentrations up to 5×10^{-5} M where the dimer formation is believed to begin. The SHG signal increased further for higher concentrations and the Langmuir model was not appropriate to describe the second adsorption process. This is believed to be due to the onset of dimer formation at the water surface and future work is needed to investigate the transition from monomer to dimer and aggregate formation.

Chapter 9

Appendices

9.1 Appendix A1

The measured macroscopic quantity $\vec{\chi}^{(2)}$ is related to the molecular hyperpolarisability by:

$$\chi_{IJK} = N_s \sum < \mathrm{T}(\varphi, \theta, \psi) > \beta_{ijk} \tag{9.1}$$

where N_s is the surface number density of molecules, **T** is the transformation matrix which relates the hyperpolarisability in the laboratory coordinate system (*I*,*J*,*K*) and surface molecular coordinate system (*i*,*j*,*k*), and the brackets indicate an average over all molecules.

An isotropic surface possess azimuthal symmetry and ϕ has a random or uniform distribution, only two Euler angles remain so that $f(\phi,\theta,\psi)=(\theta,\psi)$. The molecular hyperpolarisability tensors that remain after the isotropic averaging are: β_{zzz}, β_{zxx}, β_{xzx}, β_{zyy}, β_{yzy}, with $\beta_{ijk}=\beta_{ikj}$ because SHG process uses two photons of the same energy. The following equations apply for the β_{zzz}, β_{zxx}, and β_{xzx} molecular tensors but the results apply the same to the other two tensors if you substitute $\beta_{zxx}=\beta_{zyy}$ and $\beta_{xzx}=\beta_{yzy}$. The general formula for the non-linear susceptibilities $\chi^{(2)}_{ZZZ}$, $\chi^{(2)}_{ZXX}$ and $\chi^{(2)}_{XZX}$ are:

$$\chi^{(2)}_{ZZZ} = \frac{N_s}{\epsilon_o}[< \cos^3\theta > \beta_{zzz} + < \sin^2\psi \cos\theta \sin^2\theta > (\beta_{zxx} + 2\beta_{xzx})] \tag{9.2}$$

$$\chi^{(2)}_{ZXX} = \frac{N_s}{2\epsilon_o}[< \sin^2\theta \cos\theta > \beta_{zzz} - < \sin^2\psi \cos\theta \sin^2\theta > (\beta_{zxx} + 2\beta_{xzx}) + \\ + < \cos\theta > \beta_{zxx}] \tag{9.3}$$

$$\chi^{(2)}_{XZX} = \frac{N_s}{2\epsilon_o}[< \sin^2\theta \cos\theta > \beta_{zzz} - < \sin^2\psi \cos\theta \sin^2\theta > (\beta_{zxx} + 2\beta_{xzx}) + \\ + < \cos\theta > \beta_{xzx}] \tag{9.4}$$

The <> indicate averaging over all molecules present at the interface. The above equations are used for the determination of the molecular orientation parameters.

The SHG intensities that we record depend on the polarisation angle γ of the input fundamental laser beam and the output polarisation angle Γ of the harmonic beam. The Fresnel coefficients a_1-a_5 depend on the geometry of the experiment and the sample we study and in general they can be calculated. The general equation for the detected harmonic signal intensity has the form:

$$\begin{aligned} I_{\Gamma}^{(2\omega)} \propto |(a_1\chi^{(2)}_{XZX}\sin 2\gamma)\sin\Gamma + [(a_2\chi^{(2)}_{XZX} + a_3\chi^{(2)}_{ZXX} + a_4\chi^{(2)}_{ZZZ})\cos^2\gamma + \\ + a_5\chi^{(2)}_{ZXX}\sin^2\gamma]\cos\Gamma|^2 I^2(\omega) \end{aligned} \tag{9.5}$$

The following cases can be assumed about the dominant hyperpolarisability tensors responsible for the second harmonic generation signal and the molecular orientational parameters D and R are shown for each case. The <> averaging has been omitted.

- β_{zzz} dominant

$$\chi^{(2)}_{ZZZ} = N_s cos^3\theta\beta_{zzz} \tag{9.6}$$

$$\chi^{(2)}_{ZXX} = \chi^{(2)}_{XZX} = \frac{1}{2}N_s\sin^2\theta\cos\theta\beta_{zzz} \tag{9.7}$$

$$D = \frac{\chi^{(2)}_{ZZZ}}{\chi^{(2)}_{ZZZ} + 2\chi^{(2)}_{ZXX}} \tag{9.8}$$

- β_{zxx} dominant
  ψ=random

$$\chi^{(2)}_{ZZZ} = \frac{N_s}{2\epsilon_o}\cos\theta\sin^2\theta\beta_{zxx} \tag{9.9}$$

$$\chi^{(2)}_{ZXX} = \frac{N_s}{4\epsilon_o}(\cos\theta\beta_{zxx} + \cos^3\theta\beta_{zxx}) \tag{9.10}$$

$$\chi^{(2)}_{XZX} = -\frac{N_s}{4\epsilon_o}\cos\theta\sin^2\theta\beta_{zxx} \tag{9.11}$$

$$D = \frac{2\chi^{(2)}_{ZXX} - \chi^{(2)}_{ZZZ}}{2\chi^{(2)}_{ZXX} + \chi^{(2)}_{ZZZ}} \tag{9.12}$$

ψ=90^o

$$\chi^{(2)}_{ZZZ} = \frac{N_s}{\epsilon_o}\cos\theta\sin^2\theta\beta_{zxx} \tag{9.13}$$

$$\chi^{(2)}_{ZXX} = \frac{N_s}{2\epsilon_o}\cos^3\theta\beta_{zxx} \tag{9.14}$$

$$\chi^{(2)}_{XZX} = -\frac{N_s}{2\epsilon_o}\cos\theta\sin^2\theta\beta_{zxx} \tag{9.15}$$

$$D = \frac{2\chi^{(2)}_{ZXX}}{2\chi^{(2)}_{ZXX} + \chi^{(2)}_{ZZZ}} \tag{9.16}$$

- β_{xzx} dominant
  ψ=random

$$\chi^{(2)}_{ZZZ} = \frac{N_s}{\epsilon_o}\cos\theta\sin^2\theta\beta_{xzx} \tag{9.17}$$

$$\chi^{(2)}_{ZXX} = -\frac{N_s}{2\epsilon_o}\cos\theta\sin^2\theta\beta_{xzx} \tag{9.18}$$

$$\chi^{(2)}_{XZX} = \frac{N_s}{2\epsilon_o}\cos^3\theta\beta_{xzx} \tag{9.19}$$

$$D = \frac{\chi^{(2)}_{XZX}}{\chi^{(2)}_{XZX} - \chi^{(2)}_{ZXX}} \tag{9.20}$$

ψ=90^o

$$\chi^{(2)}_{ZZZ} = \frac{2N_s}{\epsilon_o}\cos\theta\sin^2\theta\beta_{xzx} \tag{9.21}$$

$$\chi^{(2)}_{ZXX} = -\frac{N_s}{\epsilon_o}\cos\theta\sin^2\theta\beta_{xzx} \tag{9.22}$$

$$\chi^{(2)}_{XZX} = -\frac{N_s}{\epsilon_o}(\cos\theta\sin^2\theta\beta_{xzx} + \cos\theta\beta_{xzx}) \tag{9.23}$$

$$D = \frac{2\chi^{(2)}_{XZX} - \chi^{(2)}_{ZXX}}{2(\chi^{(2)}_{XZX} - \chi^{(2)}_{ZXX})} \tag{9.24}$$

- β_{zzz} and β_{zxx} dominant

$$R = \frac{\beta_{zzz}}{\beta_{zxx}} = \frac{\chi^{(2)}_{ZZZ} + 2\chi^{(2)}_{XZX}}{2(\chi^{(2)}_{ZXX} - \chi^{(2)}_{XZX})} \tag{9.25}$$

ψ=random

$$\chi^{(2)}_{ZZZ} = \frac{N_s}{\epsilon_o}(\frac{1}{2}\cos\theta\sin^2\theta\beta_{zxx} + \cos^3\theta\beta_{zzz}) \tag{9.26}$$

$$\chi^{(2)}_{ZXX} = \frac{N_s}{\epsilon_o}\{\frac{1}{4}(\cos\theta + \cos^3\theta)\beta_{zxx} + \frac{1}{2}\cos\theta\sin^2\theta\beta_{zzz}\} \tag{9.27}$$

$$\chi^{(2)}_{ZXX} = \frac{N_s}{\epsilon_o}(-\frac{1}{4}\cos\theta\sin^2\theta\beta_{zxx} + \frac{1}{2}\cos\theta\sin^2\theta\beta_{zzz}) \tag{9.28}$$

$$D = \frac{\chi^{(2)}_{ZZZ} - \chi^{(2)}_{ZXX} + \chi^{(2)}_{XZX}}{\chi^{(2)}_{ZZZ} - \chi^{(2)}_{ZXX} + 3\chi^{(2)}_{ZXX}} \tag{9.29}$$

ψ=90^o

$$\chi^{(2)}_{ZZZ} = \frac{N_s}{\epsilon_o}(\cos\theta\sin^2\theta\beta_{zxx} + \cos^3\theta\beta_{zzz}) \tag{9.30}$$

$$\chi^{(2)}_{ZXX} = \frac{N_s}{2\epsilon_o}(\cos\theta\beta_{zxx} - \cos\theta\sin^2\theta\beta_{zxx} + \cos\theta\sin^2\theta\beta_{zzz}) \tag{9.31}$$

$$\chi^{(2)}_{XZX} = \frac{N_s}{2\epsilon_o}(-\cos\theta\sin^2\theta\beta_{zxx} + \cos\theta\sin^2\theta\beta_{zzz}) \tag{9.32}$$

$$D = \frac{\chi^{(2)}_{ZZZ} - 2\chi^{(2)}_{ZXX} + 2\chi^{(2)}_{XZX}}{\chi^{(2)}_{ZZZ} - 2\chi^{(2)}_{ZXX} + 4\chi^{(2)}_{XZX}} \tag{9.33}$$

- β_{zzz} and β_{xzx} dominant

$$R = \frac{\beta_{zzz}}{\beta_{xzx}} = \frac{\chi^{(2)}_{ZZZ} + 2\chi^{(2)}_{ZXX}}{2(\chi^{(2)}_{XZX} - \chi^{(2)}_{ZXX})} \tag{9.34}$$

ψ=random

$$\chi^{(2)}_{ZZZ} = \frac{N_s}{\epsilon_o}(\cos\theta\sin^2\theta\beta_{xzx} + \cos^3\theta\beta_{zzz}) \tag{9.35}$$

$$\chi^{(2)}_{ZXX} = \frac{N_s}{2\epsilon_o}(-\cos\theta\sin^2\theta\beta_{xzx} + \cos\theta\sin^2\theta\beta_{zzz}) \tag{9.36}$$

$$\chi^{(2)}_{XZX} = \frac{N_s}{2\epsilon_o}(\cos^3\theta\beta_{xzx} + \cos\theta\sin^2\theta\beta_{zzz}) \tag{9.37}$$

$$D = \frac{\chi^{(2)}_{ZZZ} - 2\chi^{(2)}_{XZX} + 2\chi^{(2)}_{ZXX}}{\chi^{(2)}_{ZZZ} - 2\chi^{(2)}_{XZX} + 4\chi^{(2)}_{ZXX}} \tag{9.38}$$

ψ=90^o

$$\chi^{(2)}_{ZZZ} = \frac{N_s}{\epsilon_o}(2\cos\theta\sin^2\theta\beta_{xzx} + \cos^3\theta\beta_{zzz}) \tag{9.39}$$

$$\chi^{(2)}_{ZXX} = \frac{N_s}{\epsilon_o}(-\cos\theta\sin^2\theta\beta_{xzx} + \frac{1}{2}\cos\theta\sin^2\theta\beta_{zzz}) \tag{9.40}$$

$$\chi^{(2)}_{XZX} = \frac{N_s}{\epsilon_o}(\cos^3\theta\beta_{xzx} - \frac{1}{2}\cos\theta\beta_{xzx} + \frac{1}{2}\cos\theta\sin^2\theta\beta_{zzz}) \tag{9.41}$$

$$D = \frac{1/2\chi^{(2)}_{ZZZ} - 2\chi^{(2)}_{XZX} + 2\chi^{(2)}_{ZXX}}{1/2\chi^{(2)}_{ZZZ} - 2\chi^{(2)}_{XZX} + 3\chi^{(2)}_{ZXX}} \tag{9.42}$$

- β_{zxx} and β_{xzx} dominant

$$R = \frac{\beta_{zzz}}{\beta_{xzx}} = \frac{\chi^{(2)}_{ZZZ} + 2\chi^{(2)}_{ZXX}}{\chi^{(2)}_{ZZZ} + 2\chi^{(2)}_{XZX}} \tag{9.43}$$

ψ=random

$$\chi^{(2)}_{ZZZ} = \frac{N_s}{\epsilon_o}(\frac{1}{2}\cos\theta\sin^2\theta\beta_{zxx} + \cos\theta\sin^2\theta\beta_{xzx}) \tag{9.44}$$

$$\chi^{(2)}_{ZXX} = \frac{N_s}{\epsilon_o}\{\frac{1}{4}(\cos\theta + \cos^3\theta)\beta_{zxx} - \frac{1}{2}\cos\theta\sin^2\theta\beta_{xzx}\} \tag{9.45}$$

$$\chi^{(2)}_{XZX} = \frac{N_s}{\epsilon_o}(-\frac{1}{4}\cos\theta\sin^2\theta\beta_{zxx} + \frac{1}{2}\cos^3\theta\beta_{xzx}) \tag{9.46}$$

$$D = \frac{\chi^{(2)}_{ZZZ} + 4\chi^{(2)}_{XZX} + 2\chi^{(2)}_{ZXX}}{3\chi^{(2)}_{ZZZ} + 4\chi^{(2)}_{XZX} + 2\chi^{(2)}_{ZXX}} \tag{9.47}$$

ψ=90°

$$\chi^{(2)}_{ZZZ} = \frac{N_s}{\epsilon_o}(\cos\theta\sin^2\theta\beta_{zxx} + 2\cos\theta\sin^2\theta\beta_{xzx}) \tag{9.48}$$

$$\chi^{(2)}_{ZXX} = \frac{N_s}{\epsilon_o}(\frac{1}{2}\cos^3\theta\beta_{zxx} - \cos\theta\sin^2\theta\beta_{xzx}) \tag{9.49}$$

$$\chi^{(2)}_{XZX} = \frac{N_s}{\epsilon_o}(-\frac{1}{2}\cos\theta\sin^2\theta\beta_{zxx} + \cos^3\theta\beta_{xzx} - \frac{1}{2}\cos\theta\beta_{xzx}) \tag{9.50}$$

$$D = \frac{-\chi^{(2)}_{ZZZ} + 2\chi^{(2)}_{XZX} + \chi^{(2)}_{ZXX}}{2\chi^{(2)}_{XZX} + \chi^{(2)}_{ZXX}} \tag{9.51}$$

9.2 Appendix A2

In this section the theoretical $\vec{\chi}^{(2)}$ tensors and their ratios are plotted versus the molecular tilt angle θ (0-180^o) for different cases about the dominant hyperpolarisability tensor components. The predicted SHG polarisation curves for the S and P output harmonic wavelengths are shown for different tilt molecular angles as a function of the input polarisation angle γ.

9.2.1 β_{zzz} dominant

Equations 9.6 and 9.7 were used to calculate the $\vec{\chi}^{(2)}$ tensor values and ratios using the estimated Fresnel coefficients for the air/water interface and assuming no absorption from the interfacial molecules at the fundamental or harmonic wavelength. The hyperpolarisability tensor value β_{zzz} was set to 100 and N_s/ϵ_o was set to one.

9.2.1.1 $\vec{\chi}^{(2)}$ tensor values and ratios

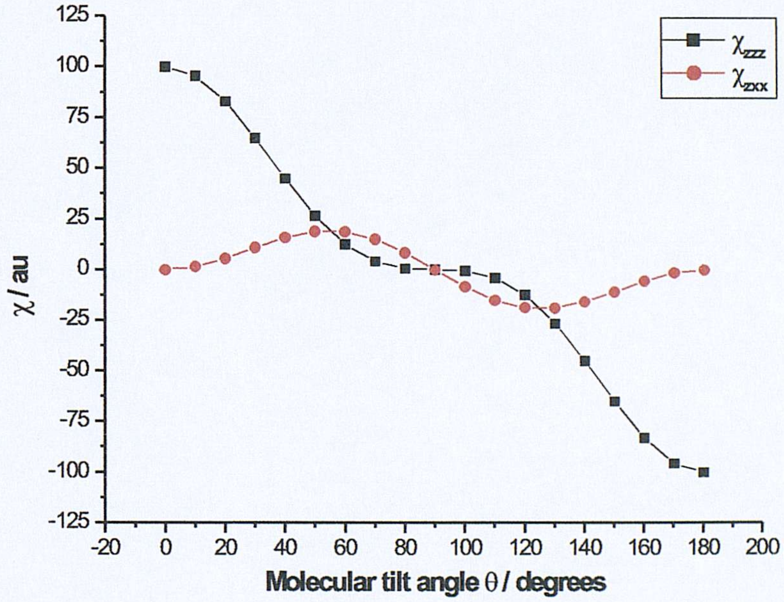

Figure 9.1: The $\vec{\chi}^{(2)}$ tensor components ($\chi^{(2)}_{ZZZ}$ and $\chi^{(2)}_{ZXX} = \chi^{(2)}_{XZX}$) as a function of the molecular tilt angle θ assuming the β_{zzz} tensor is dominant.

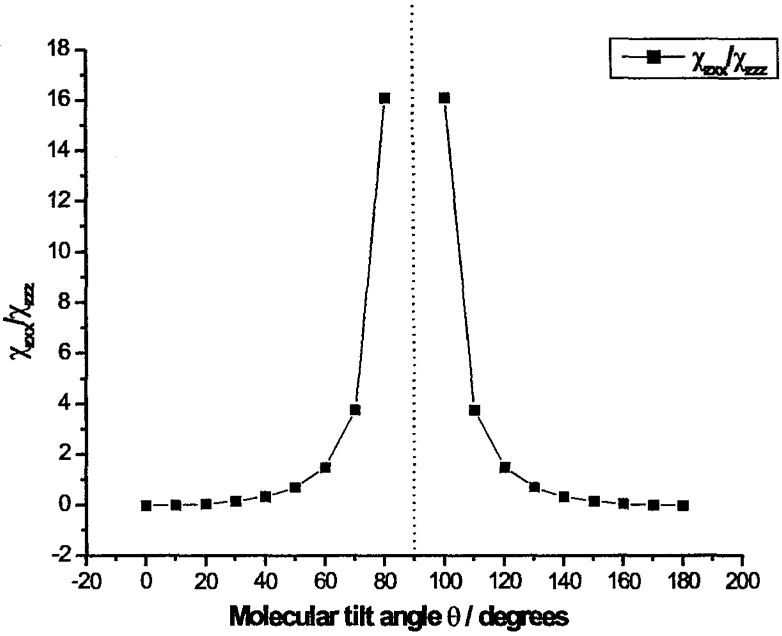

Figure 9.2: The $\vec{\chi}^{(2)}$ tensor ratio $(\chi^{(2)}_{ZXX}/\chi^{(2)}_{ZZZ})$ as a function of the tilt molecular angle θ assuming the β_{zzz} tensor is dominant.

9.2.1.2 P and S output SHG polarisation curves

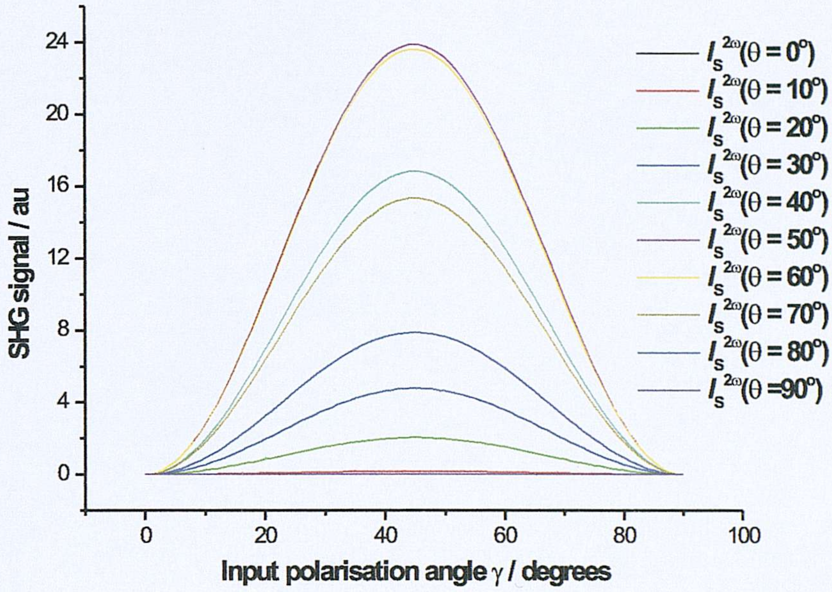

Figure 9.3: $I_{\mathrm{S}}^{(2\omega)}$ SHG intensities for different molecular tilt angles as a function of the input polarisation angle γ assuming the β_{zzz} tensor is dominant.

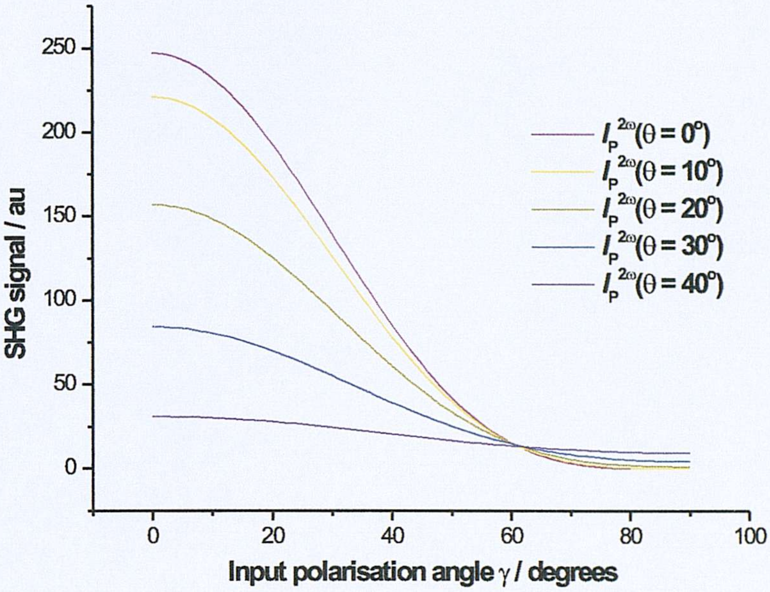

Figure 9.4: $I_{\mathrm{P}}^{(2\omega)}$ SHG intensities for different molecular tilt angles (0-40^o) as a function of the input polarisation angle γ assuming the β_{zzz} tensor is dominant.

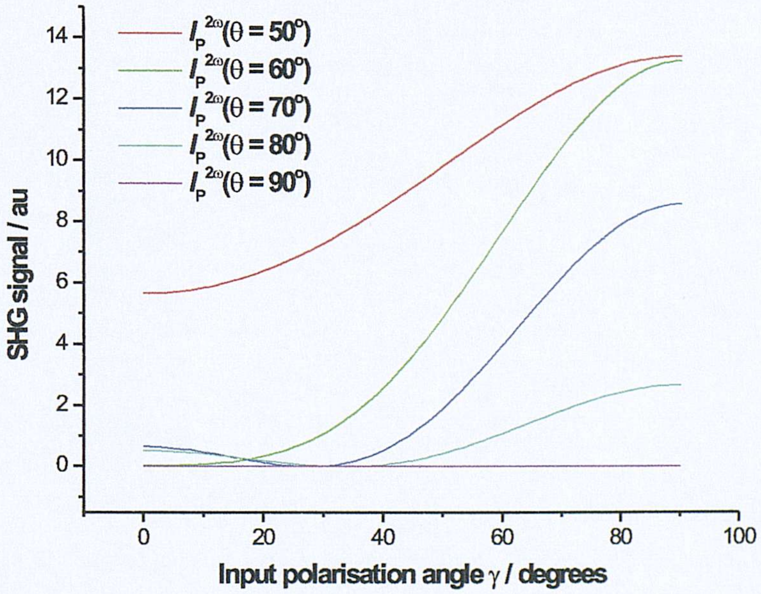

Figure 9.5: $I_{\mathrm{P}}^{(2\omega)}$ SHG intensities for different molecular tilt angles (50-90^o) as a function of the input polarisation angle γ assuming the β_{zzz} tensor is dominant.

9.2.2 β_{zxx} dominant

Equations 9.9-9.11 for a random distribution for the ψ angle were used to calculate the $\vec{\chi}^{(2)}$ tensor values and ratios using the estimated Fresnel coefficients for the air/water interface and assuming no absorption from the interfacial molecules at the fundamental or harmonic wavelength. The hyperpolarisability tensor value β_{zxx} was set to 100 and N_s/ϵ_o was set to one.

9.2.2.1 $\vec{\chi}^{(2)}$ tensor values and ratios

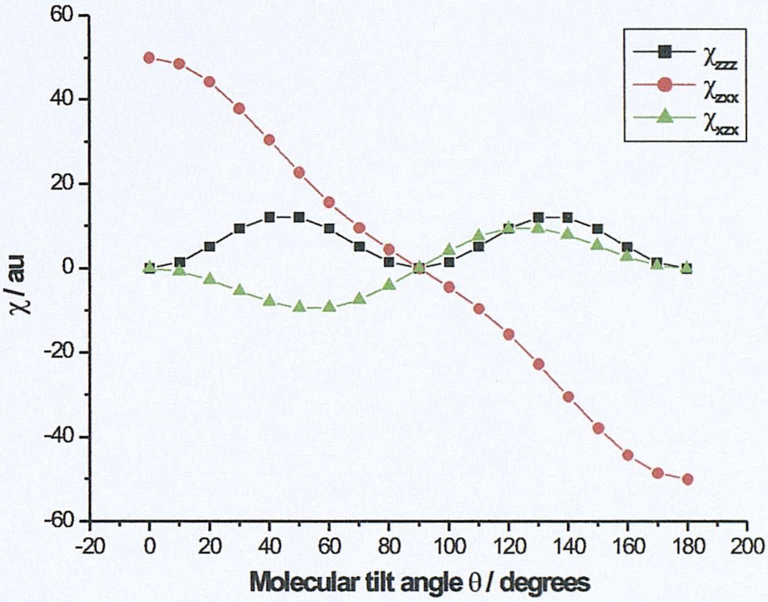

Figure 9.6: The $\vec{\chi}^{(2)}$ tensor components ($\chi^{(2)}_{ZXX}$, $\chi^{(2)}_{ZXX}$ and $\chi^{(2)}_{XZX}$) as a function of the molecular tilt angle θ assuming the β_{zxx} tensor is dominant.

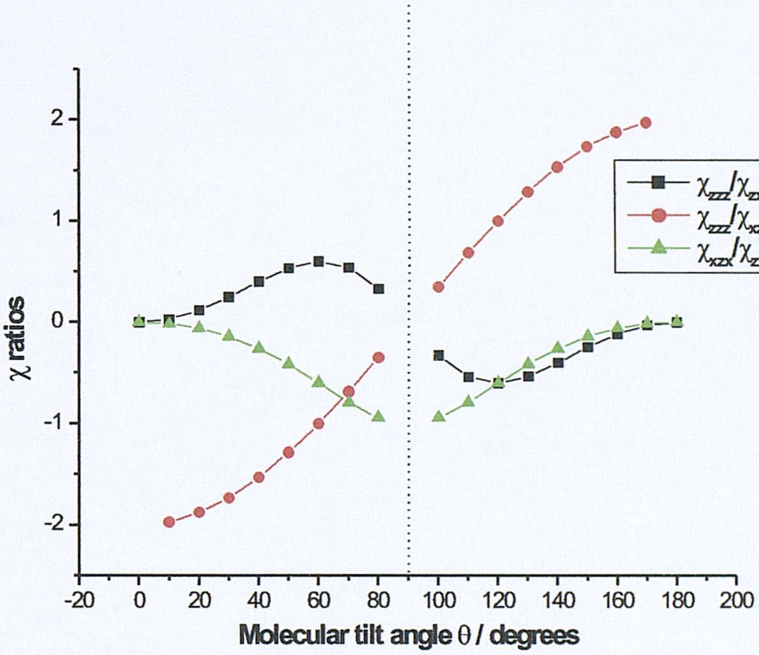

Figure 9.7: The $\vec{\chi}^{(2)}$ tensor ratios ($\chi^{(2)}_{ZZZ}/\chi^{(2)}_{ZXX}$, $\chi^{(2)}_{ZZZ}/\chi^{(2)}_{XZX}$ and $\chi^{(2)}_{XZX}/\chi^{(2)}_{ZXX}$) as a function of the tilt molecular angle θ assuming the β_{zzz} tensor is dominant.

9.2.2.2 P and S output SHG polarisation curves

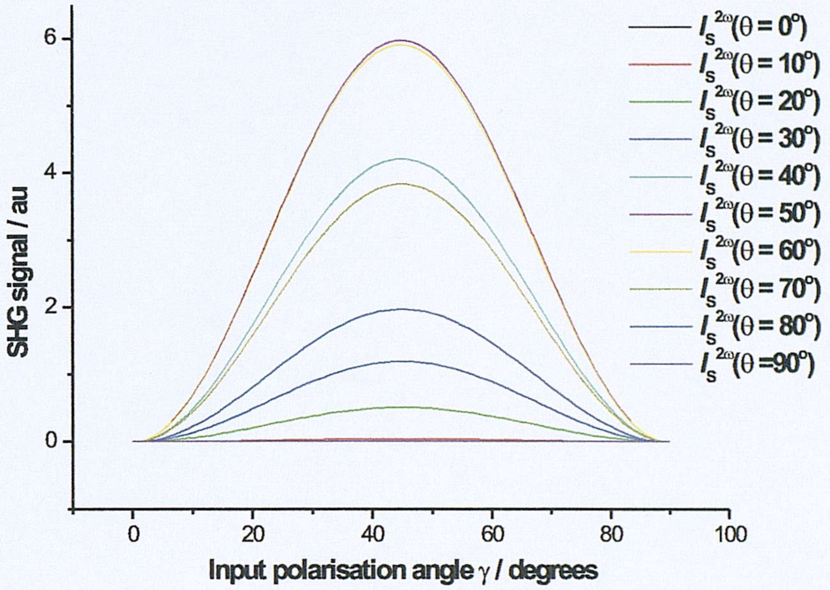

Figure 9.8: $I_S^{(2\omega)}$ SHG intensities for different molecular tilt angles as a function of the input polarisation angle γ assuming the β_{zxx} tensor is dominant.

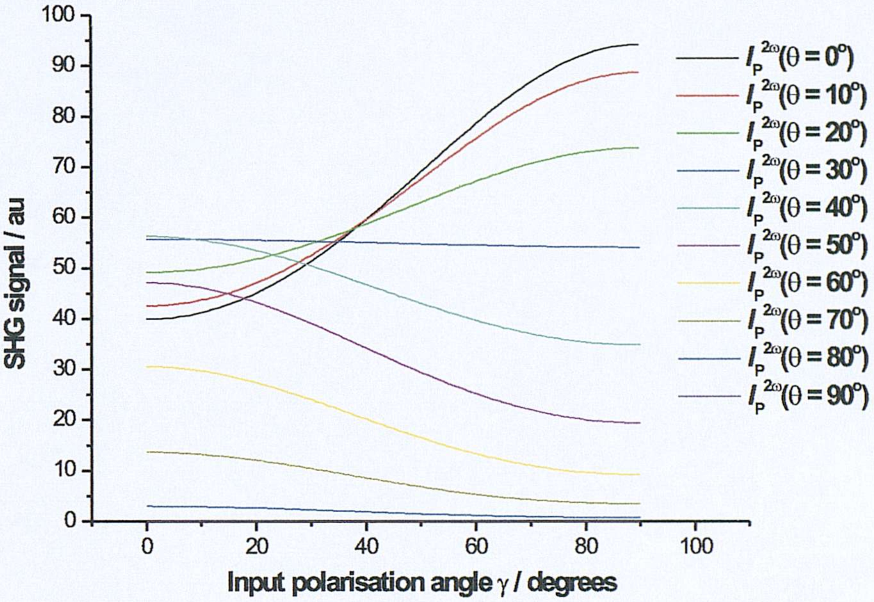

Figure 9.9: $I_{\rm P}^{(2\omega)}$ SHG intensities for different molecular tilt angles (0-90^o) as a function of the input polarisation angle γ assuming the β_{zxx} tensor is dominant.

9.2.3 β_{xzx} dominant

Equations 9.17-9.19 for a random distribution for the ψ angle were used to calculate the $\vec{\chi}^{(2)}$ tensor values and ratios using the estimated Fresnel coefficients for the air/water interface and assuming no absorption from the interfacial molecules at the fundamental or harmonic wavelength. The hyperpolarisability tensor value β_{xzx} was set to 100 and N_s/ϵ_o was set to one.

9.2.3.1 $\vec{\chi}^{(2)}$ tensor values and ratios

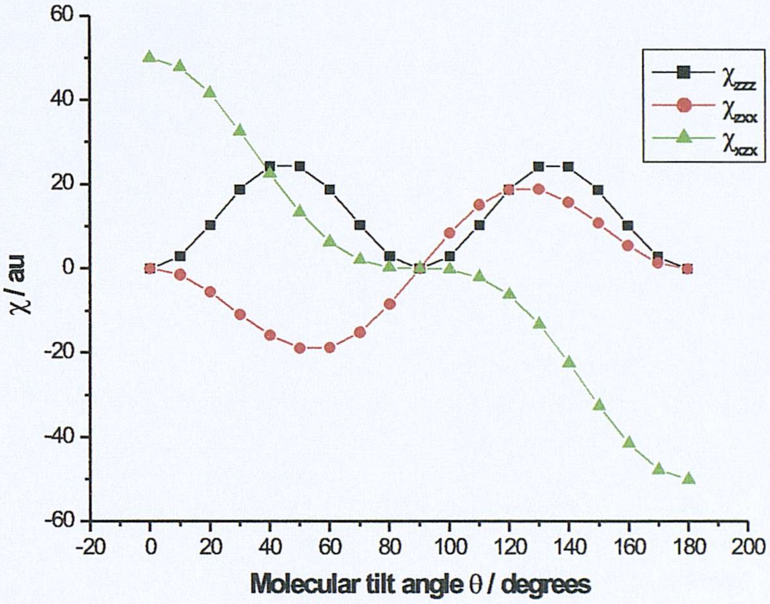

Figure 9.10: The $\vec{\chi}^{(2)}$ tensor components ($\chi^{(2)}_{ZZZ}$, $\chi^{(2)}_{ZXX}$ and $\chi^{(2)}_{XZX}$) as a function of the molecular tilt angle θ assuming the β_{xzx} tensor is dominant.

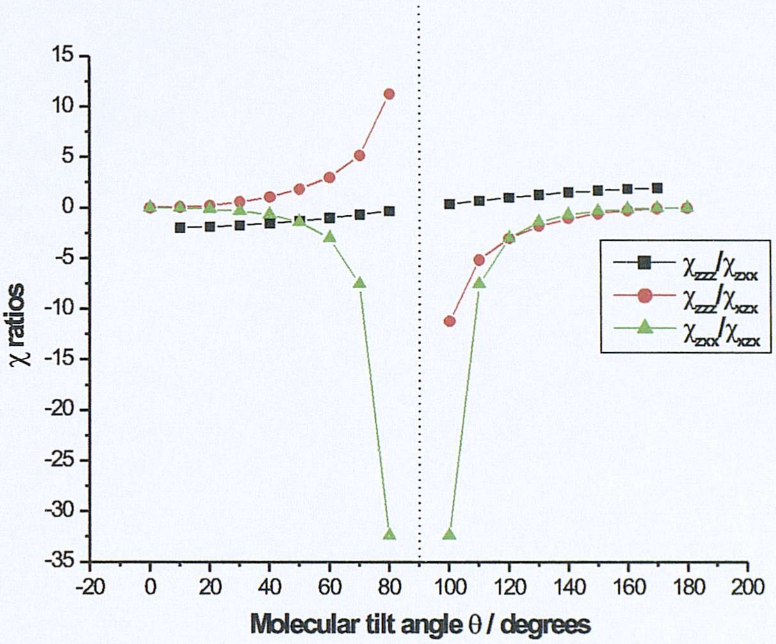

Figure 9.11: The $\vec{\chi}^{(2)}$ tensor ratio ($\chi^{(2)}_{ZZZ}/\chi^{(2)}_{ZXX}$, $\chi^{(2)}_{ZZZ}/\chi^{(2)}_{XZX}$ and $\chi^{(2)}_{ZXX}/\chi^{(2)}_{XZX}$) as a function of the tilt molecular angle θ assuming the β_{xzx} tensor is dominant.

9.2.3.2 P and S output SHG polarisation curves

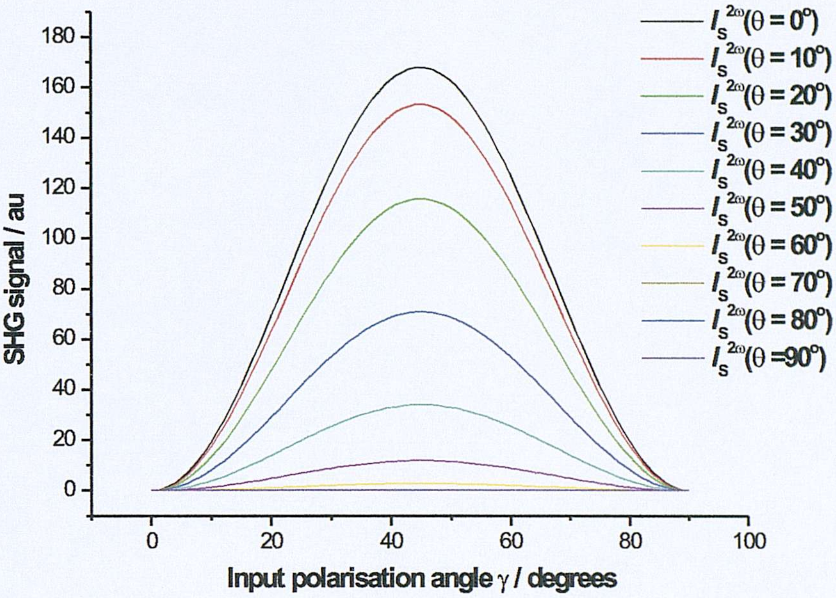

Figure 9.12: $I_{\mathrm{S}}^{(2\omega)}$ SHG intensities for different molecular tilt angles as a function of the input polarisation angle γ assuming the β_{xzx} tensor is dominant.

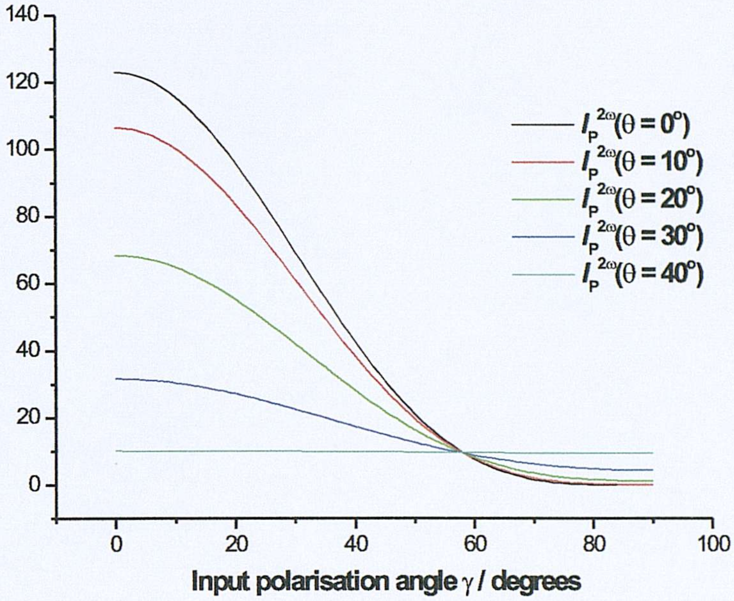

Figure 9.13: $I_P^{(2\omega)}$ SHG intensities for different molecular tilt angles (0-40^o) as a function of the input polarisation angle γ assuming the β_{xzx} tensor is dominant.

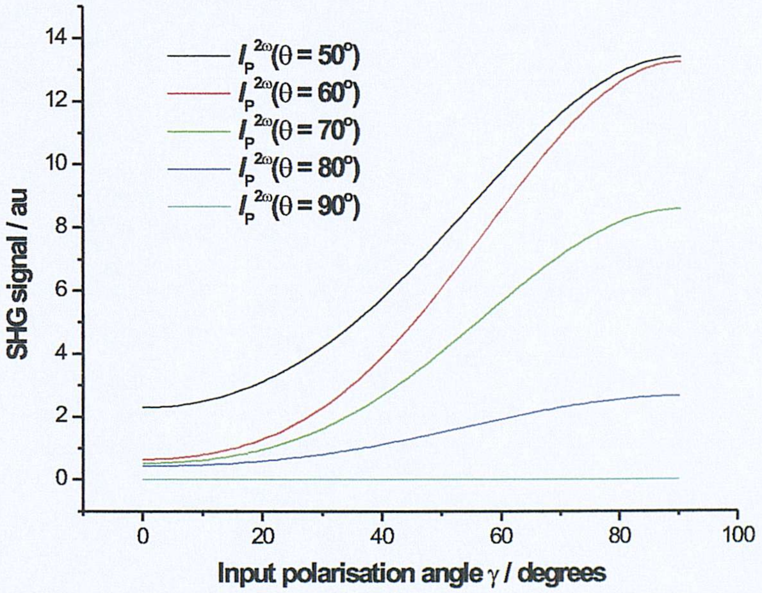

Figure 9.14: $I_P^{(2\omega)}$ SHG intensities for different molecular tilt angles (50-90^o) as a function of the input polarisation angle γ assuming the β_{xzx} tensor is dominant.

9.2.4 β_{zzz} and β_{zxx} dominant

Equations 9.26-9.28 for a random distribution for the ψ angle were used to calculate the $\vec{\chi}^{(2)}$ tensor values and ratios using the estimated Fresnel coefficients for the air/water interface and assuming no absorption from the interfacial molecules at the fundamental or harmonic wavelength. The hyperpolarisability tensor value for the ratio $\beta_{zxx}/bzzz$ was set to -0.20 and N_s/ϵ_o was set to one.

9.2.4.1 $\vec{\chi}^{(2)}$ tensor values and ratios

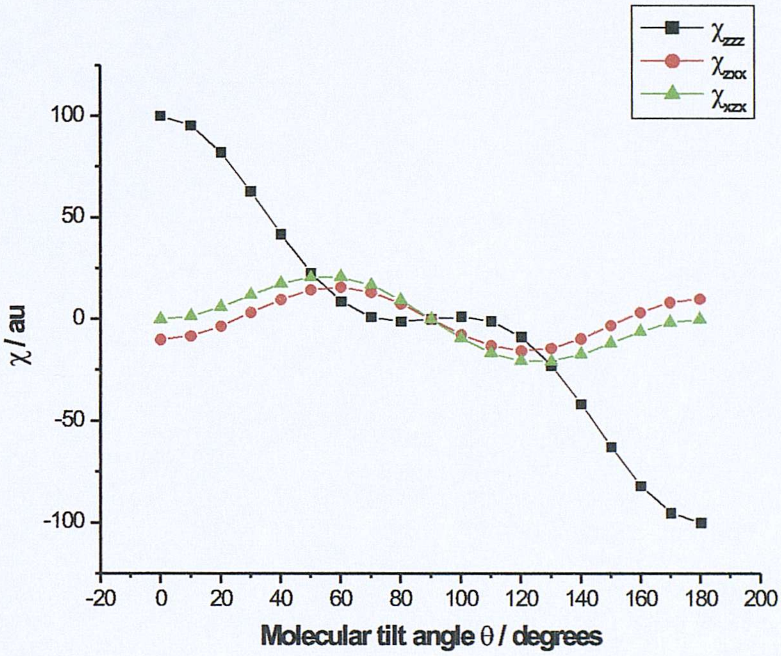

Figure 9.15: The $\vec{\chi}^{(2)}$ tensor components ($\chi^{(2)}_{ZZZ}$, $\chi^{(2)}_{ZXX}$ and $\chi^{(2)}_{XZX}$) as a function of the molecular tilt angle θ assuming the β_{zzz} and β_{zxx} tensors to be dominant.

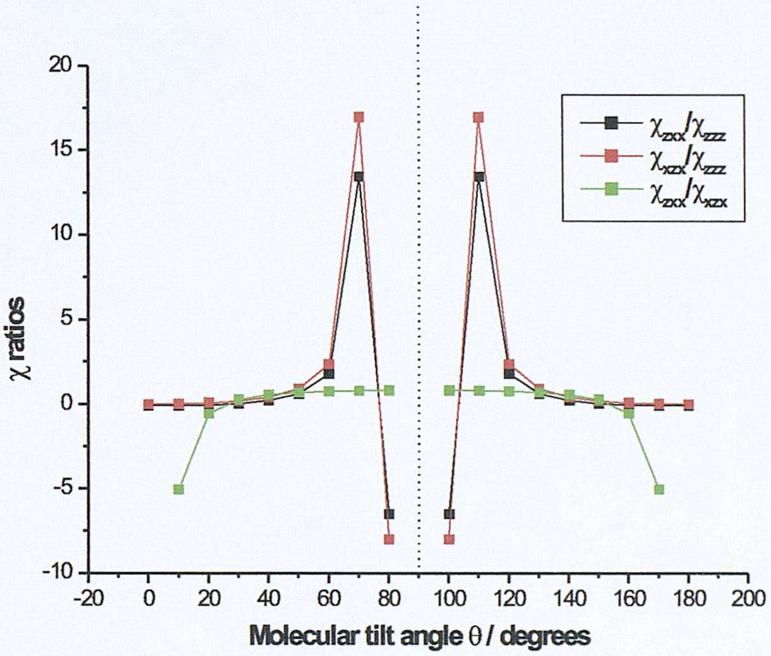

Figure 9.16: The $\vec{\chi}^{(2)}$ tensor ratio ($\chi^{(2)}_{ZXX}/\chi^{(2)}_{ZZZ}$, $\chi^{(2)}_{XZX}/\chi^{(2)}_{ZZZ}$ and $\chi^{(2)}_{ZXX}/\chi^{(2)}_{XZX}$) as a function of the tilt molecular angle θ assuming the β_{zzz} and β_{zxx} tensors to be dominant.

9.2.4.2 P and S output SHG polarisation curves

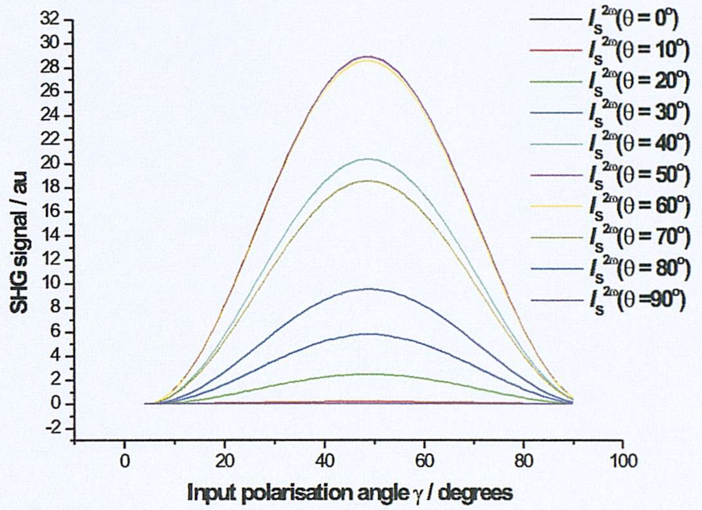

Figure 9.17: $I_{\mathrm{S}}^{(2\omega)}$ SHG intensities for different molecular tilt angles as a function of the input polarisation angle γ assuming the β_{zzz} and β_{zxx} tensors to be dominant.

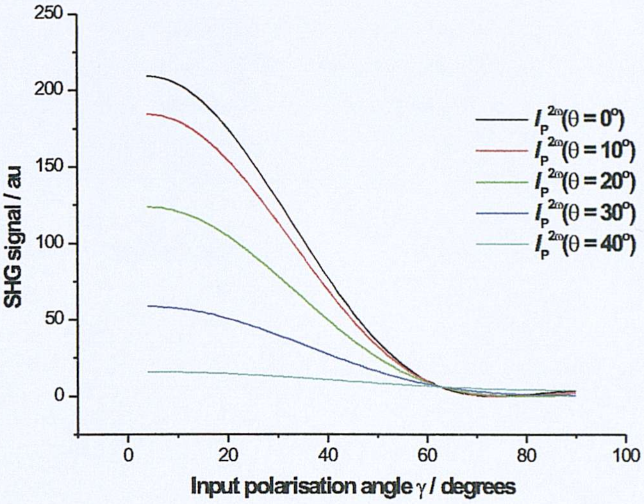

Figure 9.18: $I_P^{(2\omega)}$ SHG intensities for different molecular tilt angles (0-40^o) as a function of the input polarisation angle γ assuming the β_{zzz} and β_{zxx} tensors to be dominant.

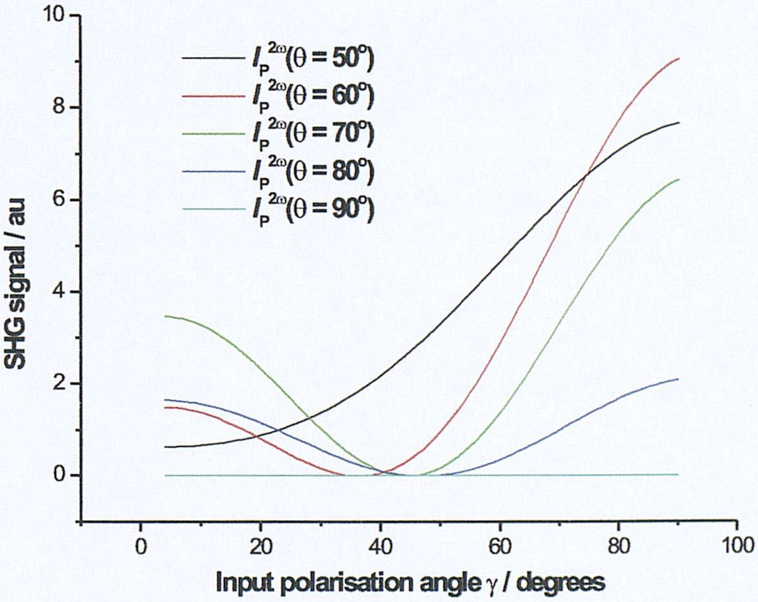

Figure 9.19: $I_P^{(2\omega)}$ SHG intensities for different molecular tilt angles (50-90^o) as a function of the input polarisation angle γ assuming the β_{zzz} and β_{zxx} tensors to be dominant.

9.2.5 β_{zzz} and β_{xzx} dominant

Equations 9.35-9.37 for a random distribution for the ψ angle were used to calculate the $\vec{\chi}^{(2)}$ tensor values and ratios using the estimated Fresnel coefficients for the air/water interface and assuming no absorption from the interfacial molecules at the fundamental or harmonic wavelength. The hyperpolarisability tensor value for the ratio $\beta_{zxx}/bzzz$ was set to 0.20 and N_s/ϵ_o was set to one.

9.2.5.1 $\vec{\chi}^{(2)}$ tensor values and ratios

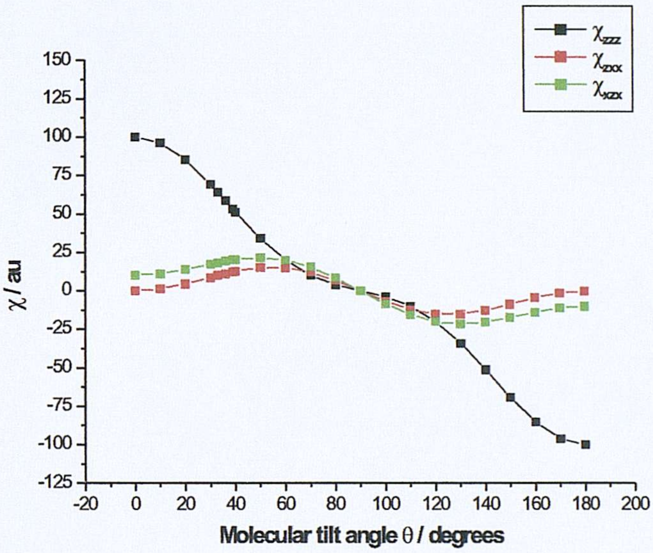

Figure 9.20: The $\vec{\chi}^{(2)}$ tensor components ($\chi^{(2)}_{ZZZ}$, $\chi^{(2)}_{ZXX}$ and $\chi^{(2)}_{XZX}$) as a function of the molecular tilt angle θ assuming the β_{zzz} and β_{xzx} tensors to be dominant.

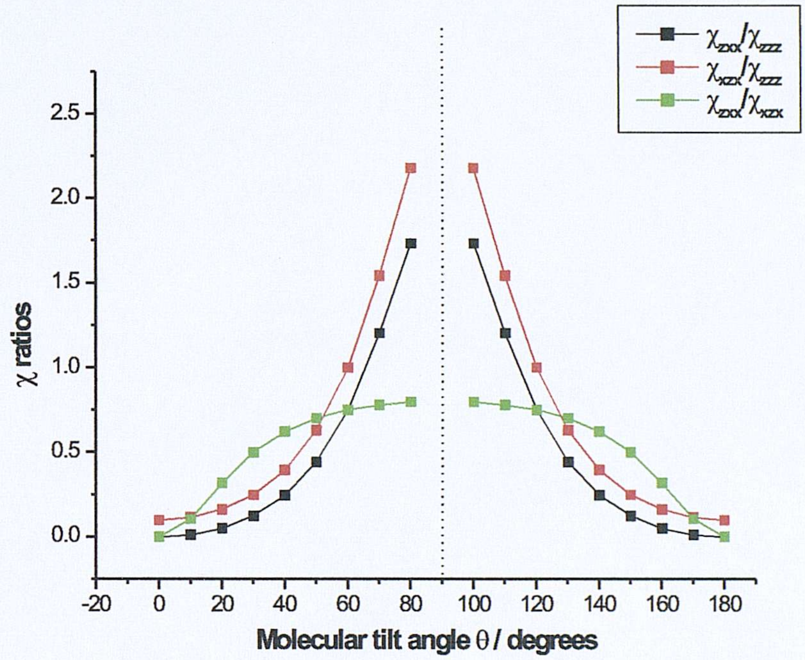

Figure 9.21: The $\vec{\chi}^{(2)}$ tensor ratio ($\chi^{(2)}_{ZXX}/\chi^{(2)}_{ZZZ}$, $\chi^{(2)}_{XZX}/\chi^{(2)}_{ZZZ}$ and $\chi^{(2)}_{ZXX}/\chi^{(2)}_{XZX}$) as a function of the tilt molecular angle θ assuming the β_{zzz} and β_{xzx} tensors to be dominant.

9.2.5.2 P and S output SHG polarisation curves

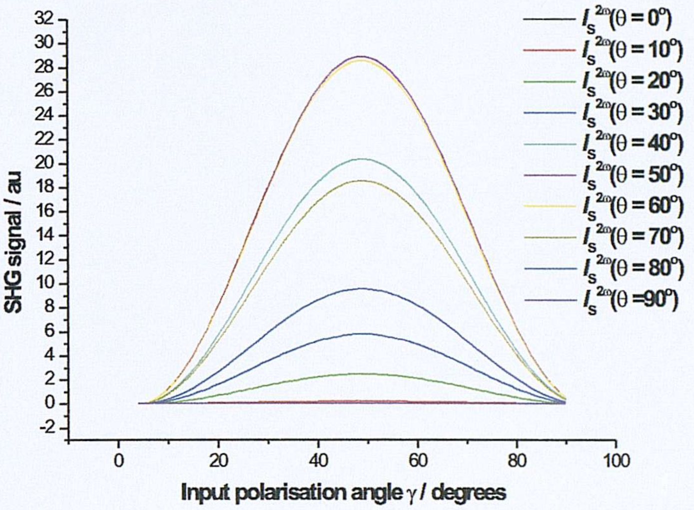

Figure 9.22: $I_s^{(2\omega)}$ SHG intensities for different molecular tilt angles as a function of the input polarisation angle γ assuming the β_{zzz} and β_{xzx} tensors to be dominant.

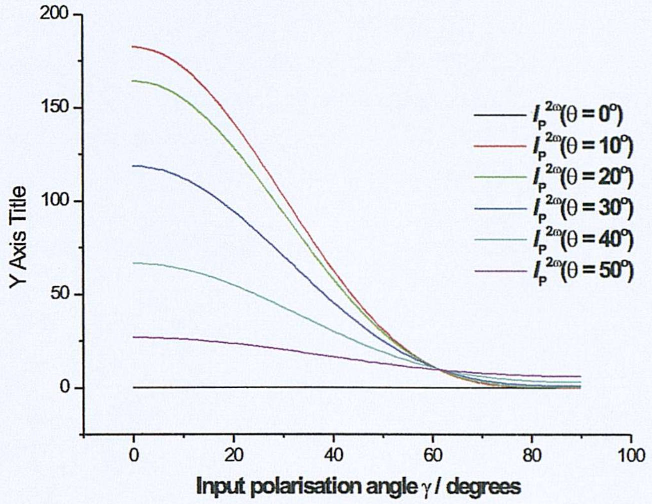

Figure 9.23: $I_P^{(2\omega)}$ SHG intensities for different molecular tilt angles (0-50^o) as a function of the input polarisation angle γ assuming the β_{zzz} and β_{xzx} tensors to be dominant.

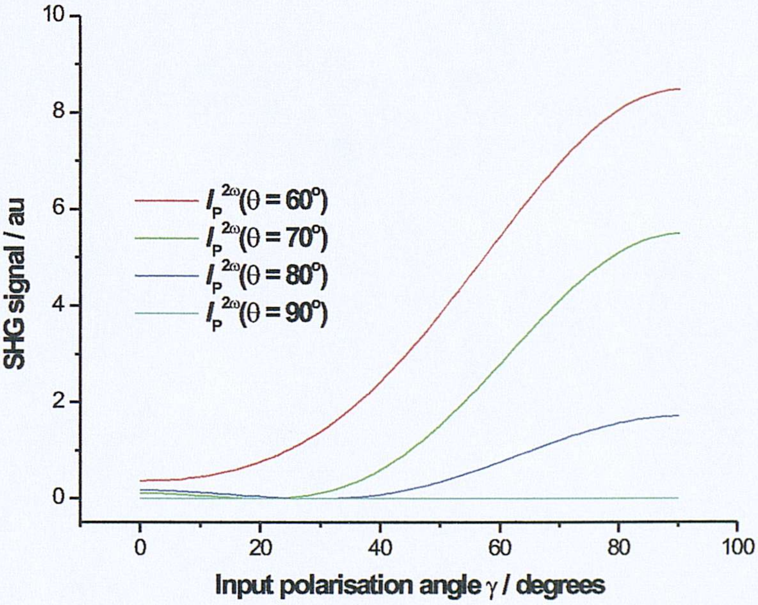

Figure 9.24: $I_P^{(2\omega)}$ SHG intensities for different molecular tilt angles (60-90^o) as a function of the input polarisation angle γ assuming the β_{zzz} and β_{zxx} tensors to be dominant.

9.2.6 β_{zxx} and β_{xzx} dominant

Equations 9.44-9.46 for a random distribution for the ψ angle were used to calculate the $\vec{\chi}^{(2)}$ tensor values and ratios using the estimated Fresnel coefficients for the air/water interface and assuming no absorption from the interfacial molecules at the fundamental or harmonic wavelength. The hyperpolarisability tensor value for the ratio β_{zxx}/β_{xzx} was set to 1.3 and N_s/ϵ_o was set to one.

9.2.6.1 $\vec{\chi}^{(2)}$ tensor values and ratios

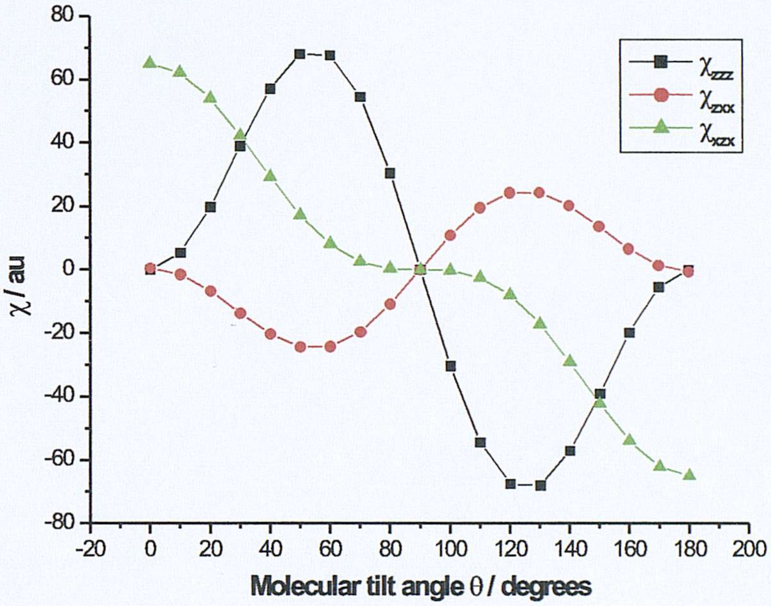

Figure 9.25: The $\vec{\chi}^{(2)}$ tensor components ($\chi^{(2)}_{ZZZ}$, $\chi^{(2)}_{ZXX}$ and $\chi^{(2)}_{XZX}$) as a function of the molecular tilt angle θ assuming the β_{zxx} and β_{xzx} tensors to be dominant.

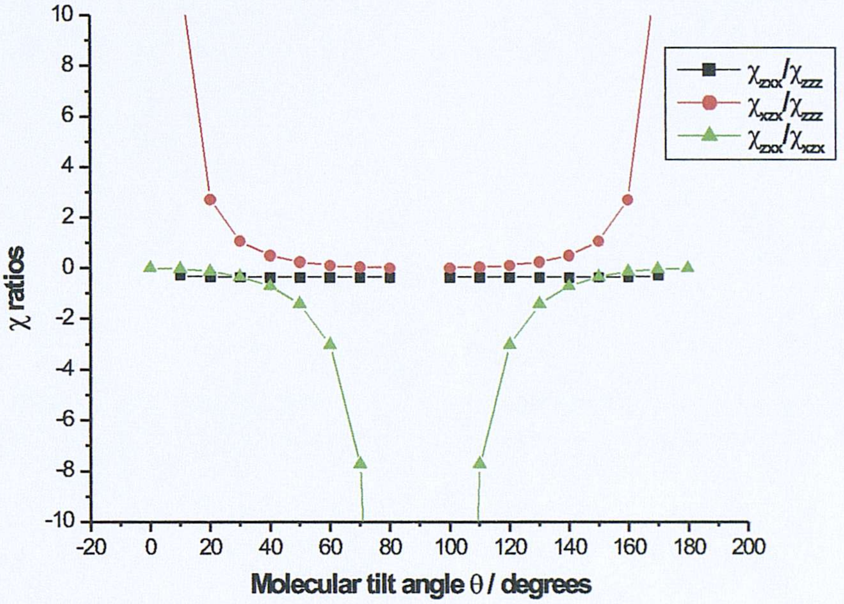

Figure 9.26: The $\vec{\chi}^{(2)}$ tensor ratio ($\chi^{(2)}_{ZXX}/\chi^{(2)}_{ZZZ}$, $\chi^{(2)}_{XZX}/\chi^{(2)}_{ZZZ}$ and $\chi^{(2)}_{ZXX}/\chi^{(2)}_{XZX}$) as a function of the tilt molecular angle θ assuming the β_{zxx} and β_{xzx} tensors to be dominant.

9.2.6.2 P and S output SHG polarisation curves

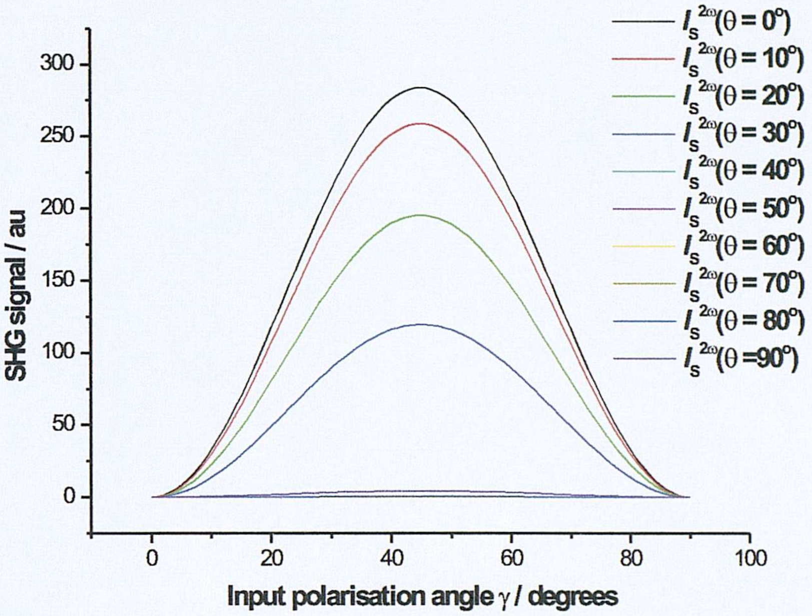

Figure 9.27: $I_s^{(2\omega)}$ SHG intensities for different molecular tilt angles as a function of the input polarisation angle γ assuming the β_{zxx} and β_{xzx} tensors to be dominant.

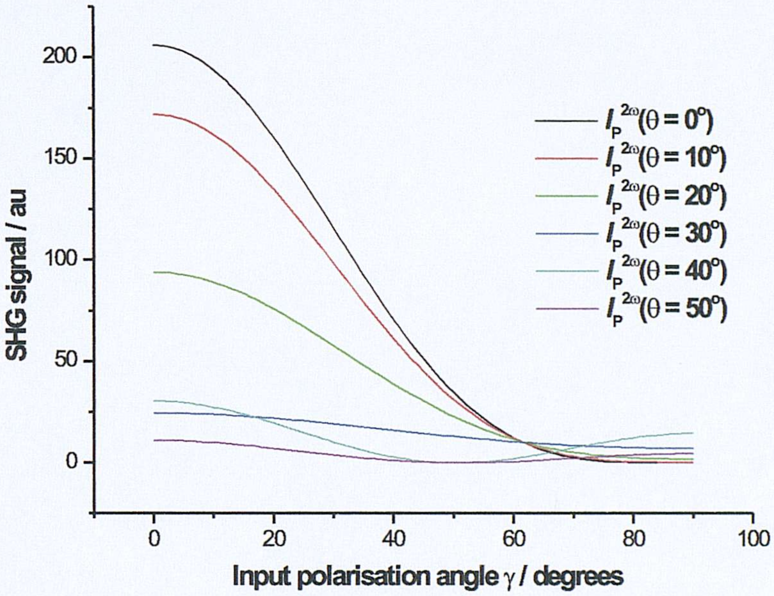

Figure 9.28: $I_P^{(2\omega)}$ SHG intensities for different molecular tilt angles (0-50^o) as a function of the input polarisation angle γ assuming the β_{zxx} and β_{xzx} tensors to be dominant.

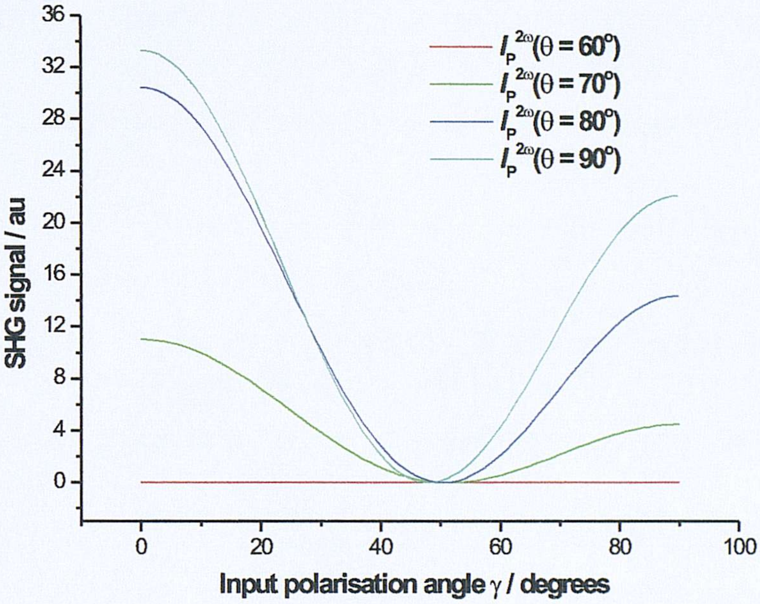

Figure 9.29: $I_P^{(2\omega)}$ SHG intensities for different molecular tilt angles (60-90^o) as a function of the input polarisation angle γ assuming the β_{zxx} and β_{xzx} tensors to be dominant.

Bibliography

[1] A. W. Adamson and A. P. Gast, *Physical Chemistry of Surfaces*, sixth ed. (Wiley, New York, 1997).

[2] M. J. Jaycock and G. D. Parfitt, *Chemistry of Interfaces*, *Chemical Science* (Ellis Horwood, Chichester, 1987).

[3] G. A. Somorjai, *Introduction to Surface Chemistry and Cataysis* (Wiley, New York, 1994).

[4] D. P. Woodruff and T. A. Delchar, *Modern techniques of Surface Science* (Cambridge University Press, Cambridge, 1994).

[5] C. M. Banwell and E. M. McCash, *Fundamentals of Molecular Spectroscopy*, fourth edition ed. (Tata McGraw-Hill, New Delhi, 1994).

[6] J. M. Hollas, *Modern Spectroscopy*, third edition ed. (John Wiley and Sons, Chichester, 1996).

[7] F. Trager, H. Confal, and T. J. Chuang. *Phys. Rev. Lett.* **49**, 1720 (1982).

[8] S. Weiss. *Science* **283**, 1689–1695 (1999).

[9] C. A. Royer, *Fluorescence Spectroscopy in Protein Stability and Folding* (Humana Press, Totowa, NJ, 1995), Vol. 40.

[10] D. J. Shaw, *Introduction to colloid and surface science*, third edition ed. (Butterworths, London, 1980).

[11] G. Tompkins, *A User's Guide to Ellipsometry* (Academic Press, New York, 1993).

[12] F. M. Mirabella, *Internal Reflection Spectroscopy: Theory and Applications (Practical Spectroscopy)* (Marcel Dekker, London, 1992).

[13] Y. R. Shen. *Annu. Rev. Phys. Chem.* **40**, 327–350 (1989).

[14] K. B. Eisenthal. *Annu. Rev. Phys. Chem.* **43**, 627–661 (1992).

[15] R. M. Corn and D. A. Higgins. *Chem. Rev.* **94**, 107 (1994).

[16] C. T. Williams and D. A. Beattie. *Surf. Sci.* **500**, 545–576 (2002).

[17] P. F. Brevet, *Surface Second Harmonic Generation* (Presses Polytechniques et Universitaires Romandes, Lausanne, 1997).

[18] P. B. Miranda and Y. R. Shen. *J. Phys. Chem. B* **103**, 13090 (1999).

[19] F. Jensen, *Introduction to Computational Chemistry* (John Wiley and Sons, New York, 1999).

[20] T. H. Maiman. *Nature* **187**, 493 (1960).

[21] J. Hecht, *Understanding Lasers* (Howard W. Sams and Company, Indianapolis, 1988).

[22] D. L. Andrews and A. A. Demidov, *An Introduction to Laser Spectroscopy* (Plenium Press, New York, 1995).

[23] O. Svelto, *Principles of Lasers* (Plenum Press, New York, 1998).

[24] R. M. Corn. *Anal. Chem.* **63**, 4285 (1991).

[25] K. B. Eisenthal. *Acc. Chem. Res.* **26**, 636–643 (1993).

[26] K. B. Eisenthal. *Chem. Rev.* **96**, 1343–1360 (1996).

[27] Y. R. Shen. *Annu. Rev. Mater. Sci.* **16**, 69–86 (1986).

[28] G. J. Simpson and K. L. Rowlen. *Acc. Chem. Res.* **33**, 781–789 (2000).

[29] G. J. Simpson and K. L. Rowlen. *Anal. Chem.* **72**, 3399–3406 (2000).

[30] G. J. Simpson and K. L. Rowlen. *Anal. Chem.* **72**, 3407–3411 (2000).

[31] T. F. Heinz, C. K. Chen, D. Ricard, and Y. R. Shen. *Phys. Rev. Lett.* **48**, 478–481 (1982).

[32] S. Haslam, S. G. Croucher, C. G. Hickman, and J. G. Frey. *Phys. Chem. Chem. Phys. (PCCP)* **2**, 3235–3245 (2000).

[33] S. R. Meech and K. Yoshihara. *Chem. Phys. Lett.* **174**, 423–427 (1990).

[34] A. Castro, E. V. Sitzmann, D. Zhang, and K. B. Eisenthal. *J. Phys. Chem.* **95**, 6752–6753 (1991).

[35] D. Zimdars, J. I. Dadap, K. B. Eisenthal, and T. F. Heinz. *Chem. Phys. Lett.* **301**, 112–120 (1999).

[36] R. Antoine, A. A. Tamburello-Luca, P. Hebert, P. F. Brevet, and H. H. Girault. *Chem. Phys. Lett.* **288**, 138–146 (1998).

[37] J. A. Ekhoff and K. L. Rowlen. *Anal. Chem.* **74**, 5954–5959 (2002).

[38] D. A. Higgins, S. K. Byerly, M. B. Abrams, and R. M. Corn. *J. Phys. Chem.* **95**, 6984–6990 (1991).

[39] J. G. Frey. *Chem. Phys. Lett.* **323**, 454–459 (2000).

[40] A. Castro, K. Bhattacharyya, and K. B. Eisenthal. *J. Chem. Phys.* **95**, 1310–1315 (1991).

[41] M. C. Petty, *Langmuir-Blodgett Films-An Introduction* (Cambridge University Press, Cambridge, 1996).

[42] X. Zhuang, P. B. Miranda, D. Kim, and Y. R. Shen. *Phys. Rev. B* **59**, 12632–12640 (1999).

[43] Y. A. Gruzdkov and V. N. Parmon. *J. Chem. Soc.-Faraday Trans.* **89**, 4017–4026 (1993).

[44] A. H. Welsh, R. A. Mansson, J. G. Frey, and L. Danos. *Submitted to Chemometrics and Intelligent Laboratory Systems* , (2003).

[45] http://cran.r-project.org.

[46] W. N. Venables and B. D. Ripley, *Modern Applied Statisticas with S*, *Statistics and Computing*, fourth ed. (Springer, New York, 2002).

[47] G. H. Grant and W. G. Richards, *Computational Chemistry* (Oxford University Press, Oxford, 1996).

[48] J. M. Dyke, Introduction to Electronic Structure Theory, 2003.

[49] E. J. Baerends, J. A. Autschbach, A. Brces, C. Bo, P. M. Boerrigter, L. Cavallo, D. P. Chong, R. L. Deng, M. Dickson, D. E. Ellis, L. Fan, T. H. Fischer, C. F. Guerra, S. J. A. v. Gisbergen, J. A. Groeneveld, O. V. Gritsenko, M. Grning, F. E. Harris, P. v. d. Hoek, H. Jacobsen, G. v. Kessel, F. Kootstra, E. v. Lenthe, V. P. Osinga, S. Patchkovskii, P. H. T. Philipsen, D. Post, C. C. Pye, W. Ravenek, P. Ros, P. R. T. Schipper, G. Schreckenbach, J. G. Snijders, M. Sola, M. Swart, D. Swerhone, G. t. Velde, P. Vernooijs, L. Versluis, O. Visser, E. v. Wezenbeek, G. Wiesenekker, S. K. Wolff, T. K. Woo, and T. Ziegler, *ADF2002.03* (SCM, Theoretical Chemistry, Vrije Universiteit,, Amsterdam, The Netherlands, http://www.scm.com, 2002).

[50] M. J. Frisch, G. W. Trucks, H. B. Schlegel, P. M. W. Gill, B. G. Johnson, M. A. Robb, J. R. Cheeseman, T. Keith, G. A. Petersson, J. A. M. Jr, K. Raghavachari, M. A. Al-Laham, V. G. Zakrzewski, J. V. Ortiz, J. B. Foresman, J. Cioslowski, B. B. Stefanov, A. Nanayakkara, M. Challacombe, C. Y. Challacombe, P. Y. Ayala, A. W. Chen, M. W. Wong, J. L. Andres, E. S. Replogle, R. Gomperts, R. L. Martin, D. J. Fox, J. S. Binkley, D. J. Fox, J. Baker, J. J. P. Stewart, M. Head-Gordon, C. Gonzalez, and J. A. Pople, *GAUSSIAN94* (Gaussian Inc., Pittsburgh, PA, 1995).

[51] M. J. Frisch, G. W. Trucks, H. B. Schlegel, G. E. Scuseria, M. A. Robb, J. R. Cheeseman, V. G. Zakrzewski, J. A. M. Jr., R. E. Stratmann, J. C. Burant, S. Dapprich, J. M. Millam, A. D. Daniels, K. N. Kudin, M. C. Strain, O. Farkas, J. Tomasi, V. Barone, M. Cossi, R. Cammi, B. Mennucci, C. Pomelli, C. Adamo, S. Clifford, J. Ochterski, G. A. Petersson, P. Y. Ayala, Q. Cui, K. Morokuma, N. Rega, P. Salvador, J. J. Dannenberg, D. K. Malick, A. D. Rabuck, K. Raghavachari, J. B. Foresman, J. Cioslowski, J. V. Ortiz, A. G. Baboul, B. B. Stefanov, G. Liu, A. Liashenko, P. Piskorz, I. Komaromi, R. Gomperts, R. L. Martin, D. J. Fox, T. Keith, M. A. Al-Laham, C. Y. Peng, A. Nanayakkara, M. Challacombe, P. M. W. Gill,

B. Johnson, W. Chen, M. W. Wong, J. L. Andres, C. Gonzalez, M. Head-Gordon, E. S. Replogle, and J. A. Pople, *GAUSSIAN98, Revision A7* (Gaussian, Inc., Pittsburgh, PA, 1998).

[52] R. D. Amos, I. L. Alberts, J. S. Andrews, S. M. Colwell, N. C. Handy, D. Jayatilaka, P. J. Knowles, R. Kobayashi, G. J. Laming, A. M. Lee, P. E. Maslen, C. W. Murray, P. Palmieri, J. E. Rice, E. D. Simandiras, A. J. Stone, M.-D. Su, and D. J. Tozer, *CADPAC6.5.* (The Cambridge Analytic Derivatives Package, Cambridge, UK, 1998).

[53] M. W. Schmidt, K. K. Baldridge, J. A. Boatz, S. T. Elbert, M. S. Gordon, J. J. Jensen, S. Koseki, N. Matsunaga, K. A. Nguyen, S. Su, T. L. Windus, M. Dupuis, and J. A. Montgomery. *J. Comput. Chem* **14**, 1347–1363 (1993).

[54] C. C. J. Roothaan. *Review of Modern Physics* **23**, 69–89 (1951).

[55] R. G. Parr, *The Quantum Theory of Molecular Electronic Structure* (W. A. Benjamin, New York, 1964).

[56] K. Raghavachari and J. B. Anderson. *J. Phys. Chem* **100**, 12960–12973 (1996).

[57] W. Kohn, A. D. Becke, and R. G. Parr. *J. Phys. Chem* **100**, 12974–12980 (1996).

[58] P. Hohenberg and W. Kohn. *Phys. Rev.* **136**, 864 (1964).

[59] W. kohn and L. J. Sham. *Phys. Rev.* **140**, 1133 (1965).

[60] W. Koch and M. C. Holthausen, *A Chemists Guide to Density Functional Theory.*, second edition ed. (Wiley-VCH Verlag GmbH, Weinheim, 2001).

[61] S. J. A. v. Gisbergen, J. G. Snijders, and E. J. Baerends. *J. Chem. Phys.* **109**, 10644–10656 (1998).

[62] H. H. Heinze, F. D. Sala, and A. Grling. *J. Chem. Phys.* **116**, 9624–9640 (2002).

[63] N. C. Handy and D. J. Tozer. *J. Comput. Chem.* **20**, 106–113 (1999).

[64] A. J. Cohen, N. C. Handy, and D. J. Tozer. *Chem. Phys. Lett.* **303**, 391–398 (1999).

[65] C. Møller and M. S. Plesset. *Phys. Rev.* **46**, 618 (1934).

[66] I. N. Levine, *Quantum Chemistry*, fourth ed. (Prentice Hall, New Jersey, 1991).

[67] P. W. Atkins and R. S. Friedman, *Molecular Quantum Mechanics*, third edition ed. (Oxford University Press, New York, 1997).

[68] D. P. Shelton and J. E. Rice. *Chem. Rev.* **94**, 3–29 (1994).

[69] A. Willetts, J. E. Rice, and D. M. Burland. *J. Chem. Phys.* **97**, 7590–7599 (1992).

[70] J. E. Rice, R. D. Amos, S. M. Colwell, N. C. Handy, and J. Sanz. *J. Chem. Phys.* **93**, 8828 (1990).

[71] J. E. Rice and N. C. Handy. *Int. J. Quantum Chem.* **43**, 91 (1992).

[72] S. P. Karna and M. Dupuis. *Journal of Computational Chemistry* **12**, 487 (1991).

[73] H. Sekino and R. J. Barlett. *J. Chem. Phys.* **85**, 976–989 (1986).

[74] H. Sekino and R. J. Barlett. *Int. J. Quantum Chem.* **43**, 119 (1992).

[75] M. Stahelin, D. M. Burland, and J. E. Rice. *Chem. Phys. Lett.* **191**, 245 (1992).

[76] L. T. Cheng, W. Tam, S. H. Stevenson, G. R. Meredith, G. Rikken, and S. R. Marder. *J. Phys. Chem.* **95**, 10631 (1991).

[77] S. J. A. v. Gisbergen, J. G. Snijders, and E. J. Baerends. *J. Chem. Phys.* **109**, 10657–10668 (1998).

[78] B. Champagne, E. A. Perpete, D. Jacquemin, S. J. A. van Gisbergen, E. J. Baerends, C. Soubra-Ghaoui, K. A. Robins, and B. Kirtman. *J. Phys. Chem. A* **104**, 4755–4763 (2000).

[79] Z.-L. Cai, K. Sendt, and J. R. Reimers. *J. Chem. Phys.* **117**, 5543–5549 (2002).

[80] D. J. Tozer and N. C. Handy. *J. Chem. Phys.* **109**, 10180–10189 (1998).

[81] D. J. Tozer and N. C. Handy. *J. Phys. Chem.* **102**, 3162–3168 (1998).

[82] D. J. Tozer and N. C. Handy. *J. Chem. Phys.* **108**, 2545–2555 (1998).

[83] F. A. Hamprecht, A. J. Cohen, D. J. Tozer, and N. C. Handy. *J. Chem. Phys.* **109**, 6264–6271 (1998).

[84] A. D. Becke. *J. Chem. Phys.* **107**, 8554–8560 (1997).

[85] G. A. Petersson, D. K. Malick, W. G. Wilson, J. W. Ochterski, J. A. Montgomery, and M. J. Frisch. *J. Chem. Phys.* **109**, 10570 (1998).

[86] R. v. Leeuwen and E. J. Baerends. *Phys. Rev. A* **49**, 2421 (1994).

[87] R. Antoine, F. Bianchi, P. F. Brevet, and H. H. Girault. *J. Chem. Soc.-Faraday Trans.* **93**, 3833–3838 (1997).

[88] W. A. Kreiner, H. D. Rudolph, and B. T. Tan. *J. Mol. Spectrosc.* **48**, 86–99 (1973).

[89] P. J. Breen, J. A. Warren, and E. R. Bernstein. *J. Chem. Phys.* **87**, 1917 (1987).

[90] R. D. Gordon and J. M. Hollas. *Chem. Phys. Lett.* **164**, 255–260 (1989).

[91] P. C. Chen and C. W. Wu. *J. Phys. Chem.* **99**, 15023–15027 (1995).

[92] H. F. Hameka and J. O. Jensen. *J. Mol. Struct. (Theochem)* **331**, 203–214 (1995).

[93] H. F. Hameka and J. O. Jensen. *J. Mol. Struct. (Theochem)* **362**, 325–330 (1996).

[94] T. Iijima. *Z. Naturforsch* **32 A**, 1063 (1977).

[95] R. Seip, G. Schultz, I. Hargittai, and Z. G. Szabo. *Z. Naturforsch* **32 A**, 1178–1183 (1977).

[96] D. T. Cramb, S. C. Martin, and S. C. Wallace. *J. Phys. Chem.* **100**, 446–448 (1996).

[97] H. Du, R.-C. A. Fuh, J. Li, L. A. Corkan, and J. S. Lindsey. *Photochem. Photobiol.* **68**, 141–142 (1998).

[98] I. B. Berlman, *Handbook of Fluorescence Spectra of Aromatic Molecules* (Academic Press Inc., New York, 1965).

[99] S. J. Vosko, L. Wilk, and M. Nusair. *Can. J. Phys.* **58**, 1200 (1980).

[100] R. G. Parr and W. Yang, *Density functional Theory of Atoms and Molecules* (Oxford University Press, Oxford, UK, 1989).

[101] A. D. Becke. *Phys. Rev. A* **38**, 3098 (1988).

[102] C. Lee, W. Yang, and R. G. Parr. *Phys. Rev. B* **37**, 785 (1988).

[103] J. P. Perdew, K. Burke, and M. Ernzerhof. *Phys. Rev. Lett.* **77**, 3865 (1996).

[104] J. P. Perdew and Y. Wang. *Phys. Rev. B* **33**, 8800 (1986).

[105] J. P. Perdew and Y. Wang. *Phys. Rev. B* **45**, 13244 (1992).

[106] A. D. Boese, N. L. Doltsinis, N. C. Handy, and M. Spriek. *J. Chem. Phys.* **112**, 1670 (2000).

[107] A. D. Boese and N. C. Handy. *J. Chem. Phys.* **114**, 5497 (2001).

[108] A. D. Becke. *J. Chem. Phys.* **98**, 5648 (1993).

[109] P. J. Stephens, F. J. Devlin, C. F. Chabalowski, and M. J. Frisch. *J. Phys. Chem.* **98**, 11623 (1994).

[110] M. Ernzerhof and G. E. Scuseria. *J. Chem. Phys.* **110**, 5029 (1999).

[111] C. Adamo and V. Barone. *J. Chem. Phys.* **110**, 6158 (1999).

[112] M. Grning, O. V. Gritsenko, S. J. A. v. Gisbergen, and E. J. Baerends. *J. Chem. Phys.* **114**, 652–660 (2001).

[113] P. R. T. Schipper, O. V. Gritsenko, S. J. A. v. Gisbergen, and E. J. Baerends. *J. Chem. Phys.* **112**, 1344–1352 (2000).

[114] G. Menconi and D. J. Tozer. *Chem. Phys. Lett.* **360**, 3846 (2002).

[115] R. Bauernschmitt and R. Ahlrichs. *Chem. Phys. Lett.* **256**, 454 (1996).

[116] M. E. Casida, C. Jamorski, K. C. Casida, and D. R. Salahub. *J. Chem. Phys.* **108**, 4439 (1998).

[117] E. P. A'zary and C. C. Bigelow. *Can. J. Biochem.* **48**, 953–961 (1970).

[118] T. Verbiest, S. Houbrechts, M. Kauranen, K. Clays, and A. Persoons. *J. Mater. Chem.* **7**, 2175–2189 (1997).

[119] B. J. Sherman, S. Sen, and V. Galiatsatos. *Polymer* **37**, 1759–1764 (1996).

[120] K. Kemnitz, K. Bhattacharyya, J. M. Hinks, G. R. Pinto, K. B. Eisenthal, and T. F. Heinz. *Chem. Phys. Lett.* **131**, 285–290 (1986).

[121] B. D. Casson and C. D. Bain. *Langmuir* **17**, 5465 (1997).

[122] P. Guyot-Sionnest and Y. R. Shen. *Appl. Phys. B* **42**, 237 (1987).

[123] H. El-Kashef. *Opt. Mater.* **20**, 81–86 (2002).

[124] A. A. Tamburello-Luca, P. Hebert, P. Brevet, and H. H. Girault. *J. Chem. Soc.-Faraday Trans.* **91**, 1763–1768 (1995).

[125] T. L. Mazely and W. M. Hetherington. *J. Chem. Phys.* **86**, 3640–3647 (1986).

[126] J. A. Ekhoff, M. J. Farrow, D. M. Walba, and K. L. Rowlen. *Talanta* **13**, 1–8 (2003).

[127] X. Cao and G. Fischer. *J. Mol. Struct. (Theochem)* **519**, 153–163 (2000).

[128] L. C. Snoek, E. G. Robertson, R. T. Kroemer, and J. P. Simons. *Chem. Phys. Lett.* **321**, 49–56 (2000).

[129] J. S. Salafsky. *Chem. Phys. Lett.* **342**, 485–491 (2001).

[130] V. Vogel and B. L. Smiley. *SPIE-INT. Soc. Opt. Eng.* **1922**, 86–93 (1992).

[131] B. L. Smiley and V. Vogel. *SPIE-INT. Soc. Opt. Eng.* **2125**, 59–67 (1994).

[132] S. A. Asher, M. Ludwig, and C. R. Johnson. *J. Am. Chem. Soc.* **108**, 3186–3197 (1986).

[133] S. J. Martinez, J. C. Alfano, and D. H. Levy. *J. Mol. Spectrosc.* **156**, 421–430 (1992).

[134] S. J. Martinez, J. C. Alfano, and D. H. Levy. *J. Mol. Spectrosc.* **158**, 82–93 (1993).

[135] P. S. Kushwaha and P. C. Mishra. *J. Photochem. Photobio. A* **137**, 79–86 (2000).

[136] H. F. Hameka and J. O. Jensen. *J. Mol. Struct. (Theochem)* **288**, 9–16 (1993).

[137] K. T. Lee, J. Sung, K. J. Lee, S. K. Kim, and Y. D. Park. *J. Chem. Phys.* **116**, 8251–8254 (2002).

[138] F. M. Siu, N. L. Ma, and C. W. Tsang. *J. Am. Chem. Soc.* **123**, 3397–3398 (2001).

[139] R. C. Dunbar. *J. Phys. Chem. A* **104**, 8067–8074 (2000).

[140] J. P. Duneau, N. Garnier, G. Cremelb, G. Nullansb, P. Hubertb, D. Genesta, M. Vincentc, J. Gallay, and M. Genesta. *Biophys. Chem.* **73**, 109–119 (1998).

[141] D. L. Andrews, *Lasers in Chemistry*, third edition ed. (Springer, London, 1997).

[142] A. Fischer, C. Cremer, and E. H. K. Stelzer. *Appl. Optics* **34**, 1989–2003 (1995).

[143] G. J. Simpson and K. L. Rowlen. *J. Am. Chem. Soc.* **121**, 2635–2636 (1999).

[144] D. A. Steinhurst and J. C. Owrutsky. *J. Phys. Chem. B* **105**, 3062–3072 (2000).

[145] D. W. Quick, Mres thesis, University of Southampton, 1997.

[146] A. Maxwell, Mres thesis, University of Southampton, 2000.

[147] K. Bhattacharyya, A. Castro, E. V. Sitzmann, and K. B. Eisenthal. *J. Chem. Phys.* **89**, 3376–3377 (1988).

[148] X. Zhao, S. Subrahmanyan, and K. B. Eisenthal. *Chem. Phys. Lett.* **171**, 558–562 (1990).

[149] A. A. Tamburello-Luca, P. Hebert, R. Antoine, P. F. Brevet, and H. H. Girault. *Langmuir* **13**, 4428–4434 (1997).

[150] J. E. Selwyn and J. I. Steinfeild. *J. Phys. Chem.* **76**, 762 (1972).

[151] T. P. Burghardt, J. E. Lyke, and K. Ajtai. *Biophys. Chem.* **59**, 119 (1996).

[152] L. Arbeloa and P. R. Ojeda. *Chem. Phys. Lett.* **87**, 556 (1982).

[153] R. W. Chambers, T. Kajiwara, and D. R. Kearns. *J. Phys. Chem.* **78**, 380 (1974).

[154] D. Toptygin, B. Z. Packard, and L. Brand. *Chem. Phys. Lett.* **277**, 430–435 (1997).

[155] A. Rose, Quarterly report, University of Southampton (unpublished).

[156] E. G. McRae and M. Kasha. *J. Chem. Phys.* **28**, 721 (1958).

[157] R. M. Hochstrasser and M. Kasha. *Photochem. Photobiol.* **3**, 317 (1964).

[158] M. Kasha, H. R. Rawls, and M. A. El-Bayoumi. *Pure Appl. Chem.* **11**, 371 (1965).

[159] T. Kikteva, D. Star, Z. Zhao, T. L. Baisley, and G. W. Leach. *J. Phys. Chem. B* **103**, 1124–1133 (1999).

[160] O. N. Slyadneva, M. N. Slyadnev, V. M. Tsukanova, T. Inoue, A. Harata, and T. Ogawa. *Langmuir* **15**, 8651–8658 (1999).

[161] A. Alexander, Ph.d. thesis, University of Southampton, 2001.

[162] X. Shi, E. Borguet, A. N. Tarnovsky, and K. B. Eisenthal. *Chem. Phys.* **205**, 167–178 (1996).

[163] N. E. Levinger, K. Y. Kung, B. M. Luther, and D. M. Willard. *Proceedings of SPIE* **2547**, 400–410 (1995).

[164] H. F. Wang, E. Borguet, and K. B. Eisenthal. *J. Phys. Chem. A* **101**, 713–718 (1997).

[165] H. F. Wang, E. Borguet, and K. B. Eisenthal. *J. Phys. Chem. B* **102**, 4927–4932 (1998).

[166] B. Dick. *Chem. Phys.* **96**, 199–215 (1985).

[167] T. Kikteva, D. Star, and G. W. Leach. *J. Phys. Chem. B* **104**, 2860–2867 (2000).

[168] This work is underway.